NASA/CR—2000-209805

Laser-Induced Fluorescence Measurements and Modeling of Nitric Oxide in Counterflow Diffusion Flames

Rayavarapu V. Ravikrishna and Normand M. Laurendeau
Purdue University, West Lafayette, Indiana

February 2000

The NASA STI Program Office . . . in Profile

Since its founding, NASA has been dedicated to the advancement of aeronautics and space science. The NASA Scientific and Technical Information (STI) Program Office plays a key part in helping NASA maintain this important role.

The NASA STI Program Office is operated by Langley Research Center, the Lead Center for NASA's scientific and technical information. The NASA STI Program Office provides access to the NASA STI Database, the largest collection of aeronautical and space science STI in the world. The Program Office is also NASA's institutional mechanism for disseminating the results of its research and development activities. These results are published by NASA in the NASA STI Report Series, which includes the following report types:

- TECHNICAL PUBLICATION. Reports of completed research or a major significant phase of research that present the results of NASA programs and include extensive data or theoretical analysis. Includes compilations of significant scientific and technical data and information deemed to be of continuing reference value. NASA's counterpart of peer-reviewed formal professional papers but has less stringent limitations on manuscript length and extent of graphic presentations.

- TECHNICAL MEMORANDUM. Scientific and technical findings that are preliminary or of specialized interest, e.g., quick release reports, working papers, and bibliographies that contain minimal annotation. Does not contain extensive analysis.

- CONTRACTOR REPORT. Scientific and technical findings by NASA-sponsored contractors and grantees.

- CONFERENCE PUBLICATION. Collected papers from scientific and technical conferences, symposia, seminars, or other meetings sponsored or cosponsored by NASA.

- SPECIAL PUBLICATION. Scientific, technical, or historical information from NASA programs, projects, and missions, often concerned with subjects having substantial public interest.

- TECHNICAL TRANSLATION. English-language translations of foreign scientific and technical material pertinent to NASA's mission.

Specialized services that complement the STI Program Office's diverse offerings include creating custom thesauri, building customized data bases, organizing and publishing research results . . . even providing videos.

For more information about the NASA STI Program Office, see the following:

- Access the NASA STI Program Home Page at ***http://www.sti.nasa.gov***

- E-mail your question via the Internet to help@sti.nasa.gov

- Fax your question to the NASA Access Help Desk at (301) 621-0134

- Telephone the NASA Access Help Desk at (301) 621-0390

- Write to:
  NASA Access Help Desk
  NASA Center for AeroSpace Information
  7121 Standard Drive
  Hanover, MD 21076

NASA/CR—2000-209805

Laser-Induced Fluorescence Measurements and Modeling of Nitric Oxide in Counterflow Diffusion Flames

Rayavarapu V. Ravikrishna and Normand M. Laurendeau
Purdue University, West Lafayette, Indiana

Prepared under Grants NAG3–1782 and NAG3–2251

National Aeronautics and
Space Administration

Glenn Research Center

February 2000

Trade names or manufacturers' names are used in this report for identification only. This usage does not constitute an official endorsement, either expressed or implied, by the National Aeronautics and Space Administration.

Available from

NASA Center for Aerospace Information
7121 Standard Drive
Hanover, MD 21076
Price Code: A09

National Technical Information Service
5285 Port Royal Road
Springfield, VA 22100
Price Code: A09

TABLE OF CONTENTS

Page

LIST OF TABLES vi

LIST OF FIGURES vii

LIST OF SYMBOLS xiv

1. INTRODUCTION 1

   1.1 Background 1
   1.2 Contents of Thesis 4

2. THEORY AND LITERATURE REVIEW 7

   2.1 Introduction 7
   2.2 Laser-induced Fluorescence Theory 7
   2.3 NO Kinetics 16
   2.4 Counterflow Diffusion Flames 19
      2.4.1. Flame Structure 21
      2.4.2. Partial Premixing 26
      2.4.3. NO_x Formation 28
         2.4.3.1. NO_x Formation in Counteflow Diffusion Flames 28
         2.4.3.2. NO_x Formation in Counterflow Partially-premixed Flames 30

3. EXPERIMENTAL APPARATUS AND PROCEDURE 32

   3.1 Introduction 32
   3.2 Atmospheric Pressure LSF/LIF/PLIF Facility 32
   3.3 Thin Filament Pyrometry 39
   3.4 High-pressure LIF Facility 41

4. QUANTIFICATION OF PLIF MEASUREMENTS OF NITRIC OXIDE IN LAMINAR PARTIALLY-PREMIXED FLAMES 45

Page

4.1 Introduction 45
4.2 Experimental Techniques 47
4.3 Results and Discussion 49
4.4 Conclusions 60

5. COMPARISON OF LSF AND LINEAR LIF MEASUREMENTS OF NITRIC OXIDE IN COUNTERFLOW DIFFUSION FLAMES 62

5.1 Introduction 62
5.2 Experimental Techniques 63
5.3 Results and Discussion 65
5.4 Conclusions 82

6. LIF MEASUREMENTS AND MODELING OF NITRIC OXIDE IN METHANE-AIR AND ETHANE-AIR COUNTERFLOW DIFFUSION FLAMES 84

6.1 Introduction 84
6.2 Experimental Techniques 86
6.3 Calibration Procedures 88
6.4 Results and Discussion 90
6.5 Conclusions 99

7. LIF MEASUREMENTS AND MODELING OF NITRIC OXIDE IN COUNTERFLOW PARTIALLY-PREMIXED FLAMES 101

7.1 Introduction 101
7.2 Experimental Techniques 103
7.3 Calibration Procedures 105
7.4 Results and Discussion 107
7.5 Conclusions 117

8. LIF MEASUREMENTS AND MODELING OF NITRIC OXIDE IN HIGH-PRESSURE COUNTERFLOW DIFFUSION FLAMES 119

8.1 Introduction 119
8.2 Experimental Techniques 119
8.3 Results and Discussion 123
8.4 Conclusions 137

9. CONCLUSIONS AND RECOMMENDATIONS 138

9.1 Conclusions 138

Page

9.2 Recommendations..... 141

LIST OF REFERENCES..... 143

APPENDICES

Appendix A: Thin Filament Pyrometry..... 153
Appendix B: Error Analysis..... 156
B.1 Propagation of Errors..... 156
B.2 Atmospheric Pressure LIF Measurements..... 157
B.3 High-pressure LIF Measurements..... 159
B.4 Error Calculations..... 160
Appendix C: [NO] Measurements Data..... 162
Appendix D: [NO] Measurements in Counterflow Diffusion Flames at 6-12 atm.. 168

LIST OF TABLES

Table Page

8.1: Gas flow rates for all flame conditions.....123

B.1: Typical values used in the uncertainty analysis of [NO] measurements.....161

C.1: [NO] data in ethane-air counterflow diffusion flames at 1atm..... 162

C.2: [NO] data in methane-air counterflow diffusion flames at 1atm..... 163

C.3: [NO] data in methane-air counterflow partially-premixed flames at 1 atm..... 164

C.4: [NO] data in methane-air counterflow diffusion flames at 2 atm..... 165

C.5: [NO] data in methane-air counterflow diffusion flames at 3 atm..... 166

C.6: [NO] data in methane-air counterflow diffusion flames at 4 atm..... 167

C.7: [NO] data in methane-air counterflow diffusion flames at 5 atm..... 167

D.1: [NO] data in methane-air counterflow diffusion flames at 6-12 atm 170

LIST OF FIGURES

Figure Page

2.1: Simplified, two-level model for LIF studies. Shown are the rate coefficients for absorption (W_{lu}), stimulated emission (W_{ul}), spontaneous emission (A_{ul}), and quenching (Q_{ul})..... 9

2.2: Molecular dynamics for LIF studies. The upper and lower laser-coupled rotational levels are labeled u and l, respectively. Vibrational quantum numbers in the upper and lower electronic states are indicated as v' and v", respectively. Specific rotational levels in the excited and ground electronic states are indicated by j and k, respectively. Shown in the vibrational model are the rate coefficients for absorption (W_{lu}), stimulated emission (W_{ul}), spontaneous emission ($A_{v',v''}$), and photoionization (W_i). Rate coefficients for the rotational model include those for electronic quenching (Q_e), rotational relaxation ($Q_r(m,n)$) and spontaneous emission ($A(j,k)$). Vibrational quenching (Q_v) in the ground electronic state is not shown for the sake of clarity..... 14

2.3: Classification of counterflow diffusion flames into four types (Tsuji, 1982)..... 20

2.4: Velocity profile in a typical counterflow diffusion flame stabilized between opposing flows of fuel and oxidizer showing the stagnation point and approximate location of the flame zone. This profile was generated using the OPPDIF code for a flame stretch of 24.4 s^{-1}..... 22

3.1: Schematic of the experimental setup used for the LSF/LIF measurements. M1, M2, M3 - Mirrors; PD:A, PD:B - Photodiodes; SP1, SP2 - Splitter plates; A1, A2, A3 - Apertures; SL1, SL2, SL3 - Spherical Lenses; IR - Image Rotator..... 33

3.2: Schematic of the atmospheric pressure counterflow burner..... 36

Figure Page

3.3: Schematic of the experimental setup used for the PLIF measurements. M1, M2 - Mirrors; FA - Frenel Attenuator; ORS - Overlap Reference System; SP1, SP2, SP3, SP4 - Splitter Plates; PD:A, B, C - Photodiodes; A1, A2, A3 - Apertures; SL1 - Spherical Lens; CL - Cylindrical Lens; S - Slit; FS1 - Filter Stack; LS - Camera Lens System..... 38

3.4: Schematic of the optical arrangement used in the thin filament pyrometry technique..... 40

3.5: Schematic of the counterflow burner used for making the high-pressure LIF measurements of NO..... 44

4.1: Schematic of burner used for studying co-flow, partially premixed flames..... 50

4.2: LSF point measurements of radial [NO] profiles at various elevations in the ϕ_B=2.22 flame..... 51

4.3: LSF point measurements of radial [NO] profiles at various elevations in the ϕ_B=1.33 flame..... 52

4.4: Quantified PLIF image of the ϕ_B=2.22 flame. The color bar indicates the [NO] in ppm relative to the calibration flame. The image spans 24-mm in the radial direction and 20-mm in the axial direction..... 56

4.5: Quantified PLIF image of the ϕ_B=1.33 flame. The color bar indicates the [NO] in ppm relative to the calibration flame. The image spans 24-mm in the radial direction and 20-mm in the axial direction..... 57

4.6: Comparison of quantified PLIF and LSF measurements of [NO] at elevations of 5, 15 and 25 mm in the ϕ_B=2.22 flame. Since the temperature of the calibration flame is known, these relative concentrations can also be expressed in terms of an absolute number density. A measured concentration of 10 ppm corresponds to a number density of 4.35×10^{13} cm^{-3}..... 58

4.7: Comparison of quantified PLIF and LSF measurements of [NO] at elevations of 5, 10 and 15 mm in the ϕ_B=1.33 flame. Since the temperature of the calibration flame is known, these relative concentrations can also be expressed in terms of an absolute number density. A measured concentration of 20 ppm corresponds to a number density of 8.69×10^{13} cm^{-3}..... 59

5.1: Schematic of the counterflow burner used for obtaining atmospheric pressure LSF/LIF measurements of NO..... 67

Figure Page

5.2: Comparison of predicted and measured temperatures in the flame with a strain rate of 35.03 s^{-1}. The measured temperatures are not corrected for radiative heat loss..... 69

5.3: Comparison of both uncorrected and corrected LIF measurements with LSF measurements in the flame with a strain rate of 5.12 s^{-1}. The uncertainty bars for the LIF measurements are not shown for the sake of clarity..... 71

5.4: Comparison of corrected LIF and LSF measurements in the flame with a strain rate of 20.53 s^{-1}. The uncertainty bars for the LIF measurements are not shown for the sake of clarity..... 72

5.5: Comparison of corrected LIF and LSF measurements in the flame with a strain rate of 35.03 s^{-1}. The uncertainty bars for the LIF measurements are not shown for the sake of clarity..... 73

5.6: Comparison of corrected LIF and LSF measurements in the flame with a strain rate of 48.34 s^{-1}. The uncertainty bars for the LIF measurements are not shown for the sake of clarity..... 74

5.7: Variation of the local electronic quenching rate coefficient and computed mole fractions of hydrocarbon species as a function of mixture fraction in the flame with a strain rate of 5.12 s^{-1}. The variation is typical of all four flames considered in our study..... 75

5.8: Predictions of $R_{u,c}$ and collisional branching ratio necessary to correct the LSF measurements to the LIF measurements in the 5.12 s^{-1} flame. The data presented here assume that the LIF measurements are quantitative and depict the collisional branching ratio required to correct the rich-side discrepancy in the NO measurements. The lean electronic quenching rate coefficient, Q_e^{lean}, and the assumed rotational relaxation rate coefficient, $R_{u,c}^{lean}$, are listed in the figure..... 80

6.1: Comparison of measured and predicted temperatures in a methane-air counterflow diffusion flame at global strain rates of 5, 20, and 35 s^{-1}. The temperatures are measured using thin SiC filament pyrometry..... 91

6.2: LIF measurements of NO vs. modeling in a methane-air counterflow diffusion flame at a global strain rate of 5 s^{-1}. The dashed line indicates modeling using the GRI mechanism (version 2.11). The dotted line indicates modeling with a modified rate coefficient for the prompt-NO initiation reaction..... 92

Figure Page

6.3: LIF measurements of NO vs. modeling in a methane-air counterflow diffusion flame at a global strain rate of 20 s^{-1}. The dashed line indicates modeling using the GRI mechanism (version 2.11). The dotted line indicates modeling with a modified rate coefficient for the prompt-NO initiation reaction..... 93

6.4: LIF measurements of NO vs. modeling in a methane-air counterflow diffusion flame at a global strain rate of 35 s^{-1}. The dashed line indicates modeling using the GRI mechanism (version 2.11). The dotted line indicates modeling with a modified rate coefficient for the prompt-NO initiation reaction..... 94

6.5: LIF measurements of NO vs. modeling in an ethane-air counterflow diffusion flame at global strain rates of 5 s^{-1} and 20 s^{-1}. The dashed line indicates modeling using the GRI mechanism (version 2.11). The dotted line indicates modeling with a modified rate coefficient for the prompt-NO initiation reaction..... 95

6.6: LIF measurements of NO vs. modeling in an ethane-air counterflow diffusion flame at global strain rates of 35 s^{-1} and 48 s^{-1}. The dashed line indicates modeling using the GRI mechanism (version 2.11). The dotted line indicates modeling with a modified rate coefficient for the prompt-NO initiation reaction..... 96

7.1: Comparison of measured and predicted temperatures in the counterflow partially-premixed flames with fuel-side equivalence ratios of 1.45, 1.6, 1.8, and 2.0.....108

7.2: Comparison of LIF [NO] measurements and modeling in the counterflow partially-premixed flames with fuel-side equivalence ratios of 1.45 and 1.6.....109

7.3: Comparison of LIF [NO] measurements and modeling in the counterflow partially-premixed flames with fuel-side equivalence ratios of 1.8 and 2.0.....110

7.4: Spatial variation of the molar production rates for the prompt-NO initiation reaction ($CH+N_2 \Leftrightarrow HCN+N$) and the main thermal-NO reaction ($N_2+O \Leftrightarrow NO+N$) in the flame with a fuel-side equivalence ratio of 1.45.....113

7.5: NO pathway analysis showing relative contribution of the prompt and thermal mechanisms in the flame with a fuel-side equivalence ratio of 1.45.....114

Figure Page

7.6: Comparison of LIF [NO] measurements and model predictions with radiation in the counterflow partially-premixed flames with fuel-side equivalence ratios of 1.45 and 1.6. The dotted line represents the predictions of the model with radiation using the GRI mechanism (version 2.11) in its original form. The dashed line represents the model with radiation using a modified rate coefficient for the prompt-NO initiation reaction..... 115

7.7: Comparison of LIF [NO] measurements and model predictions with radiation in the counterflow partially-premixed flames with fuel-side equivalence ratios of 1.8 and 2.0. The dotted line represents the predictions of the model with radiation using the GRI mechanism (version 2.11) in its original form. The dashed line represents the model with radiation using a modified rate coefficient for the prompt-NO initiation reaction..... 116

8.1: Schematic of the counterflow burner used in the high-pressure LIF studies of NO..... 121

8.2: Detection scans obtained in fuel-lean and fuel-rich regions of a counterflow diffusion flame at 5 atm..... 127

8.3: LIF measurements of NO vs. modeling in methane-air counterflow diffusion flames at 2 atm and global strain rates of 20, 30 and 40 s^{-1}. The dashed line indicates modeling using the GRI mechanism (version 2.11). The dash-and-dot line represents modeling using the modified OPPDIF code that accounts for radiative heat loss. The dotted line indicates modeling accounting for radiative heat loss when using a modified rate coefficient for the prompt-NO initiation reaction..... 128

8.4: LIF measurements of NO vs. modeling in methane-air counterflow diffusion flames at 3 atm and global strain rates of 15, 20, 30 and 40 s^{-1}. The dashed line indicates modeling using the GRI mechanism (version 2.11). The dash-and-dot line represents modeling using the modified OPPDIF code that accounts for radiative heat loss. The dotted line indicates modeling accounting for radiative heat loss when using a modified rate coefficient for the prompt-NO initiation reaction..... 129

8.5: LIF measurements of NO vs. modeling in methane-air counterflow diffusion flames at 4 atm and global strain rates of 15, 20, 30 and 40 s^{-1}. The dashed line indicates modeling using the GRI mechanism (version 2.11). The dash-and-dot line represents modeling using the modified OPPDIF code that accounts for radiative heat loss. The dotted line indicates modeling accounting for radiative heat loss when using a modified rate coefficient for the prompt-NO initiation reaction..... 130

Figure Page

8.6: LIF measurements of NO vs. modeling in methane-air counterflow diffusion flames at 5 atm and global strain rates of 20, 30 and 40 s^{-1}. The dashed line indicates modeling using the GRI mechanism (version 2.11). The dash-and-dot line represents modeling using the modified OPPDIF code that accounts for radiative heat loss. The dotted line indicates modeling accounting for radiative heat loss when using a modified rate coefficient for the prompt-NO initiation reaction..... 131

8.7: Effect of radiative heat loss on predicted peak [NO] as a function of pressure. The predictions shown here correspond to a strain rate of 20 s^{-1} and are obtained using the modified rate coefficient for the prompt-NO initiation reaction.....134

8.8: Variation of peak measured and predicted [NO] as a function of pressure at a strain rate of 40 s^{-1}. The predictions are obtained using the modified rate coefficient for the prompt-NO initiation reaction. The atmospheric pressure datum was obtained using a different counterflow burner at a slightly different strain rate, but has been included here to aid in comparison..... 135

8.9: Variation of peak predicted CH concentration as a function of pressure. The predictions correspond to a strain rate of 40 s^{-1}..... 136

A.1: Temperature as a function of the ratio of the detector signal in the actual flame to that in the calibration flame. The calibration flame temperature is 1383 K... 155

D.1: Ratio of NO fluorescence signal to actual NO concentration in ppm for counterflow premixed flames as a function of pressure..... 171

D.2: The variation of NO absorption with pressure. The absorption is calculated at a temperature of 1800 K at each pressure..... 172

D.3: Comparison of LIF Measurements of [NO] and model predictions in a 30 s^{-1} strain rate flame at 6 atm. The dashed line indicates predictions accounting for radiation, whereas the dotted line indicates predictions with radiation and a previously modified rate coefficient for the prompt-NO initiation reaction..... 173

D.4: Comparison of LIF Measurements of [NO] and model predictions in a 30 s^{-1} strain rate flame at 8 atm. The dashed line indicates predictions accounting for radiation, whereas the dotted line indicates predictions with radiation and a previously modified rate coefficient for the prompt-NO initiation reaction..... 174

Figure Page

D.5: Comparison of LIF Measurements of [NO] and model predictions in a 30 s^{-1} strain rate flame at 10 atm. The dashed line indicates predictions accounting for radiation, whereas the dotted line indicates predictions with radiation and a previously modified rate coefficient for the prompt-NO initiation reaction..... 175

D.6: Comparison of LIF Measurements of [NO] and model predictions in a 30 s^{-1} strain rate flame at 12 atm. The dashed line indicates predictions accounting for radiation, whereas the dotted line indicates predictions with radiation and a previously modified rate coefficient for the prompt-NO initiation reaction..... 176

LIST OF SYMBOLS

English Symbols

Symbol	Description	Units
A_{ul}	Einstein A coefficient for spontaneous emission	s^{-1}
c	Speed of light	cm/s
C_B	Concentration of the NO standard gas	ppm
C_F	Calibration Factor	ppm/V
D_P	Doped [NO] relative to calibration flame products	ppm
f_B	Boltzmann fraction	-
g	Degeneracy of the electronic level	-
E_g	Spectral emissive power	W/μm•sr
G	Photomultiplier gain	V/W
h	Planck's constant	J•s
I	Irradiance	W/cm^2
k	Boltzmann constant	J/K
L	Fraction of NO destroyed in the calibration flame	-
L_P	Signal corresponding to laser power	V
N	Number density in rovibronic level	cm^{-3}
N_A	Avogadro's number	molecules/kgmole

Symbol	Description	Units
N_l^0	Number density in the lower laser-coupled level	cm^{-3}
N_T	Total number density	cm^{-3}
P	Absolute pressure	N/m^2
Q_e	Electronic quenching rate coefficient	s^{-1}
Q_r	Rotational relaxation rate coefficient	s^{-1}
Q_{ul}	Electronic quenching rate coefficient	s^{-1}
Q_v	Vibrational relaxation rate coefficient	s^{-1}
R_u	Universal gas constant	J/kgmole•K
R	Detector response function	-
S	Infrared detector signal	V
S_F	Fluorescence signal	V
T	Temperature	K
T_r	Transmission of optics	-
V_c	Fluorescence collection volume	cm^3
$\dot{V}R$	Volumetric flow rate ratio	-
W_{lu}	Stimulated absorption rate coefficient	s^{-1}
W_{ul}	Stimulated emission rate coefficient	s^{-1}
W_I	Rate coefficient for photoionization	s^{-1}

Greek Symbols

Symbol	Description	Units
β	Detection efficiency of collection optics	-
ε_f	Fluorescence emission	$W/(cm^3 \bullet sr)$
ε	Emissivity	-
εX	Relative uncertainty in the parameter X (95% confidence level)	-
δX	Absolute uncertainty in the parameter X (95% confidence level)	X
ν	Wavenumber	cm^{-1}
σ	One-photon absorption cross-section	cm^2
Ω_c	Solid collection angle of detection optics	sr
λ	Wavelength	μm
Γ	Spectral overlap fraction	-

Subscripts

Symbol	Description
abs	Refers to absolute value of measured quantity
ACC	Refers to the accuracy
b	Refers to background
c	Refers to measurements at calibration conditions
f	Fluorescence
I	Refers to interferences

Symbol	Description
j, k, m, n	Specific rotational levels
l	Refers to lower rovibronic level
L	Laser
ppm	Refers to NO concentration in parts-per-million
PRE	Refers to the precision
rel	Refers to relative value of measured quantity
u	Refers to upper rovibronic level
v'	Upper vibrational state quantum number
v"	Lower vibrational state quantum number

1. INTRODUCTION

1.1 Background

Among the various industrial exhaust emissions, oxides of nitrogen and sulfur have been identified as particularly hazardous to the environment because of their role in photochemical smog, acid rain and stratospheric ozone depletion. The aircraft industry has become particularly aware of NO_x because of the future proximity of aircraft emissions to the protective ozone layer. An important goal of NASA over the next ten years is to reduce the environmental impact of new civilian aircraft engines by decreasing their NO_x emissions at cruise conditions by at least 70%. Lean prevaporized premixed (LPP) combustion offers the lowest possible NO_x emission index, but this strategy is plagued by problems with autoignition and flashback at the higher pressures of future gas turbine combustors. Lean direct injection (LDI) seeks rapid vaporization and mixing of liquid fuel with air at the entrance of the combustor so as to avoid autoignition and flashback problems. However, the initial mixing region leads to partially premixed flamelets which can produce high local levels of NO. The eventual performance of any future advanced subsonic transport (AST) will require *in situ* measurements of NO concentrations for various injector modules and combustor designs so as to optimize the final LDI system. Hence, a need exists for making quantitative measurements of NO number density at AST conditions for which pressures are in the range of 40-50 atm, and temperatures in excess of 1800 K.

Laser-induced fluorescence (LIF) is an optical technique that has recently been used to quantitatively measure NO concentrations in combustive environments. LIF and other laser-based diagnostic techniques have undergone extensive development and refinement and have achieved the ability to produce quantitative measurements of minor

species, such as nitric oxide, with accuracies of ± 20% and detection limits approaching 1 part-per-million (Reisel et al., 1993). To achieve the goal of making NO measurements at AST conditions, the first step is to obtain quantitative NO measurements in nonpremixed and partially premixed flames at atmospheric and higher pressures. The most useful flame geometry for this purpose is the counterflow configuration wherein opposing streams of fuel and oxidizer impinge and produce a stagnation plane whose location depends on the fuel and oxidizer velocities. Because of the nature of the flow field, the fuel diffuses and burns with the oxidizer in a flat flame on the oxidizer side of the stagnation plane. An excellent review on counterflow diffusion flames is provided by Tsuji (1982). This particular flame geometry is ideal because temperature and concentration measurements can easily be made away from potentially interfering surfaces. Also, such measurements can be compared to model predictions using an existing computer simulation (Lutz et al., 1996) and a recent comprehensive chemical mechanism (GRI Mech. version 2.11). Thus, the major goal of this research is to obtain quantitative laser-induced fluorescence measurements of NO in laminar, methane-air counterflow diffusion flames for various flame stretch rates and with different levels of partial premixing.

Planar laser-induced fluorescence (PLIF) is an optical diagnostic tool for making two-dimensional measurements of relevant species concentrations. However, obtaining a quantitative species image from a raw PLIF image requires correcting that image for errors associated with variations in the Boltzmann fraction, the overlap fraction, and the electronic quenching rate coefficient. Owing to these problems, PLIF is most often used as a qualitative field diagnostic. Recent improvements in both the measurement of electronic quenching cross-sections at flame temperatures (Drake and Ratcliffe, 1993) and the modeling of electronic quenching rate coefficients (Paul et al., 1993) have enabled the implementation of numerically based correction schemes (Paul et al., 1994). However, these correction schemes require spatially-resolved measurements of major-species concentrations. Thus, the implementation of numerically-based correction schemes for PLIF measurements requires significant lead-time for cross-section measurements and model validation, plus a more complicated and expensive experimental setup. As an

alternative, an additional goal of this research is to develop experimentally-based correction schemes in flames where significant variations in the quenching rate coefficient occur such as in partially-premixed co-flow flames.

Laser-saturated fluorescence (LSF) measurements are relatively independent of both the laser irradiance and the electronic quenching rate coefficient. Hence, LSF measurements are fairly quantitative, with a detection limit of ~1 ppm (Reisel et al., 1993). Since it is very difficult to quantify the effects of electronic quenching in co-flow flames, both linear LIF and LSF measurements can be conducted in flames where the major species concentrations are reasonably well-known, such as in counterflow diffusion flames. The linear LIF profiles can be corrected for quenching variations by using the major-species profiles predicted by the OPPDIF code (Lutz et al., 1996) plus a recent model for NO quenching (Paul et al., 1995), and then compared with independently measured LSF profiles. Thus, by using both LSF and linear LIF, the feasibility of quantitative NO concentration ([NO]) measurements in nonpremixed flames can be assessed at atmospheric pressure.

High-pressure LIF measurements of NO have been obtained in premixed flames in the past (Reisel et al., 1993; Reisel and Laurendeau, 1994a; Battles et al., 1994; Thomsen et al., 1997), but there has been no previous work on NO measurements in diffusion flames at high pressure. Since the LDI strategy involves diffusion and partially-premixed flames, there is a need for NO measurements in such flames at high pressure. Fortunately, the effect of O_2 interferences has been assessed at high pressure in premixed flames (Partridge et al., 1996; Thomsen et al., 1997). The main concern in diffusion flames at high pressure is thus the possible effect of polycyclic aromatic hydrocarbons (PAHs) in the fuel-rich region. Once this effect has been assessed, quantitative NO measurements can be obtained at high pressures in diffusion flames. These [NO] measurements can then form a database for validating chemical kinetic mechanisms at high pressure.

To summarize the goals of this research, an experimentally-based quantification procedure is to be developed for PLIF measurements in co-flow, partially-premixed flames. Since it is difficult to quantify the effect of variations in the quenching rate

coefficient in such flames, an additional goal is to compare LSF and linear LIF measurements in counterflow diffusion flames. However, the main goal of this research is to obtain quantitative [NO] measurements in counterflow diffusion and partially-premixed flames at atmospheric pressure, and to utilize these measurements to assess the latest NO chemical kinetic mechanisms, such as the GRI (version 2.11) mechanism. Furthermore, quantitative [NO] measurements are to be obtained in counterflow diffusion flames at high pressures (up to 5 atm) which will form a database for validating chemical kinetic mechanisms at these pressures and higher.

1.2 Contents of Thesis

The following chapter presents a brief review of LIF theory, specifically the techniques of linear laser-induced fluorescence and laser-saturated fluorescence (LSF). The various NO chemical kinetic pathways are introduced and a detailed review of counterflow diffusion flames is presented. Previous work regarding the structure of counterflow diffusion flames, the effect of partial premixing, and NO_x formation in counterflow diffusion and partially-premixed flames is described. Chapter 3 provides a description of the experimental apparatus used in performing temperature and NO measurements. Chapter 4 describes a procedure to quantify PLIF measurements of [NO] in laminar, co-flow, partially-premixed flames based on a single LSF measurement. The quantified PLIF measurements are then assessed by comparison with an independent two-dimensional array of LSF measurements. The comparisons show good agreement between PLIF and LSF measurements at all elevations in both flames. In fact, over 90% of the PLIF measurements fall within the uncertainty of the LSF measurements.

In Chapter 5, the utility of the broad-band LSF technique is further assessed by comparison to similar measurements of NO using linear LIF. The linear LIF measurements are corrected for variations in the local electronic quenching rate coefficient by using major species profiles generated by an opposed diffusion flame code and available correlations for the quenching cross-sections of NO. The corrected LIF profiles compare

favorably with the LSF profiles. A four-level model is used to investigate the effects of rotational energy transfer (RET) on the LSF measurements. The excellent comparison between the quenching-corrected linear LIF and the LSF measurements at locally fuel-lean to stoichiometric mixture fractions verifies the validity of the LSF technique for these conditions.

LIF measurements of [NO] are compared with model predictions in atmospheric methane-air and ethane-air counterflow diffusion flames at different strain rates in Chapter 6. Temperature measurements are also made using thin SiC filament pyrometry in the methane-air counterflow diffusion flames. The excellent agreement between measurements and model predictions indicates the efficacy of the new calibration method developed for the thin filament pyrometry technique. The model with the GRI mechanism (version 2.11) consistently underpredicts the peak [NO] in all flames indicating a need for refinement of both CH and prompt-NO chemistry, especially the rate coefficient for the prompt-NO initiation reaction. A modified rate coefficient proposed for the prompt-NO initiation reaction significantly improves the agreement between modeling and measurements in methane-air and ethane-air flames.

Similar comparisons between [NO] measurements and modeling are presented in Chapter 7 for atmospheric methane-air counterflow partially-premixed flames. The effect of partial premixing was studied by investigating flames with fuel-side equivalence ratios (ϕ_B) of 1.45, 1.6, 1.8 and 2.0 at a constant global strain rate near 20 s^{-1}. Corrected linear LIF measurements of [NO] and temperatures measured using thin filament pyrometry are compared with numerical predictions from an opposed-flow flame code by utilizing the GRI mechanism for the NO kinetics. The effect of radiative heat loss on code predictions is accounted for by using an optically thin radiation model. Reasonably good agreement was found to exist between LIF [NO] measurements and predictions in all flames.

Quantitative LIF measurements of [NO] in methane-air counterflow diffusion flames from 2 to 5 atm are presented in Chapter 8. Comparison of these measurements with modeling shows that the GRI mechanism underpredicts prompt-NO by a factor of two to three at all pressures. The underprediction is maximum at 2 and 3 atm, and

decreases with pressure from 3 to 5 atm. Although the GRI mechanism does not predict this trend, predictions with a modified rate coefficient for the prompt-NO initiation reaction displays qualitative agreement with the experimentally observed trend. Finally, conclusions and recommendations for future work are presented in Chapter 9.

2. THEORY AND LITERATURE REVIEW

2.1 Introduction

In this chapter, a review is presented of the basic theory for laser-induced fluorescence (LIF), an optical technique to measure NO concentrations in flames. A brief review is also given of the relevant kinetics involved in NO formation. Finally, a detailed review is presented of the literature on counterflow diffusion flames, with specific attention given to flame structure, the effect of partial premixing, and NO_x formation.

2.2 Laser-Induced Fluorescence Theory

Laser-induced fluorescence is an optical technique that can withstand the harsh conditions of combustive environments without disturbing either the flowfield or the chemical kinetics. This technique has become important for the detection and measurement of a variety of radical species, such as NO, that are found in combustive systems. The fundamentals of LIF can most easily be understood by studying the two-level model described by Laurendeau and Goldsmith (1989). However, broadband LIF measurements of NO require the inclusion of several processes not considered in the simple two-level model (Reisel et al., 1993). To provide a detailed presentation of the LIF technique, the two-level model will be presented followed by a discussion of additional rate processes.

The two-level model is based on four simplifying assumptions (Laurendeau and Goldsmith, 1989):

1. The excitation beam is uniform and linearly polarized.

2. The entire population is assumed to be in the ground electronic state before laser excitation ($N_l + N_u = N_l^0$).
3. The fluorescence signal is measured at the peak of the emissive pulse where the upper level population is at steady state.
4. The fluorescence signal consists of a single wavelength corresponding to a single rovibronic transition.

Given these assumptions, the two-level model consists of four rate processes with their corresponding rate coefficients (s^{-1}). These processes and their coefficients, demonstrated in Fig. 2.1, consist of absorption (W_{lu}), stimulated emission (W_{ul}), spontaneous emission (A_{ul}), and collisional quenching (Q_{ul}). A portion of the spontaneous emission, which radiates equally in all directions, is collected as the fluorescence signal.

Considering only the above four rate processes, the rate equations can be written for the change in number density of each electronic level. These equations are

$$\frac{dN_l}{dt} = -N_l W_{lu} + N_u\left(W_{ul} + A_{ul} + Q_{ul}\right) \quad , \tag{2.1}$$

and

$$\frac{dN_u}{dt} = N_l W_{lu} - N_u\left(W_{ul} + A_{ul} + Q_{ul}\right) \quad . \tag{2.2}$$

At the peak of the laser pulse, where we have assumed steady state, the above two equations will both equal zero. Thus we can solve either of them to obtain an equation for the ground state number density N_l. Noting that $N_l + N_u = N_l^0$ from our second assumption, we obtain

$$N_u = \frac{N_l^0}{\left\{\left(W_{ul} + A_{ul} + Q_{ul}\right) / W_{lu}\right\} + 1} \quad . \tag{2.3}$$

At this point, one of two simplifying assumptions can be made based on the experimental conditions. For large laser irradiances at lower pressures, stimulated emission and absorption dominate. In other words, both W_{ul} and W_{lu} are large compared to A_{ul} and Q_{ul}.

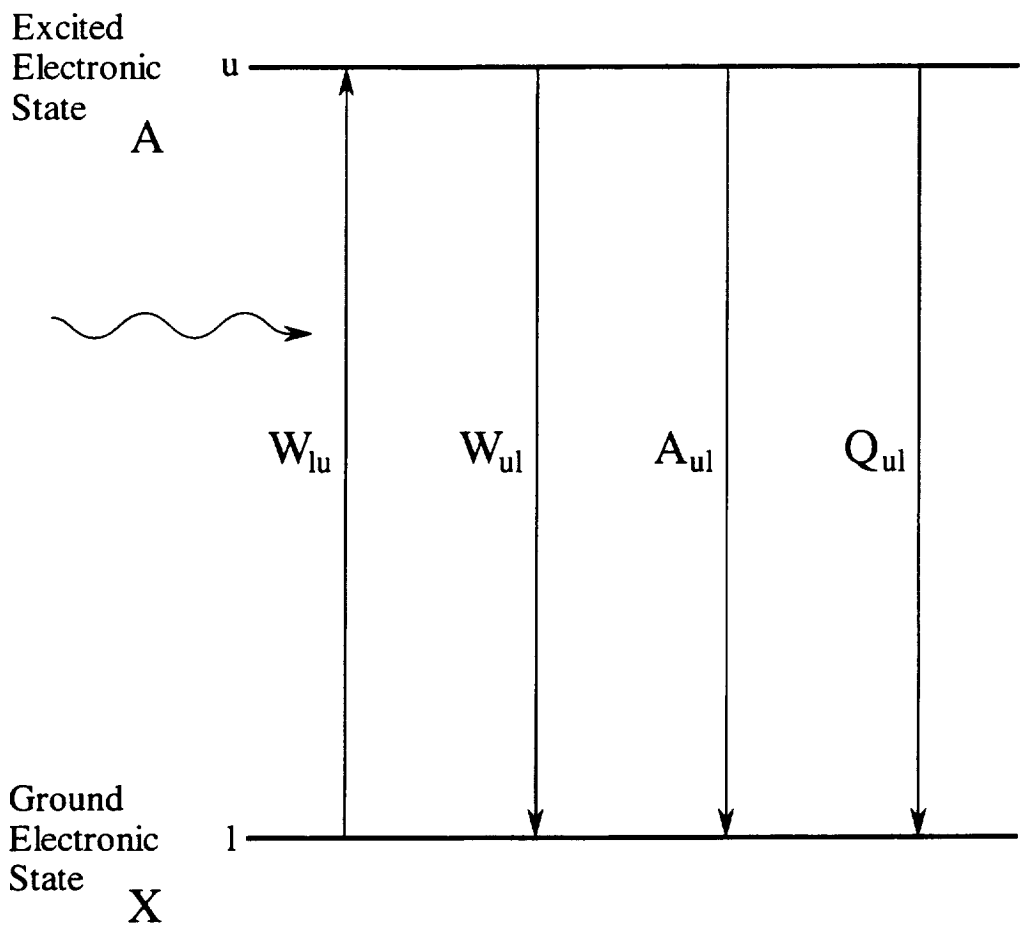

Figure 2.1: Simplified, two-level model for LIF studies. Shown are the rate coefficients for absorption (W_{lu}), stimulated emission (W_{ul}), spontaneous emission (A_{ul}), and quenching (Q_{ul}).

This condition is referred to as the laser-saturated fluorescence (LSF) regime. Thus, neglecting quenching and spontaneous emission, Eq. (2.3) becomes

$$N_u = \frac{W_{lu}}{W_{lu} + W_{ul}} N_l^0 \quad . \tag{2.4}$$

Now, the rate coefficients for stimulated emission and absorption are related by the degeneracies of the upper and lower levels (g_u and g_l) according to

$$g_l W_{lu} = g_u W_{ul} \quad . \tag{2.5}$$

Combining Eqs. (2.4) and (2.5), we obtain for the LSF upper-level population,

$$N_u = \frac{g_u}{g_l + g_u} N_l^0 \quad . \tag{2.6}$$

The second possible simplification concerns the case for which the laser irradiance is much less than that required to saturate the transition. For high-pressure LIF, this is almost always the case. Here, the simplifying assumption is that W_{ul} and W_{lu} are small compared to A_{ul} and Q_{ul}. Thus, for this linear LIF regime, quenching and spontaneous emission are the dominant processes. Based on this assumption, Eq. (2.3) becomes

$$N_u = \frac{W_{lu}}{A_{ul} + Q_{ul}} N_l^0 \quad . \tag{2.7}$$

It is important to note at this point that although the rate coefficients for quenching and spontaneous emission are independent of laser power, the rate coefficient for stimulated absorption depends on laser power via the equation

$$W_{lu} = \frac{\sigma \Gamma I_L^\circ}{hc\nu_L} \quad , \tag{2.8}$$

where σ is the one-photon fluorescence cross-section of the molecule (cm^2), Γ is the spectral overlap fraction, I_L° is the normalized laser irradiance (W/cm^2), and ν_L is the wavenumber of the laser irradiance (cm^{-1}). The spectral overlap fraction physically represents the ratio of the total photon absorption rate in the actual broadened system to that which exists in the monochromatic limit. Combining Eqs. (2.7) and (2.8), we obtain for the LIF upper-level population,

$$N_u = \frac{\left(\sigma \Gamma I_L^\circ / hc\nu_L\right)}{Q_{ul}} N_l^0 \quad , \tag{2.9}$$

where we have assumed $Q_{ul} >> A_{ul}$.

Considering Eqs. (2.6) and (2.9), we note that for LSF, the upper-level number density is independent of both laser power and quenching, which is its major advantage. Unfortunately, for higher pressure studies, saturation cannot be achieved; thus, both laser power and quenching must be accounted for in such LIF measurements.

The fluorescence emission ε_f (W/cm^3•sr) is related to the upper-level number density through the relation (Laurendeau and Goldsmith, 1989)

$$\varepsilon_f = \frac{hc\nu_f A_{ul}}{4\pi} N_u \quad . \tag{2.10}$$

where ν_f (cm^{-1}) represents the wavenumber at which fluorescence occurs. For the simple two-level atomic model, $\nu_f = \nu_L$. However, this would not be the case for molecular LIF as discussed later. The fluorescence signal depends on both the collection optics and detection electronics through

$$S_F = \beta G \Omega_c V_c \varepsilon_f \quad , \tag{2.11}$$

where S_F is the fluorescence voltage, β accounts for the efficiency of the collection optics, G is the photomultiplier gain (V/W), Ω_c is the solid collection angle of the optics (sr), and V_c is the fluorescence collection volume (cm^3). The total number density (N_T) of the probed species is typically of greater interest than the number density in the lower laser-coupled level. The Boltzmann fraction, $f_B(T)$, relates these two number densities via

$$f_B(T) = \frac{N_l^0}{N_T} \quad . \tag{2.12}$$

Combining Eqs. (2.10) and (2.11) with Eqs. (2.6), (2.9), and (2.12), we obtain fluorescence signal expressions for each technique. For LSF, we find

$$S_F = \beta hc\nu_f G V_c \left(\frac{\Omega_c}{4\pi}\right)\left(\frac{g_u}{g_l + g_u}\right) A_{ul} f_B(T) N_T \quad . \tag{2.13}$$

For linear LIF, we obtain

$$S_F = \beta\left(\frac{\nu_f}{\nu_L}\right) G V_c \sigma \left(\frac{\Omega_c}{4\pi}\right)\left(\frac{A_{ul}}{Q_{ul}}\right) \Gamma I_L^{\circ} f_B(T) N_T \quad . \tag{2.14}$$

Thus, LSF measurements are essentially independent of laser power and quenching, whereas these factors have to accounted for in the case of linear LIF measurements. The two-level model described above is applicable to atomic species, and for a few diatomics at lower pressures. A more detailed model is needed to describe the various processes that occur for most species of interest. Figure 2.2 shows the various processes that have to be considered in molecular LIF studies. A brief description of additional processes such as rotational energy transfer (RET), vibrational energy transfer, and ionization are considered next.

Each electronic energy level contains several vibrational energy levels. Assuming that only a single vibrational transition is being excited, the upper level can undergo spontaneous emission to multiple vibrational levels in the ground electronic state. An additional mode of energy transfer that needs to be considered owing to the presence of various vibrational energy levels is vibrational quenching. In other words, within each electronic state, quenching can occur between various vibrational levels. Moreover, electronic quenching can also occur from the upper electronic state to a variety of vibrational levels in the lower electronic state. Each vibrational energy level will also contain a number of rotational energy levels, which further complicates LIF. As for the vibrational levels, the rotational levels increase the number of levels available for both emission and quenching. Rotational energy transfer (RET) or relaxation is so rapid in both the excited and ground electronic states that it can become quite important in LIF studies.

One approach to the complications presented by molecular LIF is to develop a new fluorescence equation by modeling the fraction of molecules that would transfer out of the directly excited rotational level before fluorescing (Carter et al., 1987). This approach can be used for species such as OH where sufficient signal is available even for a single rovibronic transition. Another approach, known as broadband LIF, involves detecting a significant portion of a vibrational band containing many rovibronic transitions (Reisel et

al., 1993). Although this technique provides a much larger signal, the larger detection window can pick up additional interferences. One concern arises from the large irradiances used in the broadband LSF technique. During stimulated absorption from the lower laser-coupled level to an excited upper level, it is possible that the depopulated lower level is repopulated via RET from neighboring ground rovibronic levels. Thus, more molecules could actually be excited than predicted by a simple two-level model, necessitating a more detailed model. A final process which must be considered is photoionization. This process involves depleting the excited state without emitting a photon. For some molecules, photoionization, rather than quenching, can constitute the limiting depletion rate in LIF. However, for NO, photoionization can generally be neglected in comparison to the electronic quenching rate for our experimental conditions.

By including the above mentioned processes in our two-level model, we now have seven types of rate processes, each with their corresponding rate coefficient (s^{-1}), as shown in Fig. 2.2. These are absorption (W_{lu}), stimulated emission (W_{ul}), spontaneous emission ($A(j,k)$), electronic quenching (Q_e), vibrational quenching (Q_v), rotational relaxation ($Q_r(m,n)$), and photoionization (W_i). Since the ground vibrational level in the upper electronic state is generally used for excitation, little vibrational quenching will occur in the excited electronic state. Thus, for most applications, we can neglect this effect. In our rate equations, the subscript j will represent each rovibronic level in the excited electronic state and k each such level in the ground electronic state. For the directly excited rovibronic levels, the rate equation can be written as

$$\begin{aligned}\frac{dN_u}{dt} = N_l W_{lu} - N_u\{W_{ul} + Q_e + W_i\} - \sum_{j\neq u} N_u Q_r(u,j) \\ - \sum_k N_u A(u,k) + \sum_{j\neq u} N_j Q_r(j,u) \quad .\end{aligned} \tag{2.15}$$

The rate equation for the remaining levels in the excited state can be expressed as

$$\frac{dN_j}{dt} = \sum_{m\neq j}\{N_m Q_r(m,j) - N_j Q_r(j,m)\} - \sum_k N_j A(j,k) - N_j(Q_e + W_i) \quad . \tag{2.16}$$

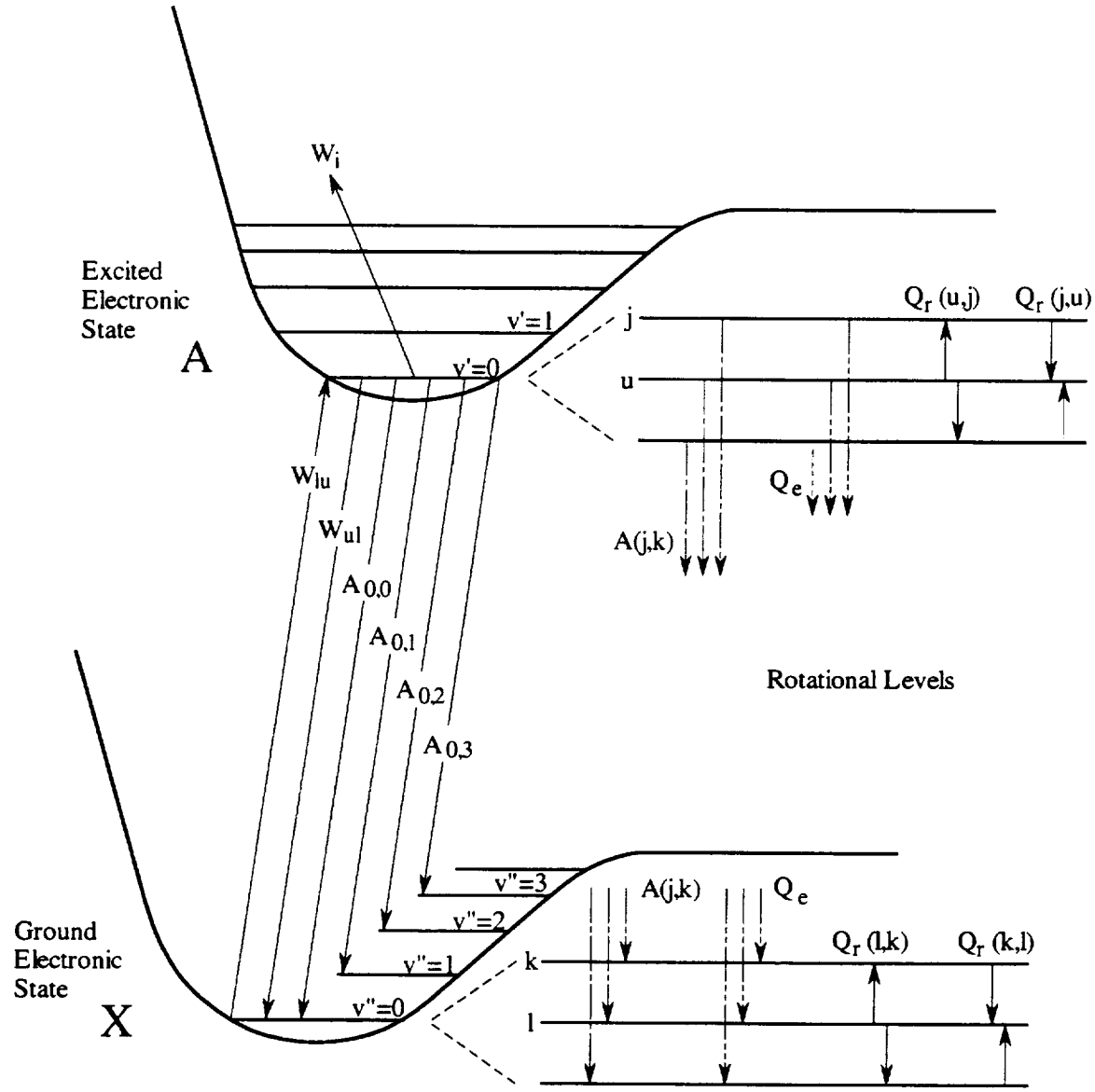

Figure 2.2: Molecular dynamics for LIF studies. The upper and lower laser-coupled rotational levels are labeled *u* and *l*, respectively. Vibrational quantum numbers in the upper and lower electronic states are indicated as v' and v", respectively. Specific rotational levels in the excited and ground electronic states are indicated by *j* and *k*, respectively. Shown in the vibrational model are the rate coefficients for absorption (W_{lu}), stimulated emission (W_{ul}), spontaneous emission ($A_{v', v''}$), and photoionization (W_i). Rate coefficients for the rotational model include those for electronic quenching (Q_e), rotational relaxation ($Q_r(m,n)$) and spontaneous emission ($A(j,k)$). Vibrational quenching (Q_v) in the ground electronic state is not shown for the sake of clarity.

With the assumption of steady state we can now obtain expressions for the number density of each excited rovibronic level. For the directly excited level,

$$N_u = \frac{N_l W_{lu} + \sum_{j \neq u} N_j Q_r(j,u)}{W_{ul} + Q_e + W_i + \sum_{j \neq u} Q_r(u,j) + \sum_k A(u,k)} \quad . \tag{2.17}$$

For the remaining excited rovibronic levels,

$$N_j = \frac{\sum_{m \neq j} N_m Q_r(m,j)}{Q_e + W_i + \sum_{m \neq j} Q_r(j,m) + \sum_k A(j,k)} \quad . \tag{2.18}$$

For broadband detection, fluorescence from all of these excited levels is collected, so that the overall fluorescence signal will be the sum of each of these transitions. Again, using Eqs. (2.10) and (2.11), we obtain the following equation for the overall broadband fluorescence signal,

$$S_{F,b} = \beta hcGV_c \left(\frac{\Omega_c}{4\pi} \right) \left\{ \nu_f(u,k) A(u,k) N_u + \sum_{j \neq u} \nu_f(j,k) A(j,k) N_j \right\} \quad . \tag{2.19}$$

The term $\nu_f(j,k)$ in the above equation refers to the wavenumber of the specific fluorescence transition. Since the individual rate coefficients for rotational energy transfer are not well known (Crosley, 1992), it would be nearly impossible to use Eqs. (2.17) and (2.18) to determine directly the number densities of each excited level. However, the above formulation does demonstrate how more signal is available via broadband detection as compared to that for a single transition with narrowband detection.

The NO measurement strategy involves calibrating the NO fluorescence signal via a calibration flame and transporting the calibration to the actual flame being studied. In general, the temperature at the measurement location is not equal to that in the calibration flame. In addition, the major species concentrations at the measurement location may be different from those in the calibration flame. Thus, for linear LIF, there is a need to correct the measured NO number density to account for differences in the Boltzmann fraction, the electronic quenching rate coefficient, and the spectral overlap fraction. This

can be accomplished by dividing Eq. (2.14) for the flame under consideration by the same expression written for the calibration flame. Thus, for the same laser irradiance, we obtain

$$\frac{S_F}{S_{F,c}} = \left(\frac{Q_{ul,c}}{Q_{ul}}\right)\left(\frac{\Gamma}{\Gamma_c}\right)\left(\frac{f_B(T)}{f_B(T_c)}\right)\left(\frac{N_T}{N_{T,c}}\right) \quad , \tag{2.20}$$

where the subscript c refers to the calibration flame. From the ideal gas law, the NO number density is related to the NO concentration in ppm via the following equation,

$$N_T = \left(\frac{PN_A}{R_u T}\right)\frac{N_{ppm}}{10^6} \quad , \tag{2.21}$$

where P is the absolute pressure, T is the absolute temperature, N_A is Avogadro's number, and R_u is the universal gas constant. Writing Eq. (2.21) for both the flame under consideration and the calibration flame, and substituting the resulting expressions into Eq. (2.20), we obtain

$$\frac{S_F}{S_{F,c}} = \left(\frac{Q_{ul,c}}{Q_{ul}}\right)\left(\frac{\Gamma}{\Gamma_c}\right)\left(\frac{f_B(T)}{f_B(T_c)}\right)\left(\frac{T_c}{T}\right)\left(\frac{N_{ppm}}{N_{ppm,c}}\right) \quad . \tag{2.22}$$

Rearranging Eq. (2.22), the absolute NO concentration in ppm can be expressed as

$$N_{ppm,abs} = \left(\frac{T}{T_c}\right)\left(\frac{f_B(T_c)}{f_B(T)}\right)\left(\frac{\Gamma_c}{\Gamma}\right)\left(\frac{Q_{ul}}{Q_{ul,c}}\right)N_{ppm,RT} \quad , \tag{2.23}$$

where $N_{ppm,RT}$ is the NO concentration in ppm relative to the calibration flame and is given by $(S_F/S_{F,c})N_{ppm,c}$. Equation (2.23) has been developed for linear LIF measurements. For LSF measurements, we start with Eq. (2.13) and follow an identical development to arrive at the following equation:

$$N_{ppm,abs} = \left(\frac{f_B(T_c)}{f_B(T)}\right)\left(\frac{T}{T_c}\right)N_{ppm,RT} \quad . \tag{2.24}$$

2.3 NO Kinetics

NO is produced through three main reaction mechanisms (Miller and Bowman, 1989; Drake and Blint, 1991): (1) the Zeldovich, or thermal-NO mechanism, (2) the N_2O-

intermediate mechanism, and (3) the prompt-NO mechanism. The amount of NO formed through each of these mechanisms depends on the temperature, pressure and equivalence ratio of the flame (Thomsen, 1996).

The Zeldovich or thermal-NO pathway (Zeldovich, 1946) is the simplest of all the NO formation mechanisms and represents the break-down of atmospheric nitrogen into nitrogen atoms and the subsequent formation of NO. It most commonly includes the following three reactions (R1-R3) (Miller and Bowman, 1989):

$$O+N_2 \Leftrightarrow NO+N \tag{R1}$$

$$N+O_2 \Leftrightarrow NO+O \tag{R2}$$

$$N+OH \Leftrightarrow NO+H \tag{R3}$$

The rate limiting step for Zeldovich NO formation is the initiation reaction (R1) while reactions (R2) and (R3) are the primary bimolecular pathways for the conversion of N atoms to NO. NO formed via the Zeldovich NO pathway can basically be divided into two categories, that generated within the flame-front and that produced in the post-flame zone. Flame-front Zeldovich NO formation is enhanced by super-equilibrium concentrations of O atoms (Drake and Blint, 1989) and leads to a sharp increase in NO over a very short distance within the flame. Zeldovich NO production within the post-flame zone is characterized by a high activation temperature (~1800 K) and is the dominant form of post-flame NO production. For low-temperature flames ($T < 1800$ K), the amount of NO produced through this mechanism is small. However, for high temperature flames, the thermal NO mechanism becomes the dominant pathway (Corr et al., 1992).

The N_2O intermediate pathway, though relatively unimportant in stoichiometric to rich flames, has been found to play a significant role with respect to flamefront NO formation in lean premixed flames (Malte and Pratt, 1974; Corr et al., 1992). This mechanism has five primary steps:

$$N_2 + O + M \Leftrightarrow N_2O + M \tag{R4}$$

$$N_2O + O \Leftrightarrow NO + NO \tag{R5}$$

$$N_2O + O \Leftrightarrow N_2 + O_2 \tag{R6}$$

$$N_2O + H \Leftrightarrow NO + NH \tag{R7}$$

$$N_2O + H \Leftrightarrow N_2 + OH \quad . \tag{R8}$$

Several additional reactions involving N_2O must be considered when performing detailed kinetics calculations (Nicol et al., 1993). As for the Zeldovich pathway, the N_2O-intermediate pathway is enhanced by super-equilibrium concentrations of OH and O in the flame front (Drake et al., 1990).

The prompt NO mechanism is the most complicated of the NO formation pathways. This mechanism is dominant in low temperature (< 1800 K) diffusion flames (Ravikrishna and Laurendeau, 1999a) and contributes significantly in partially-premixed flames (Li et al., 1997; Blevins and Gore, 1999; Ravikrishna and Laurendeau, 1999b). The term "prompt" NO, originally used to account for the seemingly instantaneous formation of NO in the flamefront, now more specifically refers to NO formed via carbon-nitrogen species interactions within the flame. More importantly, the latter still accounts for the dominant amount of flamefront NO formation in stoichiometric to rich flames (Drake and Blint, 1991). The initiation step for the prompt NO pathway is generally agreed to be

$$CH + N_2 \Leftrightarrow HCN + N \quad . \tag{R9}$$

The manner by which the prompt mechanism converts the resulting HCN and N radicals into NO is a matter of some debate. Many authors suggest that the N radical is the ultimate intermediate, with NO then being formed via the Zeldovich reactions (R2) and (R3) (Glarborg et al., 1986; Morley, 1981; Bockhorn et al., 1991). Other authors suggest that the NH radical is the controlling intermediate, with NO being formed through relevant amine radical reactions (Bian et al., 1990; Vandooren, 1992). Prompt NO is primarily formed through a reaction sequence that involves the rapid reaction of hydrocarbon radicals with molecular nitrogen (Miller and Bowman, 1989). Thus, this mechanism tends to produce much more NO under moderately fuel-rich conditions than under fuel-lean conditions. However, prompt-NO production is also significantly curtailed for highly fuel-rich combustion. Reisel and Laurendeau (1994) demonstrated the importance of the rate coefficient for reaction (R9) with respect to the overall prediction of NO in rich ethane

flames. Unfortunately, there appears to be considerable uncertainty in the rate coefficient for this reaction (Drake and Blint, 1991).

2.4 Counterflow Diffusion Flames

Counterflow diffusion flames have been of great interest because they provide a suitable method to study in detail the structure of pure diffusion flames, to estimate the overall reaction rate for fuel-oxidant combinations, and to examine the effectiveness of flame inhibitors. Such flames have also been used to understand the interactions between fluid mixing processes and chemical kinetics, which is essential in making reliable calculations of flame structure and pollutant formation. In the past decade, laminar opposed-flow diffusion flame studies have gained added importance because turbulent diffusion flame structure can often be described as an ensemble of stretched laminar flames (Williams, 1975).

In general, counterflow diffusion flames can be established in the zone of impingement of two opposed gaseous flows of fuel and oxidant. As shown in Fig. 2.3, Tsuji (1982) has subdivided these flames into four types: (I) the three-dimensional or flat counterflow diffusion flame established between two opposed jets from circular tubes or rectangular nozzles (*Type I Flame*) (Otsuka and Niioka, 1972), (II) the flat counterflow diffusion flame established between two opposed matrix burners ejecting individual reactants (*Type II Flame*) (Pandya and Weinberg, 1963), (III) the counterflow diffusion flame established in the forward stagnation region of a spherical or hemispherical porous burner (*Type III Flame*) (Spalding, 1953; Simmons and Wolfhard, 1957), and (IV) the counterflow diffusion flame established in the forward stagnation region of a cylindrical porous burner (*Type IV Flame*) (Tsuji and Yamaoka, 1967). For over thirty years, these four types of flames have been used to study the overall reaction rate for various combinations of fuel and oxidant and the detailed structure and reaction mechanism of various laminar diffusion flames.

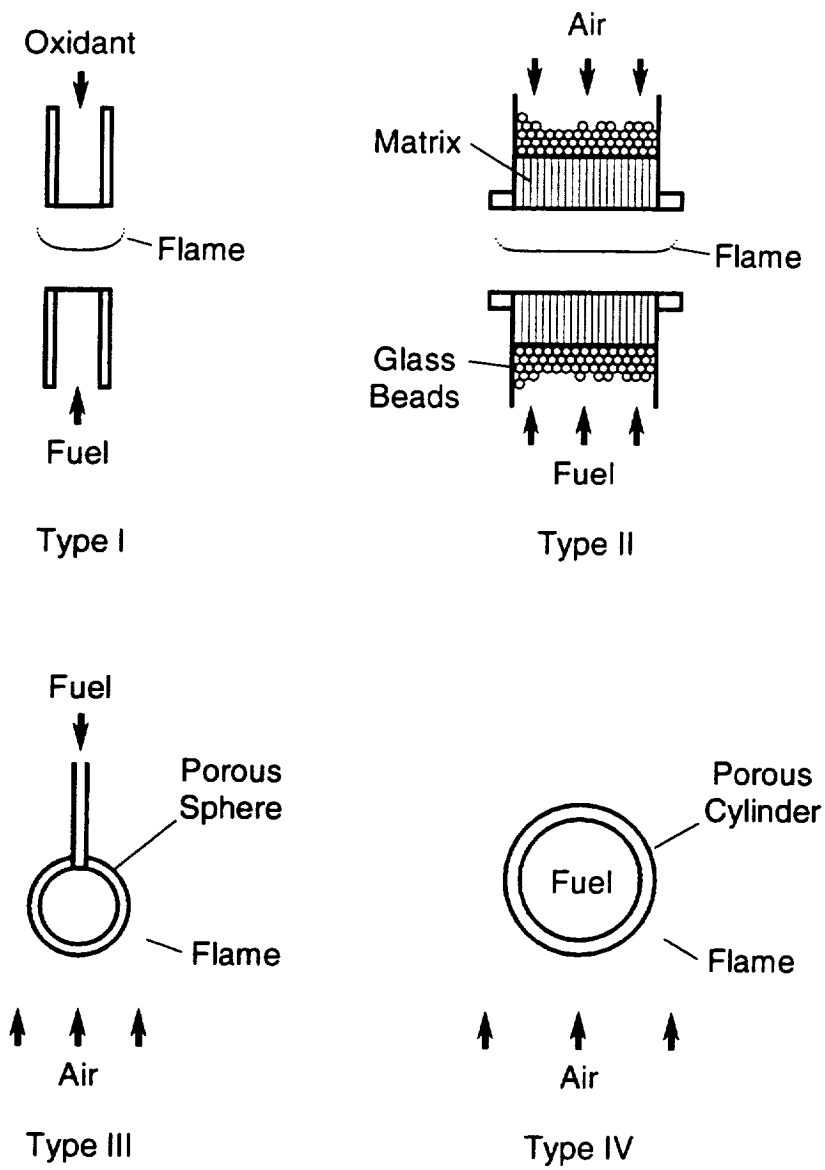

Figure 2.3: Classification of counterflow diffusion flames into four types (Tsuji, 1982).

2.4.1 Flame Structure

The flat counterflow diffusion flame (*Type II Flame*) is especially suitable for optical and spectroscopic investigations of the structure of diffusion flames. Pandya and Weinberg (1963) used optical methods such as interferometry and deflection mapping in ethylene-air flames. They also used techniques like sodium line reversal, illuminated particle tracking, and gas chromatography to study flow patterns, refractive index fields, temperature distributions, and gas compositions. The most significant observation of their research was that the zone of heat release is about ten times wider than would be expected of an equivalent premixed flame, thus making diffusion flames applicable to the study of faster flame reactions. This work was followed by studies on the thermal structure of ethylene, methane and carbon monoxide flames by Patel and Chu (1970), the absorption spectrum of an ethylene flame by Laud and Gaydon (1971), and the thermo-aerodynamic structure of ethanol flames by Pandya and Srivastava (1972; 1975). The latter employed interferometry and particle-tracking techniques, and revealed that the luminous ethanol-air flame was accompanied by endothermic zones on both the fuel and oxidizer sides.

The laminar counterflow diffusion flame established in the forward stagnation region of a porous cylinder (*Type IV Flame*) has also been extensively used for studying the flame structure of gaseous fuels. As the fuel-ejection velocity is decreased or the air-stream velocity is increased, the flame approaches the cylindrical surface and eventually becomes detached from the stagnation region and converted into a so-called wake flame. This flame is especially suited for studying flame-extinction phenomena because the flame extinction limit can be observed with good reproducibility, and the physical meaning of the extinction parameter is quite clear. The structure of this hydrocarbon-air diffusion flame was investigated by Tsuji and Yamaoka (1971) and Abdel-Khalik et al. (1975). The measured velocity was found to decrease linearly on approaching the flame zone where the increase in temperature caused the gas to expand accordingly. The velocity reached its maximum near the fuel side of the luminous flame zone, and decreased rapidly towards the stagnation point. Figure 2.4 shows a typical velocity profile in a counterflow diffusion

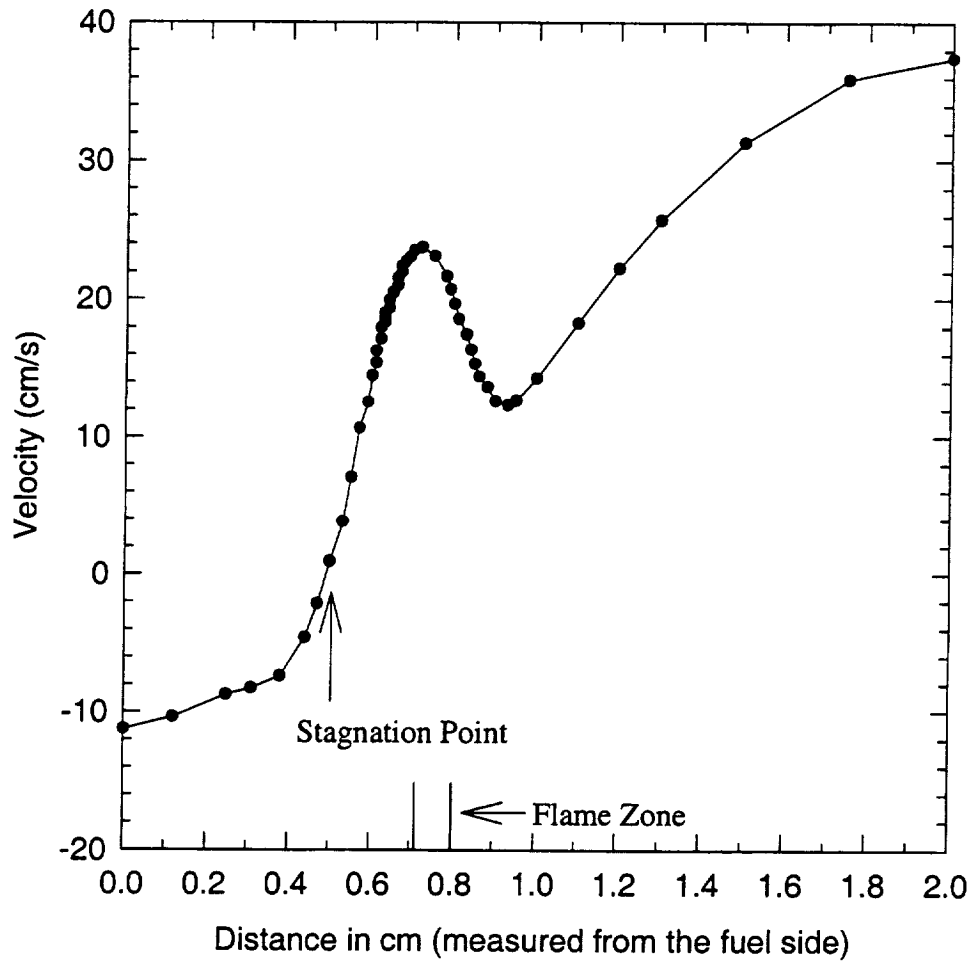

Figure 2.4: Velocity profile in a typical counterflow diffusion flame stabilized between opposing flows of fuel and oxidizer showing the stagnation point and approximate location of the flame zone. This profile was generated using the OPPDIF code for a flame stretch of 24.4 s^{-1}.

flame stabilized between opposing flows of fuel and oxidizer, as generated using the OPPDIF code (Lutz et al., 1996). The temperature was found to peak in the luminous flame zone and to decrease rapidly toward both the fuel and air sides. The fuel concentration decreased rapidly towards the luminous flame zone and disappeared almost completely at the air side of the flame zone. The oxygen concentration decreased rapidly from the air side towards the flame zone, but there was always some oxygen on the fuel side of the flame. It was concluded that the diffusion of small amounts of oxygen into the fuel side through the flame zone is a general characteristic of hydrocarbon-air laminar diffusion flames. The other major species such as carbon dioxide, water vapor, hydrogen, and carbon monoxide have their maximum concentrations in and around the luminous flame zone. Their concentrations decrease toward both the fuel and air sides of the flame, but they exist over a considerably wide region on the fuel and air sides.

The first significant numerical investigation of the counterflow diffusion flame was made by Dixon-Lewis et al. (1984). A similarity solution was invoked so that the problem could be treated as one-dimensional in space. The structure and extinction limits of a methane-air counterflow diffusion flame were modeled with complex chemistry and a detailed formulation of the transport fluxes. The analysis began with the boundary-layer equations and imposed a potential flow from a point-source located infinitely far from the stagnation surface. The radial and tangential velocity components were specified in terms of the potential-flow velocity gradient. The axial pressure gradient was zero (boundary-layer assumption) and the radial pressure gradient was simply imposed. Although this model reasonably predicts the major structural features of the flow, the overall system does not behave as a straightforward boundary layer flow. To match the experimental results of Tsuji and Yamaoka (1969; 1971), Dixon-Lewis et al. (1984) found it necessary to modify the measured velocity gradient of 100 s^{-1} for the cold flow to near 130 s^{-1} in the flame region.

In the above approach, the strain field was characterized by a single parameter, the potential flow velocity gradient, and the analysis was applied to a semi-infinite domain. To model the flame more realistically, Kee et al. (1988) dropped the single-parameter

description of the strain field and their analysis considered a finite domain as opposed to a semi-infinite domain. Also, the radial pressure gradient was computed instead of being prescribed from the potential flow, as in previous analyses. In the usual boundary-layer analysis, an explicit boundary condition cannot be imposed on the inlet velocity – once the potential-flow velocity gradient is set, the inlet velocity follows from the solution. This particular analysis, however, allowed for a more general prescription of the inlet velocity. As might be expected, this formulation gave better agreement with extinction measurements when compared to previous analyses.

In the earlier analysis of Dixon-Lewis et al. (1984), the point-source solution was characterized by a single strain rate, which determines both components of the velocity and the pressure gradient. The disadvantage with this analysis is that there is no length scale for the problem. In other words, this formulation could not account for the distance between the nozzles. In contrast, the more general formulation of Kee et al. (1988) does consider the nozzle separation, as described earlier. In this model, the flame stretch or strain rate was derived from the solution by computing a velocity gradient rather than supplying it to the model as in the earlier analysis. Several definitions of the strain rate have been proposed in the literature. To characterize the strain rate in the absence of velocity measurements, Puri and Seshadri (1986) derived an expression based on assuming a large Reynolds number and a thin mixing layer. However, laser-doppler velocimetry (LDV) measurements (Chelliah et al., 1990) showed that this expression overpredicted the strain rate by a factor of two. Kee et al. (1988) and Chelliah et al. (1990) defined an effective strain rate as the maximum value of the oxidizer-side velocity gradient just prior to the flame. Quite often, it is convenient to use a global strain rate parameter which is directly indicative of the fuel/air nozzle exit velocity rather than a local strain rate which is a nonlinear function of the velocity and density of the fuel/air streams. Magre et al. (1995) have defined a global strain rate as the sum of the fuel and oxidizer nozzle exit velocities divided by the nozzle separation distance. We have adopted this definition of global strain rate in our work. Recently, Lutz et al. (1996) developed the OPPDIF code based on the

model of Kee et al. (1988) to compute the structure of counterflow diffusion flames. In this study, we use this code to model all of our laboratory counterflow diffusion flames.

Progress in the numerical modeling of counterflow diffusion flames has been complemented by recent advances in nonintrusive measurements of temperature and species concentrations. Trees et al. (1995) have performed an experimental and numerical study to characterize the structure of diffusion flames formed between counterflowing streams of hydrogen diluted with nitrogen and air diluted with nitrogen. Using a UV Raman scattering system, mass fraction profiles of the species H_2, O_2, H_2O and N_2, and temperature profiles were measured at two conditions, one close to and the other far from the critical conditions of extinction, and both with low concentrations of hydrogen in the reactant stream. Numerical calculations using detailed H_2-O_2 chemistry were performed to predict the flame structure and the results were found to agree well with measurements. The success of the numerical predictions was attributed to the accuracy of the chemical reaction mechanism employed to describe the combustion of hydrogen, particularly at low concentrations of hydrogen in the reactant stream.

Magre et al. (1995) conducted temperature and concentration measurements by CARS in counterflow laminar propane-air diffusion flames. They used a combination of broadband CARS thermometry for nitrogen and a narrowband technique for detection of a second major species, *viz.* CO. Temperature profiles were measured for various conditions of strain and equivalence ratio. The agreement between experiments and calculations using a one-dimensional model with detailed kinetics was satisfactory, except at high equivalence ratios. At lower equivalence ratios, in certain cases, the temperature predictions were within the experimental uncertainty of the measurements with reference to both the reaction zone width and the peak temperature. At higher equivalence ratios, however, the temperature was overpredicted by more than 100 K. This was attributed to interferences in the CARS signal from soot precursors.

Sun et al. (1996a) conducted experimental and computational studies in counterflow premixed and diffusion flames to examine the response of flame structure to strain rate and pressure variations. Temperature profiles measured using spontaneous

Raman scattering agreed well with computed profiles using detailed kinetics and transport properties. For diffusion flames, it was observed that the flame structure at different pressures largely scales with the density-weighted strain rate instead of the strain rate alone. Sun et al. (1996b) measured temperature and major species concentrations in ethylene/oxygen/nitrogen and acetylene/oxygen/nitrogen counterflow diffusion flames using spontaneous Raman scattering. Numerical predictions using detailed kinetics and transport properties were in reasonable agreement with measurements. It was observed that acetylene is the major intermediate species in the ethylene flame, having a significant influence on the heat release, overall fuel destruction, and molecular mass growth of PAHs.

2.4.2 Partial Premixing

Partially premixed flames are of interest owing to their applications in gas appliances and other practical combustors. However, the stretch rates in partially premixed co-flow flames vary with axial position, and the relatively complex flow caused by their two-dimensional geometry is not convenient for an evaluation of relevant chemical kinetic processes. On the other hand, stretch rates in counterflow flat flames are independent of radial location along the flame surface. Therefore, the counterflow configuration is ideal for the study of partially-premixed flames.

Yamaoka and Tsuji (1974; 1976; 1978) conducted pioneering experimental studies of the structure of partially premixed counterflow flames using measurements of the mole fractions of major species. Smooke et al. (1988) reported results from experimental and numerical studies of counterflow partially premixed methane-air flames. Experimental data obtained for the temperature profile, axial velocity profile, and concentration profiles of various stable species compared favorably with numerical predictions. It was observed that partial premixing of the reactant streams made the flame less resistant to stretch. In addition, numerical calculations showed that the reaction zone of a partially premixed flame exhibits both a diffusion flame- and a premixed flame-like structure. In particular, a

fuel consumption layer was found to exist where methane reacts with radicals to form CO and H_2 followed by a region where H_2 and CO oxidize to form H_2O and CO_2.

Mastorakos et al. (1992) studied the extinction and temperature characteristics of a flat turbulent counterflow diffusion flame in the stagnation region between two opposed turbulent jets. Extinction was achieved by increasing the bulk velocity, decreasing the tube separation, increasing the turbulence intensity, and decreasing the air volume fraction. The total strain rate at extinction was constant to within 20% and depended only on the degree of partial premixing. Contrary to the observed behavior in laminar flames (Smooke et al., 1988), it was found that partial premixing made the flame more strain resistant, and hence could be used to aid the stability of turbulent nonpremixed flames.

Regarding the structure of these flames, Tanoff et al. (1996) have demonstrated through experimental and computational investigations that slight perturbations in the degree of premixedness may result in severe changes to the structure and character of the flame. Partially premixed methane-air counterflow flames seemed to abruptly change in character from diffusive to premixed (at a given strain rate) as the equivalence ratio in the fuel jet was lowered from ϕ=1.5 to ϕ=1.3. Flames with fuel stream equivalence ratios of ϕ=1.5 and higher were found to be purely diffusive in character from low strain rates up to the extinction point. At strain rates approaching extinction, even flames with a fuel premixedness of ϕ=1.3 behaved like counterflow diffusion flames, as fluid dynamic time scales were too short to allow kinetic processes to develop a premixed flame prior to the development of a diffusion flame.

Tseng et al. (1996) studied the effect of partial premixing on acetylene (C_2H_2) and ethylene (C_2H_4) mole fractions in methane-air counterflow flames, as these species have a significant influence on soot formation and growth. The peak mole fractions of C_2H_2 and C_2H_4 decreased with an increase in the level of partial premixing for a fixed oxidizer stretch rate. The mole fractions of C_2H_2 were significantly overpredicted for nonpremixed and partially premixed flames, whereas the mole fractions of C_2H_4 were overpredicted only for the partially premixed flames. Quantitative reaction path diagrams were used to

explain the above observations on the basis of a shift in the reaction path with increasing levels of partial premixing.

2.4.3 NO_x Formation

Counterflow diffusion flames have played a very useful role in the study of kinetic mechanisms of pollutant formation. However, there have been few investigations of the formation of NO_x in these flames. The following sections review previous work on NO_x formation in counterflow diffusion and partially-premixed flames.

2.4.3.1 NO_x formation in Counterflow Diffusion Flames

The first detailed investigation on NO_x formation was conducted by Hahn and Wendt (1981). The structure of the flame was modeled by coupling the momentum and energy conservation equations and by using detailed finite rate kinetics. Measurements of NO_x were made in two flames with very low stretch rates of 1.88 s^{-1} and 3.62 s^{-1} using probe sampling and a chemiluminescent NO/NO_x analyzer. Qualitatively, good agreement was found between the predicted and measured temperature and [NO] profiles. However, quantitative discrepancies existed in the comparison of both the temperature and [NO] profiles. The peak temperatures were overpredicted by about 150 K, and the peak NO concentrations were underpredicted by about 50%. The oxidation and pyrolysis of fuel nitrogen, as ammonia, was also investigated by first injecting ammonia in the fuel and then in the air, and comparing the predicted versus measured [NO] profiles. The comparatively good agreement between model and experiment when ammonia was injected with the fuel indicated that the chemistry of ammonia pyrolysis in the presence of fuel hydrocarbon fragments was reasonably described by the chosen mechanism.

Drake and Blint (1989) investigated the effect of flame stretch on thermal NO_x formation in laminar, counterflow diffusion flames with $CO/H_2/N_2$ as fuel. Detailed chemistry-transport model calculations of temperature were in reasonable agreement with

previous experimental results for flames with stretch rates of 70 s^{-1} and 180 s^{-1}. There was, however, a significant discrepancy between the measured and predicted [NO] profiles. This was attributed to the very poor spatial resolution of the probe sampling measurements. Major corrections applied to account for this factor improved the agreement between the measured and predicted [NO] profiles. Additional model calculations were obtained over a wide range of flame stretch (0.1 - 5000 s^{-1}). Calculated NO_x concentrations decreased dramatically with increasing flame stretch. This decrease was caused by declines in both the reaction time in high temperature flame zones and in the net NO_x formation rate. The net NO_x formation rate is affected by flame stretch owing to changes in the peak flame temperature, superequilibrium oxygen atom concentration, NO destruction reactions, and N_2O formation reactions. Most of the NO_x in flames at low stretch is formed by the Zeldovich mechanism, while the N_2O pathway dominates NO_x formation in flames at very high stretch for which the peak temperatures are lower. It was observed that a very effective way to reduce thermal NO_x formation in the stagnation region of counterflow diffusion flames is to increase flame stretch.

Drake and Blint (1991) also studied the relative importance of Zeldovich, N_2O, and prompt mechanisms in laminar counterflow diffusion flames with nitrogen-diluted methane as fuel. They found that for all values of flame stretch, prompt-NO was the dominant pathway of NO formation. The remaining NO is formed approximately equally by the Zeldovich and N_2O mechanisms. Probe measurements of [NO] by Atreya et al. (1996) in low strain rate, sooty counterflow diffusion flames revealed that a significant reduction in NO formation occurs because of a decrease in flame temperature caused by flame radiation. Soot was also observed to interact with NO formation through the major radical species produced in the primary reaction zone. More recently, Sick et al. (1998) reported comparisons of PLIF measurements of [NO] in *Type IV* counterflow diffusion flames with model predictions. Their results indicated a need for refinement of both the CH and NO reburn chemistry. They observed that a rate coefficient for the prompt-NO initiation reaction that was 2.5 times that used in the GRI (version 2.11) mechanism provided excellent agreement between [NO] measurements and predictions. They also

suggested the need for accurate determination of the $CH+H_2O \Leftrightarrow CH_2OH$ and the $HCCO+NO \Leftrightarrow HCN+CO_2$ reactions.

There has been only one study concerning the formation of NO in counterflow diffusion flames at high pressure (Bonturi et al., 1997), and that has been numerical in nature. Bonturi et al. (1997) performed computations of methane-air counterflow diffusion flames at pressures up to 30 atm and strain rates up to 1000 s^{-1}. They observed that at a constant strain rate, the computed [NO] increases with pressure uniformly from 1 to 30 atm. Their study involved undiluted fuel and preheated air, and peak temperatures were between 2000 and 2500 K. Although prompt-NO was found to be dominant in their flames, a significant contribution also existed from thermal-NO owing to these high flame temperatures.

2.4.3.2 NO_x formation in Counterflow Partially-Premixed Flames

There have been no previous experimental studies on NO_x formation in counterflow partially-premixed flames. Nishioka et al. (1993) conducted a numerical study of the NO emission characteristics of methane-air Bunsen-type flames in terms of the counterflow flame. A detailed kinetic calculation using C_2 chemistry with both the thermal and prompt NO mechanisms was used to predict the flow, temperature, and concentration fields. The equivalence ratio of the rich mixture was varied from 1.55 to infinity (which corresponds to a pure diffusion flame), while keeping the flame stretch constant. The NO emission index of the double flame was found to be of the same order of magnitude as that of the pure diffusion flame. Moreover, the NO production in the double flame was not as large as might have been expected from the thick, high-temperature region. The main reason for this characteristic was the appearance of a negative production rate through a reverse Fenimore mechanism. The emission index was found to be rather insensitive to equivalence ratio, whereas it decreased rapidly with increased flame stretch. The main source of NO formation was found to be thermal at low stretch rates with a shift to Fenimore at higher stretch rates. This is because production

through the thermal mechanism decreases very rapidly, while that through the Fenimore mechanism first increases and then decreases gradually with increasing flame stretch.

Numerical computations of NO profiles were obtained by Li et al. (1997) in counterflow partially-premixed flames with water sprays added to the air stream. Prompt-NO was found to play a dominant role in NO_x formation, and the NO_x emission index was found to depend strongly on the flame structure and mass fraction of water added in the air stream. Recent computations by Blevins and Gore (1999) for low strain-rate, counterflow partially-premixed flames have focused on understanding the flame structure with respect to NO formation. Two flame fronts were found to exist on opposite sides of the stagnation plane for flames with fuel-side equivalence ratios below 2.5. These flame fronts were found to contain two CH radical concentration peaks, one at the location of the CH_4/air premixed flame front and the other at the fuel-side edge of the CO/H_2/air nonpremixed flame front. NO formation zones were found on the air-side of the premixed CH peak and near the temperature peak corresponding to the CO/H_2/air nonpremixed flame front. NO was found to be consumed via reburn reactions with hydrocarbons in a destruction zone which begins on the reactant side of the CH_4/air premixed flame front and persists throughout the broad region between the two CH peaks.

More recently, Zhu et al. (1999) investigated the effect of thermal radiation on NO predictions in counterflow partially-premixed flames by modifying the OPPDIF code (Lutz et al., 1996) to account for the effect of radiation. Radiation heat loss was calculated in the optically thin limit by employing Planck mean absorption coefficients for CO_2, H_2O, CO, and CH_4. The temperature dependence of the Planck mean absorption coefficients was accounted for by using fourth-order polynomial fits to the results of narrowband calculations. They found that radiative heat loss caused by gaseous emission changes the temperature and NO mole fractions significantly in partially-premixed flames at low fuel-side equivalence ratios.

3. EXPERIMENTAL APPARATUS AND PROCEDURE

3.1 Introduction

The PLIF measurements of [NO], the LIF and LSF measurements of [NO] in ethane-air and methane-air counterflow diffusion flames, and the LIF measurements of [NO] in partially-premixed flames were obtained in an atmospheric pressure LIF facility. The LIF measurements of [NO] in methane-air counterflow diffusion flames at 2 to 12 atm were obtained in a high-pressure LIF facility. The following sections contain descriptions of the experimental apparatus used in these facilities.

3.2 Atmospheric Pressure LSF/LIF/PLIF Facility

The atmospheric LSF/LIF/PLIF facility consists of a laser system to generate the requisite UV radiation, an optical train of apertures and lenses to focus and size the beam, a burner assembly, a detection system which measures the NO fluorescence, and a data acquisition system. A detailed description of each subsystem is presented below. While the LSF and LIF measurements were obtained using the same experimental apparatus, the PLIF measurements employed a different set of excitation optics and detection system.

The laser system used for generating the UV radiation for NO excitation consisted of a Quanta-Ray GCR-4 Nd:YAG laser, a PDL-3 dye laser, and a WEX-2C wavelength extender. Figure 3.1 shows a schematic of the experimental apparatus. Excitation of NO was achieved through use of the $Q_2(26.5)$ line in the $\gamma(0,0)$ band. The $Q_2(26.5)$ line was chosen because (1) the Boltzmann fraction is relatively insensitive to temperature variations over the range of temperatures of our flames, and (2) other species, such as O_2,

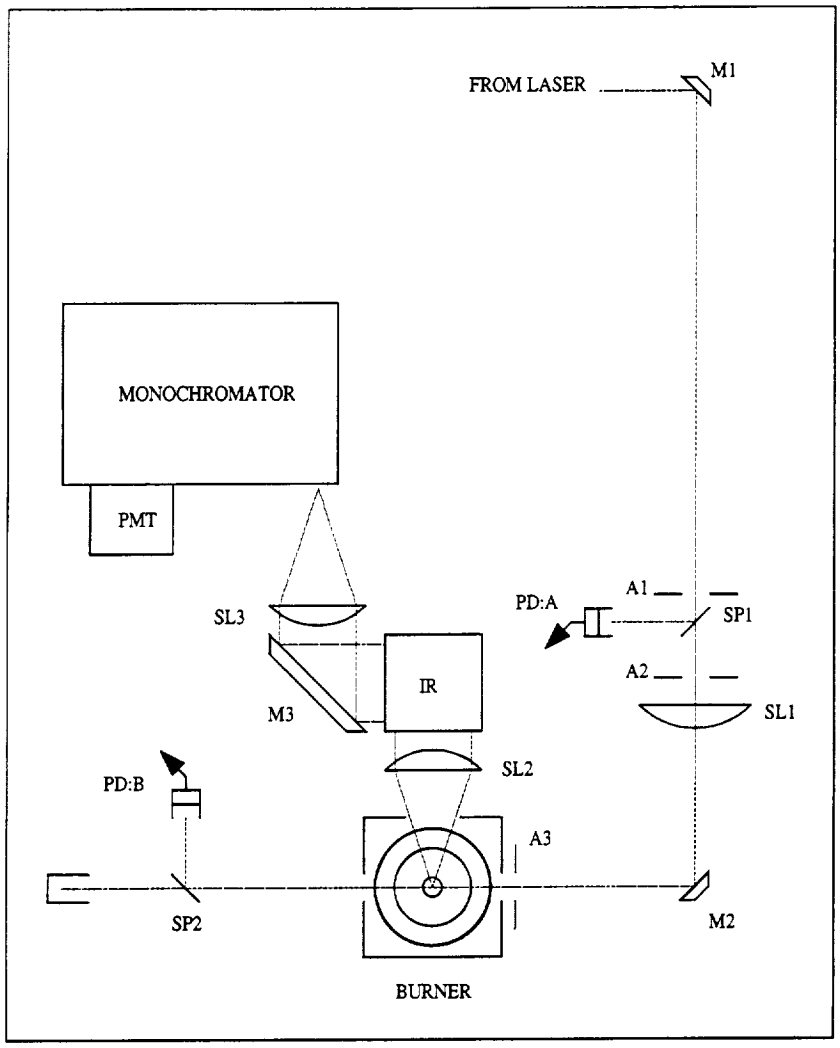

Figure 3.1: Schematic of the experimental setup used for the LSF/LIF measurements. M1, M2, M3 - Mirrors; PD:A, PD:B - Photodiodes; SP1, SP2 - Splitter plates; A1, A2, A3 - Apertures; SL1, SL2, SL3 - Spherical Lenses; IR - Image Rotator.

do not interfere spectrally with this NO absorption line (Partridge et al., 1996). The excitation wavelength was generated by employing the second harmonic (λ= 532 nm) of the Nd:YAG laser to pump the PDL-3 dye laser, which provided visible radiation at approximately 574 nm. The dye fundamental was frequency-doubled ($\lambda/2 \approx 287$ nm) in the WEX-2C wavelength extender and the residual Nd:YAG fundamental (1064 nm) was frequency-mixed with the dye second harmonic to produce a mixed beam at ~226 nm. The four concentric beams (1064, 574, 287, 226 nm) were dispersed using a Pellin-Broca prism, and the mixed beam exited the WEX vertically polarized.

After the beam left the WEX, it was focused into the probe volume using a 1000-mm focal-length fused silica lens. The beam diameter and Rayleigh range were ~200 μm and ~8 mm, respectively. The beam diameter was measured experimentally by passing a razor blade through the beam in steps of 10 μm while monitoring the beam energy using a photodiode. The beam diameter is defined as the distance between locations corresponding to the 90% and 10% relative signal levels. A Fabry-Perot wavelength stabilization system was used to control PDL drift (Cooper and Laurendeau, 1997). Splitter plates were used to split off small portions of the beam for power monitoring via photodiodes. For the linear LIF measurements, a photomultiplier tube was used to monitor the beam energy because of the requisite low laser powers. The measurement of the beam energy is required for normalization of the fluorescence signal in the case of linear LIF measurements, and to ensure saturation in the case of LSF measurements.

For LSF/LIF detection, a portion of the isotropically emitted fluorescence was captured and collimated by a 50-mm diameter, 254-mm focal-length fused silica spherical lens. To raise the collimated fluorescence beam vertically to the monochromator entrance slit height, an image rotator and a 76-mm diameter mirror were used. The raised collimated beam was then focused onto the entrance slit of a 3/4-m monochromator by another 254-mm focal-length lens. The detector is a Hamamatsu R106UH-HA photomultiplier tube which was optimized for temporal resolution of the fluorescence signal (Harris et al., 1976). A 110-mm × 110-mm, 1200-groove/mm holographic grating with a 250-nm blaze angle was used in first order to provide a dispersion of 1.1 nm/mm at

the exit slit. A 1.818-mm wide exit slit was employed so as to spectrally integrate over a 2-nm region of the fluorescence spectrum centered on the $\gamma(0,1)$ band of NO.

For all the LSF experiments, the entrance slit was 68-μm wide by 1-mm tall, thus defining a probe volume which was 68-μm wide along the diameter of the beam and 1-mm long along the axis of the beam. Using this probe volume, the minimum laser fluence needed for ~90% saturation was 16.4 $mJ/mm^2 \bullet pulse$. A smaller slit width was chosen for the LSF measurements so as to collect fluorescence only from the center of the beam where the laser irradiance was sufficiently high to ensure saturation. A 500-ps temporal window was also sampled at the peak of the fluorescence pulse using a Stanford Research Systems SR255 fast sampler and an SR200 gate scanner. This procedure was employed to again ensure that the data was collected under saturated conditions. An SR250 gated integrator was used to capture the signals from the photodiode, thus measuring the relative laser power. The output voltages from the fast sampler and gated integrator were digitized with the SR245 computer interface, and sent to a computer for storage and analysis. For the linear LIF measurements, the probe volume was again 1-mm long, but widened to 170 μm along the diameter of the beam. This was done to collect additional fluorescence from the wings of the beam. The maximum laser fluence permitted for the linear LIF measurements (~0.1 $mJ/mm^2 \bullet pulse$) was determined by attenuating the beam so as to obtain a linear variation of the fluorescence signal with laser fluence. A temporal gate width of 7 ns was used for the linear LIF measurements. Each data point for both the LSF and LIF measurements was averaged over 400 laser shots.

The atmospheric pressure burner system consisted of two opposed cylindrical ducts, each 2.54 cm in diameter, as shown in Fig. 3.2. Fuel was injected through the bottom duct and oxidizer through the top, resulting in a flame stabilized on the oxidizer side of the stagnation plane. To shield the flame from ambient disturbances, an annular flow of nitrogen was passed through a duct surrounding the fuel inlet stream. A water-cooled co-annular heat exchanger was used to cool the upper portion of the burner

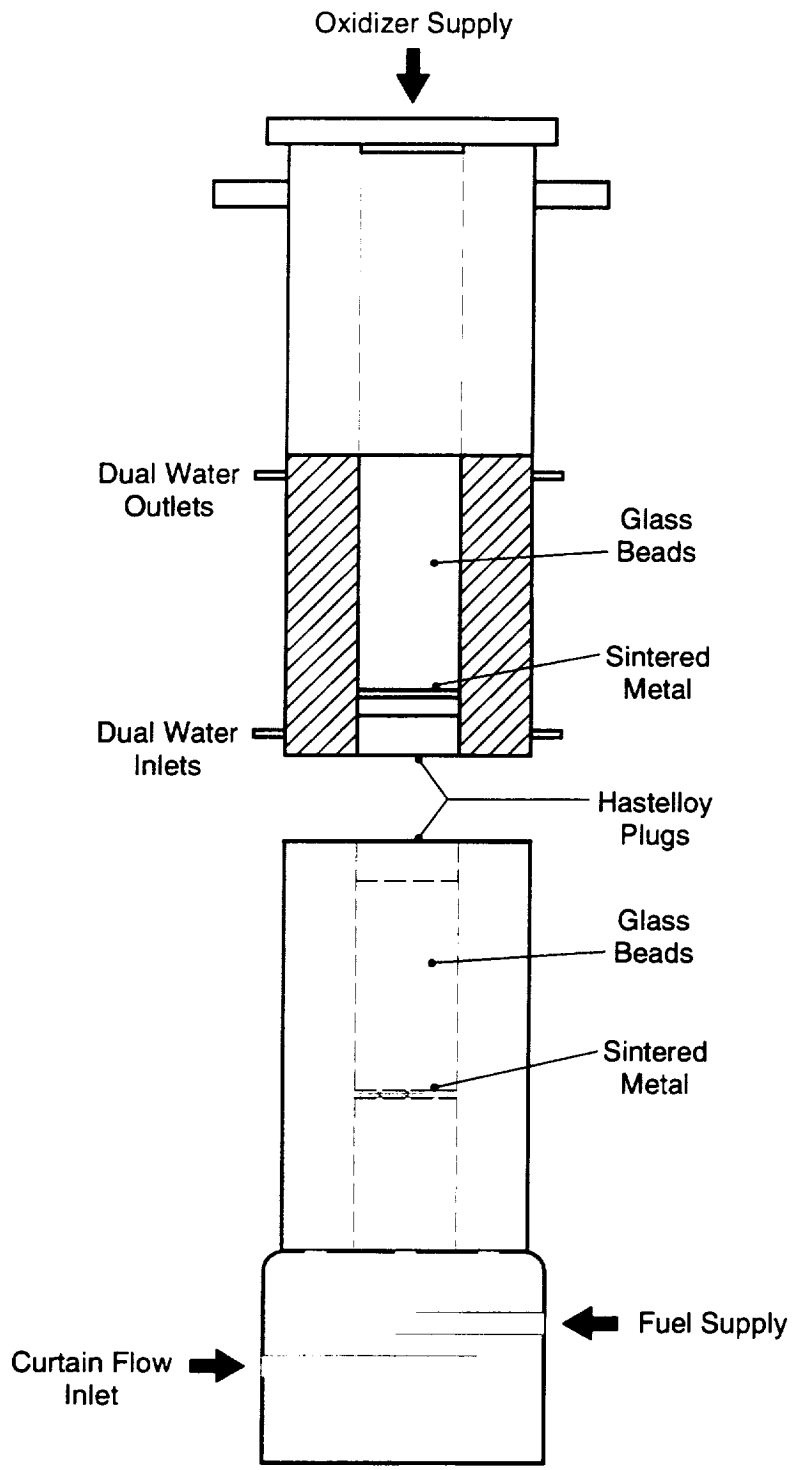

Figure 3.2: Schematic of the atmospheric pressure counterflow burner.

assembly. A water bath in conjunction with a temperature controller was employed to maintain the temperature of the circulating water high enough to avoid condensation on the burner.

For the PLIF measurements, the excitation optics are mostly the same as that used for the LSF measurements. A schematic of the PLIF experimental setup is shown in Fig. 3.3. In addition to the LSF excitation optics, a cylindrical lens was used to vertically expand and collimate the beam, and an aperture/slit assembly was used to clip the wings of the sheet. Since the Fabry-Perot wavelength stabilization system (Cooper and Laurendeau, 1997) was not available at the time of the PLIF measurements, an overlap reference system was used instead. The overlap reference system was composed of excitation optics, a burner to provide a hot NO source, and a separate detection system to detect any NO fluorescence induced by the tuned laser. The dye laser was manually tuned to the NO transition before each experiment by maximizing the signal obtained via the detection system.

In comparison to the LSF measurements, a broadband detection system was used for the PLIF measurements. A wide-band interference filter spectrally centered at 250 nm with a 92-nm FWHM and 6 mm of UG5 CG filter was used in conjunction with an aberration-corrected, fused-silica, UV-Micro-Nikkor 105-mm focal length, f/4.5 lens. The spectrally filtered PLIF image was spatially amplified, discretized, and registered using a Princeton Instruments ICCD detector which incorporated a 578 × 384 pixel charge-coupled device (CCD). To minimize thermal noise, a thermoelectric cooler was used in conjunction with an external water chiller/circulator to reduce the temperature of the CCD to -38°C. A pulse generator was used to provide a gate of appropriate delay and width to the ICCD, and a detector controller was used to control all ICCD voltages, the thermoelectric cooler, and the CCD readout. For each image, 1800 fluorescence events were integrated on chip. Image analysis and reduction were performed on a laboratory Sparc station using PV-WAVE v.5.0 software (Visual Numerics, Inc.).

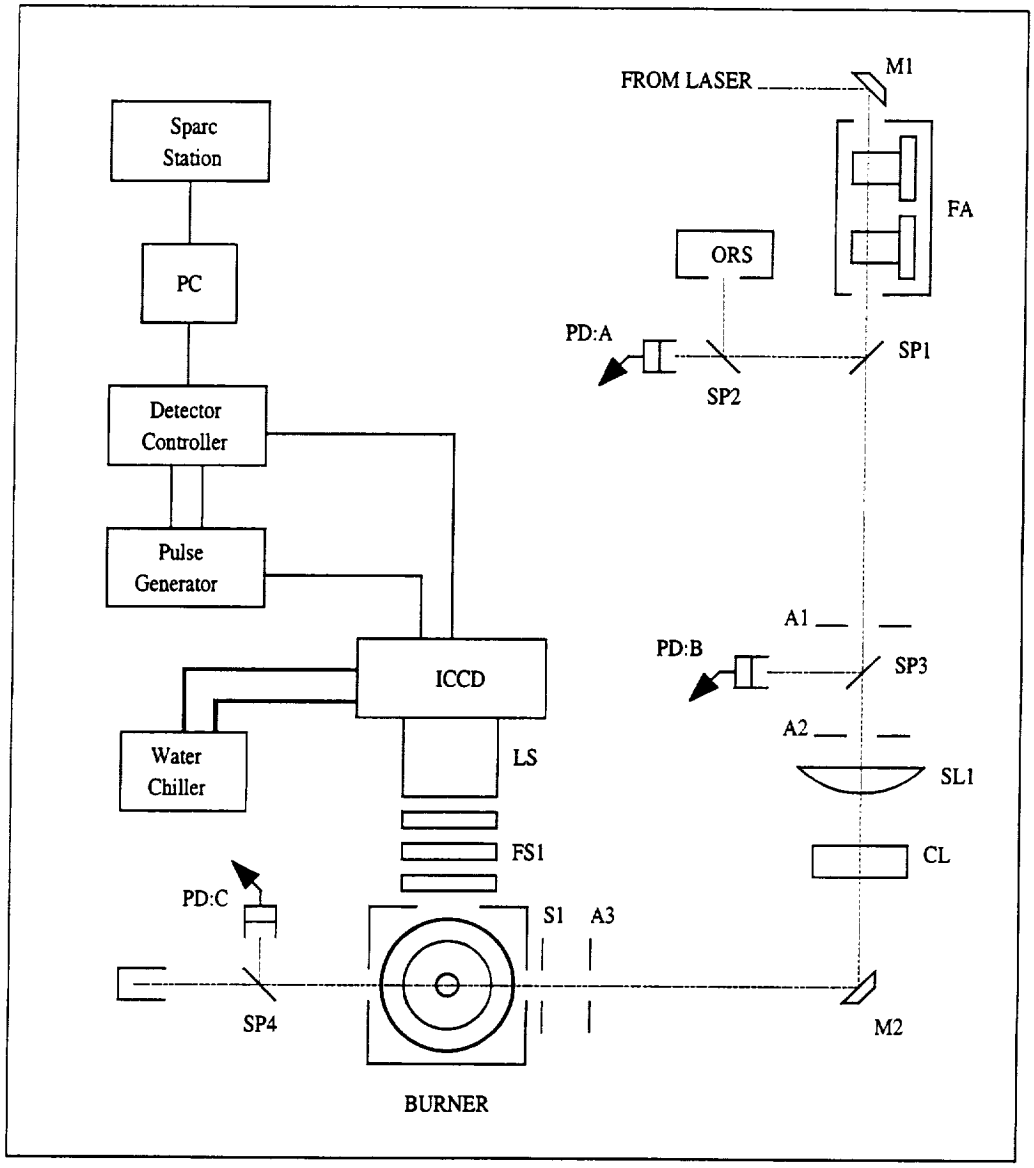

Figure 3.3: Schematic of the experimental setup used for the PLIF measurements. M1, M2 - Mirrors; FA - Frenel Attenuator; ORS - Overlap Reference System; SP1, SP2, SP3, SP4 - Splitter Plates; PD:A, B, C - Photodiodes; A1, A2, A3 - Apertures; SL1 - Spherical Lens; CL - Cylindrical Lens; S - Slit; FS1 - Filter Stack; LS - Camera Lens System.

3.3 Thin Filament Pyrometry

The thin filament pyrometry (TFP) technique (Vilimpoc et al., 1988; Ramakrishna et al., 1995) was used to measure temperatures in the atmospheric pressure methane-air counterflow diffusion and partially-premixed flames. This technique involves extending a 10-20 μm diameter silicon carbide (SiC) fiber with weighted free ends across the centerline of the flame and measuring the radiant emission of the fiber using an infrared detector. A schematic of the optical arrangement consisting of a collimating calcium fluoride (CaF_2) lens, a CaF_2 focusing lens, a chopper, a unidirectionally adjustable slit, and a liquid-nitrogen cooled, indium antimonide (InSb) detector (Graseby Model IS-1), is shown in Fig. 3.4. The InSb detector has a spectral response over a wide range of wavelengths in the infrared regime extending from 1.1 to 5.6 μm. In this wavelength range, the fiber acts as a gray surface with an emittance of 0.88 (Vilimpoc et al., 1988). The infrared radiation from the filament is collimated by the first CaF_2 lens, and focused onto the adjustable slit by the second CaF_2 lens. A 30-μm slit size in the radial direction is selected in order to minimize detection of background flame emission. The detector output is amplified using a pre-amplifier (Graseby Model DP-8100) before being sent to a lock-in amplifier. The optical chopper is used to modulate the infrared radiation at 500 Hz, and the input to the lock-in amplifier is conditioned at the same frequency. The output signal from the lock-in amplifier is sampled at 3 Hz. Each temperature measurement is averaged over 30 samples.

The conversion of detector output voltage to temperature requires a non-linear calibration since the detector output is directly proportional to the emitted radiation and not to the temperature. Additional details are provided in Appendix A. Initial integrations with respect to wavelength of the filament graybody emission convoluted with the detector response and the optics transmission curve are needed for a range of flame temperatures. The ratio of the above integral to the same integral evaluated at the calibration temperature is tabulated as a function of temperature. A fifth-order polynomial fit to this calibration curve is used to convert the measured voltage ratio to temperature. Background infrared radiation from the flame is measured and subtracted from the

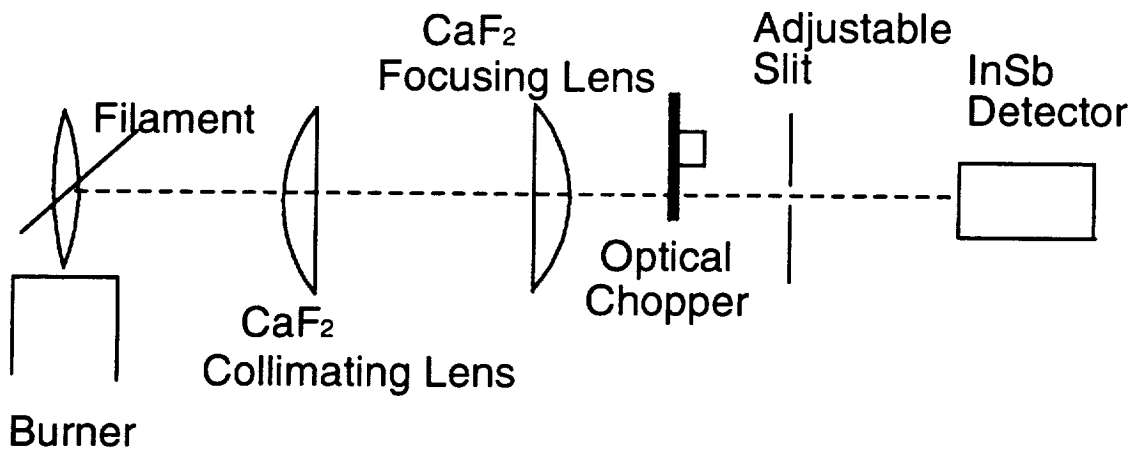

Figure 3.4: Schematic of the optical arrangement used in the thin filament pyrometry technique.

filament emission before the data is reduced. The filament temperature is corrected for radiation losses to obtain the gas temperature. Temperatures thus measured yielded a precision of ± 5 K at peak temperatures and ± 40 K for temperatures below 1000 K.

One of the limitations of the TFP technique is the need for a flame system with an accurately known temperature. To address this issue, we calibrated the SiC filament in the flat flame of a 24-mm square Hencken burner. The surface-mixing Hencken burner produces a flame that is flat, uniform, steady and nearly adiabatic under the right flow conditions. At high enough flow rates, heat losses to the burner are minimal, and thus flame temperatures can be calculated accurately with an adiabatic equilibrium code. Recently, Hancock et al. (1997) have confirmed this presumption using nitrogen CARS thermometry and equilibrium calculations. The combined hydrogen and air flow rate for the calibration flame was 70.1 SLPM at an equivalence ratio of 0.37. The equilibrium temperature of 1383 K for these conditions was verified by thermocouple measurements. The actual filament temperature was then found by an inverse radiative heat loss calculation. Temperatures were subsequently measured using this calibrated filament.

3.4 High-pressure LIF facility

The requisite UV radiation for NO excitation in the high-pressure LIF facility is generated using a Quanta-Ray DCR-3G Nd:YAG laser, a PDL-2 dye laser, and a WEX-1 wavelength extender. As in the case of the atmospheric pressure measurements, excitation of NO is achieved through use of the $Q_2(26.5)$ transition within the $\gamma(0,0)$ band. The excitation wavelength is generated by employing the second harmonic (λ= 532 nm) of the Nd:YAG laser to pump the PDL-2 dye laser, which provides visible radiation at approximately 572 nm. The dye fundamental is frequency-doubled ($\lambda/2 \approx 286$ nm) in the WEX-1 wavelength extender and the residual Nd:YAG fundamental is frequency-mixed with the dye second harmonic to produce a mixed beam at ~226 nm. The four concentric beams (1064, 572, 286, 226 nm) are dispersed using a Pellin-Broca prism, and the mixed

beam exits the WEX vertically polarized. A Fabry-Perot wavelength stabilization system similar to the one used in the atmospheric pressure LSF/LIF/PLIF facility was also incorporated into the high-pressure LIF facility to control PDL drift.

After leaving the laser system, the beam is focused with a 600-mm focal length lens, producing a spot size of ~250 μm over a 1-cm diameter counterflow burner designed for use in the high-pressure combustion facility described by Carter et al. (1989). The pressure vessel has four optical ports, two of which provide optical access for the laser beam through the combustion facility. Before entering the vessel, the beam passes through two fused silica plates, which direct two portions of the beam toward UV-sensitive photodiodes. The first photodiode is used to produce a triggering pulse for the electronics. The beam energy monitored using the second photodiode is used to correct the LIF signal for variations in beam energy. A two-mirror beam steering assembly is then used to raise and direct the main beam through the center of the optical ports and thus over the burner. The remainder of the beam leaving the high-pressure facility is directed to a beam dump.

For fluorescence detection, we make use of an optical port perpendicular to the laser entrance and exit ports. A 254-mm focal-length fused silica lens is used to collimate the fluorescence. A mirror assembly then raises and rotates the fluorescence by 90°. The fluorescence is next focused by a 400-mm focal-length fused silica lens onto the entrance slit of a 1-m monochromator. The detector is a Hamamatsu R108UH-HA photomultiplier tube which is optimized for temporal resolution of the fluorescence signal (Harris et al., 1976). The broadband fluorescence signal encompasses a spectral width of ~3 nm and is detected over a spectral region centered at ~236 nm, corresponding to the $\gamma(0,1)$ band of NO. Each data point is averaged over 600 laser shots.

The burner used for the high-pressure [NO] measurements was designed and fabricated specifically for the high-pressure facility in our laboratory. Figure 3.5 shows a schematic of the burner. It is entirely made from stainless steel so as to withstand corrosion in the high-temperature, high-moisture environment inside the pressure vessel. The counterflow burner system consists of two identical burners mounted on two plates

and facing each other. The top plate was moved relative to the bottom plate by means of a ball screw which was fixed to the bottom plate. For stability, two shafts in addition to the ball screw were fixed vertically on the bottom plate. Bearings provided in the top plate allowed free movement of the top plate over the shafts. The relative movement of the top plate with respect to the bottom plate permitted variation of the distance between the two burners.

Each burner consists of a 1-cm i.d. inner tube surrounded by a 1.68-cm i.d. outer tube. The fuel or air is introduced through the inner tube, while the annular region between the tubes is used to provide a nitrogen guard flow which helps in isolating the combustion environment from extraneous air currents. Since guard flow is provided in both directions, minimal influence of the external flow field is ensured on the flame. Furthermore, the guard flow rate is adjusted so that the velocity of the guard flow always matches that of the fuel and air. Multiple disks of sintered metal are placed within both tubes to avoid radial and circumferential gradients in the flow. Hastelloy honeycomb disks are placed at the end of the tubes to provide a uniform velocity profile at the exit of the burners. The outer tube is surrounded by an annular region in which water is circulated to cool the burner. A high-pressure pump is used to maintain sufficient flow of water at high vessel pressures. In addition, a heater is used to maintain the temperature of the cooling water high enough to avoid condensation on the surface of the burners.

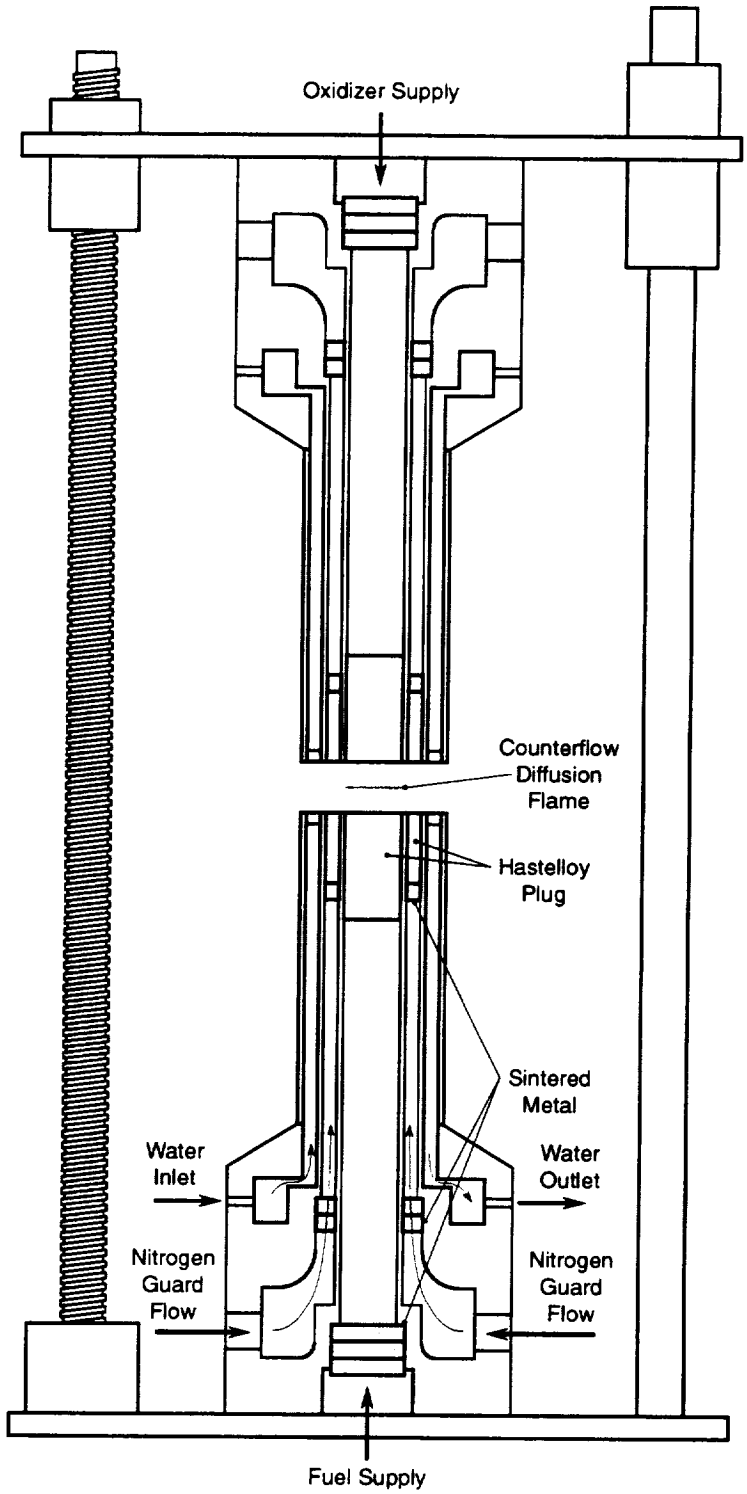

Figure 3.5: Schematic of the counterflow burner used for making the high-pressure LIF measurements of NO.

4. QUANTIFICATION OF PLIF MEASUREMENTS OF NITRIC OXIDE IN LAMINAR PARTIALLY-PREMIXED FLAMES

4.1 Introduction

Planar laser-induced fluorescence (PLIF) is a nonintrusive optical diagnostic tool for making two-dimensional measurements of relevant species concentrations. PLIF measurements achieve high temporal and spatial resolution via the use of both high-power pulsed lasers and intensified-charge-coupled-device (ICCD) detectors. However, obtaining quantitative species concentrations from a raw PLIF image requires correcting that image for errors associated with variations in the Boltzmann fraction, the overlap fraction and the electronic quenching rate coefficient. These measurement parameters depend to varying degrees on the local temperature, pressure, and major-species concentrations. Of these three measurement parameters, correcting for the influence of variations in the electronic quenching rate coefficient is the most difficult, and represents the primary limitation to realizing quantitative PLIF imaging of species concentrations (Hanson et al., 1990). Owing to this difficulty, PLIF is most often used as a qualitative field diagnostic. On the other hand, laser-saturated fluorescence (LSF) measurements are relatively independent of both the laser spectral irradiance and the electronic quenching rate coefficient. Thus, PLIF measurements can be made more quantitative by utilizing selected LSF point measurements.

Recent advancements in both the measurement of electronic quenching cross-sections at flame temperatures (Drake and Ratcliffe, 1993) and the modeling of electronic quenching rate coefficients (Paul et al., 1993) allow for improved PLIF concentration images. These improvements can be used to implement numerically-based correction schemes (Paul et al., 1994) which enhance the quantitative nature of PLIF concentration

images. However, in addition to electronic quenching cross-sections for the major species, these advanced correction schemes require spatially-resolved measurements of the major-species concentrations. Although such measurements are feasible, they require extensive if not unique experimental resources. Moreover, the requisite major-species electronic quenching cross-sections have been measured for only a limited number of probe species. Hence, the general implementation of numerically-based correction schemes for PLIF measurements would require significant lead-time for both cross-section measurements and model validation.

Based on these difficulties, the objectives of this study are to obtain PLIF images of nitric oxide (NO) concentration [NO] in laminar partially-premixed flames and to demonstrate an experimentally-based PLIF quantification procedure. The efficacy of the quantification procedure is assessed by comparison of calibrated PLIF measurements with quantitative LSF point measurements. The work presented here is an extension of a previous investigation (Partridge, 1996) which assessed the quantitative nature of PLIF measurements in an inverse-diffusion flame (IDF). This previous study was conducted in an axial inverse-diffusion flame centered within an annular fuel-rich premixed combustion zone. The quantitative nature of PLIF images of [NO] in the inverse-diffusion flame was assessed relative to 290 independent LSF measurements of [NO] taken throughout the imaged environment. Comparisons between the two measurements were made by sampling the PLIF image at locations and areas corresponding to the 290 point measurements. Here, instead of assessing uncorrected PLIF measurements, we focus on obtaining semi-quantitative PLIF images of [NO] in flames that present potentially harsher environments than the previous inverse-diffusion flame.

Partially-premixed flames offer a difficult environment for the assessment of PLIF because of their wide range of temperatures, stoichiometries and major-species concentrations. On this basis, we investigated two flame configurations stabilized on a concentric-tube burner with an overall equivalence ratio of 0.5 and fuel-tube equivalence ratios of 1.33 and 2.22, respectively. These flames were selected because previous work (Kim et al., 1995) over a wide range of fuel-tube equivalence ratios (1.1 - 10)

demonstrated that the NO emission indices were at their maximum and minimum, respectively, for these flame conditions. For both configurations, NO production occurs primarily between an inner premixed and an outer nonpremixed flame front, which constitutes the characteristic dual-flame structure of partially-premixed flames (Kim et al., 1995).

4.2 Experimental Techniques

We begin with a brief description of the experimental facility used in the PLIF and LSF measurements. A more detailed description is provided by Reisel et al. (1993). Excitation of NO is achieved through use of the $Q_2(26.5)$ line in the $\gamma(0,0)$ band. The $Q_2(26.5)$ line was chosen because (1) the Boltzmann fraction is relatively insensitive to temperature variations over the range of temperatures of our flames, and (2) other species, such as O_2, do not interfere spectrally with this NO absorption line (Partridge et al., 1996). The excitation wavelength is generated by employing the second harmonic (λ= 532 nm) of a Quanta-Ray GCR-4 Nd:YAG laser to pump a PDL-3 dye laser, which provided visible radiation at approximately 574 nm. The dye fundamental was frequency-doubled ($\lambda/2 \approx 287$ nm) in a WEX-2C wavelength extender and the residual Nd:YAG fundamental was frequency-mixed with the dye second harmonic to produce a mixed beam at ~226 nm. The four concentric beams (1064, 574, 287, 226 nm) were dispersed using a Pellin-Broca prism, and the mixed beam exited the WEX vertically polarized.

After the beam left the WEX, it was focused into the probe volume where the waist diameter and Rayleigh range were ~50 μm and ~8 mm, respectively. A Fabry-Perot wavelength stabilization system was used to control PDL drift (Cooper and Laurendeau, 1997). Splitter plates were used to split off small portions of the beam for power monitoring via photodiodes. The beam energy monitored by the photodiodes is required for normalization of the fluorescence signal in the case of PLIF, and to ensure saturation in the case of LSF measurements. For the LSF measurements, the fluence needed for ~90% saturation is 16.4 $mJ/mm^2 \cdot$pulse. In addition, for the PLIF measurements, a cylindrical

lens was used to vertically expand and collimate the beam, and an aperture/slit assembly was used to clip the wings of the sheet.

For LSF detection, a portion of the isotropically emitted fluorescence was captured and the collimated beam was focused onto the entrance slit of a 3/4-m monochromator. The detector is a Hamamatsu R106UH-HA photomultiplier tube which was optimized for temporal resolution of the fluorescence signal (Harris et al., 1976). For all the LSF experiments, the entrance slit was 68-μm wide by 1-mm tall, thus defining a probe volume which is 68-μm wide along the diameter of the beam and 1-mm long along the axis of the beam. A 110-mm × 110-mm, 1200-groove/mm holographic grating with a 250-nm blaze angle was used in first order to provide a dispersion of 1.1 nm/mm at the exit slit. A 1.818-mm wide exit slit is used so as to spectrally integrate over a 2-nm region of the fluorescence spectrum centered on the γ(0,1) band of NO. A 500-ps window at the peak of the fluorescence pulse is sampled using a Stanford Research Systems SR255 fast sampler and an SR200 gate scanner. Each data point was averaged over 400 laser shots.

In comparison to the LSF measurements, a broad-band detection system was used for the PLIF measurements. A wide-band interference filter spectrally centered at 250 nm with a 92-nm FWHM and 6 mm of UG5 CG filter was used in conjunction with an aberration-corrected, fused-silica, UV-Micro-Nikkor 105-mm focal length, f/4.5 lens. The spectrally filtered PLIF image was spatially amplified, discretized, and registered using a Princeton Instruments ICCD detector (Princeton Instruments ST-130) which incorporated a 578 × 384 pixel charge-coupled device (CCD). To minimize thermal noise, a thermoelectric cooler was used in conjunction with an external water chiller/circulator (Lauda RMT-6, Brinkmann Instruments) to reduce the temperature of the CCD to -38° C. A pulse generator was used to provide a gate of appropriate delay and width to the ICCD, and a detector controller was used to control all ICCD voltages, the thermoelectric cooler, and the CCD readout. For each image, 1800 fluorescence events were integrated on chip. Image analysis and reduction were performed on a laboratory Sparc station using PV-WAVE v.5.0 software (Visual Numerics, Inc.)

The annular co-flow burner used in this study is shown in Fig. 4.1. It consisted of a central 4.6 mm i.d. fuel tube and a concentric co-flow air tube 25 mm in diameter. Partial premixing was accomplished by adding the desired amount of air to ethane in the fuel tube at a sufficient distance before the burner assembly so as to obtain molecularly mixed flow. The flow rate of the fuel was held at 0.15 slpm for both flames. The annular air tube was used to deliver a co-flow of oxygen in nitrogen at a dilution ratio of 3.76. Finally, an outer argon guard flow was employed to separate the combustion environment from the surrounding room air.

4.3 Results and Discussion

Using the aforementioned experimental apparatus, PLIF and LSF measurements of [NO] were made in atmospheric pressure, laminar, ethane-air partially premixed flames. In particular, we investigated two flames with fuel-tube equivalence ratios (ϕ_B) of 1.33 and 2.22, respectively, and an overall equivalence ratio ϕ_o=0.5. The calibration factor for the LSF measurements was determined using a standard NO doping technique in a ϕ=0.8 premixed $C_2H_6/O_2/N_2$ flame with a dilution ratio of 3.76 (Reisel et al., 1993). The calibration was conducted at a height of 4 mm from the burner surface. The NO concentration relative to the calibration flame temperature was then determined from a combination of Eqs. (2.13) and (2.21), i.e.,

$$N_{ppm,RT} = C_F S_F , \tag{4.1}$$

where C_F is a calibration factor determined from the slope of the fit to the calibration data, and S_F is the digital fluorescence signal.

Although LSF measurements can be considered quantitative, it is important to address the limitations associated with this method. We have recently made comparisons between LSF measurements of [NO] in ethane-air counterflow flames and similar linear LIF measurements corrected for variations in the electronic quenching rate coefficient (Ravikrishna et al., 1997). A four-level model was also used to investigate the effects of

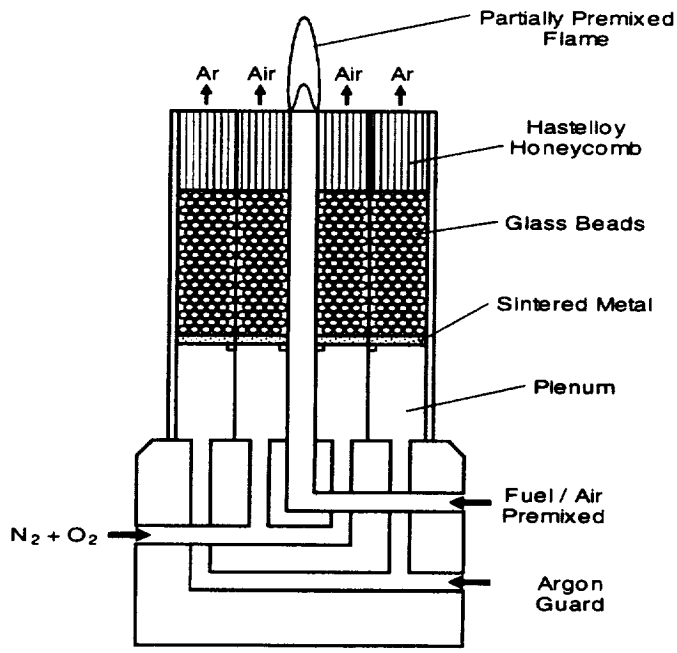

Figure 4.1: Schematic of burner used for studying co-flow, partially premixed flames.

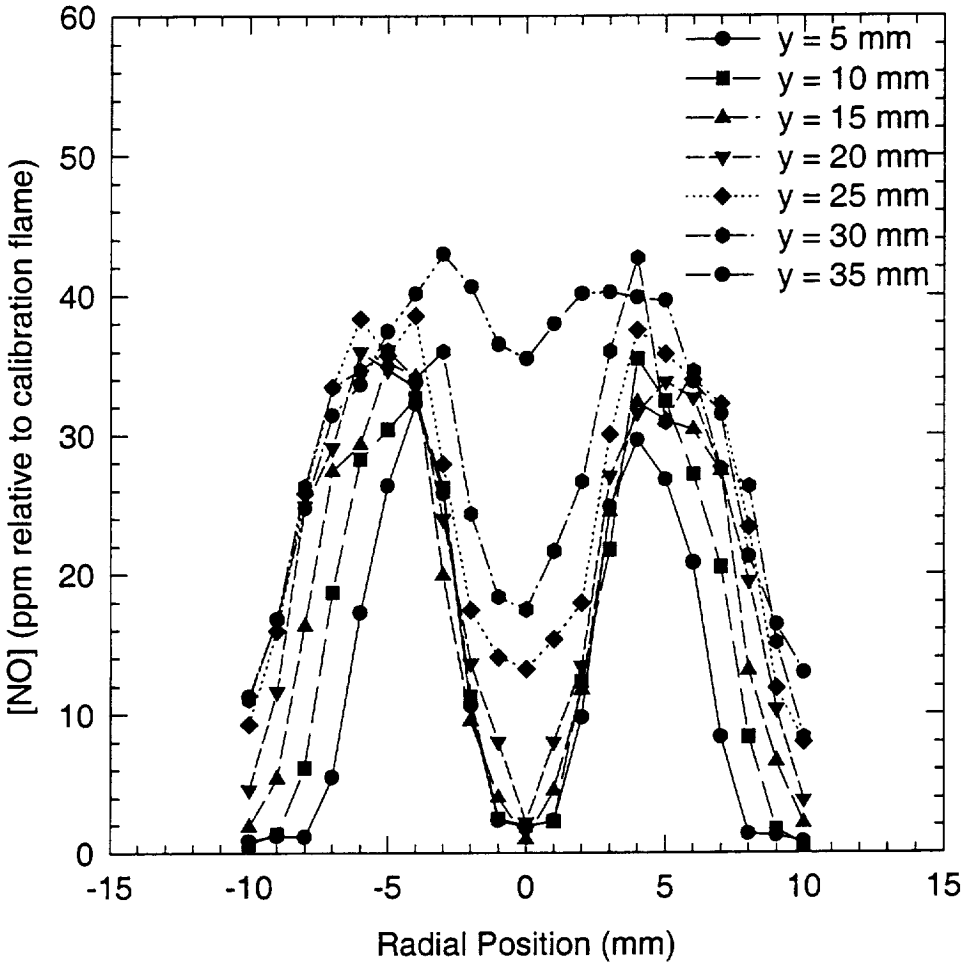

Figure 4.2: LSF point measurements of radial [NO] profiles at various elevations in the ϕ_B=2.22 flame.

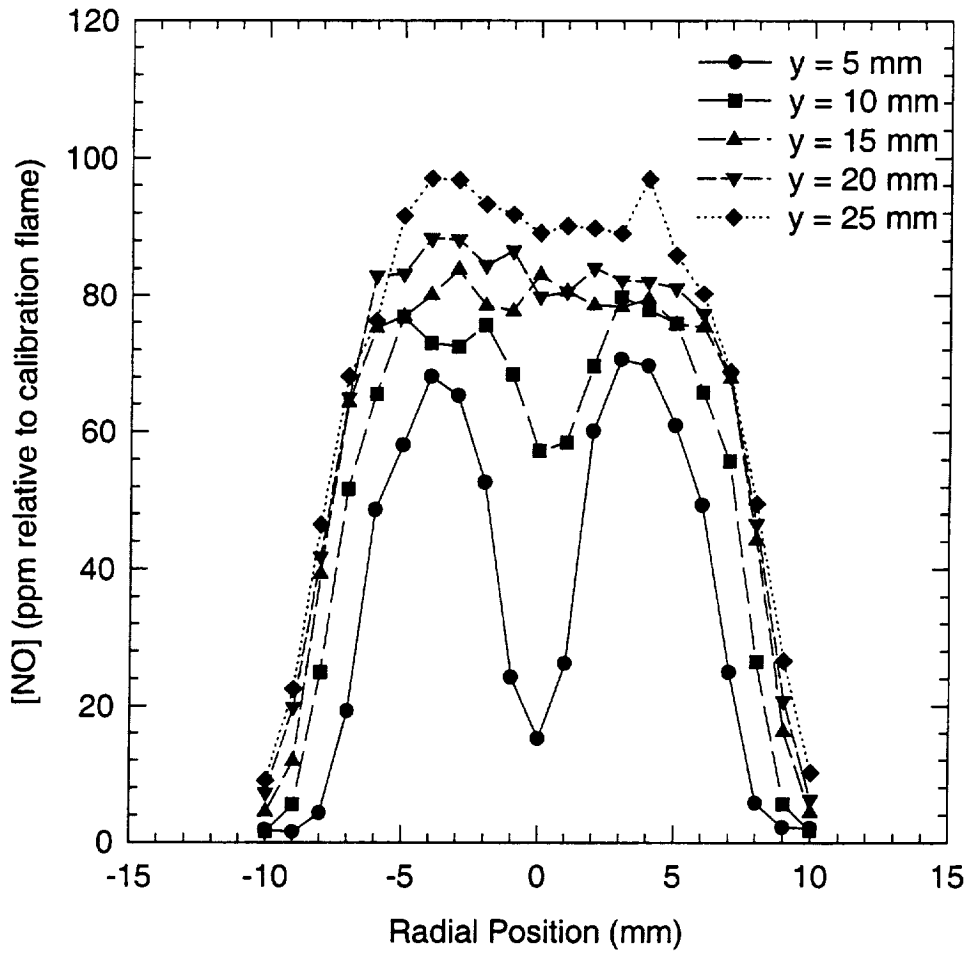

Figure 4.3: LSF point measurements of radial [NO] profiles at various elevations in the ϕ_B=1.33 flame.

rotational energy transfer (RET) on the LSF measurements. The excellent comparison (± 5-22%) between the quenching-corrected linear LIF and the LSF measurements at locally fuel-lean and stoichiometric mixture fractions verifies the validity of the LSF technique for these conditions. However, there is a slight but consistent discrepancy between the linear LIF measurements and the LSF measurements at local equivalence ratios above 1.6. If the quenching corrections for the linear LIF measurements are assumed to be accurate, then this discrepancy in the LSF measurements may be attributed to a change in the collisional branching ratio (ratio of rotational relaxation to electronic quenching rate coefficients) of a factor of three from lean to rich stoichiometries. Although little information is available in the literature on the RET dynamics of NO, this change in the collisional branching ratio might seem improbable. Another possibility is that the electronic quenching cross-sections required for fuel-rich conditions need further refinement.

For our comparison of LSF and PLIF measurements, we focus only on quenching variations as compared to other potential errors. This is because the Boltzmann fraction is relatively insensitive to temperature variations (< 10%) over our temperature range of 1000-2000 K. Moreover, both the LSF and linear LIF measurements would be corrected equally, if any correction at all were warranted. Secondly, as discussed above, quenching-corrected linear LIF measurements agree very well with LSF measurements for a wide range of stoichiometries from fuel-lean ($\phi \cong 0.6$) to moderately fuel-rich ($\phi \approx 1.6$) conditions. In the present work, this discrepancy is obviously not an issue for the ϕ_B=1.33 flame. In addition, for the ϕ_B=2.22 flame, the NO measured in the central fuel-rich region is insignificant. Most of the NO is formed in the interflame region where $\phi < 1.6$. Thus, for the present measurements, corrections for rotational relaxation are negligible. Consequently, for the flame conditions studied in this paper, we are justified in using LSF as a "standard" against which to assess the quantified PLIF measurements.

The baseline LSF measurements for the two partially-premixed flames are shown in Figs. 4.2 and 4.3. In both cases, the NO concentrations increase with increasing height above the burner. As expected, the radial [NO] profiles are generally double-humped at

lower elevations and parabolic at higher elevations in the flame (Kim et al., 1995). The parabolic structure results from radial mixing downstream of the initial annular regions of NO production and also the additional downstream formation of thermal NO along the centerline of the dual-flame region.

PLIF images of the same flames are shown in Figs. 4.4 and 4.5. Each PLIF image is carefully corrected for laser energy variations, laser sheet nonuniformities, and laser-induced background. The NO fluorescence image is not corrected for nonuniformities in the laser sheet distribution on a shot-by-shot basis, but rather via an averaged Rayleigh scattering image. For this reason, shot-to-shot fluctuations in the laser sheet get lost in the on-chip integration, and thus subtle lines appear in the final images. These PLIF images display the same general [NO] distributions as the LSF results, but with ~18 times better spatial resolution.

Experimentally-based correction schemes can be used to enhance the quantitative nature of uncorrected PLIF images (Partridge, 1996). Such correction schemes use selective, directly-measured and highly quantitative secondary measurements as input to the PLIF measurements. Implementation of such an experimentally-based scheme requires only the ability to make a few quantitative measurements, which is a significant reduction in resources needed, as compared to numerically-based correction schemes. Hence, experimentally-based correction schemes should provide a more broadly applicable method for enhancing the quantitative nature of PLIF species concentration measurements.

The number of secondary LSF measurements required for the implementation of an experimentally-based PLIF enhancement procedure is directly related to our existing knowledge concerning the flame environment. In environments with negligible variations in the electronic quenching rate coefficient, a single LSF measurement is sufficient. However, multiple LSF measurements may be required for flames with significant gradients in the quenching rate coefficient, Q_e, as $N_T \propto Q_e$. Significant gradients in Q_e are expected in partially-premixed flames owing to their wide range of temperatures, stoichiometries and major-species concentrations. Nevertheless, in this study, we utilize a

single LSF point measurement to quantify the *entire* image and then assess the resulting semi-quantitative PLIF measurements by comparison with our previous LSF measurements. The purpose of this approach is to demonstrate that sufficiently quantitative PLIF measurements can be obtained with minimal LSF point measurements. The quantitative nature of the PLIF measurements could be further enhanced by utilizing additional LSF point measurements (for example, one or more at each elevation). However, *a priori* information about the flame environment is required in order to select the optimum number and location of LSF measurements.

For the ϕ_B=2.22 flame, the PLIF image is scaled based on the LSF point measurement at an intermediate elevation of 15 mm and a radial location of -6 mm. This point lies in the interflame region of this partially-premixed flame, a region where significant NO is present. Utilization of any other point in the interflame region at any height yields similar results. This observation is indicative of the generality of this quantification technique. Similarly, for the ϕ_B=1.33 flame, the PLIF image is scaled based on the LSF point measurement at an intermediate elevation of 10 mm and a radial location of -4 mm. This again corresponds to a location in the interflame region where the NO concentration is significant.

To quantitatively compare the LSF and PLIF measurements, each PLIF image was sampled at locations corresponding to the spatial locations of the LSF measurements. Moreover, at each sample location in the image, binning was employed to create a sample region 19-pixels long in the radial dimension by 1-pixel tall in the axial dimension. This corresponded to an area in the laser sheet ~1.06-mm long by ~56-μm tall, which compares well with the area (1-mm long by 68-μm tall) sampled by the LSF measurements.

Comparisons of the binned semi-quantitative PLIF measurements with the LSF measurements are shown on an elevation-specific basis for the two partially-premixed flames in Figs. 4.6 and 4.7. Good agreement prevails at all elevations in both flames. In fact, more than 90% of the quantified PLIF measurements are within the uncertainty of

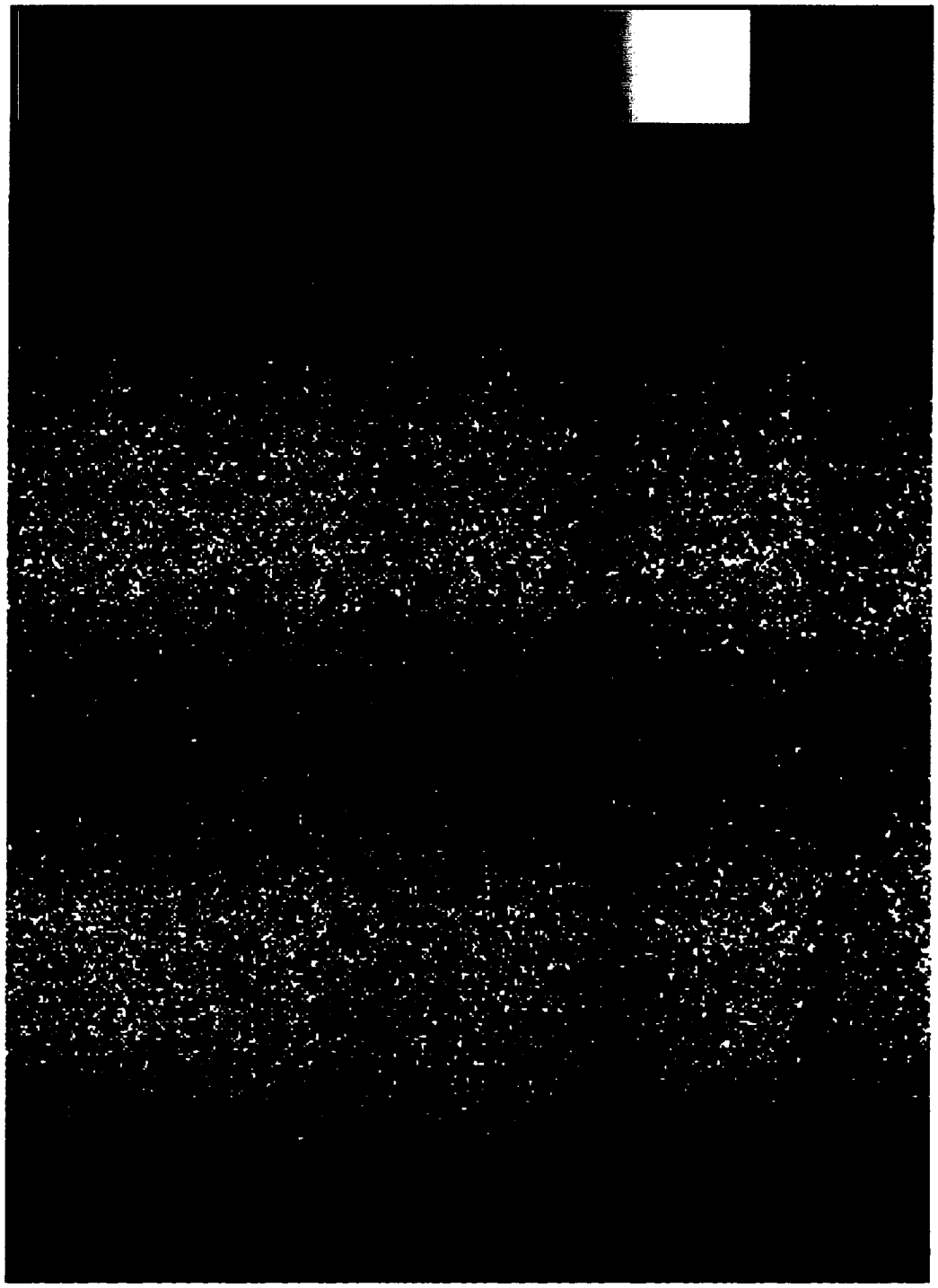

Figure 4.4: Quantified PLIF image of the ϕ_B=2.22 flame. The color bar indicates the [NO] in ppm relative to the calibration flame. The image spans 24-mm in the radial direction and 20-mm in the axial direction.

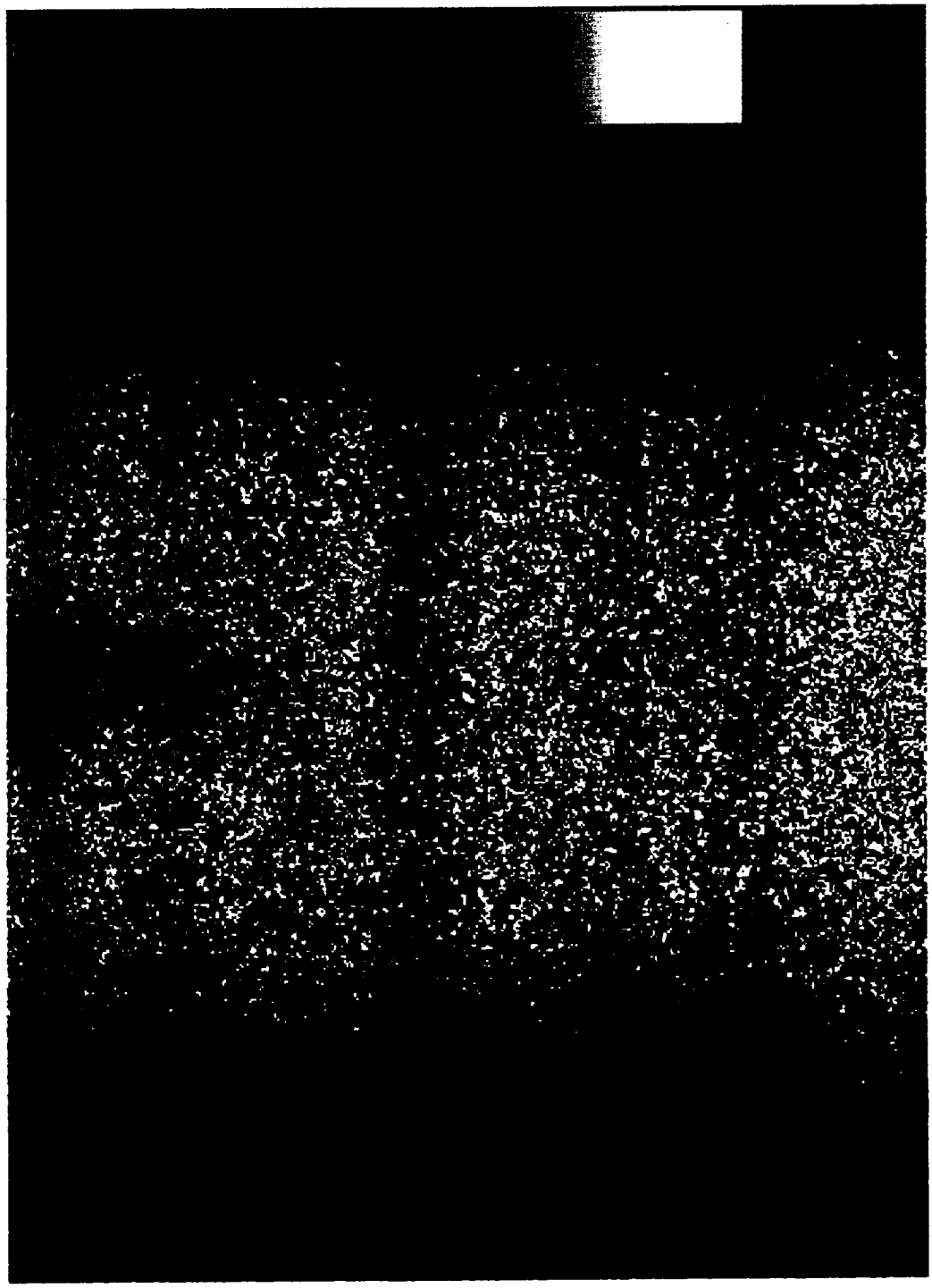

Figure 4.5: Quantified PLIF image of the ϕ_B=1.33 flame. The color bar indicates the [NO] in ppm relative to the calibration flame. The image spans 24-mm in the radial direction and 20-mm in the axial direction.

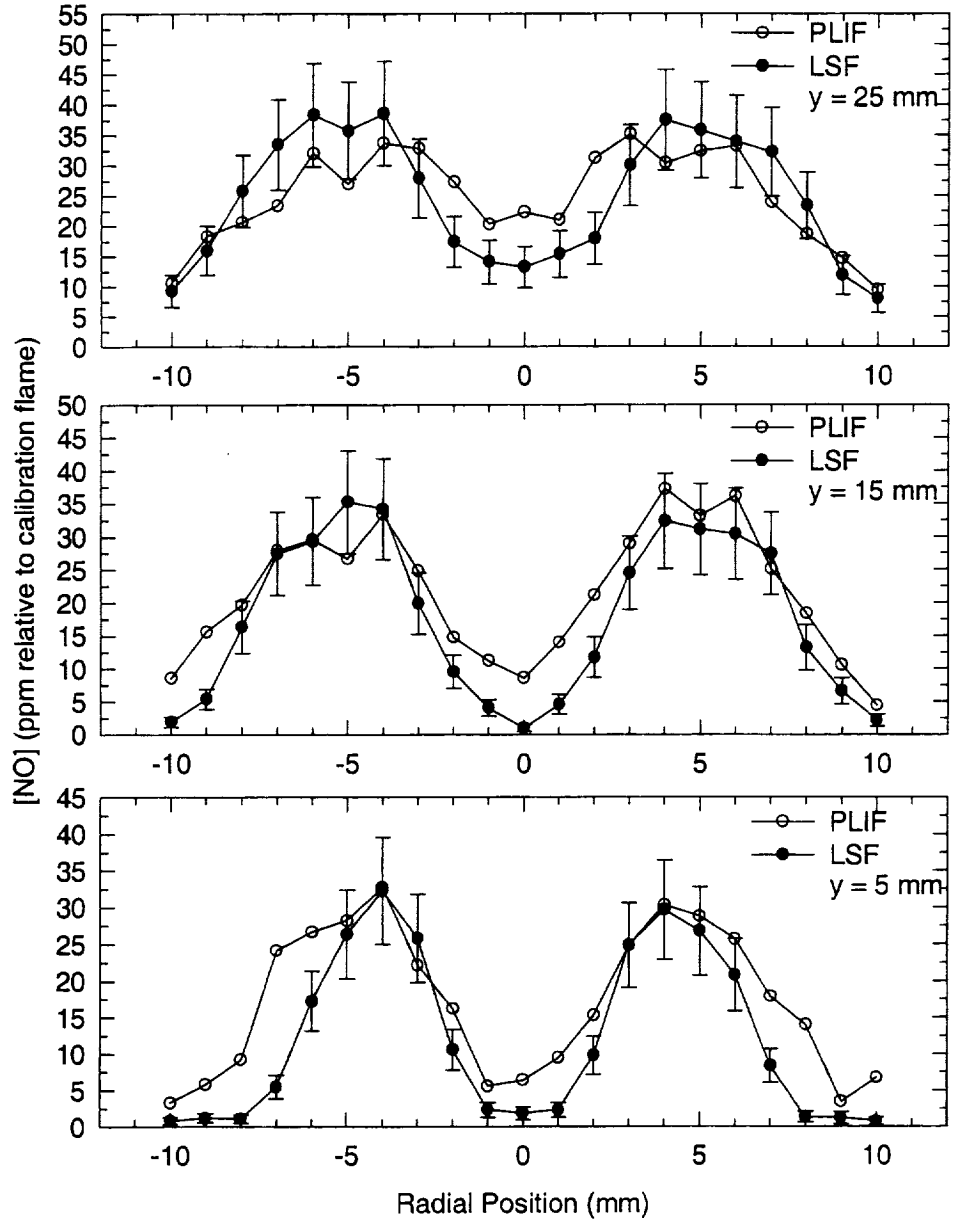

Figure 4.6: Comparison of quantified PLIF and LSF measurements of [NO] at elevations of 5, 15 and 25 mm in the ϕ_B=2.22 flame. Since the temperature of the calibration flame is known, these relative concentrations can also be expressed in terms of an absolute number density. A measured concentration of 10 ppm corresponds to a number density of 4.35×10^{13} cm^{-3}.

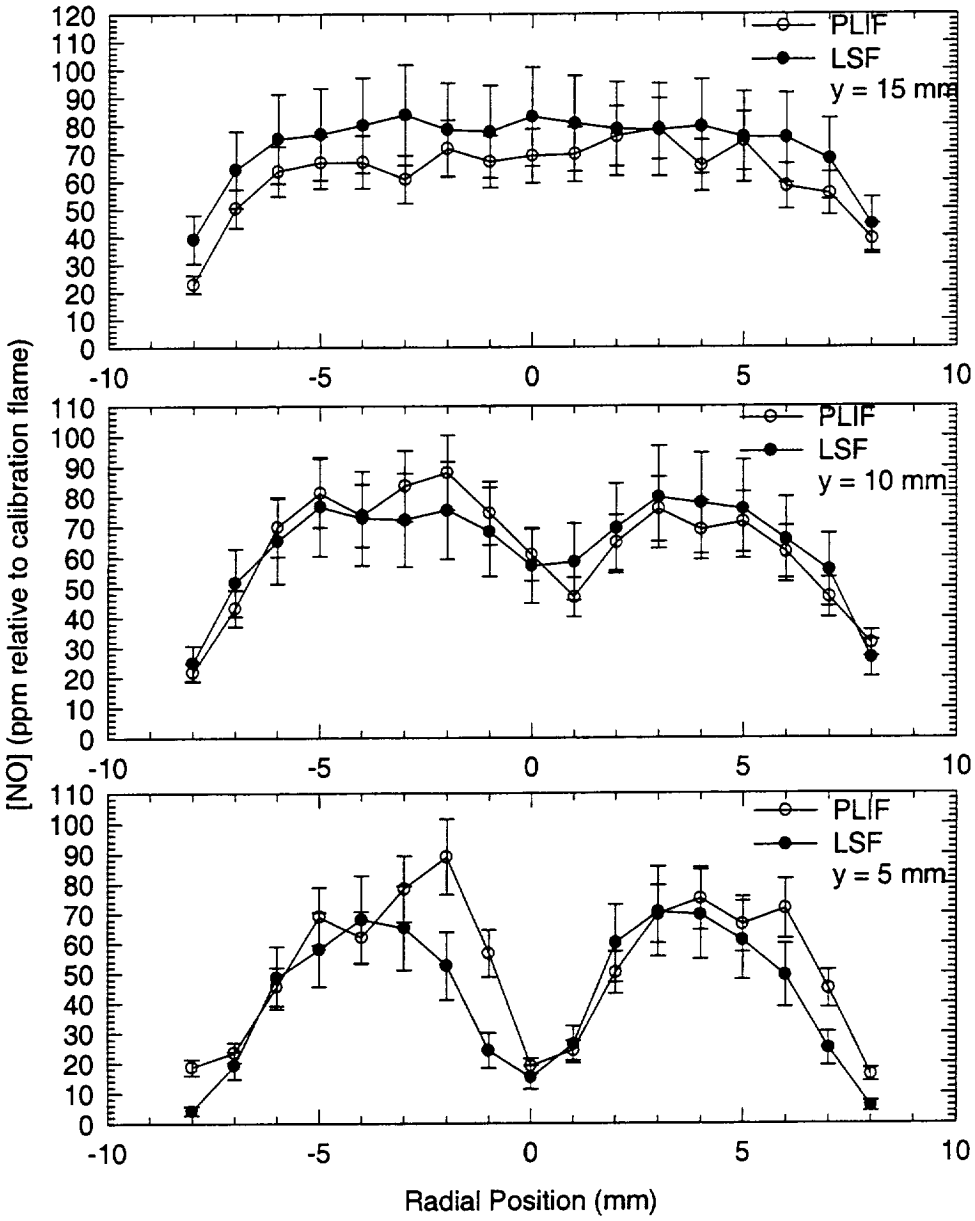

Figure 4.7: Comparison of quantified PLIF and LSF measurements of [NO] at elevations of 5, 10 and 15 mm in the ϕ_B=1.33 flame. Since the temperature of the calibration flame is known, these relative concentrations can also be expressed in terms of an absolute number density. A measured concentration of 20 ppm corresponds to a number density of 8.69×10^{13} cm^{-3}.

the LSF measurements based on a 95% confidence interval. This implies that a majority of the PLIF measurements are within ~22% of the LSF measurements at the peak NO locations. While discrepancies exist at locations in the inner premixed region and at the edge of the outer diffusion flame, the NO concentrations at these locations are small (< 10 ppm). Furthermore, although the discrepancy is slightly greater at the highest elevations, the mean error averaged over all locations with reasonable [NO] (> 10 ppm) is only 23.2% for the ϕ_B=2.22 flame and 21.9% for the ϕ_B=1.33 flame.

Since the PLIF images involved on-chip integration of multiple PLIF events, information concerning shot-to-shot fluctuations is lost. Hence, the uncertainty for PLIF was determined from multiple images of a similar flame from previous work (Partridge, 1996). In particular, because the present PLIF images were obtained using an identical experimental setup and the same image processing routines, we estimate the uncertainty in our PLIF measurements to be approximately 28% (Partridge, 1996). However, the uncertainty bars accompanying the PLIF measurements are not shown for the sake of clarity in Figs. 4.6 and 4.7.

For flame environments with more significant gradients in the electronic quenching rate coefficient, the above procedure could be extended to make PLIF measurements more quantitative. For any flame, elevation-specific corrections could be implemented in regions of high [NO] in the uncorrected PLIF image. A single LSF point measurement could be obtained in a region of significant [NO] at each elevation, and the PLIF measurements in this region could be scaled based on the local LSF measurement. PLIF measurements at intermediate elevations could be scaled by a factor which is obtained by linearly interpolating the scaling factors at the pre-selected elevations.

4.4 Conclusions

PLIF measurements of [NO] have been obtained in atmospheric pressure, laminar, partially-premixed ethane-air flames. Two flames were investigated with fuel-tube equivalence ratios of 1.33 and 2.22, respectively, and an overall equivalence ratio of 0.5.

LSF and PLIF measurements indicate the same general [NO] trends at all elevations in both flames. PLIF images for both flames are made quantitative by scaling each image based on a single LSF point measurement. The quantification procedure is assessed by comparing PLIF measurements with two-dimensional arrays of LSF measurements. The comparisons show good agreement between PLIF and LSF measurements at all elevations in both flames. In fact, over 90% of the PLIF measurements fall within the uncertainty of the LSF measurements.

We believe that the partially-premixed co-flow flames studied here represent a robust scenario with respect to typical variations in the electronic quenching rate coefficient for atmospheric pressure laminar flames, mainly because of the varying stoichiometry and temperatures across these flames. More importantly, we have successfully demonstrated that semi-quantitative PLIF measurements, which are sufficiently accurate from an engineering standpoint, can be obtained via a simple one-point calibration technique, even in such flames.

5. COMPARISON OF LSF AND LINEAR LIF MEASUREMENTS OF NITRIC OXIDE IN COUNTERFLOW DIFFUSION FLAMES

5.1 Introduction

Numerically-based correction schemes for PLIF or linear LIF measurements generally require spatially-resolved measurements of the major-species concentrations in addition to electronic quenching cross-sections for these same major species. Although such measurements are feasible, they require extensive if not unique experimental resources. We can avoid such measurements by considering instead the structure of a counterflow diffusion flame which lends itself very well to modeling owing to its quasi-one-dimensionality. Several studies using detailed chemistry and transport properties have shown that major species concentrations in counterflow diffusion flames are predicted accurately when compared to measurements (Trees et al., 1995; Magre et al., 1995; Sun et al., 1996b). Hence, this flame configuration is an ideal testbed to compare and assess various diagnostic techniques, such as LSF and linear LIF, since quenching corrections can be made by utilizing the predicted major species concentrations.

Linear LIF measurements need to be corrected for variations in both the electronic quenching rate coefficient and the laser irradiance. On the other hand, LSF measurements are relatively independent of both the laser irradiance and the electronic quenching rate coefficient. Consequently, LSF measurements are fairly quantitative, with a detection limit of ~1 ppm (Reisel et al., 1993). However, it becomes impossible to saturate NO at pressures much greater than atmospheric. Therefore, a need exists to quantify the effect of the electronic quenching rate coefficient so as to make LIF measurements feasible at higher pressures.

Motivated by the above factors, we present in this chapter a comparison of broadband LSF measurements of [NO] in atmospheric ethane-air counterflow diffusion flames with linear LIF measurements of [NO] in the same flames. The major species concentrations obtained from a Sandia opposed-flow flame code (Lutz et al., 1996) are used in conjunction with quenching cross-section correlations from the literature (Paul et al., 1995) to estimate the local rate coefficients for electronic quenching in each flame. The efficacy of the quenching correction on the linear LIF measurements and the effect of rotational energy transfer (RET) on the LSF measurements are assessed by comparing the linear LIF and LSF measurements. Four flames with strain rates varying from 5 to 48 s^{-1} were selected. The fuel stream consisted of 14.5% by volume of ethane and 85.5% by volume of nitrogen. These flames were highly diluted to avoid soot and to keep the temperatures low enough so as to avoid consideration of the influence of radiative heat loss on NO formation.

5.2 Experimental Techniques

We begin with a brief description of the experimental facility used in the LSF/LIF measurements. A more detailed description is presented elsewhere (Reisel et al., 1993). Excitation of NO is achieved through use of the $Q_2(26.5)$ line in the $\gamma(0,0)$ band. The $Q_2(26.5)$ line was chosen because (1) the Boltzmann fraction is relatively insensitive to temperature variations over the range of temperatures of our flames, and (2) other species, such as O_2, do not interfere spectrally with this NO absorption line (Partridge et al., 1996). The excitation wavelength is generated by employing the second harmonic (λ= 532 nm) of a Quanta-Ray GCR-4 Nd:YAG laser to pump a PDL-3 dye laser, which provided visible radiation at approximately 574 nm. The dye fundamental was frequency-doubled ($\lambda/2 \approx 287$ nm) in a WEX-2C wavelength extender and the residual Nd:YAG fundamental was frequency-mixed with the dye second harmonic to produce a mixed beam at ~226 nm. The four concentric beams (1064, 574, 287, 226 nm) were dispersed using a Pellin-Broca prism, and the mixed beam exited the WEX vertically polarized.

After the beam left the WEX, it was focused into the probe volume where the beam diameter and Rayleigh range were ~200 μm and ~8 mm, respectively. The beam diameter was measured experimentally by passing a razor blade through the beam in steps of 10 μm while monitoring the beam energy using a photodiode. The beam diameter is then defined as the distance between locations corresponding to the 90% and 10% relative signal levels. A Fabry-Perot wavelength stabilization system was used to control PDL drift (Cooper and Laurendeau, 1997). Splitter plates were used to split off small portions of the beam for power monitoring via photodiodes. In the case of linear LIF measurements, a photomultiplier tube was used to monitor the beam energy because of the requisite low laser powers. The measurement of the beam energy is required for normalization of the fluorescence signal in the case of linear LIF measurements, and to ensure saturation in the case of LSF measurements.

For LSF/LIF detection, a portion of the isotropically emitted fluorescence was captured and the collimated beam was focused onto the entrance slit of a 3/4-m monochromator. The detector is a Hamamatsu R106UH-HA photomultiplier tube which was optimized for temporal resolution of the fluorescence signal (Harris et al., 1976). For all the LSF experiments, the entrance slit was 68-μm wide by 1-mm tall, thus defining a probe volume which is 68-μm wide along the diameter of the beam and 1-mm long along the axis of the beam. For this probe volume, the minimum laser fluence needed for ~90% saturation was 16.4 $mJ/mm^2 \cdot pulse$. A smaller slit width was chosen for the LSF measurements so as to collect fluorescence only from the center of the beam where the laser irradiance is sufficiently high to ensure saturation. A 500-ps temporal window was also sampled at the peak of the fluorescence pulse using a Stanford Research Systems SR255 fast sampler and an SR200 gate scanner. This procedure was employed to again ensure that the data was collected under saturated conditions.

For the linear LIF measurements, the probe volume was again 1-mm long, but widened to 170 μm along the diameter of the beam. This was done to collect additional fluorescence from the wings of the beam. The maximum laser fluence permitted for the linear LIF measurements (~0.1 $mJ/mm^2 \cdot pulse$) was determined by attenuating the beam so

as to obtain a linear variation of the fluorescence signal with laser fluence. A 110-mm × 110-mm, 1200-groove/mm holographic grating with a 250-nm blaze angle was used in first order to provide a dispersion of 1.1 nm/mm at the exit slit. A 1.818-mm wide exit slit was employed so as to spectrally integrate over a 2-nm region of the fluorescence spectrum centered on the $\gamma(0,1)$ band of NO. For the LSF measurements, A temporal gate width of 7 ns was used for the linear LIF measurements. Each data point was averaged over 400 laser shots.

The burner system consisted of two opposed cylindrical ducts, each 2.54 cm in diameter (Yang and Puri, 1993), as shown in Fig. 5.1. Fuel was injected through the bottom duct and oxidizer through the top, resulting in a flame stabilized on the oxidizer side of the stagnation plane. To shield the flame from ambient disturbances, an annular flow of nitrogen was passed through a duct surrounding the fuel inlet stream. A water-cooled co-annular heat exchanger was used to cool the upper portion of the burner assembly. A water bath in conjunction with a temperature controller was employed to maintain the temperature of the circulating water high enough to avoid condensation on the burner.

Four flames were studied with strain rates varying from 5 to 48 s^{-1}. For the fuel dilution that we have chosen, these strain rates represent the entire range up to extinction. We have defined the strain rate as the sum of the fuel and oxidizer nozzle exit velocities divided by the nozzle separation distance (Magre et al., 1995). The distance between the two burners is maintained at 2 cm for all the flames. From Lin and Faeth (1996), the value of the stoichiometric mixture fraction (Z_{st}) below which soot would form in ethane-air flames is 0.13. The flames studied in this work are free of soot since dilution causes the value of Z_{st} for all the flames to be 0.29.

5.3 Results and Discussion

The calibration factor for the LSF measurements was determined using a standard NO doping technique in a ϕ=0.8 premixed $C_2H_6/O_2/N_2$ flame with a dilution ratio of 3.76

(Reisel et al., 1993). The calibration was conducted at a height of 4 mm above the burner surface. The NO concentration in ppm relative to the calibration flame temperature can then be determined from

$$N_{ppm,RT} = C_F S_F \quad , \tag{5.1}$$

where C_F is a calibration factor determined from the slope of the fit to the calibration data and S_F is the digital fluorescence signal. The [NO] in absolute ppm can be expressed as

$$N_{ppm,abs} = \left(\frac{T}{T_c}\right)\left(\frac{f_B(T_c)}{f_B(T)}\right) N_{ppm,RT} \ , \tag{5.2}$$

where T is the flame temperature, T_c is the temperature of the calibration flame, and f_B is the Boltzmann fraction. The Boltzmann fraction is relatively insensitive to temperature variations (<10%) over a temperature range of 1000 - 2000 K. Since most of the NO is formed in high temperature regions, corrections for variations in the Boltzmann fraction are unnecessary. There are a few points in the wings of the [NO] profile where the temperatures are below 1000 K; however, the NO concentrations at these locations are small and thus Boltzmann corrections are superfluous.

Numerical computations for all the flames were conducted using OPPDIF, a Sandia opposed-flow flame code (Lutz et al., 1996). The mathematical model reduces the two-dimensional, axisymmetric flow field to a one-dimensional formulation by using a similarity transformation. The model predicts the species, temperature, and velocity profiles along the centerline in the core flow between the two burners. A detailed derivation of the governing equations is given by Kee et al. (1988). The GRI mechanism, version 2.11 (Bowman et al., 1995), containing 49 species and 279 reactions is used to handle the chemical kinetics.

Temperatures were measured with a 76-μm, Pt/Pt-10%Rh uncoated thermocouple along the centerline of the region between the burners. Figure 5.2 shows a typical comparison between measured temperatures, uncorrected for radiative heat loss, and predicted temperatures. The measured temperature profile appears to be slightly thicker than the predicted profile. This can be attributed to the disturbance caused by the

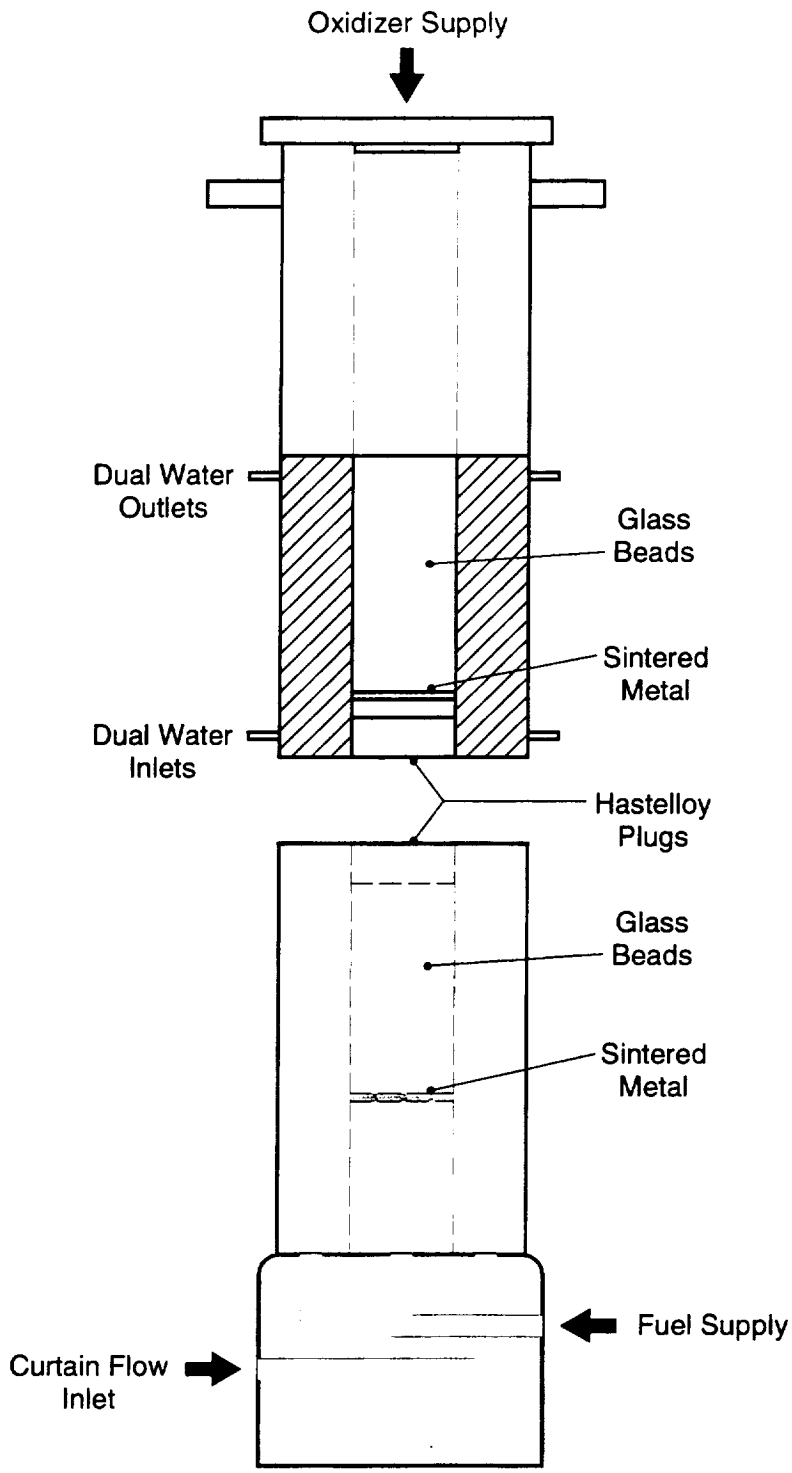

Figure 5.1: Schematic of the counterflow burner used for obtaining atmospheric pressure LSF/LIF measurements of NO.

presence of the thermocouple in the flowfield. Previous studies on the structure of counterflow diffusion flames have shown that the computed temperature profile agrees very well with the experimental temperature profile when measured using nonintrusive optical techniques such as CARS and spontaneous Raman scattering (Magre et al., 1995; Sung et al., 1995; Sun et al., 1996a). Recent temperature measurements in methane-air counterflow diffusion flames using thin filament pyrometry have also shown excellent agreement with OPPDIF model predictions (Ravikrishna and Laurendeau, 1999a). Consequently, the predicted temperature profile was used in Eq. (5.2) to evaluate [NO]. Computed peak flame temperatures varied from 1686 K at a strain rate of 5.12 s^{-1} to 1579 K at a strain rate of 48.34 s^{-1}. These low flame temperatures are consistent with NO production primarily by the prompt mechanism for our experimental conditions.

Figures 5.3-5.6 present LSF measurements of [NO] in the ethane-air counterflow diffusion flames with strain rates of 5.12, 20.53, 35.03, and 48.34 s^{-1}, respectively. The uncertainty associated with the accuracy of the LSF measurements at peak [NO] locations based on a 95% confidence interval is ~21%, with an increase to ~30% at the edges of the [NO] profile (see Appendix B). As expected, the peak NO concentrations decrease with an increase in flame stretch. This is mainly due to the decline in the residence time in high temperature zones (Drake and Blint, 1989; Nishioka et al., 1994). Since the peak temperature decreases with an increase in flame stretch, there is also a decrease in the net NO production rate. The width of the NO profile becomes narrower with an increase in stretch owing to the increased velocity gradients.

Linear LIF measurements of [NO] were also obtained in the four flames. All measurements were made in the regime for which the LIF signal response is linear with laser irradiance. This avoided problems that can be encountered with partial saturation. The absence of saturation was checked by measuring the fluorescence signal as a function of laser irradiance. The laser irradiance was varied using a Rochon prism which divides the incident beam into an ordinary beam which traverses the prism undeviated and an extraordinary beam which is deviated from the ordinary beam. Over the range of laser irradiances used, the response was clearly linear. It is very important to accurately know

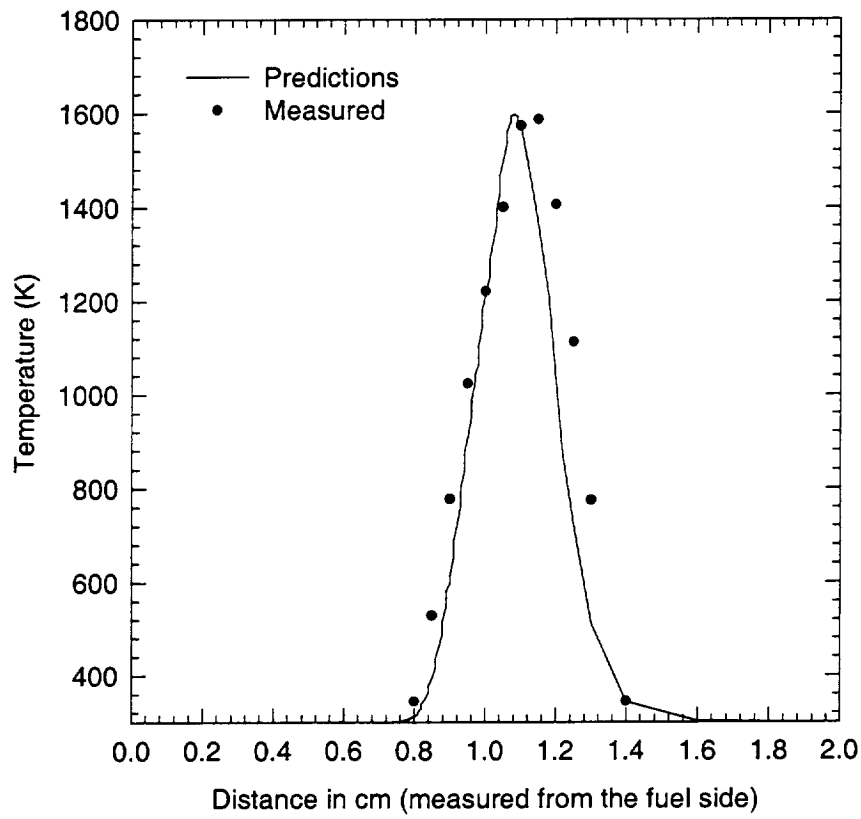

Figure 5.2: Comparison of predicted and measured temperatures in the flame with a strain rate of 35.03 s^{-1}. The measured temperatures are not corrected for radiative heat loss.

the laser irradiance used to normalize the fluorescence signal. Since the laser energy was very low, a photomultiplier tube was used to monitor the laser energy.

The calibration was performed in the same manner as for the LSF measurements. The linear LIF measurements were corrected for variations in the quenching rate coefficient so as to determine [NO] in absolute ppm by

$$N_{ppm,abs} = \left(\frac{T}{T_c}\right)\left(\frac{f_B(T_c)}{f_B(T)}\right)\left(\frac{Q_e}{Q_{e,c}}\right)N_{ppm,RT} \ , \tag{5.3}$$

where Q_e is the local electronic quenching rate coefficient and $Q_{e,c}$ is the electronic quenching rate coefficient in the calibration flame. Equation (5.3) can be simplified from Eq. (2.23) since the overlap fraction is nearly constant among flames at constant pressure. The electronic quenching rate coefficient is calculated using the major species concentrations from the OPPDIF code (Lutz et al., 1996) and the quenching cross-sections from Paul et al. (1995). Although the GRI mechanism is more suitable for modeling methane-air flames, major-species concentrations for ethane-air flames are still predicted quite well (Reisel et al., 1997) and such species account for over 93% of the total electronic quenching rate for our conditions.

Figures 5.3-5.6 also present comparisons of corrected LIF measurements with LSF measurements in the four counterflow flames. In addition, Fig. 5.3 shows a comparison between the uncorrected LIF and the LSF measurements. The agreement between the LSF and the corrected LIF measurements is excellent in the peak [NO] region and on the fuel lean side of the flame. At these locations, the corrected LIF measurements fall within the uncertainty of the LSF measurements in all four flames. A complete uncertainty analysis for these measurements is presented in Appendix B. The agreement is also reasonable on the fuel-rich side. The quenching correction for the LIF measurements is almost negligible on the fuel-lean side, increasing to about 20% at stoichiometric conditions and increasing further to 50% on the fuel-rich side. The uncertainty bars for the LIF measurements are not shown in Figs. 5.3-5.6 for the sake of clarity. However, for an uncertainty in the LIF measurements that varies from ~22% at peak [NO] locations to ~35% at the edges of the [NO] profiles (95% confidence interval), we note that the

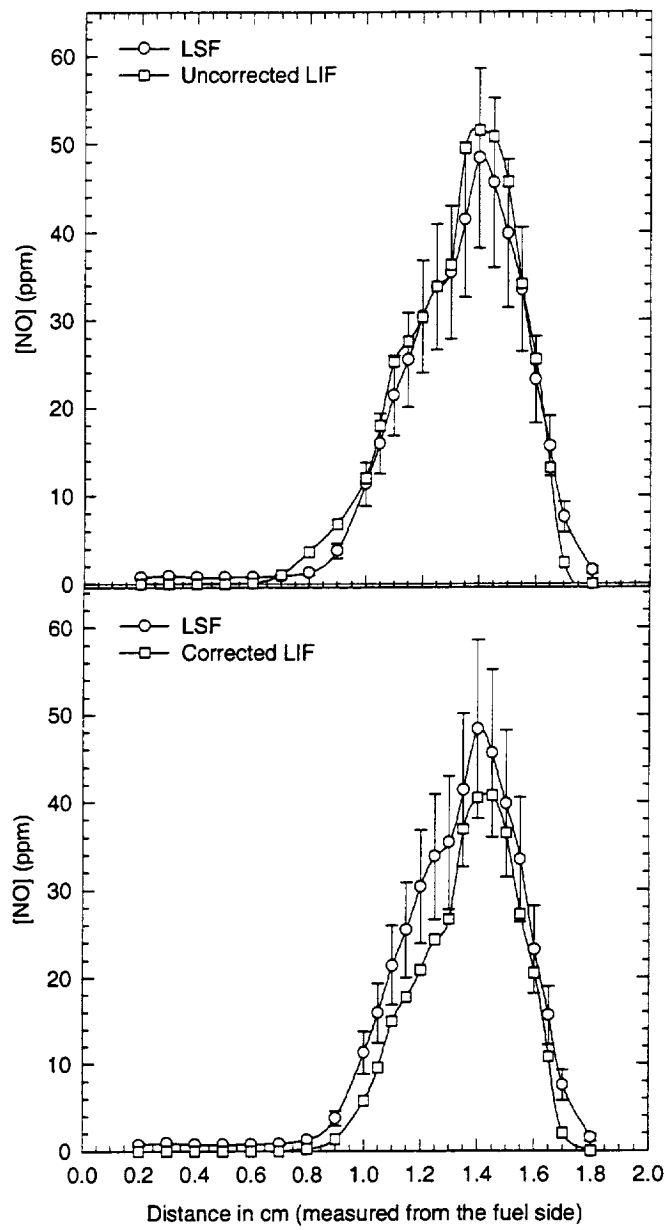

Figure 5.3: Comparison of both uncorrected and corrected LIF measurements with LSF measurements in the flame with a strain rate of 5.12 s^{-1}. The uncertainty bars for the LIF measurements are not shown for the sake of clarity.

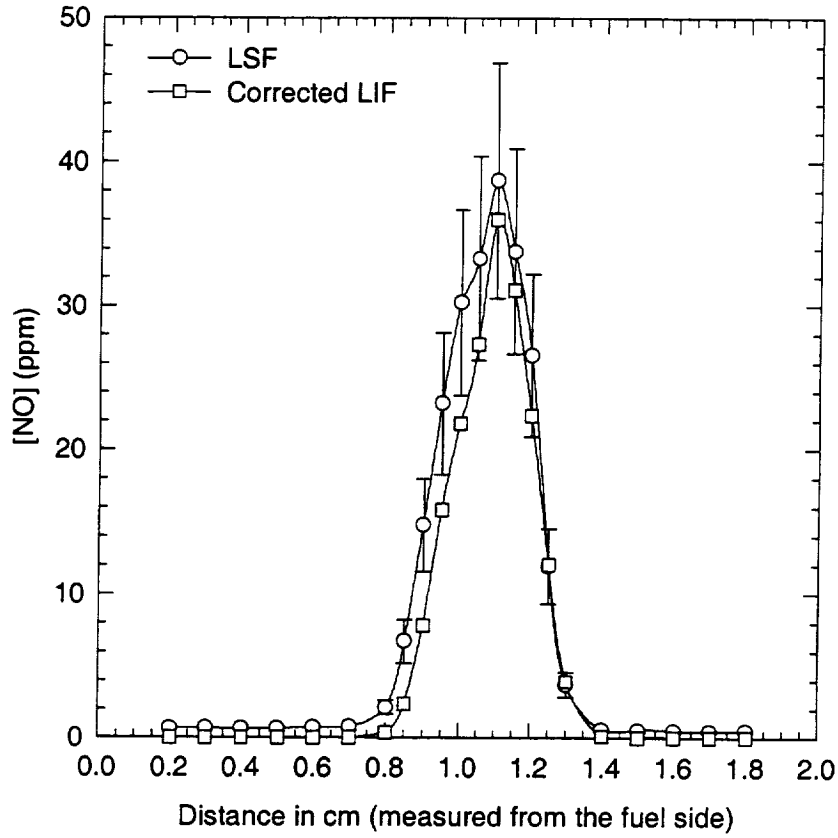

Figure 5.4: Comparison of corrected LIF and LSF measurements in the flame with a strain rate of 20.53 s^{-1}. The uncertainty bars for the LIF measurements are not shown for the sake of clarity.

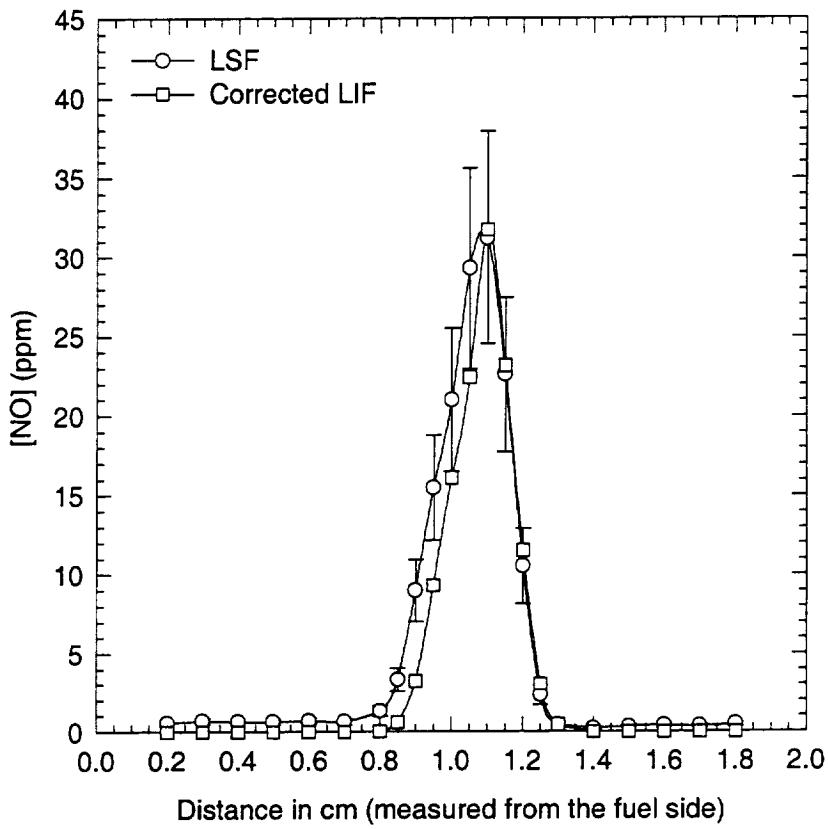

Figure 5.5: Comparison of corrected LIF and LSF measurements in the flame with a strain rate of 35.03 s^{-1}. The uncertainty bars for the LIF measurements are not shown for the sake of clarity.

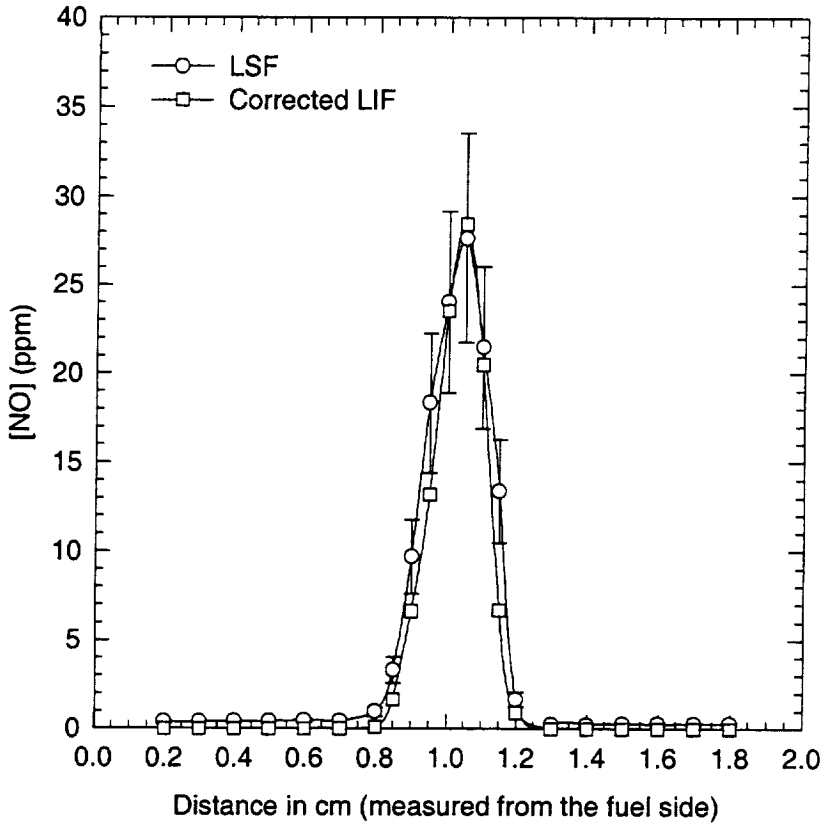

Figure 5.6: Comparison of corrected LIF and LSF measurements in the flame with a strain rate of 48.34 s^{-1}. The uncertainty bars for the LIF measurements are not shown for the sake of clarity.

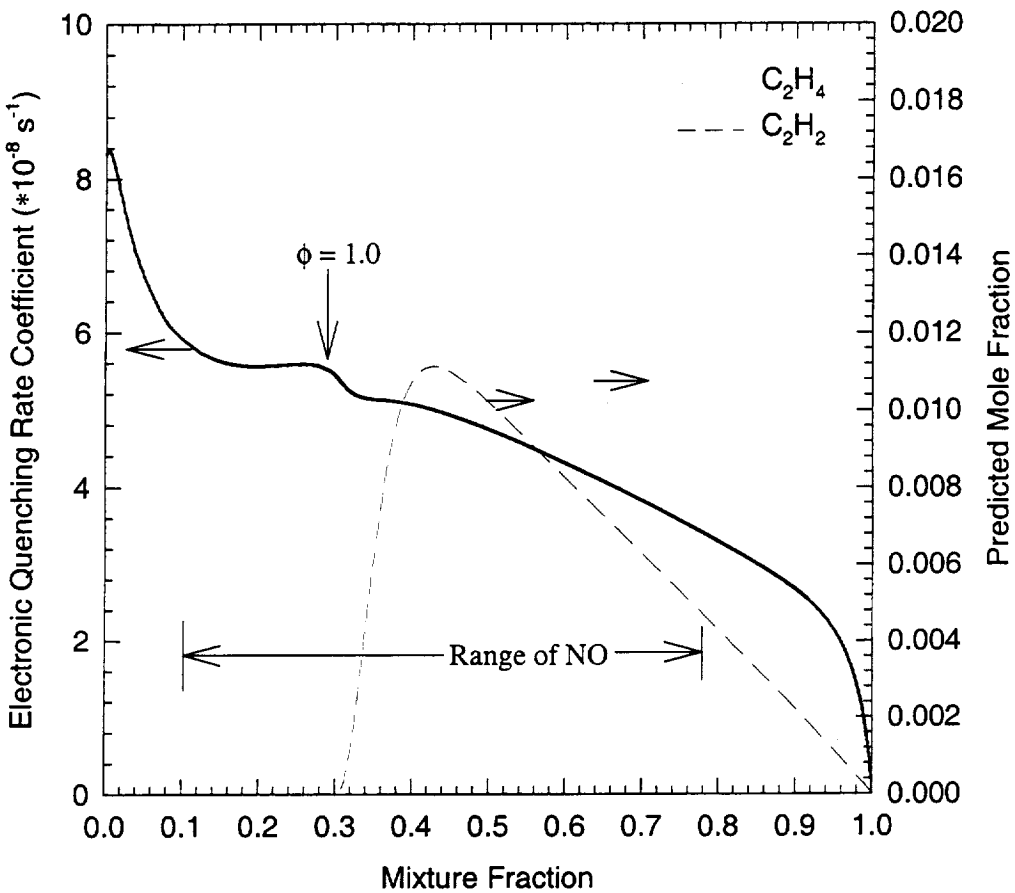

Figure 5.7: Variation of the local electronic quenching rate coefficient and computed mole fractions of hydrocarbon species as a function of mixture fraction in the flame with a strain rate of 5.12 s^{-1}. The variation is typical of all four flames considered in our study.

uncertainty bars for the LIF and LSF measurements overlap at most of the locations on the fuel-rich side in all flames. However, the slight differences between the corrected LIF and LSF measurements on the fuel-rich side are consistent and require further explanation.

The typical variation of the local electronic quenching rate coefficient (Q_e) with mixture fraction in a counterflow diffusion flame is shown in Fig. 5.7. The electronic quenching rate coefficient changes little in the fuel-lean and stoichiometric regions. However, it decreases rapidly in the fuel-rich region. Since [NO] is directly proportional to the local electronic quenching rate coefficient in accordance with Eq. (5.3), the rapid decrease in Q_e translates into slightly lower LIF measurements as compared to LSF measurements in most of the fuel-rich region. This is clearly observable in Fig. 5.3, which displays both uncorrected and corrected LIF measurements. Nevertheless, the results are generally quite satisfactory and, in fact, establish a robust protocol for making essentially quantitative measurements of [NO] in counterflow flames at higher pressures. Since it is nearly impossible to saturate NO at pressures greater than 3 atm (Reisel and Laurendeau, 1994), linear LIF measurements must be employed in such flames, which can then be corrected for variations in the electronic quenching rate coefficient via the procedures described in this chapter. The inability to saturate at high pressures is due to increased line broadening. This broadening causes wings of neighboring lines to be excited along with the primary line, thus making it difficult to maintain saturation as the wings of these lines begin to predominate.

The slight discrepancy between the LSF and linear LIF measurements cannot be solely associated with quenching variations arising out of minor species. At a typical location on the fuel-lean side, major species such as CO_2, H_2O, O_2, N_2, and CO account for nearly 99% of the quenching and minor species such as OH, O, and H account for about 1%, most of which is from OH. On the fuel-rich side, at a typical location, major species such as CO_2, H_2O, N_2, O_2, and CO account for 93% of the quenching, while the contribution from minor species such as C_2H_2 and C_2H_4 is around 7%. Further understanding of the small discrepancy in the fuel-rich region can be gained by considering computed hydrocarbon concentration profiles potentially associated with reduced

electronic quenching of NO (Fig. 5.7). In particular, the decrease in the electronic quenching rate coefficient occurs primarily in a region where intermediate hydrocarbons such as C_2H_4 and C_2H_2 display their peak concentrations. Thus, any uncertainty in their concentrations or quenching cross-sections could account for some of the observed discrepancy. For example, the maximum uncertainty in the quenching cross-sections for C_2H_4 and C_2H_2 (Paul et al., 1995) can account for ~10% of the observed discrepancy in the fuel-rich region. An additional complication is the presence of other hydrocarbon species in the fuel-rich region, which are not accounted for in the quenching correlations of Paul et al. (1995).

The effects of electronic quenching and rotational energy transfer (RET) on quantitative [NO] measurements when utilizing LSF can also be addressed by considering a generic four-level model (Cooper, 1997; Lucht et al., 1980). By calibrating in a reference flame and changing flame environments, we change both the rotational relaxation and electronic quenching rate coefficients. The amount by which these changes affect the upper state population and hence the fluorescence yield depends on the molecular dynamics governing the excitation and detection processes. One concern arises from the large irradiances used in typical LSF measurements. During stimulated absorption from the lower laser-coupled level to an excited upper level, it is possible that the depopulated lower level is repopulated via RET from neighboring ground rovibronic levels; thus, more molecules could actually be excited than predicted by a simple two-level model. It is, however, the balance of repopulation into the directly-excited ground rovibronic level and depopulation out of the directly-excited upper rovibronic level that constitutes the validity of the LSF technique, as interpreted by the balanced cross-rate model (Lucht et al., 1980).

To understand the limitations of the LSF technique, it is instructive to consider an expression for the total upper level population in a four-level model, which includes the laser-coupled excited level and the collisionally-coupled upper rovibronic levels (Reisel et al., 1993):

$$N_T^{ss} = N_1^{\circ}(1-\gamma)\left(\frac{g_u}{g_u+g_l}\right)\alpha_{sat}\left\{1+\frac{1}{Q_e/R_{u,c}+R_{c,u}/R_{u,c}}\right\}, \tag{5.4}$$

where N_T^{ss} represents the steady state value of the population in the upper manifold, $(1-\gamma)$ is the fraction of the original population remaining in the laser-coupled levels, g_u and g_l are the representative degeneracies of the upper and lower laser-coupled levels, and α_{sat} is the degree of saturation. The effect of RET is represented in Eq. (5.4) through the inverse collisional branching ratio, $Q_e/R_{u,c}$, and the ratio of RET rate coefficients into and out of the laser-coupled excited level, $R_{c,u}/R_{u,c}$, where here the subscript u represents the laser-coupled excited level and the subscript c represents the manifold of collisionally-coupled upper rovibronic levels (Carter and Laurendeau, 1994).

From a dynamic analysis of the NO molecule which includes collisional population transfer among rotational levels, the ratio $R_{c,u}/R_{u,c}$ has been estimated to be ~0.093 (Cooper, 1997). Using Eq. (5.4) to deduce the sensitivity of the broad-band LSF signal to the inverse collisional branching ratio, we find that

$$S_{\frac{Q_e}{R_{u,c}}} = \frac{-\frac{Q_e}{R_{u,c}}}{\left(\frac{Q_e}{R_{u,c}}+\frac{R_{c,u}}{R_{u,c}}\right)\left(\frac{Q_e}{R_{u,c}}+\frac{R_{c,u}}{R_{u,c}}+1\right)}. \tag{5.5}$$

For typical conditions in lean flames, the sensitivity of the broad-band LSF signal to the inverse collisional quenching ratio is found to be approximately 50%, as compared to 100% for linear LIF measurements. This is still a significant dependence which could limit the utility of broad-band LSF measurements.

In an effort to determine the origin of inherent discrepancy between the LSF and LIF measurements on the rich side of the flames presented in this paper, we have considered the implications of RET dynamics. We assume for this analysis that the broad-band LIF measurements most accurately reflect the actual NO concentrations owing to the correction procedure based on the estimated electronic quenching rate coefficients (Paul et al., 1995) and to the unimportance of rotational relaxation effects (Cooper, 1997). We

then fit the broad-band LSF data, which are sensitive to Q_e and $R_{u,c}$ through the collisional branching ratio, to the LIF data via a generic four-level model as represented in Eq. (5.4) and determine the branching ratio required to produce similar LSF and LIF NO profiles. Our analysis focuses on the flame with a strain rate of 5.12 s^{-1}, which permits the greatest resolution between mixture fractions.

To begin the analysis, we implicitly assume that the lean LIF and LSF measurements are in agreement based on the profile correlations presented for each of the flames. Moreover, we assume complete saturation and negligible population loss in the laser-coupled levels. Given the electronic quenching rate coefficients calculated from the correlations of Paul et al. (1995), we progress from lean to rich mixture fractions and calculate the necessary $R_{u,c}$ for similar LSF and LIF profiles. The results for a lean branching ratio of 6.0 are demonstrated in Fig. 5.8, where each variable displayed has been normalized to its lean value. The general trends represented by this figure are fairly insensitive to the somewhat arbitrarily chosen lean collisional branching ratio. For example, if a lean collisional branching ratio of 3.0 is chosen, the value of the normalized branching ratio at Z=0.78 is 2.5, whereas for a lean collisional branching ratio of 9.0, its maximum is 5.2.

To assess the utility of Fig. 5.8, we must decide whether or not the collisional branching ratio can change by the predicted amount, namely a factor of approximately three from lean to rich stoichiometries. Owing to the dearth of information available in the literature concerning the RET dynamics of nitric oxide in flames, we must rely on previous measurements of similar molecules and reported trends. Carter and Laurendeau (1994) compared narrow- and broad-band LSF measurements of hydroxyl concentration and found excellent comparisons with a maximum deviation of ~10% between the measurements for a wide range of flame conditions (ϕ=0.6 to 1.6). As noted by Mallard et al. (1982), the smaller rotational spacing of NO (1.7 cm^{-1}) relative to OH (17 cm^{-1}) indicates a larger cross-section for rotational energy transfer. However, the larger dipole moment of OH (1.66 D) relative to NO (0.15 D) would suggest the opposite.

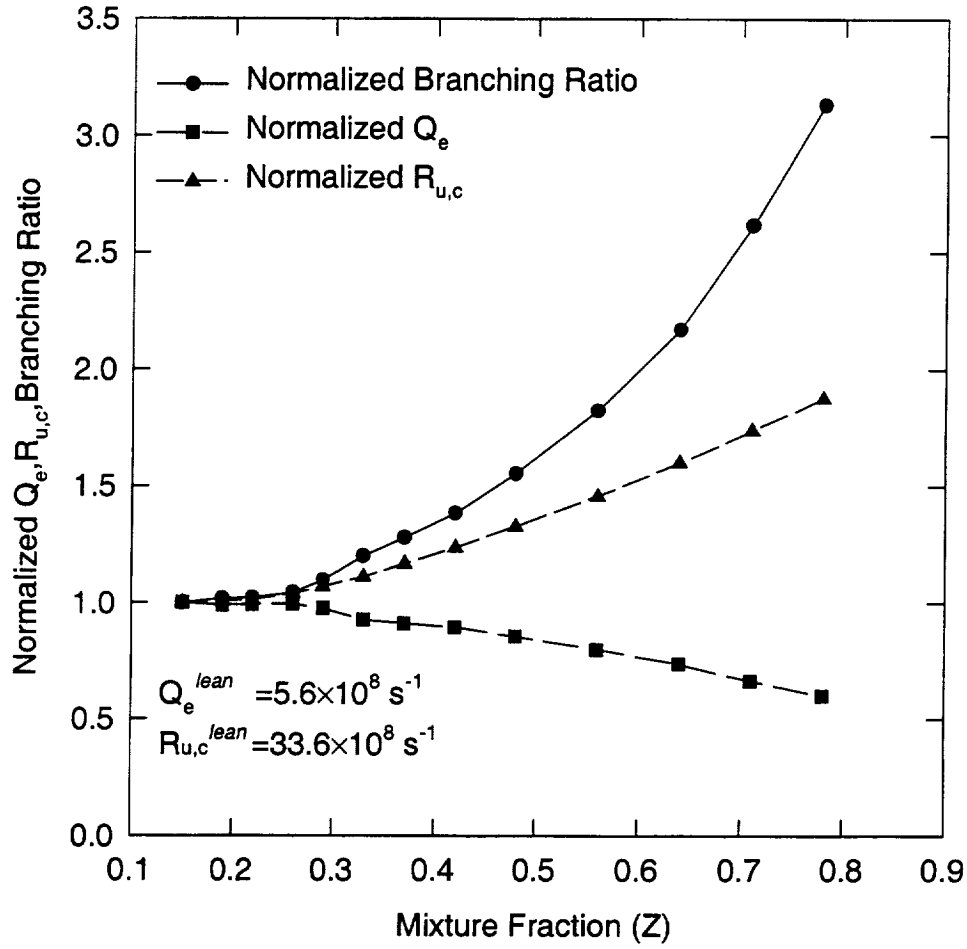

Figure 5.8: Predictions of $R_{u,c}$ and collisional branching ratio necessary to correct the LSF measurements to the LIF measurements in the 5.12 s^{-1} flame. The data presented here assume that the LIF measurements are quantitative and depict the collisional branching ratio required to correct the rich-side discrepancy in the NO measurements. The lean electronic quenching rate coefficient, Q_e^{lean}, and the assumed rotational relaxation rate coefficient, $R_{u,c}^{lean}$, are listed in the figure.

Nevertheless, the results reported by Carter and Laurendeau (1994) certainly indicate the utility of broad-band LSF over a wide range of flame conditions.

More pertinent to this work, Reisel et al. (1993) compared broad-band LSF measurements with broad-band linear LIF measurements of nitric oxide concentration in a variety of $C_2H_6/O_2/N_2$ flames at atmospheric pressure (ϕ=0.6 to 1.6) and determined that the collisional branching ratio is fairly insensitive to equivalence ratio. These measurements are termed broad-band since they involve detection of an entire vibrational band. Broad-band LIF measurements can be shown to be essentially independent of RET effects (Cooper, 1997); thus, quenching-corrected LIF measurements can be taken as quantitative. An equivalence ratio of 1.6 corresponds to a mixture fraction of 0.4 in the flames reported here. For the region shown in Fig. 5.8 between Z=0.15 and Z=0.4, the required branching ratio changes by ~40%. Given the sensitivity of LSF measurements to the collisional branching ratio, a change of ~40% would produce an error of ~20% in the measured concentration. Reisel et al. (1993) measured discrepancies of approximately 16% between LSF and LIF measurements at an equivalence ratio of unity after calibration at ϕ=0.8 and reported accuracy bars of ±20%. Hence, the work performed by these researchers suggests that a change in the electronic quenching rate coefficient parallels a similar change in the rotational relaxation rate coefficient (within the errors of the measurement technique), thus validating the utility of the LSF method for flame stoichiometries leaner than ϕ=1.6.

In summary, the purpose of this generalized RET analysis has been to illuminate the possibility that RET dynamics can complicate LSF measurements, particularly in rich regions of the flame. By comparing the LSF and LIF data and determining the collisional branching ratio required to produce similar profiles, we are acknowledging that broad-band LSF measurements can be in error owing to changes in the RET rates with respect to the lean calibration condition. The difference between the LSF and LIF measurements is then a measure of the change in the RET rate coefficient and thus the collisional branching ratio since the electronic quenching rate coefficient can be calculated. The work performed by Reisel et al. (1993) validates this generalized analysis in flames leaner than

ϕ=1.6 and demonstrates that RET effects can generally be ignored for these flames. Our conclusion is that a combination of RET effects and the lack of accurate quenching cross-sections is probably responsible for the slight discrepancy between the LIF and LSF data in rich regions of our flames.

5.4 Conclusions

Quantitative LSF measurements have been obtained along the centerline of four atmospheric pressure ethane-air counterflow flames with strain rates of 5.12, 20.53, 35.03, and 48.34 s^{-1}. As expected, the peak NO concentration decreases and the width of the NO profile becomes narrower with an increase in flame stretch. Linear LIF measurements of [NO] were also obtained in the same flames. The agreement between the corrected LIF and LSF measurements is excellent in the peak [NO] region and on the fuel-lean side of the flame. At these locations, the corrected LIF measurements fall within the uncertainty of the LSF measurements in all four flames. The agreement is also reasonable on the fuel-rich side. In fact, for a mean uncertainty in the LSF and LIF measurements of 26-28%, the uncertainty bars of the two measurements overlap at most of the locations on the fuel-rich side in all flames. However, the rapid decrease in the quenching rate coefficient for highly fuel-rich conditions (ϕ>1.6) causes the LIF measurements to be consistently lower than the LSF measurements in this region. If the quenching corrections for the linear LIF measurements are assumed to be accurate, then this discrepancy in the LSF measurements may be attributed to a change in the collisional branching ratio (ratio of rotational relaxation to electronic quenching rate coefficients) of a factor of three from lean to rich stoichiometries. Although little information is available in the literature on the RET dynamics of NO, this change in the collisional branching ratio might seem improbable. Another possibility is that the electronic quenching cross-sections of hydrocarbon species required for fuel-rich conditions need further consideration and/or refinement. We believe that the truth lies in a combination of the above two factors.

The applicability of the quenching correction procedure is limited to cases for which the flame structure may be quantitatively reproduced by flame modeling. Although this method requires faith in kinetic predictions, it must be pointed out that recent modeling efforts have reached a degree of sophistication where the agreement between predictions and measurements of major species concentrations and temperature is excellent. Hence, any errors arising out of uncertainties in temperature and major species concentrations is probably negligible, especially for fuel-lean to slightly fuel-rich conditions. The influence of uncertainties in the quenching cross-sections of the major species was also found to be negligible. Thus, corrected LIF measurements can be considered sufficiently quantitative even though there is some small dependence on kinetic predictions. Overall, the linear LIF results are very encouraging and potentially suggest a procedure for making quenching corrections to linear LIF measurements of [NO] in counterflow diffusion flames at high pressure.

6. LIF MEASUREMENTS AND MODELING OF NITRIC OXIDE IN METHANE-AIR AND ETHANE-AIR COUNTERFLOW DIFFUSION FLAMES

6.1 Introduction

Ongoing research for future aircraft engines mandates *in situ* measurements of nitric oxide concentrations ([NO]) for various injector modules and combustor designs. To achieve this goal, the feasibility of laser-induced fluorescence (LIF) measurements of [NO] must be assessed in nonpremixed and partially premixed flames at atmospheric and higher pressures. The most useful flame geometry for this purpose is the counterflow configuration wherein opposing streams of fuel and oxidizer impinge and produce a stagnation plane whose location depends on the fuel and oxidizer velocities. Because of the nature of the flow field, the fuel diffuses and burns with the oxidizer in a flat flame on the oxidizer side of the stagnation plane. Thus, concentration and temperature measurements can be made away from potentially interfering surfaces.

Among the previous experimental investigations of NO formation in counterflow difusion flames were those by Hahn and Wendt (1981), Drake and Blint (1989), Atreya et al. (1996), and Sick et al. (1998). The first detailed investigation, conducted by Hahn and Wendt (1981), involved measurements of NO_x in two flames with very low stretch rates of 1.88 s^{-1} and 3.62 s^{-1} using probe sampling and a chemiluminescent NO/NO_x analyzer. Quantitative discrepancies existed in the comparison of both the temperature and [NO] profiles. The peak temperatures were overpredicted by about 150 K, and the peak NO concentrations were underpredicted by about 50%. Drake and Blint (1989) investigated the effect of flame stretch on thermal NO_x formation in laminar, counterflow diffusion flames with $CO/H_2/N_2$ as fuel. Detailed chemistry-transport model calculations of temperature were in reasonable agreement with previous experimental results for flames

with stretch rates of 70 s^{-1} and 180 s^{-1}. There was, however, a significant discrepancy between the measured and predicted [NO] profiles. This was attributed to the very poor spatial resolution of the probe sampling measurements. Probe measurements of [NO] by Atreya et al. (1996) in low strain rate, sooty flames revealed that a significant reduction in NO formation occurs because of a decrease in flame temperature caused by flame radiation. Soot was also observed to interact with NO formation through the major radical species produced in the primary reaction zone.

We have previously reported preliminary laser-saturated fluorescence (LSF) measurements of [NO] in a laminar opposed-flow diffusion flame (Ravikrishna and Laurendeau, 1998), which to our knowledge were the first measurements of [NO] in such flames using a nonintrusive technique. We also showed that a modified rate coefficient for the prompt-NO initiation reaction which is 2.5 times that adopted in the GRI (version 2.11) mechanism gave good agreement between [NO] predictions and measurements for ethane-air flames (Ravikrishna and Laurendeau, 1997). Recently, Sick et al. (1998) have reported planar laser-induced fluorescence (PLIF) measurements of nitric oxide in a methane-air counterflow diffusion flame. They too observed that the GRI mechanism underpredicted their NO measurements by a factor of two. They further showed that using the rate coefficient proposed by Dean et al. (1990) for the prompt-NO initiation reaction gave good agreement between predictions and measurements. This rate coefficient is again approximately 2.5 times that adopted in the GRI mechanism.

In this chapter, we present a comparison of quantitative LIF measurements of [NO] in methane-air and ethane-air counterflow diffusion flames with predictions from the Sandia opposed-flow flame code (Lutz et al., 1996) utilizing the GRI (version 2.11) mechanism for the NO kinetics. The linear LIF measurements of [NO] are corrected for variations in the electronic quenching rate coefficient by using major species profiles generated by the flame code and quenching cross-sections for NO available from the literature (Paul et al., 1995). Three methane-air flames with global strain rates varying from 5 to 35 s^{-1} were investigated while maintaining a constant fuel dilution in all cases. These flames were highly diluted to avoid soot formation and the influence of radiative

heat losses on NO formation. Four ethane-air flames with global strain rates varying from 5 to 48 s^{-1} were also investigated. Temperature measurements are made in the methane-air flames by using thin SiC filament pyrometry, a technique first described by Vilimpoc et al. (1988). In applying this thermometric technique, we introduce a novel method for calibration that significantly enhances its accuracy for both present and future applications.

6.2 Experimental Techniques

We begin with a brief description of the experimental facility used in the LIF measurements. Excitation of NO is achieved through use of the $Q_2(26.5)$ line in the $\gamma(0,0)$ band. The $Q_2(26.5)$ line was chosen because (1) the Boltzmann fraction is relatively insensitive to temperature variations over the range of temperatures of our flames, and (2) other species, such as O_2, do not interfere spectrally with this NO absorption line (Partridge et al., 1996). The excitation wavelength is generated by employing the second harmonic (λ=532 nm) of a Quanta-Ray GCR-4 Nd:YAG laser to pump a PDL-3 dye laser, which provided visible radiation at approximately 574 nm. The dye fundamental was frequency-doubled ($\lambda/2\approx287$ nm) in a WEX-2C wavelength extender and the residual Nd:YAG fundamental was frequency-mixed with the dye second harmonic to produce a mixed beam at ~226 nm. The four concentric beams (1064, 574, 287, 226 nm) were dispersed using a Pellin-Broca prism, and the mixed beam exited the WEX vertically polarized.

After the beam left the WEX, it was focused into the probe volume where the beam diameter and Rayleigh range were ~200 μm and ~8 mm, respectively. A Fabry-Perot wavelength stabilization system was used to control PDL drift (Cooper and Laurendeau, 1997). Splitter plates were used to split off small portions of the beam for power monitoring via photodiodes as the beam energy is required for proper normalization of the LIF signal. For LIF detection, a portion of the isotropically emitted fluorescence was captured and the collimated beam was focused onto the entrance slit of a 3/4-m monochromator. The detector is a Hamamatsu R106UH-HA photomultiplier tube which

was optimized for temporal resolution of the fluorescence signal (Harris et al., 1976). The entrance slit was 200-μm wide by 1-mm tall, thus defining a probe volume which is 200-μm wide along the diameter of the beam and 1-mm long along the axis of the beam. The maximum laser fluence permitted for the linear LIF measurements (~0.1 mJ/mm^2•pulse) was determined by attenuating the beam so as to obtain a linear variation of the fluorescence signal with laser fluence. A 110-mm × 110-mm, 1200-groove/mm holographic grating with a 250-nm blaze angle was used in first order to provide a dispersion of 1.1 nm/mm at the exit slit. A 1.818-mm wide exit slit was employed so as to spectrally integrate over a 2-nm region of the fluorescence spectrum centered on the γ(0,1) band of NO. A temporal gate width of 7 ns was used and each data point was averaged over 400 laser shots.

The thin filament pyrometry (TFP) technique (Vilimpoc et al., 1988; Ramakrishna et al., 1995), which was used to measure temperatures, involves extending a 10-20 μm diameter SiC fiber with weighted free ends across the centerline of the flame and measuring the radiant emission of the fiber using an infrared detector. The optical arrangement consists of a collimating calcium fluoride (CaF_2) lens, a CaF_2 focusing lens, a chopper, an adjustable slit and a liquid-nitrogen cooled InSb detector (Graesby Model IS-1) which has a spectral response between 1.1 and 5.6 μm. In this wavelength range, the fiber acts as a gray surface with an emittance of 0.88 (Vilimpoc et al., 1988). The signal is conditioned with a lock-in amplifier before being sampled at 3 Hz.

The burner system consisted of two opposed cylindrical ducts, each 2.54 cm in diameter (Yang and Puri, 1993). Fuel was injected through the bottom duct and oxidizer through the top, resulting in a flame stabilized on the oxidizer side of the stagnation plane. To shield the flame from ambient disturbances, an annular flow of nitrogen was passed through a duct surrounding the fuel inlet stream. A water-cooled co-annular heat exchanger was used to cool the upper portion of the burner assembly. A water bath in conjunction with a temperature controller was used to maintain the temperature of the circulating water high enough to avoid condensation on the burner. The global strain rate, defined as the sum of the fuel and the oxidizer nozzle exit velocities divided by the nozzle

separation distance, was varied from 5 to 35 s^{-1} for three methane-air counterflow diffusion flames. The fuel stream consisted of 25% by volume CH_4 and 75% by volume N_2 in all three flames. For this fuel dilution, the selected global strain rates represented almost the entire range up to extinction. The fuel stream in the ethane-air flames consisted of 15% by volume C_2H_6 and 85% by volume N_2, with global strain rates from 5 to 48 s^{-1}. The distance between the two burners was maintained at 2 cm for all flames.

6.3 Calibration Procedures

The calibration factor for the LIF measurements was determined by using a standard NO doping technique in a ϕ=0.8 premixed $CH_4/O_2/N_2$ flame with a dilution ratio of 3.76 (Reisel et al., 1993). The calibration was conducted at a height of 4 mm above the burner surface. The NO concentration in ppm relative to the calibration flame temperature can then be determined from

$$N_{ppm,RT} = C_F S_F \,, \tag{6.1}$$

where C_F is a calibration factor determined from the slope of the fit to the calibration data and S_F is the digital fluorescence signal. The [NO] in absolute ppm can then be expressed as

$$N_{ppm,abs} = \left(\frac{T}{T_c}\right)\left(\frac{f_B(T_c)}{f_B(T)}\right)\left(\frac{Q_e}{Q_{e,c}}\right) N_{ppm,RT} \,, \tag{6.2}$$

where T is the flame temperature, T_c is the temperature of the calibration flame, f_B is the Boltzmann fraction, Q_e is the local electronic quenching rate coefficient, and $Q_{e,c}$ is the electronic quenching rate coefficient in the calibration flame. The Boltzmann fraction is relatively insensitive to temperature variations (<10%) over a temperature range of 1000 - 2000 K. Since most of the NO is formed in high temperature regions, corrections for variations in the Boltzmann fraction are unnecessary. There are a few points in the wings of the [NO] profile where the temperatures are below 1000 K; however, the NO concentrations at these locations are relatively small and thus Boltzmann corrections are superfluous.

Numerical computations for all the flames were conducted using OPPDIF, a Sandia opposed-flow flame code (Lutz et al., 1996). The mathematical model reduces the two-dimensional, axisymmetric flow field to a one-dimensional formulation by using a similarity transformation. The model predicts the species, temperature, and velocity profiles along the centerline in the core flow between the two burners. A detailed derivation of the governing equations is given by Kee et al. (1988). The GRI mechanism, version 2.11 (Bowman et al., 1995), containing 49 species and 279 reactions is used to handle the chemical kinetics.

For the temperature measurements, the conversion of detector output voltage to temperature requires a non-linear calibration since the detector output is directly proportional to the emitted radiation and not to the temperature. Initial integrations with respect to wavelength of the filament graybody emission convoluted with the detector response and the optics transmission curve are needed for a range of flame temperatures. The ratio of the above integral to the same integral evaluated at the calibration temperature is tabulated as a function of temperature. A fifth-order polynomial fit to this calibration curve is used to convert the measured voltage ratio to temperature. Background infrared radiation from the flame is measured and subtracted from the filament emission before the data is reduced. The filament temperature is corrected for radiation losses to obtain the gas temperature. Temperatures thus measured yielded a precision of $\pm$ 5 K at peak temperatures and $\pm$ 40 K for temperatures below 1000 K.

One of the limitations of the TFP technique is the need for a flame system with an accurately known temperature. To address this issue, we calibrated the SiC filament in the flat flame of a 24-mm square Hencken burner. The surface-mixing Hencken burner produces a flame that is flat, uniform, steady and nearly adiabatic under the right flow conditions. At high enough flow rates, heat losses to the burner are minimal, and thus flame temperatures can be calculated accurately with an adiabatic equilibrium code. Recently, Hancock et al. (1997) have confirmed this presumption using nitrogen CARS thermometry and equilibrium calculations. The combined hydrogen and air flow rate for the calibration flame was 70.1 slpm at an equivalence ratio of 0.37. The equilibrium

temperature of 1383 K for these conditions was verified by thermocouple measurements. The actual filament temperature was then found by an inverse radiative heat loss calculation. Temperatures were subsequently measured using this calibrated filament.

6.4 Results and Discussion

Figures 6.1 shows a comparison of measured and predicted temperatures in the three methane-air counterflow diffusion flames. Excellent agreement exists between measurements and predictions for the flames with strain rates of 35 and 20 s^{-1}. The agreement is reasonable for the flame with a strain rate of 5 s^{-1}. The slight difference in the thickness of the computed and measured profiles in this low strain-rate flame may be attributed to the strong guard flow. The strong guard flow was needed to keep the flame steady and to prevent blowout owing to room air currents. However, since the guard flow is provided only in one direction, the flame tends to be pushed slightly higher. Overall, the temperature measurements validate the model predictions reasonably well, and thus the predicted temperatures were used in Eq. (6.2) for all flames.

The comparison between [NO] measurements and modeling in the methane-air flames is shown in Figs. 6.2-6.4. The experimental [NO] data are tabulated in Appendix C. The uncertainty associated with the accuracy of the LIF measurements at peak [NO] locations based on a 95% confidence interval is ~24%, with an increase to ~35% at the edges of the [NO] profile (see Appendix B). As expected, the peak NO concentrations decrease with an increase in flame stretch. This is mainly due to the decline in residence time in high temperature zones (Drake and Blint, 1989; Nishioka et al., 1994). Since the peak temperature decreases with an increase in flame stretch, there is also a reduction in the net NO production rate. The width of the NO profile becomes narrower with an increase in stretch owing to the increased velocity gradients. The GRI mechanism (Bowman et al., 1995) reasonably predicts NO concentration in the fuel-lean region of the flames.

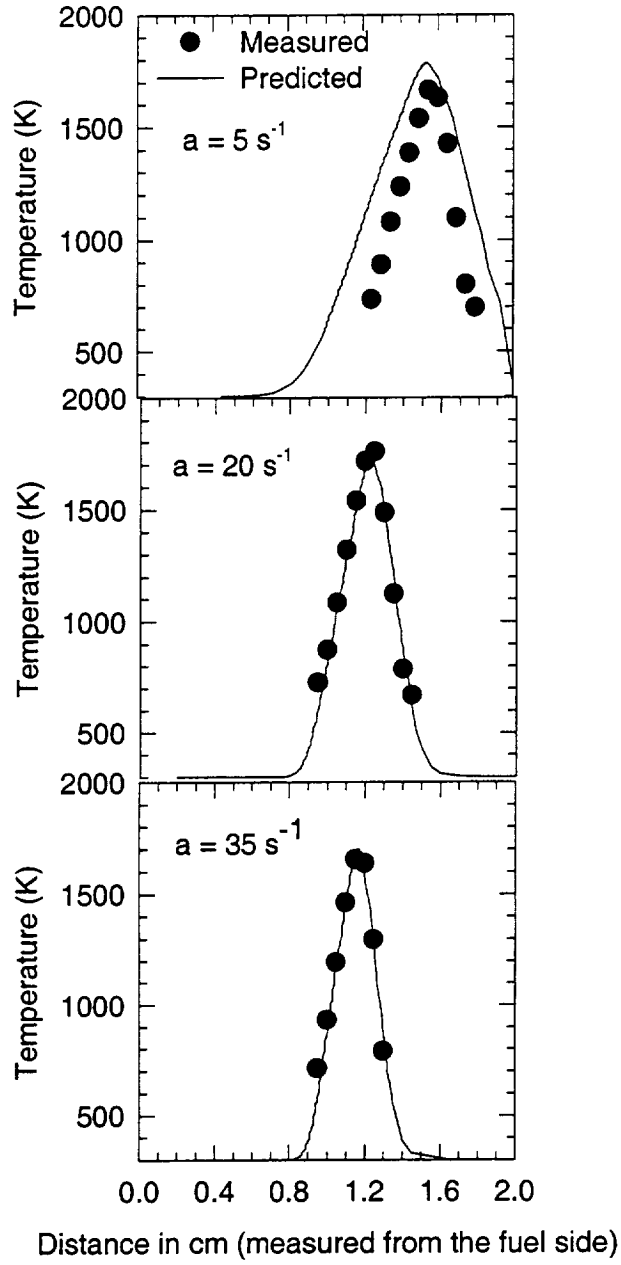

Figure 6.1: Comparison of measured and predicted temperatures in a methane-air counterflow diffusion flame at global strain rates of 5, 20, and 35 s^{-1}. The temperatures are measured using thin SiC filament pyrometry.

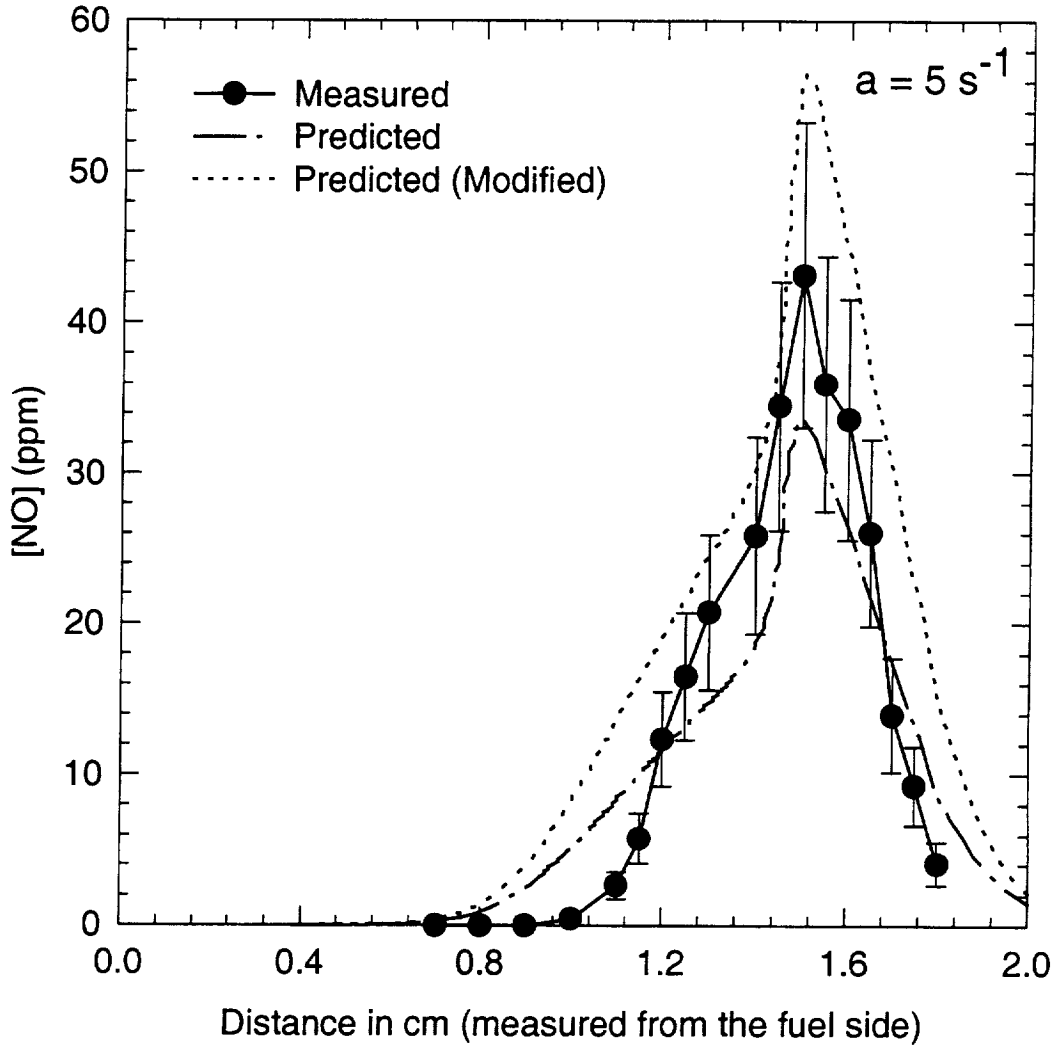

Figure 6.2: LIF measurements of NO vs. modeling in a methane-air counterflow diffusion flame at a global strain rate of 5 s^{-1}. The dashed line indicates modeling using the GRI mechanism (version 2.11). The dotted line indicates modeling with a modified rate coefficient for the prompt-NO initiation reaction.

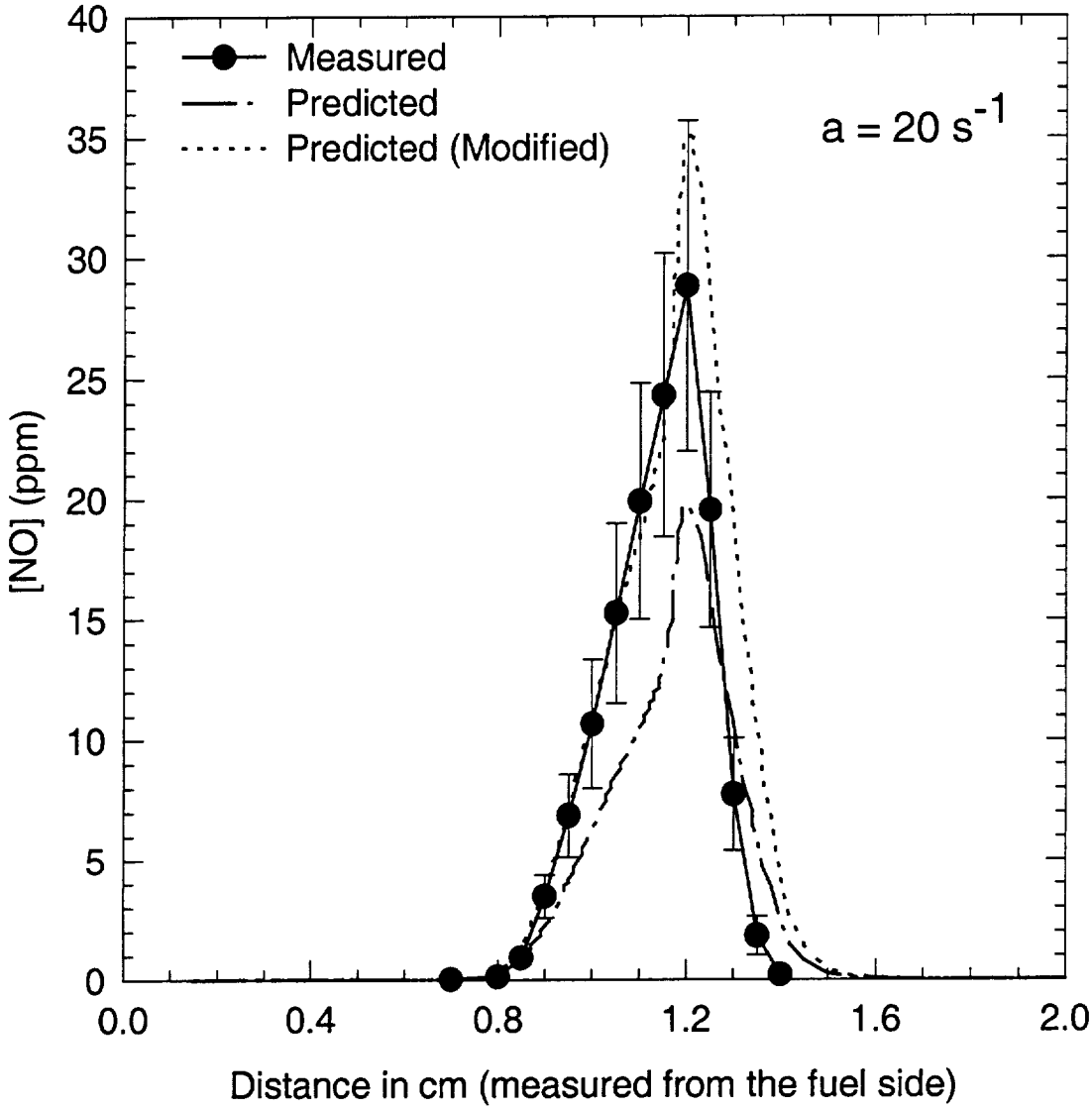

Figure 6.3: LIF measurements of NO vs. modeling in a methane-air counterflow diffusion flame at a global strain rate of 20 s^{-1}. The dashed line indicates modeling using the GRI mechanism (version 2.11). The dotted line indicates modeling with a modified rate coefficient for the prompt-NO initiation reaction.

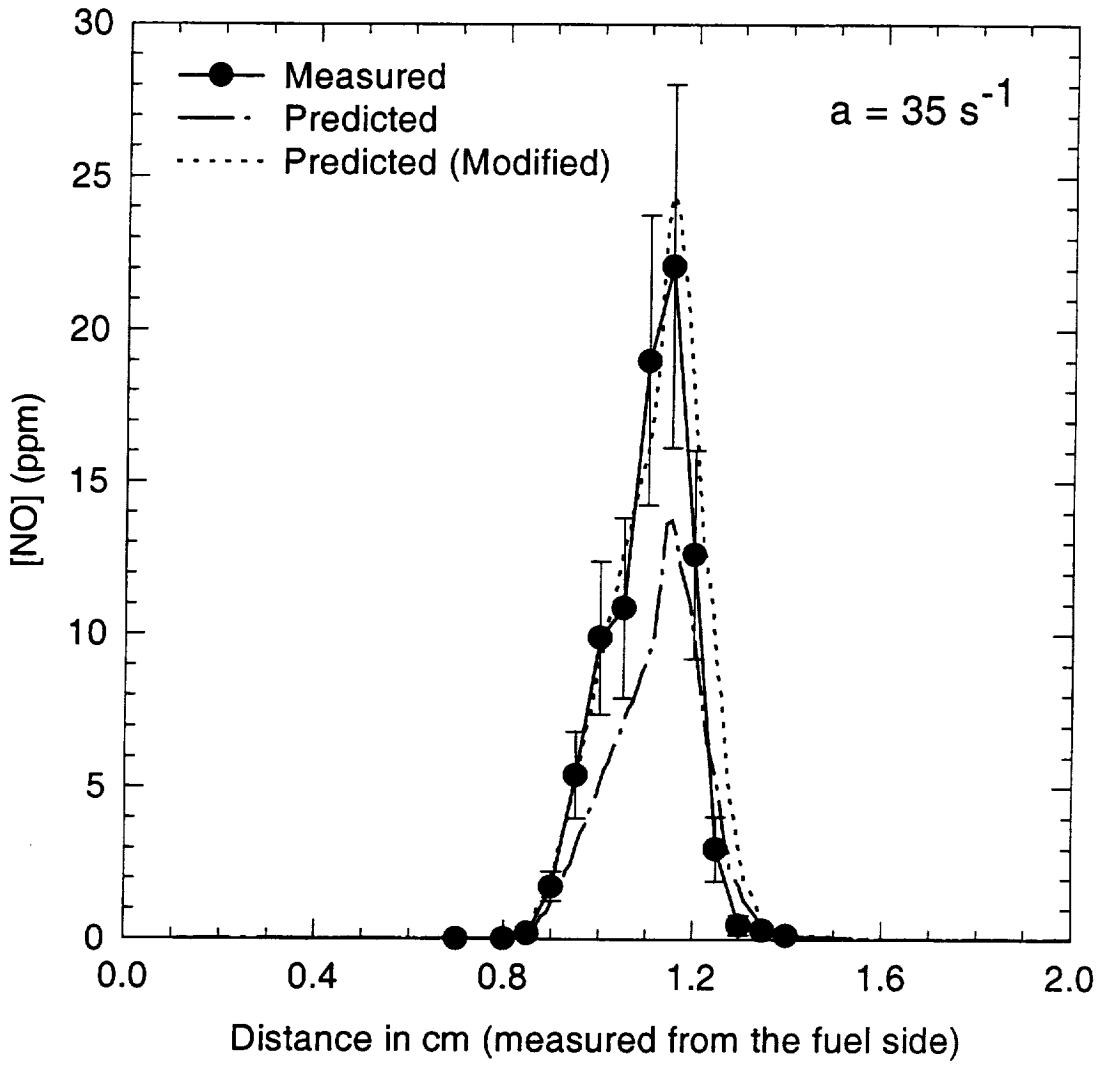

Figure 6.4: LIF measurements of NO vs. modeling in a methane-air counterflow diffusion flame at a global strain rate of 35 s^{-1}. The dashed line indicates modeling using the GRI mechanism (version 2.11). The dotted line indicates modeling with a modified rate coefficient for the prompt-NO initiation reaction.

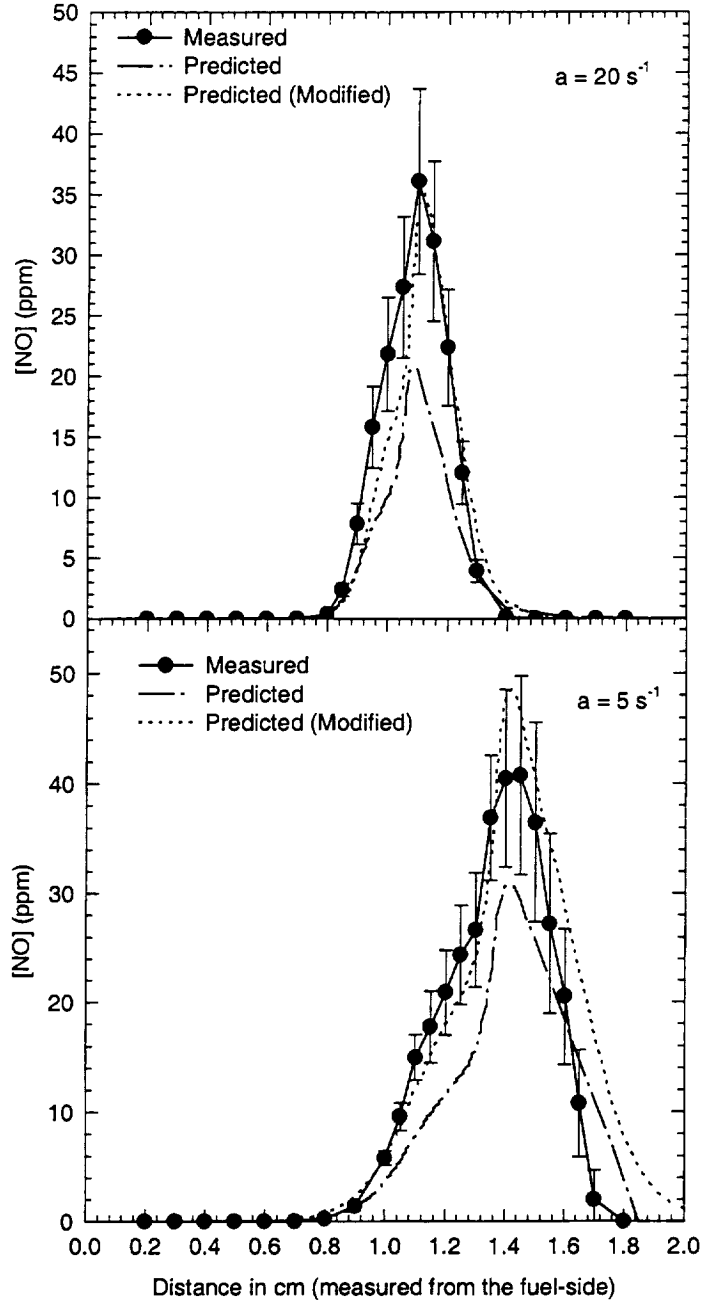

Figure 6.5: LIF measurements of NO vs. modeling in an ethane-air counterflow diffusion flame at global strain rates of 5 s^{-1} and 20 s^{-1}. The dashed line indicates modeling using the GRI mechanism (version 2.11). The dotted line indicates modeling with a modified rate coefficient for the prompt-NO initiation reaction.

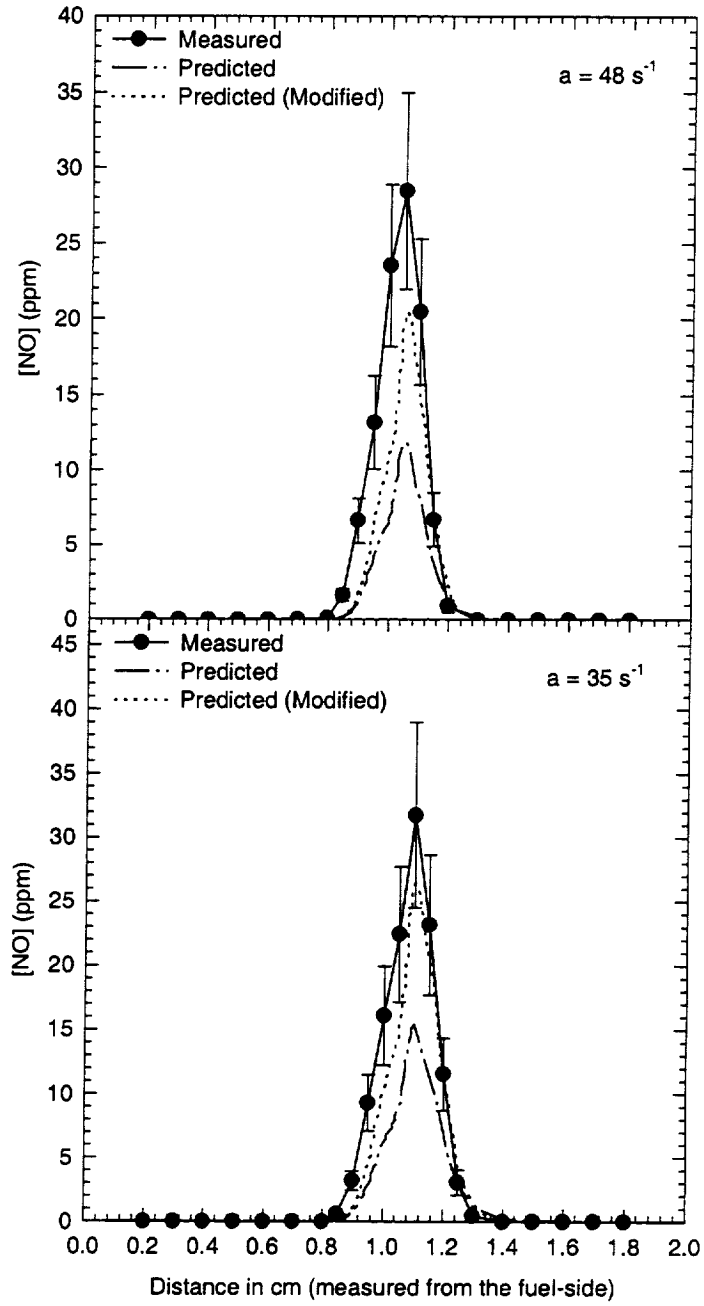

Figure 6.6: LIF measurements of NO vs. modeling in an ethane-air counterflow diffusion flame at global strain rates of 35 s^{-1} and 48 s^{-1}. The dashed line indicates modeling using the GRI mechanism (version 2.11). The dotted line indicates modeling with a modified rate coefficient for the prompt-NO initiation reaction.

However, it consistently underpredicts peak [NO] in all the flames. The [NO] is also significantly underpredicted in the fuel-rich region of the flames. The same trends are observed in the ethane-air flames. This is evident from Figs. 6.5 and 6.6, which show comparisons between modeling and measurements for the four ethane-air counterflow diffusion flames. It is interesting to note that the difference between measurements and predictions of [NO] is smaller in the lower strain rate flames. This can be explained by the fact that both temperature and residence time are highest in the lowest strain rate flames. Thus, for these flames, thermal [NO] formation is beginning to contribute, causing a decrease in the discrepancy.

The peak temperatures in all flames considered in this study are below 1800 K. Since the thermal-NO mechanism is characterized by a high activation temperature (~1800 K), the amount of NO formed through this mechanism should be small for our flames. Nishioka et al. (1994) have performed extensive modeling of NO formation in counterflow diffusion flames to investigate the contribution of the different mechanisms. They have shown that the contribution of the N_2O mechanism is very small. Hence it would seem that a major portion of the NO in these flames is formed through the prompt mechanism. This has been confirmed by our chemical reaction pathway analysis which indicates that for the methane-air flames, 83% of the peak NO in the 35 s^{-1} flame and 73% in the 5 s^{-1} strain-rate flame are formed through the prompt-NO mechanism. Similarly, for the ethane-air flames, 85% of the peak NO in the 48 s^{-1} flame and 66% in the 5 s^{-1} strain-rate flame are formed via the prompt-NO mechanism.

The above discussion suggests a need to refine the prompt-NO mechanism, especially the rate coefficient for the prompt-NO initiation reaction. The initiation step for the prompt NO mechanism is generally agreed to be

$$CH + N_2 \Leftrightarrow HCN + N. \qquad \text{(R1)}$$

Drake and Blint (1991) have indicated that there is considerable uncertainty in the rate coefficient for this reaction. Reisel et al. (1997) have suggested that much of the quantitative error in modeling could be alleviated through refinement of the rate coefficient for reaction (R1). Recently, Sick et al. (1998) have reported planar laser-

induced fluorescence (PLIF) measurements of nitric oxide in a methane-air counterflow diffusion flame. They observed that the GRI mechanism underpredicted their NO measurements by a factor of two. They also showed that using the rate coefficient proposed by Dean et al. (1990) for reaction (R1) in their modeling gave good agreement with measurements. This rate coefficient is approximately 2.5 times that adopted in the GRI mechanism. Berg et al. (1998) have recently reported LIF measurements of NO concentration in low pressure premixed $CH_4/O_2/N_2$ flames of varying stoichiometry. They observed that the GRI mechanism underpredicts prompt NO by 35 to 60%. To match their experimental data with predictions, the rate coefficient for reaction (R1) had to be increased by factors ranging from 1.7 to 3.8 in rich to lean flames. However, they suggest multiplying the rate coefficient for reaction (R1) by a factor between 2.1 and 2.8. Luque et al. (1996) previously noted that a factor of 2.3 was needed in a near-stoichiometric propane/air flame, and a factor of 2.1 was needed for a slightly rich propane/air flame. These investigations regarding the rate coefficient of reaction (R1) based on LIF measurements of NO in flames (Berg et al., 1998; Luque et al., 1996) have suggested modified rate coefficients that vary for each flame investigated. Our approach is to propose a uniform modified rate coefficient based on the NO data in a flame with the maximum prompt-NO contribution, and to assess the NO predictions in the other flames based on this modified rate coefficient.

To determine the rate coefficient for reaction (R1) based on our data, we utilized the methane-air flame with the highest strain rate. This flame has the lowest peak temperature (~ 1700 K) ensuring mostly prompt NO formation. As mentioned before, for this case, 83% of the NO at peak locations is formed via the prompt NO mechanism. The measured NO concentration data for the 35 s^{-1} strain rate flame suggests that the rate coefficient for reaction (R1) needs to be increased by a factor of 2.1. The comparison between modeling with the modified rate coefficient and experiment is shown in Figs. 6.2-6.4 for the methane-air flames. The agreement between modeling with the modified rate coefficient and measurements is good for the flames with strain rates of 35 and 20 s^{-1}. There seems to be a slight overprediction of NO in the 5 s^{-1} flame. As mentioned before,

this flame has the least contribution from the prompt-NO mechanism in comparison to the other flames. The slight overprediction in this flame may be attributed to the lack of refinement in the CH chemistry.

Figures 6.5 and 6.6 show a similar comparison for the ethane-air flames. The modified rate coefficient proposed here causes the NO predictions in the intermediate strain-rate ethane-air flames to agree very well with measurements. There is an underprediction in the highest strain rate flame and a slight overprediction in the lowest strain rate flame. Since these strain rates represent the entire range up to extinction, the modified rate coefficient proposed here seems to be a good choice over the entire strain-rate range for ethane-air flames. The slight discrepancy in the highest strain rate flame could also be attributed to the lack of refinement in the CH chemistry. Recent shock-tube measurements of CH concentration at high temperatures for fuel-rich methane oxidation showed significant deviations from GRI model predictions (Woiki et al., 1998). Since the CH radical has a very important effect on prompt-NO formation, these observations might explain the remaining discrepancy observed in some of the flames.

6.5 Conclusions

Quantitative LIF measurements of [NO] have been obtained along the centerline in atmospheric pressure methane-air and ethane-air counterflow diffusion flames. As expected, the peak NO concentration decreases and the width of the NO profile becomes narrower with an increase in flame stretch. Temperature measurements were also made using thin SiC filament pyrometry in the methane-air counterflow diffusion flames. The excellent agreement between temperature measurements and predictions indicates the efficacy of the new calibration method developed for the thin filament pyrometry technique. The model with the GRI mechanism consistently underpredicts peak [NO] in all flames. Since most of the NO in these flames is formed through the prompt mechanism, the results indicate a need for refinement of both prompt-NO and CH chemistry, especially the rate coefficient for the prompt-NO initiation reaction. A

modified rate coefficient proposed for the prompt-NO initiation reaction significantly improves the agreement between modeling and experiment in methane-air and ethane-air flames. However, there is still a slight discrepancy in some flames. This may be attributed to a lack of refinement in the CH chemistry. Overall, the modified rate coefficient proposed here seems to be a good compromise over a wide range of strain rates for both methane and ethane fuels.

7. LIF MEASUREMENTS AND MODELING OF NITRIC OXIDE IN COUNTERFLOW PARTIALLY-PREMIXED FLAMES

7.1 Introduction

The most useful flame geometry for studying partially-premixed flames is the counterflow configuration wherein opposing streams of rich fuel-air mixture and oxidizer impinge and produce a stagnation plane. This leads to a double flame structure consisting of a premixed flame formed in the fuel-rich mixture and a nonpremixed flame formed between the products of this rich, premixed flame and the opposing air stream. The advantage of this configuration is that concentration and temperature measurements can be made away from potentially interfering surfaces.

Yamaoka and Tsuji studied the structure of partially-premixed flames formed in the forward stagnation region of a porous cylinder in a previous series of pioneering experimental investigations (Yamaoka and Tsuji, 1975; 1977; 1979). However, to our knowledge, no experimental investigations have been conducted on the formation of NO in laminar counterflow partially-premixed flames. The few investigations conducted so far have been numerical in nature (Nishioka et al., 1994; Tanoff et al., 1996; Li et al., 1997; Blevins and Gore, 1999; Zhu et al., 1999). Nishioka et al. (1994) studied NO emission characteristics of Bunsen-type burner flames in terms of counterflow partially-premixed flames. The contributions of the various pathways to NO formation were investigated as well as the effects of equivalence ratio and velocity gradient on the NO emission index. The main source of NO formation was found to be thermal for low velocity gradients with a shift to the prompt mechanism at higher velocity gradients. Tanoff et al. (1996) noted that in counterflow partially-premixed flames, the flame structure changes significantly with fuel-side equivalence ratio, with an ensuing strong effect on the mode and degree of

NO formation. Numerical computations of NO profiles were obtained by Li et al. (1997) in counterflow partially-premixed flames with water sprays added to the air stream. Prompt-NO was found to play a dominant role in NO_x formation, and the NO_x emission index was found to depend strongly on the flame structure and mass fraction of water added in the air stream.

Recent computations by Blevins and Gore (1999) for low strain-rate, counterflow partially-premixed flames have focused on understanding the flame structure with respect to NO formation. Two flame fronts were found to exist on opposite sides of the stagnation plane for flames with fuel-side equivalence ratios below 2.5. These flame fronts were found to contain two CH radical concentration peaks, one at the location of the CH_4/air premixed flame front and the other at the fuel-side edge of the CO/H_2/air nonpremixed flame front. NO formation zones were found on the air-side of the premixed CH peak and near the temperature peak corresponding to the CO/H_2/air nonpremixed flame front. NO was found to be consumed via reburn reactions with hydrocarbons in a destruction zone which begins on the reactant side of the CH_4/air premixed flame front and persists throughout the broad region between the two CH peaks. More recently, Zhu et al. (1999) investigated the effect of thermal radiation on NO predictions in counterflow partially-premixed flames by using an optically thin radiation model. They found that radiative heat loss caused by gaseous emission changes the temperature and NO mole fractions significantly in flames at low fuel-side equivalence ratios.

In this chapter, we present [NO] measurements in laminar counterflow partially-premixed flames. Quantitative LIF measurements of [NO] in methane-air counterflow partially premixed flames are compared with predictions from a Sandia opposed-flow flame code (Lutz et al., 1996) utilizing the GRI (version 2.11) mechanism (Bowman et al., 1995) for the NO kinetics. The effect of radiative heat loss on NO predictions is also assessed using a modified version of the code (Gore et al., 1999). Predictions using a modified rate coefficient for the prompt-NO initiation reaction based on a previous analysis of nonpremixed flames (Ravikrishna and Laurendeau, 1999a) are also compared with measurements. The linear LIF measurements of [NO] are corrected for variations in

the electronic quenching rate coefficient by using major species profiles generated by the flame code and quenching cross-sections for NO available from the literature (Paul et al., 1995). The effect of partial premixing is studied by investigating four flames with fuel-side equivalence ratios (ϕ_B) of 1.45, 1.6, 1.8 and 2.0 at a constant global strain rate of ~20 s^{-1}. Temperature measurements are made in all flames by using thin SiC filament pyrometry via a novel calibration technique reported earlier (Ravikrishna and Laurendeau, 1999a).

7.2 Experimental Techniques

We begin with a brief description of the experimental facility used in the LIF measurements. Excitation of NO is achieved through use of the $Q_2(26.5)$ line in the $\gamma(0,0)$ band. The $Q_2(26.5)$ line was chosen because (1) the Boltzmann fraction is relatively insensitive to temperature variations over the range of temperatures of our flames, and (2) other species, such as O_2, do not interfere spectrally with this NO absorption line (Partridge et al., 1996). The excitation wavelength is generated by employing the second harmonic (λ=532 nm) of a Quanta-Ray GCR-4 Nd:YAG laser to pump a PDL-3 dye laser, which provided visible radiation at approximately 574 nm. The dye fundamental was frequency-doubled ($\lambda/2\approx287$ nm) in a WEX-2C wavelength extender and the residual Nd:YAG fundamental was frequency-mixed with the dye second harmonic to produce a mixed beam at ~226 nm. The four concentric beams (1064, 574, 287, 226 nm) were dispersed using a Pellin-Broca prism, and the mixed beam exited the WEX vertically polarized.

After the beam left the WEX, it was focused into the probe volume where the beam diameter and Rayleigh range were ~200 μm and ~8 mm, respectively. A Fabry-Perot wavelength stabilization system was used to control PDL drift (Cooper and Laurendeau, 1997). Splitter plates were used to split off small portions of the beam for power monitoring via photodiodes. The beam energy is required for proper normalization of the LIF signal.

For LIF detection, a portion of the isotropically emitted fluorescence was captured and the collimated beam was focused onto the entrance slit of a 3/4-m monochromator. The detector is a Hamamatsu R106UH-HA photomultiplier tube which was optimized for temporal resolution of the fluorescence signal (Harris et al., 1976). The entrance slit was 200-μm wide by 1-mm tall, thus defining a probe volume which is 200-μm wide along the diameter of the beam and 1-mm long along the axis of the beam. The maximum laser fluence permitted for the linear LIF measurements (~0.1 $mJ/mm^2 \bullet pulse$) was determined by attenuating the beam so as to obtain a linear variation of the fluorescence signal with laser fluence. A 110-mm × 110-mm, 1200-groove/mm holographic grating with a 250-nm blaze angle was used in first order to provide a dispersion of 1.1 nm/mm at the exit slit. A 1.818-mm wide exit slit was employed so as to spectrally integrate over a 2-nm region of the fluorescence spectrum centered on the $\gamma(0,1)$ band of NO. A temporal gate width of 7 ns was used and each data point was averaged over 400 laser shots.

The thin filament pyrometry (TFP) technique (Ravikrishna and Laurendeau, 1999a; Vilimpoc et al., 1988; Ramakrishna et al., 1995), which was used to measure temperatures, involves extending a 10-20 μm diameter SiC fiber with weighted free ends across the centerline of the flame and measuring the radiant emission of the fiber using an infrared detector. The optical arrangement consists of a collimating calcium fluoride (CaF_2) lens, a CaF_2 focusing lens, a chopper, an adjustable slit and a liquid-nitrogen cooled InSb detector (Graesby Model IS-1) which has a spectral response between 1.1 and 5.6 μm. In this wavelength range, the fiber acts as a gray surface with an emittance of 0.88 (Vilimpoc et al., 1988). The signal is conditioned with a lock-in amplifier before being sampled at 3 Hz.

The burner system consists of two opposed cylindrical ducts, each 2.54 cm in diameter (Yang and Puri, 1993). Fuel-rich $CH_4/O_2/N_2$ premixed reactant was injected through the bottom duct and air through the top, resulting in a double flame structure. To shield the flame from ambient disturbances, an annular flow of nitrogen was passed through a duct surrounding the fuel inlet stream. A water-cooled co-annular heat exchanger was used to cool the upper portion of the burner assembly. A water bath in

conjunction with a temperature controller was used to maintain the temperature of the circulating water high enough to avoid condensation on the burner. The global strain rate, defined as the sum of the fuel and the oxidizer nozzle exit velocities divided by the nozzle separation distance, was maintained nearly constant at around 20 s^{-1}. Four partially-premixed flames were simulated by varying the equivalence ratio of the rich premixed CH_4/air stream from 1.45 to 2.0. For all flames, the flow rates of the oxygen and nitrogen in the air stream were maintained at 1.20 and 4.51 SLPM, respectively, whereas the flow rate for the oxygen and nitrogen in the fuel stream were maintained at 1.06 and 4.00 SLPM, respectively. The methane flow rates for the flames with fuel-side equivalence ratios of 1.45, 1.6, 1.8 and 2.0 were 0.77, 0.85, 0.96 and 1.06 SLPM, respectively. The distance between the two burners was maintained at 2 cm for all the flames.

7.3 Calibration Procedures

The calibration factor for the LIF measurements was determined by using a standard NO doping technique in a ϕ=0.8 premixed $CH_4/O_2/N_2$ flame with a dilution ratio of 3.76 (Reisel et al., 1993). The calibration was conducted at a height of 4 mm above the burner surface. The NO concentration in ppm relative to the calibration flame temperature can then be determined from

$$N_{ppm,RT} = C_F S_F \quad , \tag{7.1}$$

where C_F is a calibration factor determined from the slope of the fit to the calibration data and S_F is the digital fluorescence signal. The [NO] in absolute ppm can be expressed as

$$N_{ppm,abs} = \left(\frac{T}{T_c}\right)\left(\frac{f_B(T_c)}{f_B(T)}\right)\left(\frac{Q_e}{Q_{e,c}}\right) N_{ppm,RT} , \tag{7.2}$$

where T is the flame temperature, T_c is the temperature of the calibration flame, f_B is the Boltzmann fraction, Q_e is the local electronic quenching rate coefficient, and $Q_{e,c}$ is the electronic quenching rate coefficient in the calibration flame. The Boltzmann fraction is relatively insensitive to temperature variations (<10%) over a temperature range of 1000 - 2000 K. Since most of the NO is formed in high temperature regions, corrections for

variations in the Boltzmann fraction are unnecessary. There are a few points in the wings of the [NO] profile where the temperatures are below 1000 K; however, the NO concentrations at these locations are relatively small and thus Boltzmann corrections are superfluous.

Numerical computations for all the flames were conducted using OPPDIF, a Sandia opposed-flow flame code (Lutz et al., 1996). The mathematical model reduces the two-dimensional, axisymmetric flow field to a one-dimensional formulation by using a similarity transformation. The model predicts the species, temperature, and velocity profiles along the centerline in the core flow between the two burners. A detailed derivation of the governing equations is given by Kee et al. (1988). The GRI mechanism, version 2.11 (Bowman et al., 1995), containing 49 species and 279 reactions is used to handle the chemical kinetics.

For the temperature measurements, the conversion of detector output voltage to temperature requires a non-linear calibration since the detector output is directly proportional to the emitted radiation and not to the temperature. Initial integrations with respect to wavelength of the filament graybody emission convoluted with the detector response and the optics transmission curve are needed for a range of flame temperatures. The ratio of the above integral to the same integral evaluated at the calibration temperature is tabulated as a function of temperature. A fifth-order polynomial fit to this calibration curve is used to convert the measured voltage ratio to temperature. Background infrared radiation from the flame is measured and subtracted from the filament emission before the data are reduced. Calibration is conducted in the flat flame of a 24-mm square Hencken burner as reported previously (Ravikrishna and Laurendeau, 1999a). The filament temperature is then corrected for radiation losses to obtain the gas temperature. Temperatures thus measured yielded a precision of ± 5 K at peak temperatures and ± 40 K at temperatures below 1000 K.

7.4 Results and Discussion

Figure 7.1 shows a comparison of measured and predicted temperature profiles for the counterflow partially premixed flames. There is good agreement between the thickness of the measured and predicted temperature profiles in all four flames. In addition, the agreement between measured and predicted temperatures is excellent in the preheat zone of the premixed flame front and on the air-side of the CO/H_2-air diffusion flame. However, the measured temperatures are 200-300 K higher than predictions in the interflame region for all flames. This disagreement might be explained by recent work (Ji et al., 1999) which shows that the assumption of constant emissivity with wavelength and temperature may not hold for SiC fibers in the range considered in our experiments. In addition, not much is known about changes that might occur to the fiber material at temperatures approaching 2000 K. Considering the excellent agreement obtained previously between temperature measurements using this technique and predictions in lower temperature ($T < 1800$ K) counterflow diffusion flames (Ravikrishna and Laurendeau, 1999a), we elected to employ predicted rather than measured temperatures in Eq. (7.2) for all the counterflow partially-premixed flames of this investigation.

A comparison between measurements and modeling of [NO] in the counterflow partially-premixed flames is shown in Figs. 7.2 and 7.3. The experimental [NO] data are tabulated in Appendix C. The uncertainty associated with the accuracy of the LIF measurements at peak [NO] locations based on a 95% confidence interval is ~24%, with an increase to ~35% at the edges of the [NO] profiles (see Appendix B). In general, good agreement exists between the measurements and modeling in all four flames. As expected, the separation distance between the premixed and diffusion flame fronts decreases with increasing equivalence ratio. NO is mostly found in the high temperature region between the premixed and diffusion flames.

The modeling results of Nishioka et al. (1994) show that the main source of NO formation in counterflow partially-premixed flames occurs via the thermal mechanism when the velocity gradient is small and shifts to the prompt mechanism as the velocity gradient rises. More recently, Blevins and Gore (1999) found that in low strain-rate

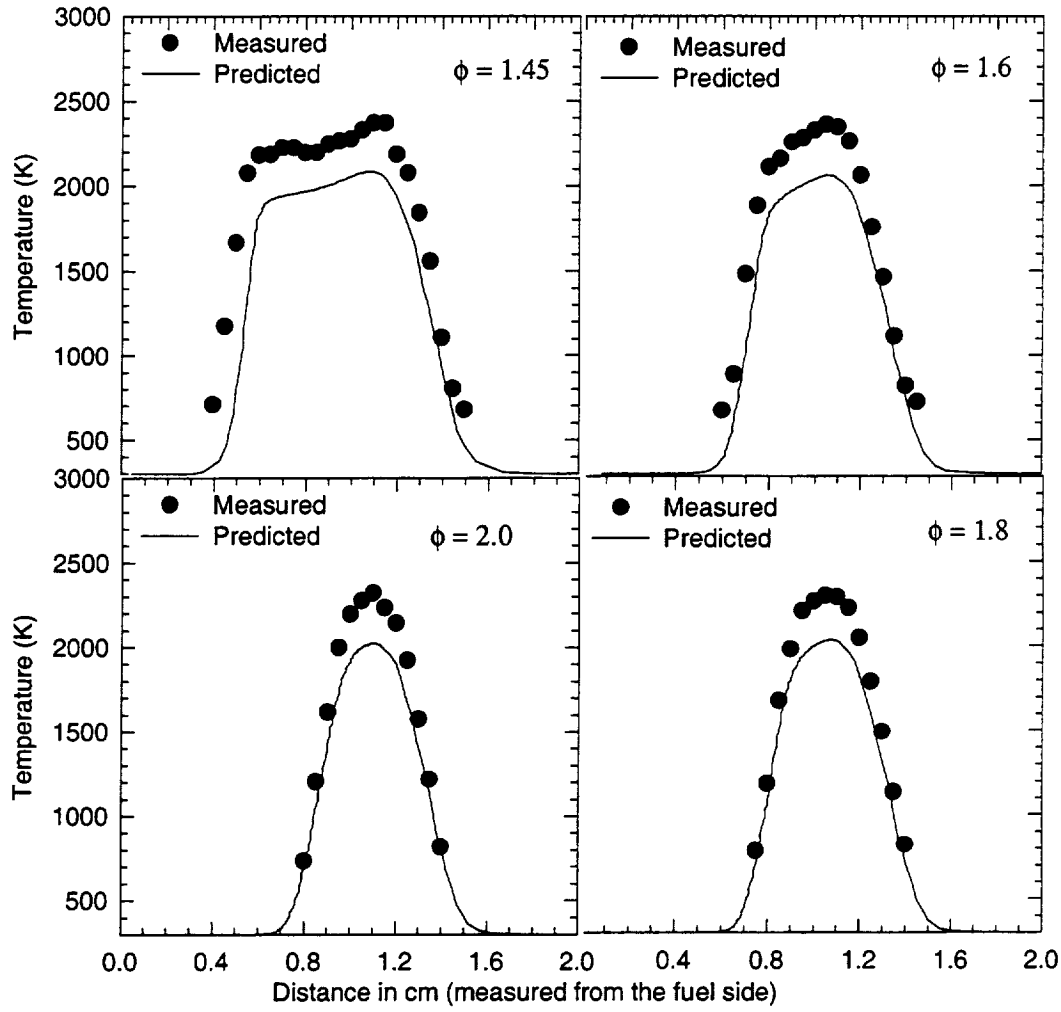

Figure 7.1: Comparison of measured and predicted temperatures in the counterflow partially-premixed flames with fuel-side equivalence ratios of 1.45, 1.6, 1.8, and 2.0.

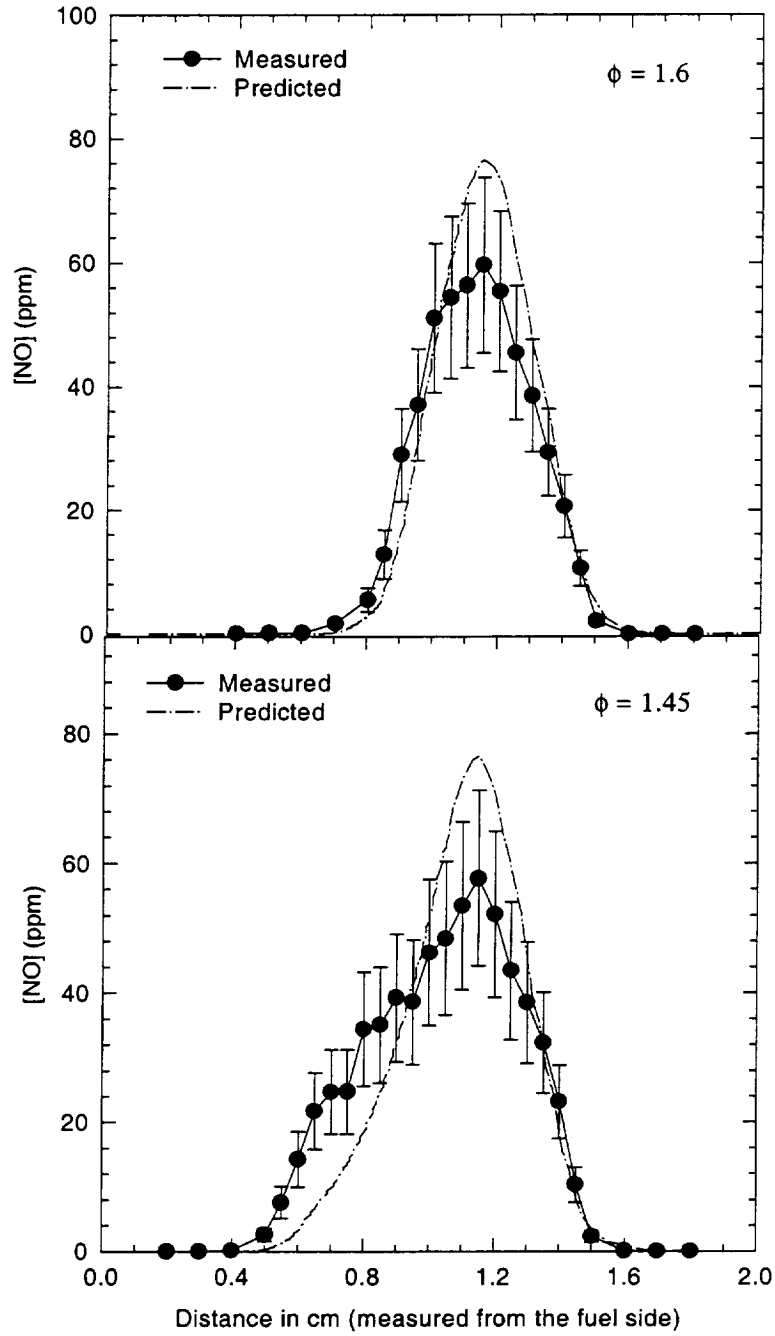

Figure 7.2: Comparison of LIF [NO] measurements and modeling in the counterflow partially-premixed flames with fuel-side equivalence ratios of 1.45 and 1.6.

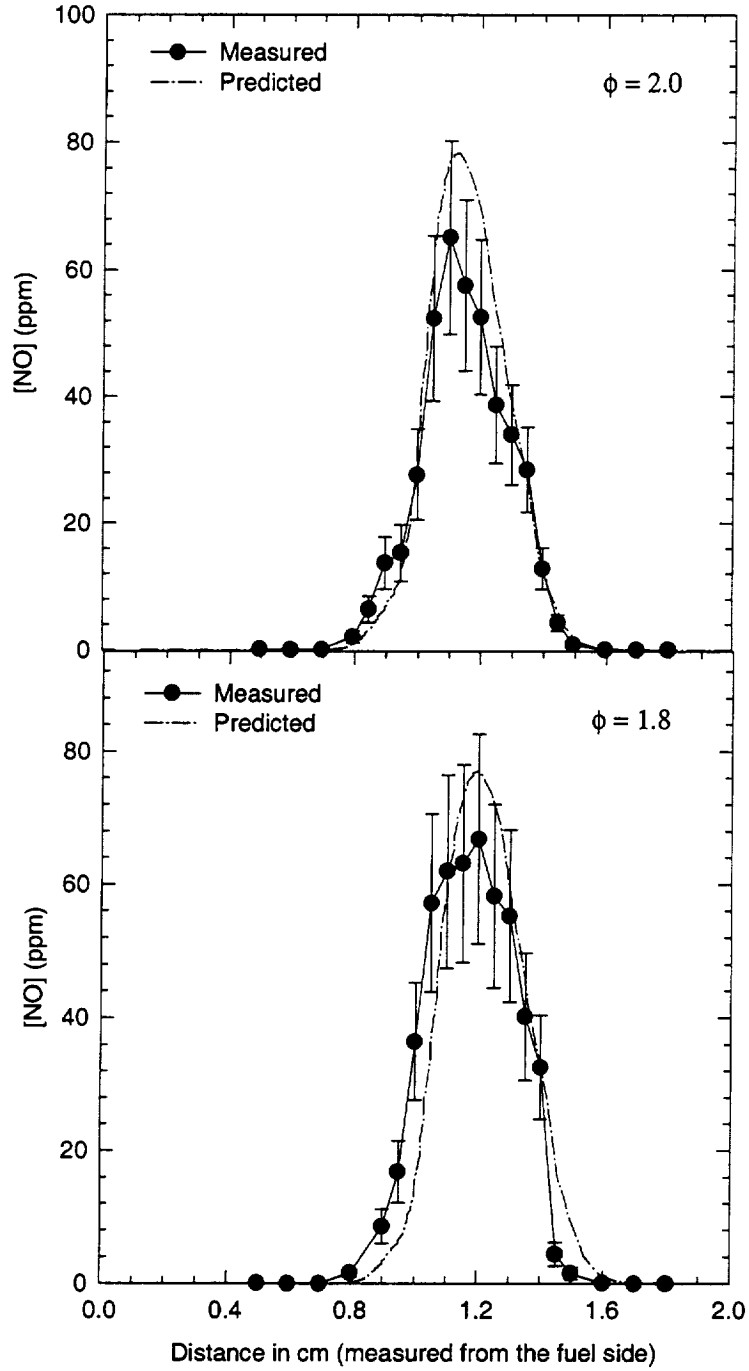

Figure 7.3: Comparison of LIF [NO] measurements and modeling in the counterflow partially-premixed flames with fuel-side equivalence ratios of 1.8 and 2.0.

counterflow partially-premixed flames, both the thermal and prompt mechanisms contribute significantly to NO formation, with the exact split depending on the equivalence ratio of the fuel-rich premixed stream. Moreover, they noticed a spatial separation between the peak NO production rates arising from the prompt and thermal mechanisms although the production rate profiles overlapped to some extent.

In our study, we focused on the ϕ_B=1.45 flame, since this flame offers the widest separation between the premixed and diffusion flame fronts. Fig. 7.4 shows the spatial variation in the production rates of the prompt-NO initiation reaction ($CH+N_2 \Leftrightarrow HCN+N$) and the main thermal-NO reaction ($N_2+O \Leftrightarrow NO+N$). The other two thermal reactions have not been included since they involve nitrogen atoms which are produced by the prompt-NO initiation reaction and hence would erroneously indicate a contribution from the thermal mechanism at the location where prompt-NO dominates. From Fig. 7.4, we note that both the prompt and thermal mechanisms contribute significantly to NO formation in a low strain rate partially-premixed flame, an observation which is in agreement with that of Blevins and Gore (1999). Although Fig. 7.4 does not include NO reburn reactions, it clearly shows that most of the prompt-NO originates at the fuel-rich premixed flame front and most of the thermal NO is produced at the high-temperature, nonpremixed flame front (Kim et al., 1995). Hence, this flame provides a unique opportunity to test NO chemical kinetic mechanisms since a spatial demarcation exists between the contributions of the two major NO pathways.

This demarcation is further illustrated by Fig. 7.5 which shows the contributions of the two mechanisms to the final NO concentration profile in the ϕ_B=1.45 flame. Since the different NO mechanisms share common species and thus affect each other, it is important to identify exactly the relative contribution and also the spatial distribution of each mechanism. This identification is accomplished by a subtraction method wherein the contribution of a particular pathway is calculated by subtracting the model prediction without that pathway from a model prediction with the full N_2 chemistry (Thomsen, 1996). We see from Fig. 7.5 that in the region from 0.6 to 0.9 cm, the prompt mechanism dominates over the thermal mechanism. Moreover, it is interesting to note from Fig. 7.2

that the GRI mechanism underpredicts [NO] by around 30-50% in this region. This observation is in agreement with our previous work (Ravikrishna and Laurendeau, 1999a) wherein the GRI mechanism was found to underpredict prompt-NO in counterflow diffusion flames. In comparison, the agreement between measurements and modeling in Fig. 7.2 is quite good in those regions dominated by thermal-NO. Since thermal-NO chemistry is well-understood, this good agreement between the model and the [NO] measurements is not unexpected.

In all flames, the peak [NO] measurements are consistently somewhat lower than model predictions as seen in Figs. 7.2 and 7.3. Since peak temperatures are more than 2000 K and the original model did not account for radiative heat losses, this feature could be attributed to a slight reduction in NO formation in the experiment owing to radiative heat losses. To account for the radiative effect, we employed a modified version of the OPPDIF code (Gore et al., 1999). Radiation heat loss was calculated in the optically thin limit by employing Planck mean absorption coefficients for CO_2, H_2O, CO, and CH_4. The temperature dependence of the Planck mean absorption coefficients was accounted for by using fourth-order polynomial fits to the results of narrow band calculations (Gore et al., 1999).

Figures 7.6 and 7.7 show comparisons between the predictions with radiation and the LIF measurements. A significant improvement occurs in the agreement between [NO] predictions and measurements. In all flames, predictions at the peak [NO] locations fall within the uncertainty of the measurements. In fact, predictions are within 10% of the measurements at these locations. There is also excellent agreement on the air-side of the diffusion flame front, i.e., predictions fall within the uncertainty of the measurements in all flames. However, some underprediction still exists near the premixed flame front where prompt-NO dominates.

We observed in our previous work that a modified rate coefficient for the prompt-NO initiation reaction significantly improved agreement between predictions and LIF [NO] measurements for prompt-NO dominated counterflow diffusion flames (Ravikrishna

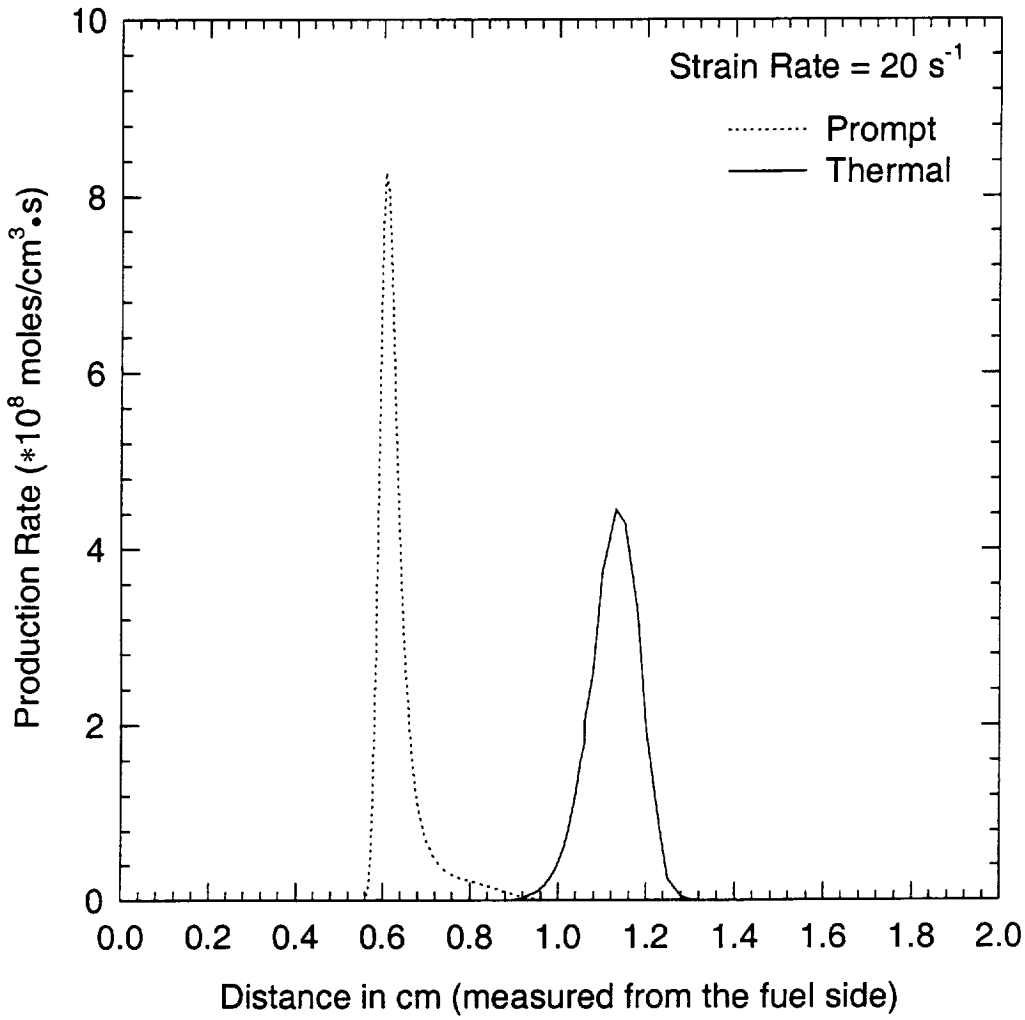

Figure 7.4: Spatial variation of the molar production rates for the prompt-NO initiation reaction ($CH+N_2 \Leftrightarrow HCN+N$) and the main thermal-NO reaction ($N_2+O \Leftrightarrow NO+N$) in the flame with a fuel-side equivalence ratio of 1.45.

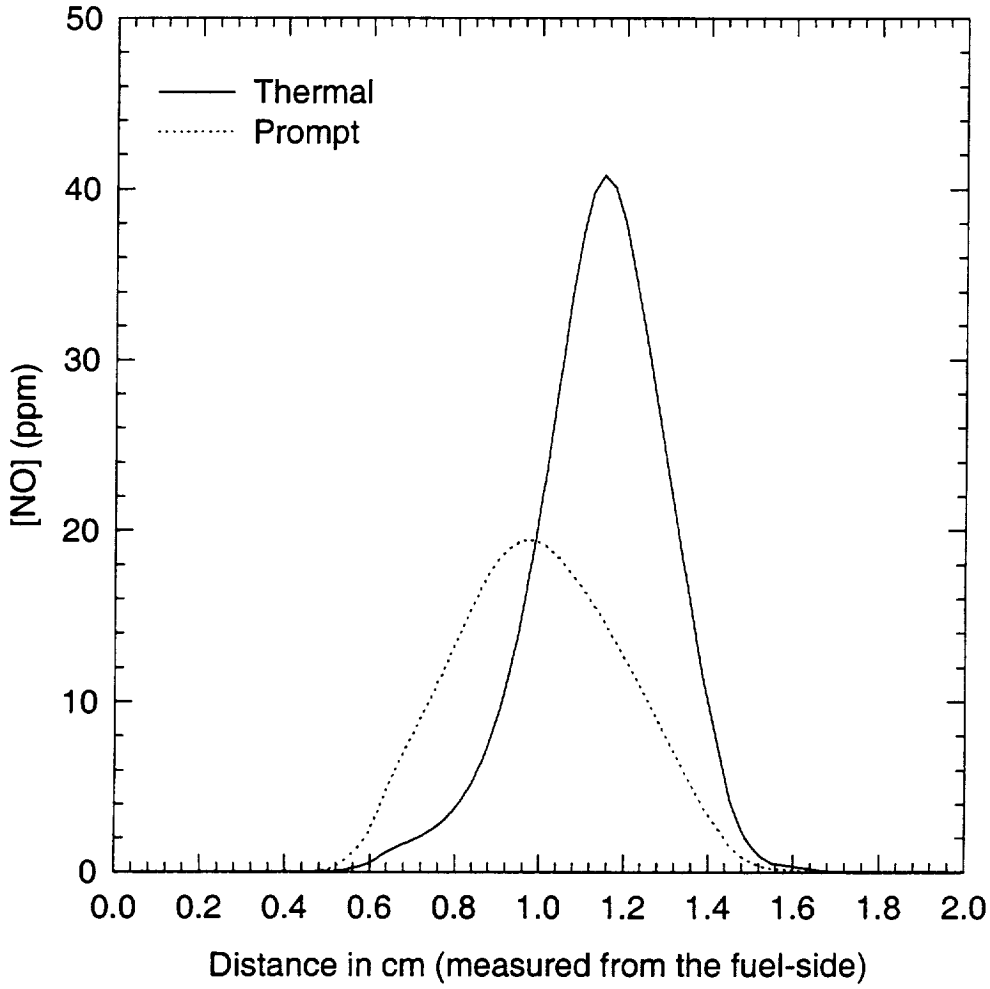

Figure 7.5: NO pathway analysis showing relative contribution of the prompt and thermal mechanisms in the flame with a fuel-side equivalence ratio of 1.45.

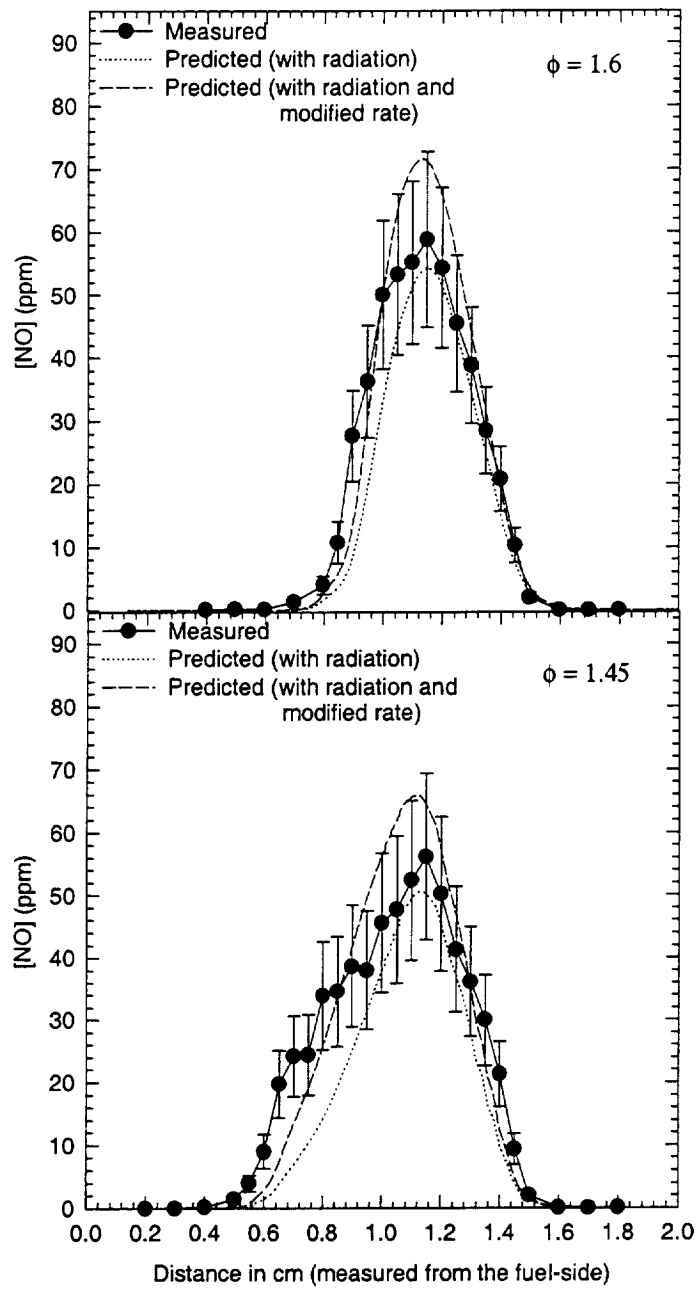

Figure 7.6: Comparison of LIF [NO] measurements and model predictions with radiation in the counterflow partially-premixed flames with fuel-side equivalence ratios of 1.45 and 1.6. The dotted line represents the predictions of the model with radiation using the GRI mechanism (version 2.11) in its original form. The dashed line represents the model with radiation using a modified rate coefficient for the prompt-NO initiation reaction.

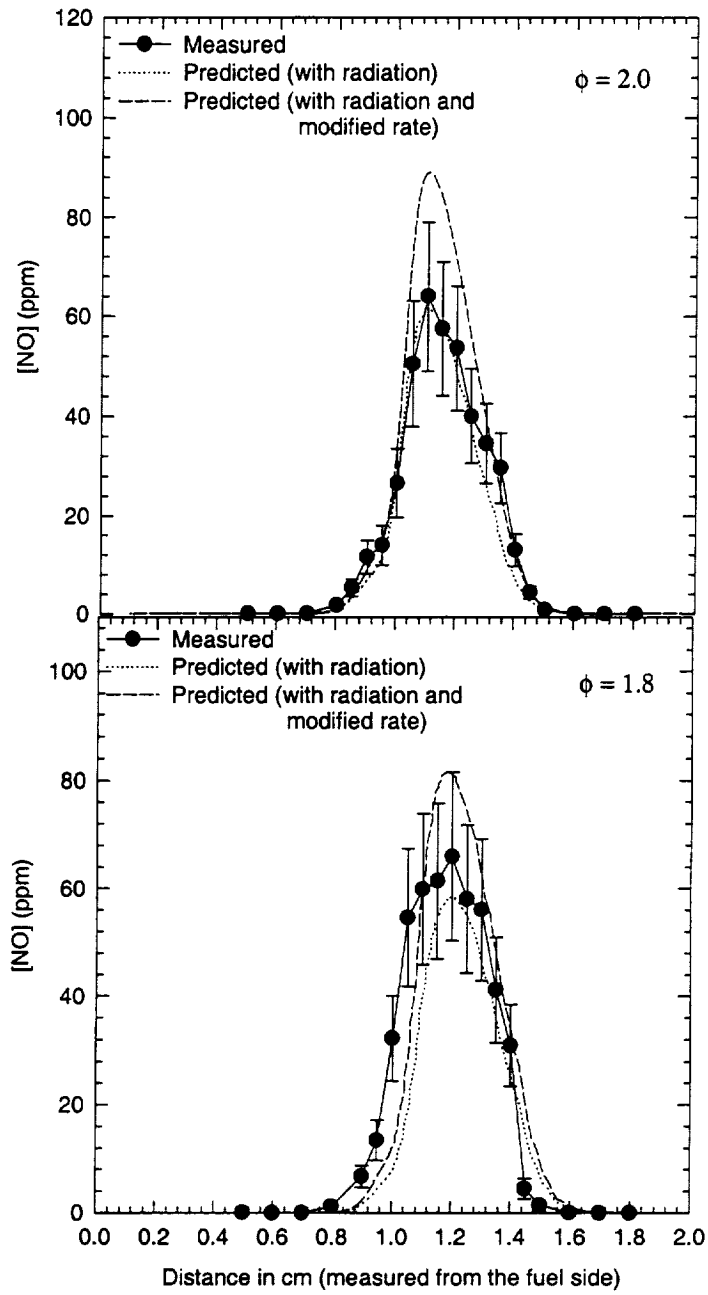

Figure 7.7: Comparison of LIF [NO] measurements and model predictions with radiation in the counterflow partially-premixed flames with fuel-side equivalence ratios of 1.8 and 2.0. The dotted line represents the predictions of the model with radiation using the GRI mechanism (version 2.11) in its original form. The dashed line represents the model with radiation using a modified rate coefficient for the prompt-NO initiation reaction.

and Laurendeau, 1999a). The effect of this rate coefficient, which was obtained by increasing the pre-exponential factor of the rate coefficient for $CH+N_2 \Leftrightarrow HCN+N$ by a factor of 2.1, is also shown in Figs. 7.6 and 7.7. The predictions with the modified rate coefficient show a significantly improved level of agreement with measurements in the region of the flames where prompt-NO dominates. While this improvement is particularly noteworthy in the region from 0.6 to 0.9 cm in the ϕ_B=1.45 flame, the improvement is not so obvious in the other flames mainly because the regions where prompt-NO and thermal-NO dominate are not as spatially separated as in the ϕ_B=1.45 flame. Unfortunately, a slight but consistent overprediction now occurs in the peak [NO] region. Since the prompt-NO initiation reaction involves the attack of the CH radical on N_2, any discrepancy in the rates of CH formation and destruction will have a significant impact on NO predictions. Recent shock-tube measurements of CH concentration at high temperatures for fuel-rich methane oxidation showed significant deviations from GRI model predictions (Woiki et al., 1998). Thus, the slight but consistent overprediction of peak [NO] using the modified rate coefficient may be attributed to a lack of refinement in the CH-chemistry of the GRI mechanism.

7.5 Conclusions

Quantitative LIF measurements of [NO] have been obtained along the centerline in atmospheric pressure, methane-air, counterflow partially-premixed flames with fuel-side equivalence ratios of 1.45, 1.6, 1.8 and 2.0. These LIF measurements of [NO] in counterflow partially-premixed flames represent the first reported measurements of [NO] in such flames. Comparisons of LIF measurements with model predictions using the GRI mechanism (version 2.11) yielded good agreement. The agreement is further improved by employing an optically thin model to account for radiative heat loss. Subsequent predictions fall within 10% of measurements at peak [NO] locations. Spatial separation was observed between regions where prompt-NO and thermal-NO dominate in the ϕ_B=1.45 flame. A modified rate coefficient for the $CH+N_2 \Leftrightarrow HCN+N$ reaction based on

previous work in counterflow diffusion flames improved agreement between predictions and measurements for counterflow partially-premixed flames in regions dominated by prompt-NO.

8. LIF MEASUREMENTS AND MODELING OF NITRIC OXIDE IN HIGH-PRESSURE COUNTERFLOW DIFFUSION FLAMES

8.1 Introduction

To achieve the goal of making quantitative [NO] measurements at AST conditions, a need exists to obtain [NO] measurements in nonpremixed flames at high pressure. High-pressure LIF measurements of NO have been made in premixed flames in the past (Reisel et al., 1993; Reisel and Laurendeau, 1994; Battles et al., 1994; Thomsen et al., 1997), but no previous [NO] measurements have been obtained in diffusion flames at high pressure. There has been only one study concerning the formation of NO in counterflow diffusion flames at high pressure (Bonturi et al., 1997), and that has been numerical in nature. Bonturi et al. (1997) performed computations of methane-air counterflow diffusion flames at pressures up to 30 atm and strain rates up to 1000 s^{-1}. They found that NO_x emissions increased with an increase in pressure and a decrease in strain rate. The dominant pathway for NO formation was found to be the prompt mechanism, especially at low pressures and high strain rates. In this chapter, we present LIF measurements and modeling of [NO] in counterflow diffusion flames at 2 to 5 atm. Preliminary LIF measurements of [NO] in counterflow diffusion flames at 6-12 atm are presented in Appendix D.

8.2 Experimental Techniques

We begin with a brief description of the experimental facility used in the LIF measurements. Excitation of NO is achieved through use of the $Q_2(26.5)$ transition within the $\gamma(0,0)$ band. The excitation wavelength is generated by employing the second

harmonic (λ= 532 nm) of a Quanta-Ray DCR-3G Nd:YAG laser to pump a PDL-2 dye laser, which provides visible radiation at approximately 572 nm. The dye fundamental is frequency-doubled ($\lambda/2 \approx 286$ nm) in a WEX-1 wavelength extender and the residual Nd:YAG fundamental is frequency-mixed with the dye second harmonic to produce a mixed beam at ~226 nm. The four concentric beams (1064, 572, 286, 226 nm) are dispersed using a Pellin-Broca prism, and the mixed beam exits the WEX vertically polarized.

After leaving the laser system, the beam is directed over a 1-cm counterflow burner designed for use in the high-pressure combustion facility described by Carter et al. (1989). The pressure vessel has four optical ports, two of which provide optical access for the laser beam through the combustion facility. The spot size produced by the optical arrangement is ~250 μm. Before entering the vessel, the beam passes through a fused silica plate, which directs a portion of the beam toward a UV-sensitive photodiode. The beam energy monitored using this photodiode is used to correct the LIF signal for variations in beam energy.

For detection, a portion of the isotropically emitted fluorescence is captured and the collimated beam is focused onto the entrance slit of a 1-m monochromator. The detector is a Hamamatsu R108UH-HA photomultiplier tube which is optimized for temporal resolution of the fluorescence signal (Harris et al., 1976). The broadband fluorescence signal encompasses a spectral width of ~3 nm and is detected over a spectral region centered at ~236 nm, corresponding to the $\gamma(0,1)$ band of NO. Each data point is averaged over 600 laser shots.

The burner used in this study was designed and fabricated specifically for the high-pressure facility in our laboratory. Figure 8.1 shows a schematic of the burner. It is entirely made from stainless steel so as to withstand corrosion in the high-temperature, high-moisture environment inside the pressure vessel. The counterflow burner system consists of two identical burners mounted on two plates and facing each other. The top plate was moved relative to the bottom plate by means of a ball screw which was fixed to

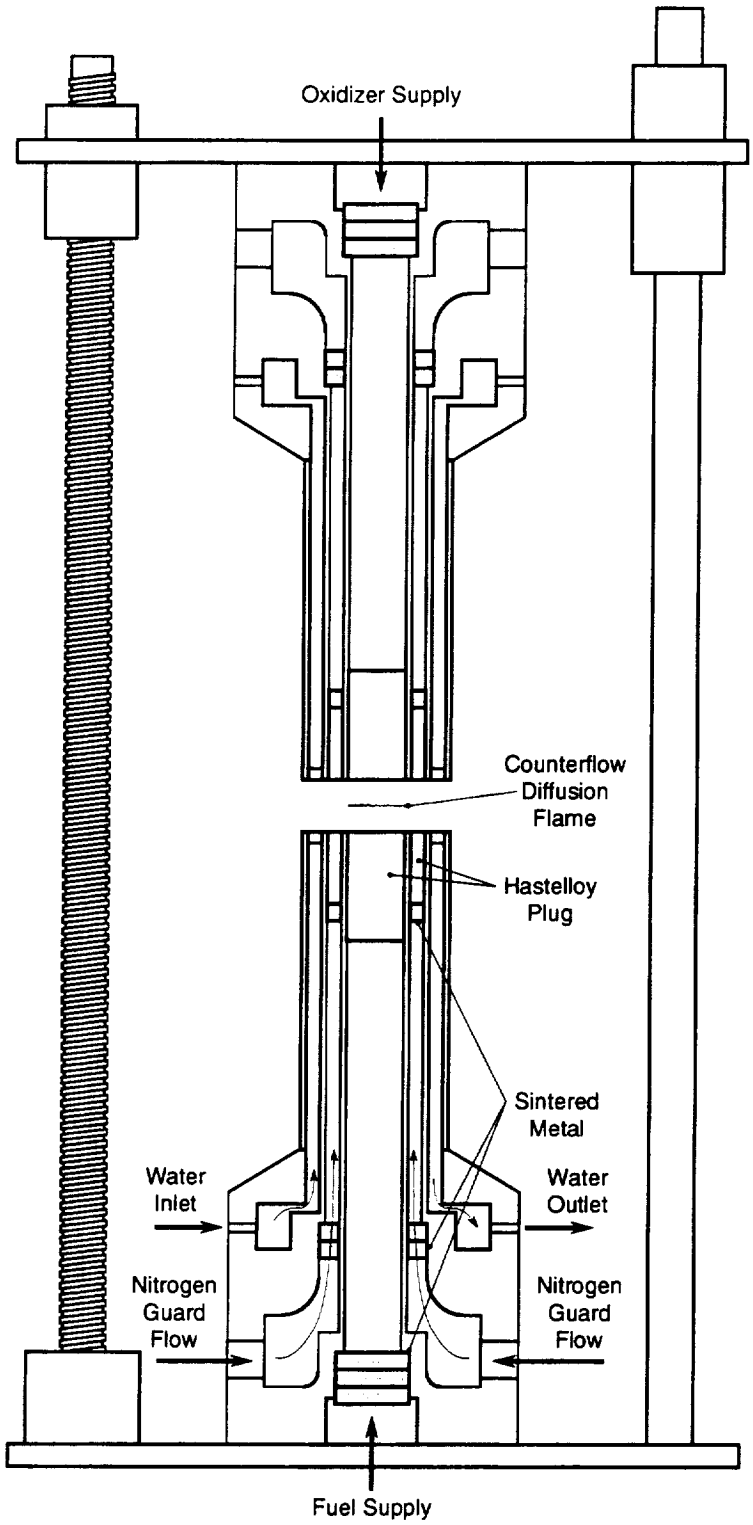

Figure 8.1: Schematic of the counterflow burner used in the high-pressure LIF studies of NO.

the bottom plate. For stability, two shafts in addition to the ball screw were fixed vertically on the bottom plate. Bearings provided in the top plate allowed free movement of the top plate over the shafts. The relative movement of the top plate with respect to the bottom plate permitted variation of the distance between the two burners.

Each burner consists of a 1-cm i.d. inner tube surrounded by a 1.68-cm i.d. outer tube. The fuel or air is introduced through the inner tube, while the annular region between the tubes is used to provide a nitrogen guard flow which helps in isolating the combustion environment from extraneous air currents. Since guard flow is provided in both directions, minimal influence of the external flow field is ensured on the flame. Furthermore, the guard flow rate is adjusted so that the velocity of the guard flow always matches that of the fuel and air. Multiple disks of sintered metal are placed within both tubes to avoid radial and circumferential gradients in the flow. Hastelloy honeycomb disks are placed at the end of the tubes to provide a uniform velocity profile at the exit of the burners. The outer tube is surrounded by an annular region in which water is circulated to cool the burner. A high-pressure pump is used to maintain sufficient flow of water at high vessel pressures. In addition, a heater is used to maintain the temperature of the cooling water high enough to avoid condensation on the surface of the burners.

The methane-air counterflow diffusion flames studied here are highly diluted, with the fuel stream consisting of 75% N_2 and 25% CH_4 by volume. This dilution avoids soot and minimizes the influence of radiative heat loss on NO formation. The low temperatures in these flames cause NO to be formed mainly through the prompt-NO pathway, enabling us to focus on prompt-NO chemistry. The global strain rate, defined here as the sum of the oxidizer and fuel stream velocities divided by the nozzle separation distance, is varied from 15 s^{-1} to 40 s^{-1} at pressures of 3 and 4 atm. In comparison, LIF measurements at 2 and 5 atm are varied over global strain rates of 20 s^{-1} to 40 s^{-1}. At a pressure of 2 atm, a strain rate of 15 s^{-1} causes soot formation. This result is consistent with recent experimental studies on sooting limits in methane-air counterflow diffusion flames (Sung et al., 1998). The 15 s^{-1} flame at 5 atm tended to blow out periodically and hence was not studied further. In general, it is difficult to experimentally stabilize a low-strain rate flame,

especially at higher pressures. The strain rates selected for this study represent essentially the entire range up to extinction, since for the fuel dilution selected, extinction occurs at a global strain rate of approximately 45 s^{-1} over our pressure range. The separation distance of the two 1-cm diameter burners was maintained at 1 cm in all cases. The flow rates for all flame conditions are shown in Table 8.1.

Table 8.1 Gas flow rates for all flame conditions

PRESSURE (ATM)	STRAIN RATE (S^{-1})	FUEL STREAM		AIR STREAM	
		CH_4 (SLPM)	N_2 (SLPM)	O_2 (SLPM)	N_2 (SLPM)
2.02	20	0.238	0.714	0.200	0.752
2.02	30	0.357	1.071	0.300	1.128
2.02	40	0.476	1.428	0.400	1.503
3.04	15	0.269	0.806	0.226	0.848
3.04	20	0.358	1.075	0.301	1.131
3.04	30	0.537	1.612	0.451	1.697
3.04	40	0.716	2.149	0.602	2.262
4.06	15	0.359	1.076	0.301	1.133
4.06	20	0.478	1.435	0.402	1.511
4.06	30	0.718	2.153	0.603	2.266
4.06	40	0.957	2.870	0.804	3.022
5.08	20	0.599	1.796	0.503	1.890
5.08	30	0.898	2.693	0.754	2.836
5.08	40	1.197	3.591	1.006	3.781

8.3 Results and Discussion

Using the above techniques, LIF measurements of NO were obtained in high-pressure counterflow methane-air flames. A new calibration procedure, based on a previous NO doping technique developed in our laboratory (Reisel et al., 1993), was used to calibrate the fluorescence signals (Thomsen and Laurendeau, 1999). This technique involved doping different levels of NO, with equal amounts into one and then into the other premixed stream of a $\phi = 0.7$ counterflow premixed flame, and measuring the corresponding fluorescence voltages in the burnt-gas region at each pressure. A calibration plot was obtained from these different doping levels, which was then applied to the fluorescence signals from the counterflow diffusion flames at a given pressure. We

assumed both that the doped NO does not react as it passes through the flame, and that summing the signals obtained from doping into each stream contributed the same amount of signal as doping into both sides simultaneously. These assumptions were supported both by computer modeling and by the linearity of the resulting calibration plot (Thomsen and Laurendeau, 1999). Measurements of the fluorescence signal using an offline excitation wavelength also confirmed that the contribution to the signal from non-NO interferences was negligible (<1%) in the counterflow premixed flames used for calibration over our range of pressures. The NO concentration in ppm relative to the calibration flame temperature can then be determined from

$$N_{ppm,RT} = C_F S_F \,, \tag{8.1}$$

where C_F is a calibration factor determined from the slope of the fit to the calibration data and S_F is the digital fluorescence signal.

We have previously developed and applied a quenching correction technique in counterflow diffusion flames at atmospheric pressure that has yielded satisfactory results (Ravikrishna et al., 1999). We have extended this technique to the high-pressure [NO] measurements presented in this chapter. The technique first involves modeling these flames using OPPDIF, a Sandia opposed-flow flame code (Lutz et al., 1996). The mathematical model reduces the two-dimensional, axisymmetric flow field to a one-dimensional formulation by using a similarity transformation. The model predicts species, temperature, and velocity profiles along the centerline in the core flow between the two burners. The GRI mechanism, version 2.11 (Bowman et al., 1995), containing 49 species and 277 reactions, can be used to handle the chemical kinetics. Once the major species are known from the OPPDIF model, quenching cross-sections from the literature (Paul et al., 1995) can be used to calculate the electronic quenching rate coefficient at each point along the centerline in the flame. The corrected NO number density in absolute ppm can then be obtained from

$$N_{ppm,abs} = \left(\frac{T}{T_c}\right)\left(\frac{f_B(T_c)}{f_B(T)}\right)\left(\frac{\Gamma_c}{\Gamma}\right)\left(\frac{Q_e}{Q_{e,c}}\right)N_{ppm,RT}\,, \tag{8.2}$$

where T is the flame temperature, T_c is the temperature of the calibration flame, f_B is the Boltzmann fraction, Γ is the local overlap fraction, Γ_c is the overlap fraction in the calibration flame, Q_e is the local electronic quenching rate coefficient, and $Q_{e,c}$ is the electronic quenching rate coefficient in the calibration flame. We have found that changes in the absorption coefficient, both from changes in the ground state Boltzmann distribution and from changes in the overlap fraction between the laser linewidth and the collisionally broadened NO spectrum, are less than 10% at 1000-2000 K for any given pressure up to 15 atm (Thomsen, 1999). Since nearly all of the NO in these flames is formed in high-temperature regions, such corrections were deemed unnecessary.

The effect of interferences at high pressure has also been assessed by comparing detection scans conducted in fuel-lean and fuel-rich regions in a counterflow diffusion flame at 5 atm, as shown in Fig. 8.2. The large feature at ~239 nm corresponds to the N_2-Raman line and is a common feature in both scans since nitrogen is present in large quantities in both the fuel and air streams. The feature at ~234.7 nm in the fuel-lean scan corresponds to an O_2 fluorescence line, and this feature is expectedly absent in the fuel-rich scan. NO fluorescence is detected in a 3-nm region from 235.3 nm to 238.3 nm, thereby avoiding the above mentioned interferences. As indicated previously, the extent of O_2 interferences has been assessed to be negligible (<1%) using an off-line excitation technique over our range of pressures. The only concern was the effect of interferences from polycyclic aromatic hydrocarbons (PAHs) in the fuel-rich region of the diffusion flames. By employing the fuel-lean detection scan as a reference, the regions under the normalized curves in the 3-nm detection window can be compared for fuel-rich vs. fuel-lean conditions. Based on this approach, the extent of interferences from PAHs was found to be less than 10% at the maximum pressure of 5 atm.

Figure 8.3 shows a comparison of measured and predicted [NO] for the 2-atm flames with strain rates of 20 s^{-1}, 30 s^{-1} and 40 s^{-1}. As expected, the measured [NO] decreases with an increase in strain rate. This result is mainly due to a decline in residence time in high temperature zones (Drake and Blint, 1989; Nishioka et al., 1994). Since the peak temperature decreases with an increase in strain rate, there is also a reduction in the

net NO production rate. In addition, the width of the NO profile becomes narrower with an increase in strain rate owing to the increased velocity gradients. From Fig. 8.3, we see that the GRI mechanism underpredicts [NO] in these flames. A pathway analysis indicates almost no thermal-NO for these flames so that the dominant contribution to NO formation is through the prompt mechanism. Hence, more specifically, the GRI mechanism underpredicts production of prompt-NO at this pressure. This result is entirely consistent with our previous observations made in atmospheric pressure counterflow diffusion flames (Ravikrishna et al., 1999; Ravikrishna and Laurendeau, 1999a).

Figure 8.4 shows a comparison of [NO] measurements with modeling for the 3-atm flames at strain rates of 15, 20, 30 and 40 s^{-1}. The [NO] measurements show the same variation with strain rate at this pressure as at 2 atm. The measured peak [NO] increases from 2 to 3 atm at each strain rate. The GRI mechanism again underpredicts [NO]; however, the discrepancy between measurements and predictions is higher at 3 atm than at 2 atm. The [NO] measurements at 4 atm are compared with predictions for strain rates of 15, 20, 30, and 40 s^{-1} in Fig. 8.5. The GRI mechanism still underpredicts [NO] although a reversal of trend occurs regarding the variation of peak measured [NO] with pressure. The peak measured [NO] decreases from 3 to 4 atm at all strain rates.

Figure 8.6 shows a final comparison between measured and predicted [NO] for the 5-atm flames at strain rates of 20, 30 and 40 s^{-1}. The decrease of peak measured [NO] continues from 4 to 5 atm. It is interesting to note that although the GRI mechanism still underpredicts [NO] at 5 atm, the discrepancy between measurements and predictions decreases from 3 to 5 atm. Overall, the variation of measured [NO] with pressure in these flames is unique and has not been reported previously. Unfortunately, the GRI mechanism in its current form does not predict this trend of peak [NO] with pressure. In fact, at a given strain rate, the predicted peak [NO] appears to be nearly constant at pressures from two to five atm.

Error bars in Figs. 8.3-8.6 are provided only at the peak [NO] location to avoid clutter in the figures. An error analysis (see Appendix B) gives a typical relative error at the 95% confidence level of ~19%. All experimental data are tabulated in Appendix C.

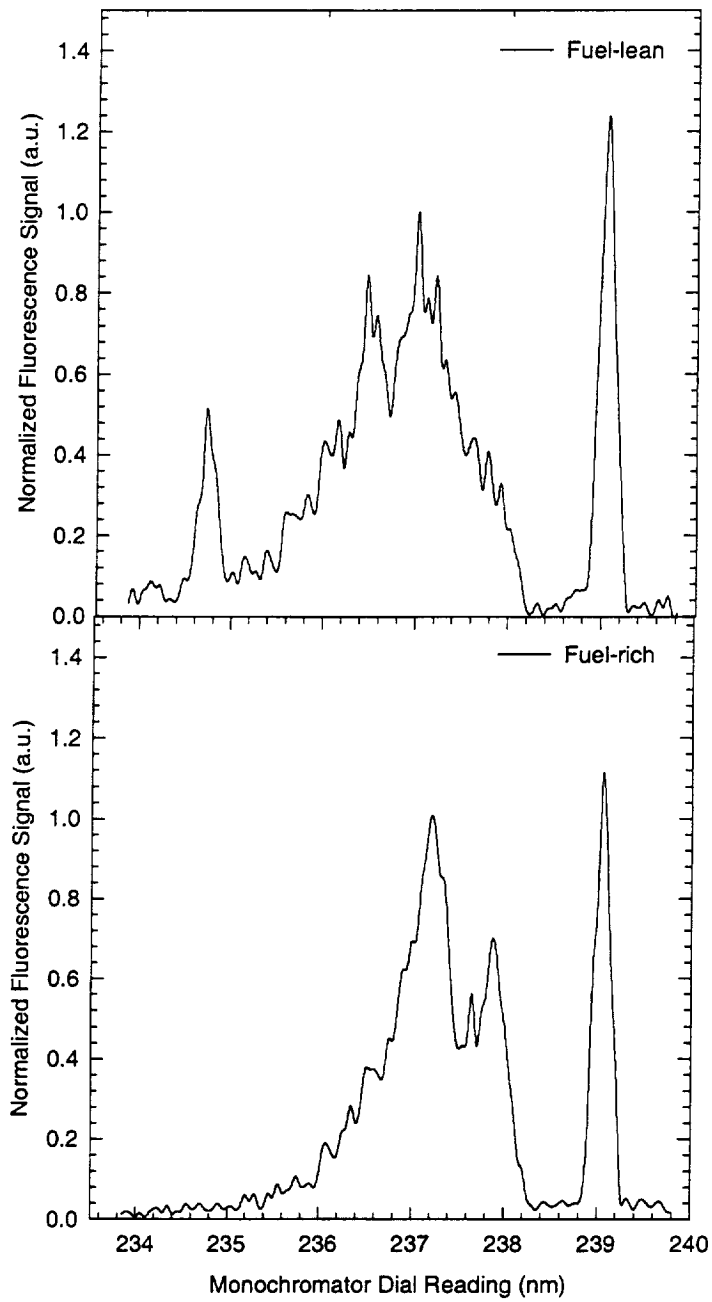

Figure 8.2: Detection scans obtained in fuel-lean and fuel-rich regions of a counterflow diffusion flame at 5 atm.

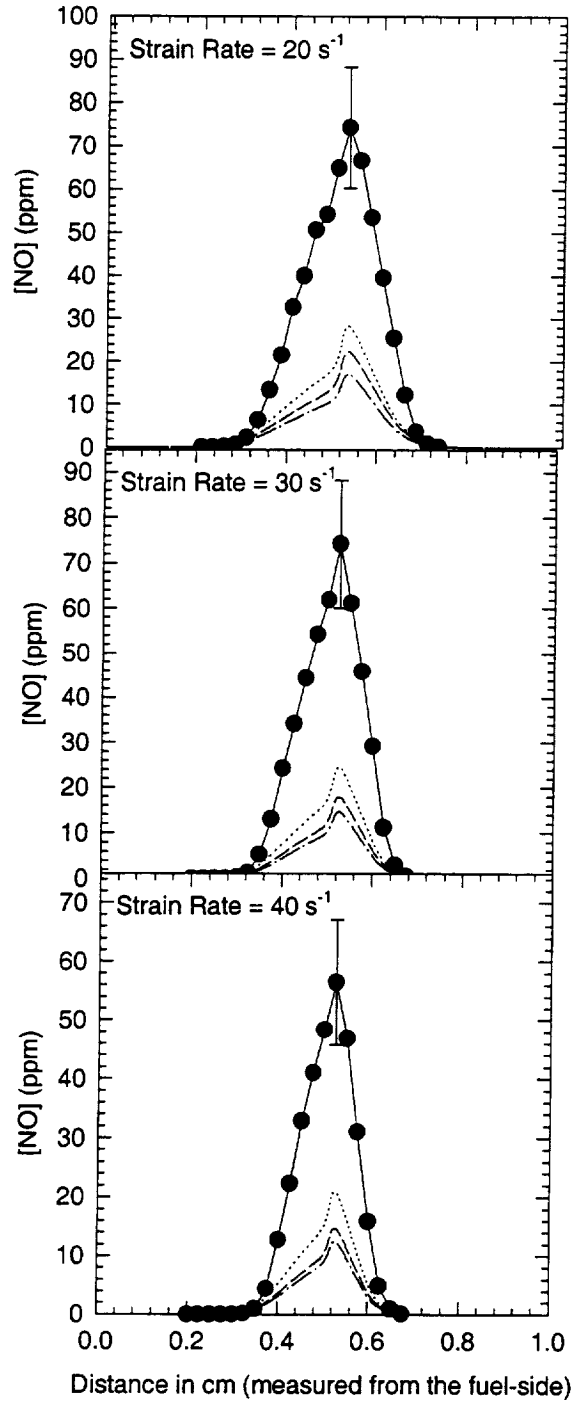

Figure 8.3: LIF measurements of NO vs. modeling in methane-air counterflow diffusion flames at 2 atm and global strain rates of 20, 30 and 40 s^{-1}. The dashed line indicates modeling using the GRI mechanism (version 2.11). The dash-and-dot line represents modeling using the modified OPPDIF code that accounts for radiative heat loss. The dotted line indicates modeling accounting for radiative heat loss when using a modified rate coefficient for the prompt-NO initiation reaction.

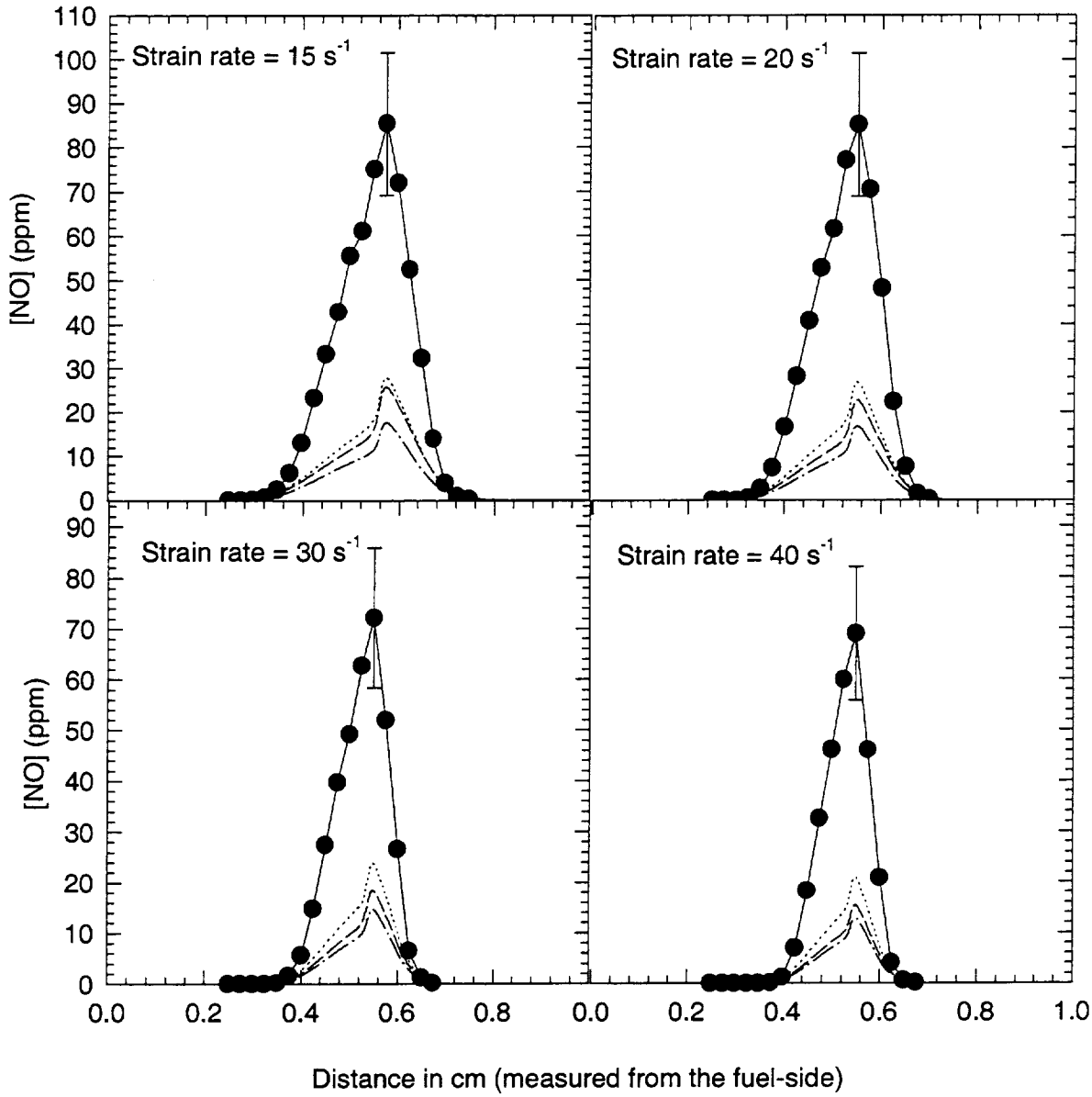

Figure 8.4: LIF measurements of NO vs. modeling in methane-air counterflow diffusion flames at 3 atm and global strain rates of 15, 20, 30 and 40 s^{-1}. The dashed line indicates modeling using the GRI mechanism (version 2.11). The dash-and-dot line represents modeling using the modified OPPDIF code that accounts for radiative heat loss. The dotted line indicates modeling accounting for radiative heat loss when using a modified rate coefficient for the prompt-NO initiation reaction.

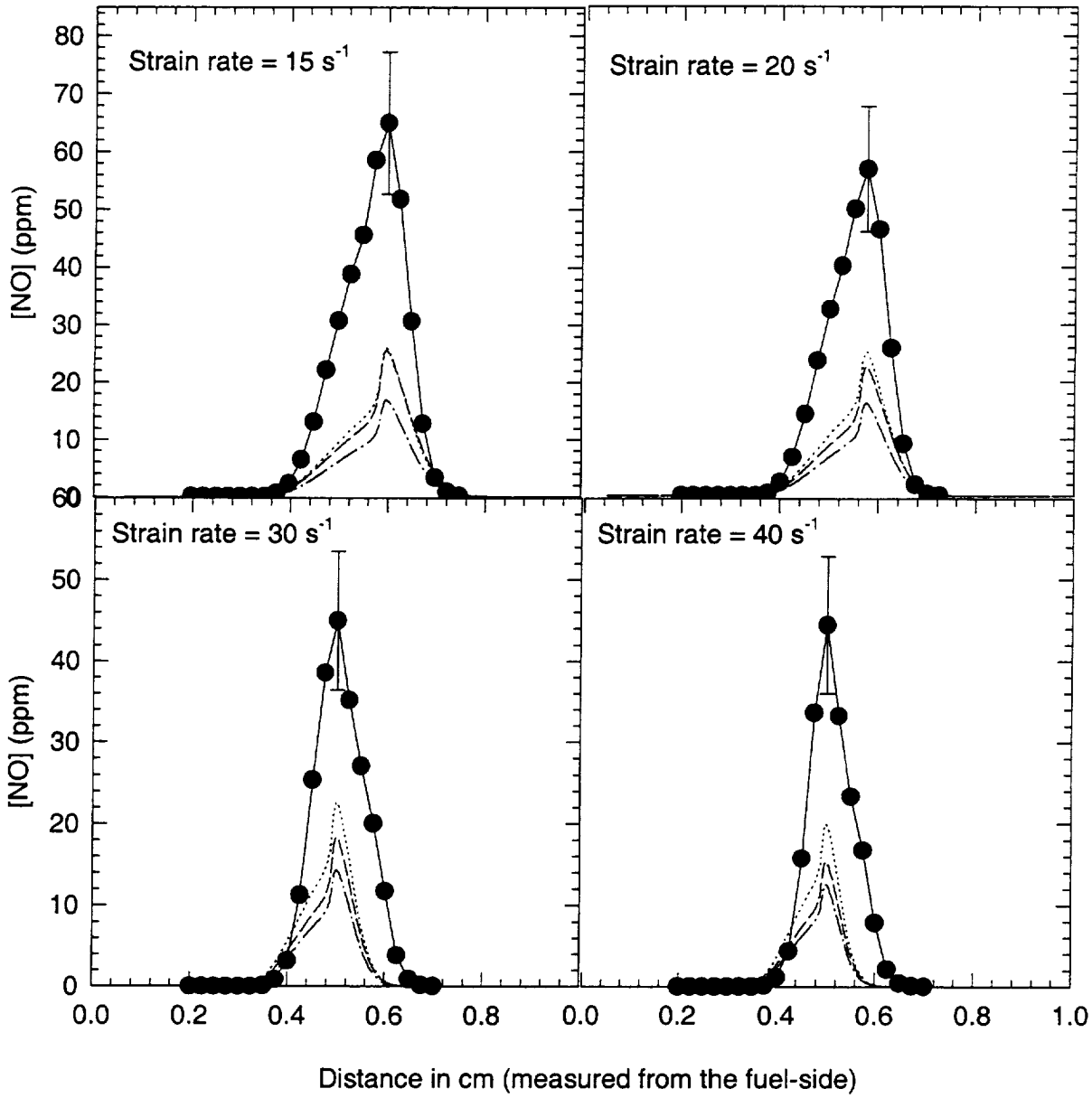

Figure 8.5: LIF measurements of NO vs. modeling in methane-air counterflow diffusion flames at 4 atm and global strain rates of 15, 20, 30 and 40 s^{-1}. The dashed line indicates modeling using the GRI mechanism (version 2.11). The dash-and-dot line represents modeling using the modified OPPDIF code that accounts for radiative heat loss. The dotted line indicates modeling accounting for radiative heat loss when using a modified rate coefficient for the prompt-NO initiation reaction.

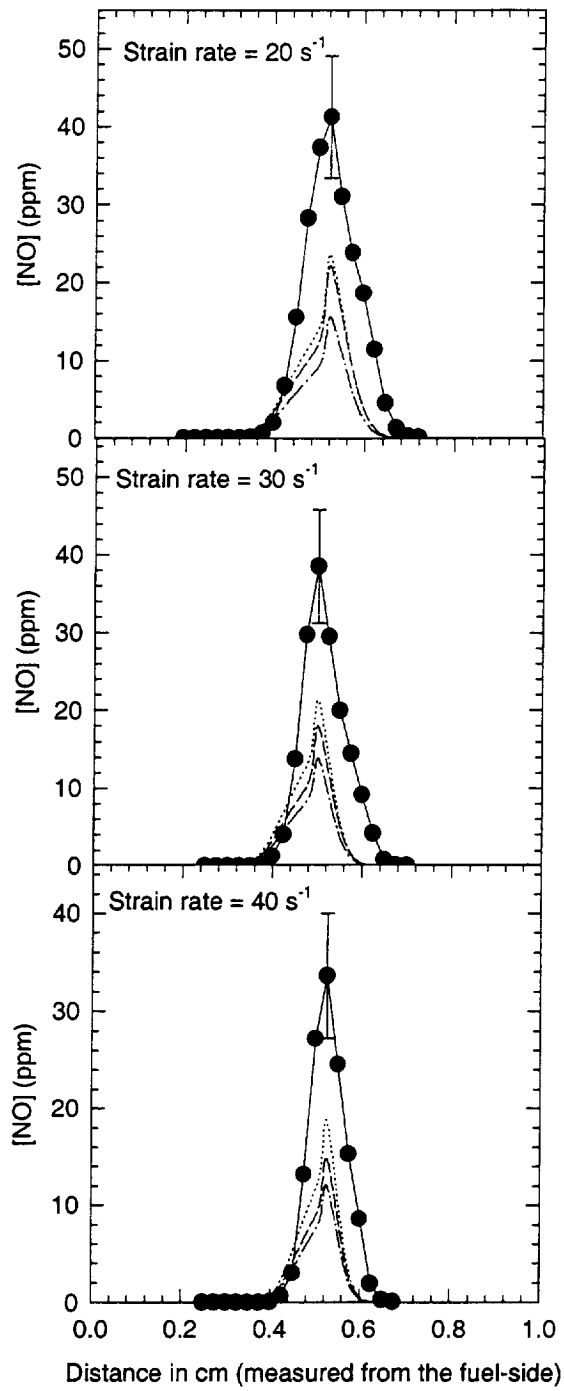

Figure 8.6: LIF measurements of NO vs. modeling in methane-air counterflow diffusion flames at 5 atm and global strain rates of 20, 30 and 40 s^{-1}. The dashed line indicates modeling using the GRI mechanism (version 2.11). The dash-and-dot line represents modeling using the modified OPPDIF code that accounts for radiative heat loss. The dotted line indicates modeling accounting for radiative heat loss when using a modified rate coefficient for the prompt-NO initiation reaction.

Our observed variation of [NO] with pressure may at first seem contrary to the predictions of Bonturi et al. (1997). They observed that at a constant strain rate, the computed [NO] increases with pressure uniformly from 1 to 30 atm. However, their study involved undiluted fuel and preheated air, and hence peak temperatures were between 2000 and 2500 K. Although prompt-NO was found to be dominant in their flames, a significant contribution also existed from thermal-NO owing to these high flame temperatures. Even if the prompt-NO contribution were to decrease with pressure, the increase in thermal-NO with pressure would more than compensate for this reduction, leading to an overall increase in [NO] with pressure. In our flames, on the other hand, there is almost no contribution from thermal-NO. A pathway analysis indicates that the contribution from thermal-NO is less than 9% at the peak [NO] locations. Hence, our observations refer specifically to the variation of prompt-NO, and thus are not contrary to the predictions of Bonturi et al. (1997).

To account for any radiative heat loss, we employed a modified version of the OPPDIF code (Gore et al., 1999). Radiation heat loss is calculated in the optically thin limit using Planck mean absorption coefficients for CO_2, H_2O, CO, and CH_4. The temperature dependence of the Planck mean absorption coefficients is considered using fourth-order polynomial fits to the results of narrow band calculations. Predictions of [NO] accounting for radiative heat loss for all flames are also shown in Figs. 8.3-8.6. Figure 8.7 shows the decrease in predicted [NO] owing to radiative heat loss at each pressure at a constant strain rate of 20 s^{-1}. It is interesting to note that a modest decrease in temperature owing to radiative heat loss causes a significant drop in predicted [NO]. For example, at 5 atm and a strain rate of 20 s^{-1}, a temperature drop of 46 K causes the peak predicted [NO] to decrease by 30%. This indicates that the prompt-NO chemistry is quite sensitive to temperature, although not as much as for thermal-NO.

We observed in our previous work that a modified rate coefficient for the prompt-NO initiation reaction significantly improved agreement between [NO] predictions and LIF measurements for prompt-NO dominated counterflow diffusion flames at atmospheric pressure (Ravikrishna and Laurendeau, 1999a). The effect of this rate coefficient, which

was obtained by increasing the pre-exponential factor of the rate coefficient for $CH+N_2 \Leftrightarrow HCN+N$ by a factor of 2.1, is also included in Figs. 8.3-8.6. In this case, modification of the prompt-NO initiation reaction is not sufficient to match the predictions with the measurements. Figure 8.8 shows the comparison between peak measured and predicted [NO] as a function of pressure from one to five atm, at a constant strain rate of 40 s^{-1}. Although the atmospheric pressure result was obtained using a different counterflow burner at a slightly different strain rate (Ravikrishna and Laurendeau, 1999a), it is nevertheless included here to aid in comparison. The predicted [NO] in Fig. 8.8 corresponds to predictions with the modified rate coefficient for the prompt-NO initiation reaction. We note that the peak predicted [NO] increases from 1 to 2 atm and then decreases from 2 to 5 atm, although this result is not very apparent owing to the magnified scale. Thus, the GRI mechanism with the modified prompt-NO initiation reaction does at least qualitatively predict the experimentally observed trend between peak [NO] and pressure at a given strain rate.

As mentioned before, modifying the rate coefficient of the prompt-NO initiation reaction is not sufficient to match the [NO] predictions with measurements. Since the prompt-NO initiation reaction involves the attack of the CH radical on N_2, any mistake in the rates of CH formation and destruction will have a significant impact on the NO predictions. The variation of peak predicted CH concentration ([CH]) with pressure is shown in Fig. 8.9. Peak [CH] decreases rapidly from one to three atm by a factor of three. A further decrease occurs from three to five atm, although this decrease is more gradual. The peak [CH] is starting to show asymptotic behavior at 5 atm. Recall from Figs. 8.3-8.6 that the discrepancy between [NO] measurements and predictions is at its maximum at 2 to 3 atm. Similarly, the biggest drop in peak [CH] occurs between 1 and 3 atm. Furthermore, the agreement between [NO] measurements and predictions begins to improve at 4 to 5 atm, with the peak [CH] beginning to stabilize at these pressures. This result strongly suggests that there is a need for refinement of the CH chemistry, especially for those CH formation and destruction reactions that are pressure dependent.

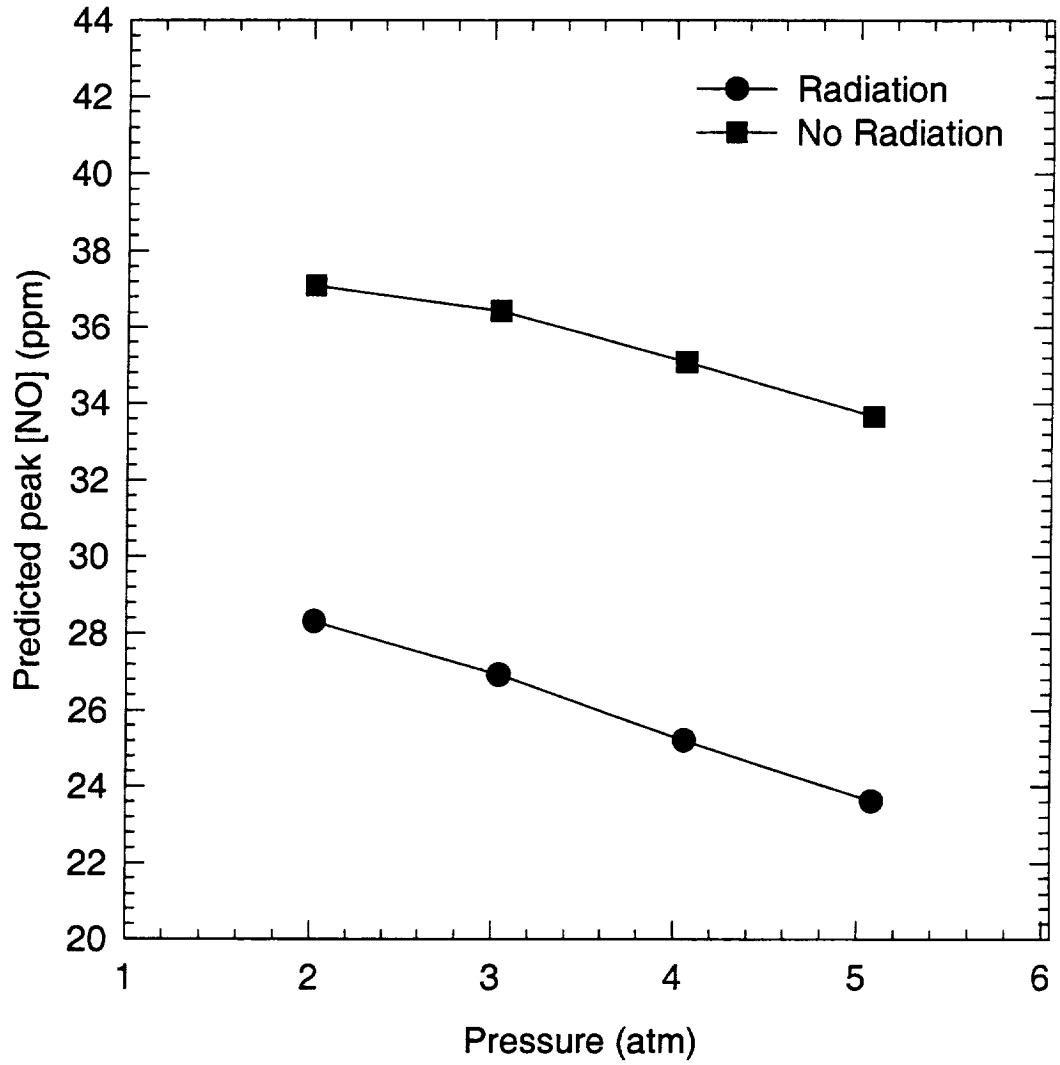

Figure 8.7: Effect of radiative heat loss on predicted peak [NO] as a function of pressure. The predictions shown here correspond to a strain rate of 20 s^{-1} and are obtained using the modified rate coefficient for the prompt-NO initiation reaction.

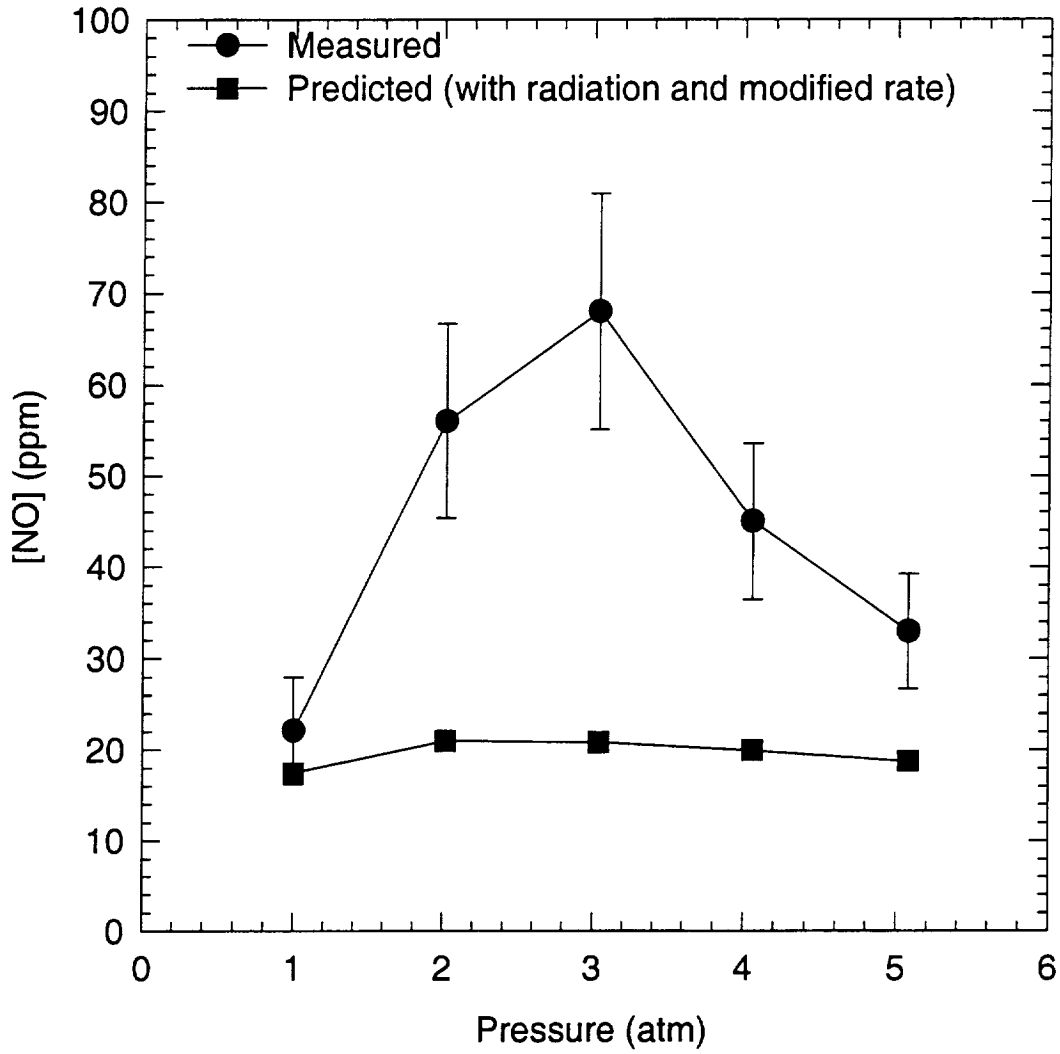

Figure 8.8: Variation of peak measured and predicted [NO] as a function of pressure at a strain rate of 40 s^{-1}. The predictions are obtained using the modified rate coefficient for the prompt-NO initiation reaction. The atmospheric pressure datum was obtained using a different counterflow burner at a slightly different strain rate, but has been included here to aid in comparison.

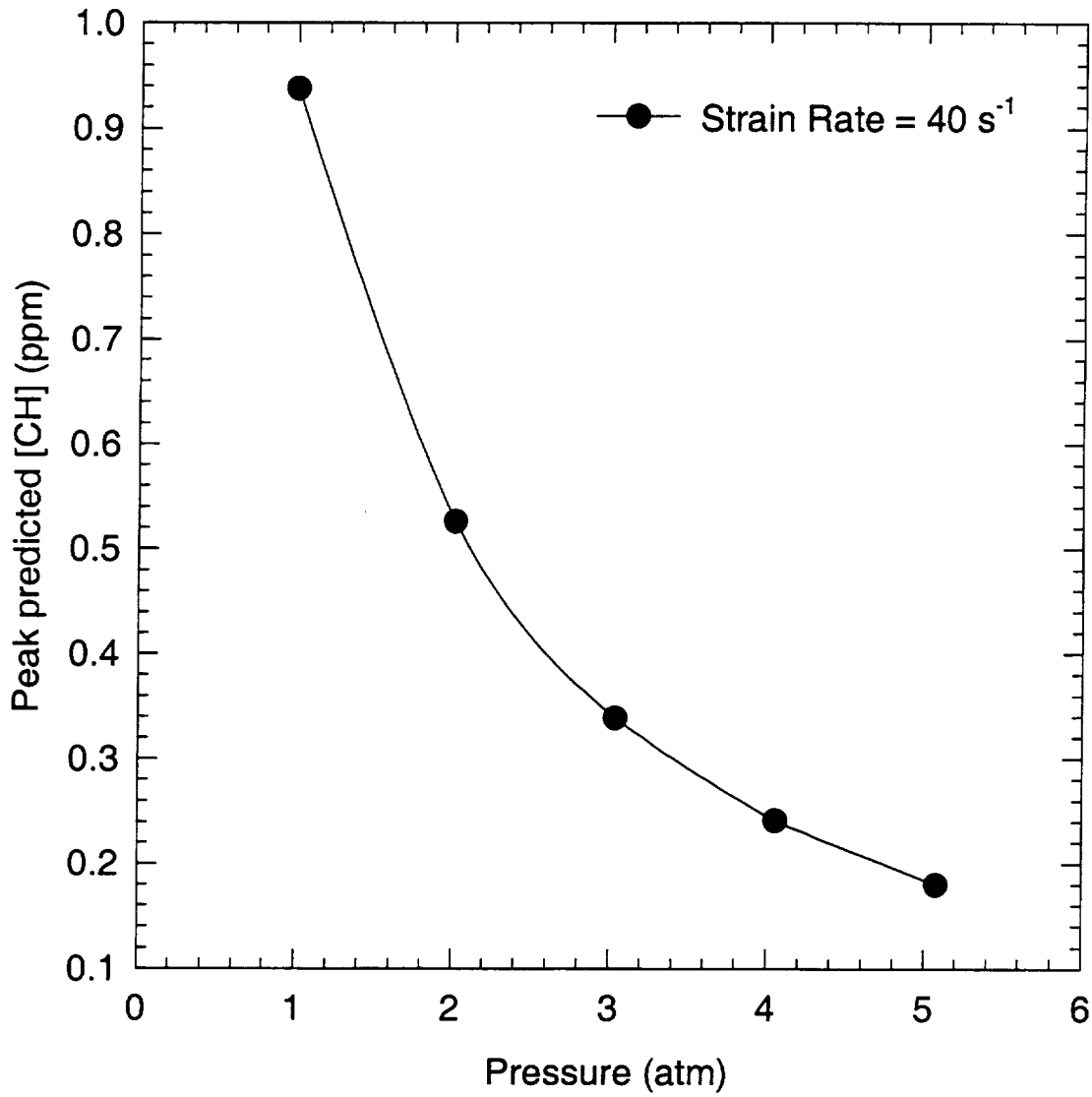

Figure 8.9: Variation of peak predicted CH concentration as a function of pressure. The predictions correspond to a strain rate of 40 s^{-1}.

8.4 Conclusions

Quantitative laser-induced fluorescence (LIF) measurements of NO concentration ([NO]) have been obtained along the centerline of prompt-NO dominated, methane-air counterflow diffusion flames at two to five atm. Global strain rates of 20, 30 and 40 s^{-1} were investigated at each pressure, with the addition of a 15 s^{-1} case at three and four atm. The LIF data presented here represent the first reported measurements of [NO] in counterflow diffusion flames at high pressure. Comparisons between [NO] measurements and predictions using the GRI (version 2.11) mechanism show that the GRI mechanism underpredicts prompt-NO by a factor of two to three at all pressures. The underprediction is maximum at 2 to 3 atm, and decreases with pressure from 3 to 5 atm. Although the GRI mechanism does not predict this trend, predictions with a modified rate coefficient for the prompt-NO initiation reaction displays the same qualitative behavior. However, modifying the rate coefficient for the prompt-NO initiation reaction is not sufficient to account for the difference between measurements and predictions, thus indicating a need for refinement of the CH chemistry, especially the pressure-dependent CH formation and destruction reactions. A modest decrease in predicted temperature owing to radiative heat loss has been found to produce a significant (~30%) decrease in predicted [NO], thus indicating the temperature sensitivity of the prompt-NO kinetics. In general, the LIF [NO] measurements presented here form a database for validating chemical kinetic mechanisms at 2-5 atm and higher.

9. CONCLUSIONS AND RECOMMENDATIONS

9.1 Conclusions

Lean direct injection (LDI) is one strategy that is being considered to meet NASA's goal of reducing NO_x emissions from civilian aircraft engines by around 70% in the next ten years. LDI seeks rapid vaporization and mixing of liquid fuel with air at the entrance of the combustor. The initial mixing region leads to partially premixed flamelets which can produce high local levels of NO. The eventual performance of any future advanced subsonic transport (AST) will require *in situ* measurements of NO concentrations for various injector modules and combustor designs so as to optimize the final LDI system. Hence, a need exists for making quantitative measurements of NO number density at AST conditions for which pressures are in the range of 40-50 atm, and temperatures around 1800 K. The overall goal of this work, which is to assess the feasibility of making NO concentration measurements at AST conditions, was addressed by making quantitative laser-induced fluorescence (LIF) measurements of [NO] in counterflow diffusion and partially-premixed flames at atmospheric and higher pressures. In addition, the techniques developed here could be used to make [NO] measurements under practical gas turbine engine conditions.

Previous work concerning NO formation in counterflow diffusion flames consisted of a few investigations where NO concentrations were measured using physical probes. These measurements suffered from lack of spatial resolution and could at best be considered semi-quantitative since the probe tends to disturb the flow field. No previous nonintrusive measurements of NO were available in counterflow diffusion flames. The [NO] measurements in counterflow diffusion flames presented in this work represent the first reported nonintrusive measurements of [NO] in such flames. Moreover, the [NO]

measurements in the counterflow partially-premixed flames and the high-pressure counterflow diffusion flames represent the first reported [NO] measurements *of any kind* in such flames. Apart from assessing the feasibility of making quantitative [NO] measurements in nonpremixed flames, there are two important aspects regarding the contribution of this work. One is the diagnostic aspect wherein two laser-based techniques viz., laser-saturated fluorescence (LSF) and linear laser-induced fluorescence (LIF) were compared and assessed. This comparison also led to the development and validation of a correction technique to account for variations in the electronic quenching rate coefficient. The other aspect is the evaluation and suggested enhancement of the NO kinetics in a comprehensive chemical kinetic mechanism that describes natural gas combustion. Once a thorough understanding of the NO kinetics is achieved, this could be used further to develop a simplified, high-pressure NO_x model capable of predicting NO formation for practical gas turbine conditions.

Comparisons between laser-saturated fluorescence (LSF) and linear LIF measurements were made in four ethane-air counterflow diffusion flames with different strain rates to assess the efficacy of a quenching correction technique for the linear LIF measurements and to address issues regarding the quantitative nature of the LSF technique. The agreement between linear LIF and LSF measurements was found to be excellent from fuel-lean to moderately fuel-rich conditions. The slight but consistent discrepancy between the LSF and linear LIF measurements in the highly fuel-rich ($\phi > 1.6$) region may be attributed to a combination of the effect of rotational energy transfer (RET) on the LSF measurements and a lack of refinement in the quenching cross-sections of hydrocarbon species affecting the linear LIF measurements. In general, the quenching correction technique, which uses major-species concentrations from the OPPDIF predictions in conjunction with quenching correlations from the literature, is effective and can be extended to higher pressures.

Linear LIF measurements of [NO] in three methane-air counterflow diffusion flames with different strain rates were compared with OPPDIF model predictions using the GRI (version 2.11) chemical kinetic mechanism. These flames were highly diluted with

nitrogen on the fuel-side to avoid soot formation and the effects of radiative heat loss on NO production. This also caused the flame temperatures to be low, which enabled us to focus on the prompt-NO chemistry. The comparisons revealed that the GRI mechanism underpredicted prompt-NO by 30-50%. These results seem to indicate some shortcomings in the prompt-NO kinetics within the GRI mechanism, either in the CH formation and destruction chemistry or in the rate coefficient of the prompt-NO initiation reaction. Based on our data, we were able to propose a modified reaction rate coefficient for the prompt-NO initiation reaction which causes the predictions to match experimental data. The rate coefficient was modified by increasing the pre-exponential factor by a factor of 2.1. Temperature measurements were also made using thin SiC filament pyrometry. A new calibration method utilizing a near-adiabatic H_2-air Hencken flame was developed. The excellent agreement between temperature measurements and predictions in the methane-air counterflow diffusion flames indicates the efficacy of the new calibration method.

Quantitative LIF measurements of [NO] have been obtained in four methane-air counterflow partially-premixed flames. Comparisons of LIF measurements with model predictions using the GRI mechanism (version 2.11) yielded good agreement. The agreement is further improved by employing an optically thin model to account for radiative heat loss. Subsequent predictions fall within 10% of measurements at peak [NO] locations. Spatial separation was observed between regions where prompt-NO and thermal-NO dominate in the ϕ_B=1.45 flame. A modified rate coefficient for the $CH+N_2 \Leftrightarrow HCN+N$ reaction based on the previous work in counterflow diffusion flames improved agreement between predictions and measurements for counterflow partially-premixed flames in regions dominated by prompt-NO.

Quantitative laser-induced fluorescence (LIF) measurements of NO concentration ([NO]) have also been obtained along the centerline of prompt-NO dominated, methane-air counterflow diffusion flames at two to five atm. Comparisons between [NO] measurements and predictions using the GRI (version 2.11) mechanism show that the GRI mechanism underpredicts prompt-NO by a factor of two to three at all pressures. The

underprediction is maximum at 2 to 3 atm, and decreases with pressure from 3 to 5 atm. Although the GRI mechanism does not predict this trend, predictions with a modified rate coefficient for the prompt-NO initiation reaction display the same qualitative behavior. However, modifying the rate coefficient for the prompt-NO initiation reaction is not sufficient to account for the difference between measurements and predictions, thus indicating a need for refinement of the CH chemistry, especially the pressure-dependent CH formation and destruction reactions. In summary, the LIF [NO] measurements presented here form a database for validating chemical kinetic mechanisms at 1-5 atm and perhaps higher.

9.2 Recommendations

The calibration technique for the LIF [NO] measurements in the high-pressure counterflow diffusion flames involved doping NO into a counterflow premixed flame. With our current counterflow burner, we were unable to stabilize a counterflow premixed flame above a pressure of 5 atm owing to buoyancy effects. Since the [NO] measurements in the counterflow diffusion flames were calibrated using a counterflow premixed flame at the same pressure, we were limited to obtaining quantitative measurements at pressures below 5 atm. This was unfortunate, especially since we could stabilize counterflow diffusion flames even at 12 atm. The structure of the counterflow premixed flame was also affected by small nonuniformities in the flow exiting the nozzles. This was more apparent at pressures above 3 atm. These problems can be mitigated to some extent by employing a counterflow burner with contoured, convergent nozzles rather than the straight-tube nozzles used in our current design. This would minimize any boundary layer effects and would guarantee a uniform velocity profile at the exit of the nozzle, even at higher pressures.

Comparison of [NO] measurements with model predictions in the counterflow diffusion flames has indicated a lack of refinement in the CH chemistry, especially at higher pressures. Thus, there is need for CH concentration measurements in these flames

in order to assess the CH kinetics. Hence, it is recommended that CH concentrations be measured in both atmospheric and high-pressure counterflow diffusion and partially-premixed flames. Simultaneously, there is also a need to identify those reactions in the CH chemistry that are most sensitive with respect to NO formation. A sensitivity analysis can be conducted when such an option becomes routinely available with the OPPDIF code. Finally, the [NO] measurements obtained in this work can be used to assess any future version of the GRI chemical kinetic mechanism by comparison with model predictions.

LIST OF REFERENCES

LIST OF REFERENCES

Abdel-Khalik, S. I., Tamaru, T., and El-Wakil, M. M. (1975). "A chromatographic and interferometric study of the diffusion flame around a simulated fuel drop," *Fifteenth Symposium (International) on Combustion*, The Combustion Institute, Pittsburgh, 389-399.

Airco (1993). *Special Gases and Equipment, Airco Gases*, Murray Hill, NJ.

Atreya, A., Zhang, C., Kim, H. K.,Shamim, T., and Suh, J. (1996). "The effect of changes in the flame structure on the formation and destruction of soot and NO_x in radiating diffusion flames," *Twenty-Sixth Symposium (International) on Combustion*, The Combustion Institute, Pittsburgh, 2181-2189.

Battles, B. E., Seitzman, J. M., and Hanson, R. K. (1994). "Quantitative planar laser-induced fluorescence imaging of radical species in high pressure flames," *AIAA Paper 94-0029*. Thirty-second Aerospace Sciences Meeting, Reno, NV.

Berg, P. A., Smith, G. P., Jeffries, J. B., and Crosley, D. R. (1998). "Nitric oxide formation and reburn in low-pressure methane flames," *Twenty-Seventh Symposium (International) on Combustion*, The Combustion Institute, Pittsburgh, 1337-1384.

Bian, J., Vandooren, J., and Van Tiggelen, P. J. (1990). "Experimental study of formation of nitrous and nitric oxides in H_2-O_2-Ar flames seeded with NO and/or NH_3," *Twenty-third Symposium (International) on Combustion*, The Combustion Institute, Pittsburgh, 379-386.

Blevins, L. G., and Gore, J. P. (1999). "The computed structure of low strain rate partially-premixed CH_4/air counterflow flames: Implications for NO formation," *Combust. Flame* **116**, 546-566.

Bockhorn, H., Chevalier, C., and Weyrauch, V. (1991). "Experimental investigation and modeling of prompt-NO formation in hydrocarbon flames," *HTD* **166**, *Heat Transfer in Fire and Combustion Systems*, ASME, 11-16.

Bonturi, S., Pourkashanian, M., Williams, A., Oskam, G., and Wilson, C. (1997). "NO_x formation in counter-flow opposed-jet diffusion CH_4/air flames," *Combust. Sci. Tech.* **121**, 217-233.

Bowman, C. T., Hanson, R. K., Davidson, D. F., Gardiner, Jr., W. C., Lissianski, V., Smith, G. P., Golden, D. A., Frenklach, M., and Goldenberg, M. (1995). *http://www.me.berkeley.edu/gri_mech/.*

Bradley, D., and Matthews, K. J. (1968). "Measurement of high gas temperatures with fine wire thermocouples," *J. Mech. Eng. Sci.* **10**, 299-305.

Carter, C. D. and Laurendeau, N. M., (1994). "Wide- and narrow-band saturated fluorescence measurements of hydroxyl concentration in premixed flames from 1 bar to 10 bar," *Appl. Phys. B* **58**, 519-528.

Carter, C. D., King, G. B., and Laurendeau, N. M. (1989). "A combustion facility for high-pressure flame studies by spectroscopic methods," *Rev. Sci. Instrum.* **60**, 2606-2609.

Chelliah, H. K., Law, C. K., Ueda, T., Smooke, M. D., and Williams, F. A. (1990). "An experimental and theoretical investigation of the dilution pressure and flowfield effects on the extinction condition of methane-air-nitrogen diffusion flames," *Twenty-Third Symposium (International) on Combustion*, The Combustion Institute, Pittsburgh, 503-511.

Cooper, C. S., and Laurendeau, N. M. (1997). *Quantitative laser-induced fluorescence measurements of NO concentration in a lean direct-injection spray flame at atmospheric pressure*, M.S. Thesis, School of Mechanical Engineering, Purdue University, West Lafayette, IN.

Cooper, C. S., and Laurendeau, N. M. (1997). "Effect of pulsed dye laser wavelength stabilization on spectral overlap in atmospheric NO fluorescence studies," *Appl. Opt.* **36**, 5262-5265.

Corr, R. A., Malte, P. C., and Marinov, N. M. (1992). "Evaluation of NO_x mechanisms for lean, premixed combustion," *Journal of Engineering for Gas Turbines and Power* **114**, 425-434.

Dean, A. J., Hanson, R. K., and Bowman, C. T. (1990). "High-temperature shock tube study of reactions of CH and C-atoms with N_2," *Twenty-Third Symposium (International) on Combustion*, The Combustion Institute, Pittsburgh, 259-265.

Dixon-Lewis, G., David, T., Gaskell, P. H., Fukutani, S., Jinno, H., Miller, J. A., Kee, R. J., Smooke, M. D., Peters, N., Effelsberg, E., Warnatz, J., and Behrendt, F. (1984). "Calculation of the structure and extinction limit of a methane-air counterflow diffusion

flame in the forward stagnation region of a porous cylinder," *Twentieth Symposium (International) on Combustion*, The Combustion Institute, Pittsburgh, 1893-1904.

Drake, M. C., and Blint, R. J. (1989). "Thermal NO_x in stretched laminar opposed-flow diffusion flames with $CO/H_2/N_2$ fuel," *Combust. Flame* **76**, 151-167.

Drake, M. C., Ratcliffe, J. W., Blint, R. J., Carter, C. D., and Laurendeau, N. M. (1990). "Measurements and modeling of flamefront NO formation and superequilibrium radical concentrations in laminar high-pressure premixed flames," *Twenty-Third Symposium (International) on Combustion*, The Combustion Institute, Pittsburgh, 387-395.

Drake, M. C., and Blint, R. J. (1991). "Relative importance of nitric oxide formation mechanisms in laminar, opposed-flow diffusion flames," *Combust. Flame* **83**, 185-203.

Drake, M. C., and Ratcliffe, J. W. (1993). "High temperature quenching cross-sections for nitric oxide laser-induced fluorescence measurements," *J. Chem. Phys.* **98**, 3850-3865.

Glarborg, P., Miller, J. A., and Kee, R. J. (1986). "Kinetic modeling and sensitivity analysis of nitrogen oxide formation in well-stirred reactors," *Combust. and Flame* **65**, 177-202.

Gore, J. P., Lim, J., Takeno, T., and Zhu, X. L. (1999). "A study of the effect of thermal radiation on the structure of methane-air counterflow diffusion flames using detailed chemical kinetics," *Proceedings of the 5th ASME/JSME Joint Thermal Engineering Conference*, San Diego.

Hahn, W. A., and Wendt, J. O. L. (1981). "NO_x formation in flat, laminar, opposed jet methane diffusion flames," *Eighteenth Symposium (International) on Combustion*, The Combustion Institute, Pittsburgh, 121-131.

Hancock, R. D., Bertagnolli, K. E., and Lucht, R. P. (1997). "Nitrogen and hydrogen CARS temperature measurements in a hydrogen/air flame using a near-adiabatic flat-flame burner," *Combust. Flame* **109**, 323-331.

Hanson, R. K., Seitzman, J. M., and Paul, P. H. (1990). "Planar laser-fluorescence imaging of combustion gases," *Appl. Phys. B* **50**, 441-454.

Harris, J. M., Lytle, F. E., and McCain, T. C. (1976). "Squirrel-cage photomultiplier base design for measurements of nanosecond fluorescence decays," *Anal. Chem.* **48**, 2095-2098.

Ji, J., Sivathanu, Y. R., and Gore, J. P. (1999). "Thin filament spectral pyrometry for flame temperature measurements," *Proceedings of the Joint Meeting of the United States Sections of the Combustion Institute*, Washington D.C.

Kee, R. J., Miller, J. A., Evans, G. H., and Dixon-Lewis, G. (1988). "A computational model of the structure and extinction of strained, opposed-flow, premixed methane-air flames," *Twenty-Second Symposium (International) on Combustion*, The Combustion Institute, Pittsburgh, 1479-1494.

Kim, T. K., Alder, B. J., Laurendeau, N. M., and Gore, J. P. (1995). "Exhaust and *in-situ* measurements of nitric oxide for laminar partially premixed C_2H_6-air flames: Effect of premixing level at constant fuel flowrate," *Combust. Sci. Tech.* **110-111**, 361-378.

Laud, B. B., and Gaydon, A. G. (1971). "Absorption spectra of ethylene diffusion flames," *Combust. Flame* **16**, 55-60.

Laurendeau, N. M., and Goldsmith, J. E. M. (1989). "Comparison of hydroxyl concentration profiles using five laser-induced fluorescence methods in a lean subatmospheric-pressure $H_2/O_2/Ar$ flame," *Combust. Sci. Tech.* **63**, 139-152.

Li, S. C., Ilincic, N., and Williams, F. A. (1997). "Reduction of NO_x formation by water sprays in strained two-stage flames," *Journal of Engineering for Gas Turbines and Power*, **119**, 836-843.

Lin, K. -C., and Faeth, G. M. (1996). "Hydrodynamic suppression of soot emissions in laminar diffusion flames," *J. Prop. Power* **12**, 10-17.

Lucht, R. P., Sweeney, D. W., and Laurendeau, N. M. (1980). "Balanced cross-rate model for saturated molecular fluorescence in flames using a nanosecond pulse length laser," *Appl. Opt.* **19**, 3295-3300.

Luque, J., Smith, G. P., and Crosley, D. R. (1996). "Quantitative CH determinations in low-pressure flames," *Twenty-Sixth Symposium (International) on Combustion*, The Combustion Institute, Pittsburgh, 959-966.

Lutz, A. E., Kee, R. J., and Grcar, J. F. (1996). *OPPDIF: A Fortran program for computing opposed-flow diffusion flames*, Sandia National Laboratories, Report No. SAND96-8243.

Magre, P., Aguerre, F., Collin, G., Versaevel, P., Lacas, F., and Rolon, J. C. (1995). "Temperature and concentration measurements by CARS in counterflow laminar diffusion flames," *Exp. Fluids* **18**, 376-382.

Mallard, W. G., Miller, J. H., and Smyth, K. C. (1982). "Resonantly enhanced two-photon photoionization of NO in an atmospheric flame," *J. Chem. Phys.* **76**, 3483-3492.

Malte, P. C., and Pratt, D. T. (1974). "The role of energy-releasing kinetics in NO_x formation; fuel-lean, jet-stirred CO-air combustion," *Combust. Sci. Tech.* **9**, 221-231.

Mastorakos, E., Taylor, A. M. K. P., and Whitelaw, J. H. (1992). "Extinction and temperature characteristics of turbulent counterflow diffusion flames with partial premixing," *Combust. Flame* **91**, 40-54.

Miller, J. A., and Bowman, C. T. (1989). "Mechanism and modeling of nitrogen chemistry in combustion," *Prog. Energy Combust. Sci.* **15**, 287-338.

Morley, C. (1981). "The mechanism of NO formation from nitrogen compounds in hydrogen flames studied by laser fluorescence," *Eighteenth Symposium (International) on Combustion*, The Combustion Institute, Pittsburgh, 23-32.

Nicol, D. G., Steele, R. C., Marinov, N. M., and Malte, P. C. (1993). "The importance of the nitrous oxide pathway to NO_x in lean-premixed combustion," *ASME Paper 93-GT-342.*

Nishioka, M., Nakagawa, S., Ishikawa, Y., and Takeno, T. (1994). "NO emission characteristics of methane-air double flame," *Combust. Flame* **98**, 127-138.

Otsuka, Y., and Niioka, T. (1972). "On the deviation of the flame from the stagnation point in opposed-jet diffusion flames," *Combust. Flame* **19**, 171-179.

Pandya, T. P., and Weinberg, F. J. (1963). "The study of the structure of laminar diffusion flames by optical methods," *Ninth Symposium (International) on Combustion*, The Combustion Institute, Pittsburgh, 587-596.

Pandya, T. P., and Srivastava, N. K. (1972). "Counterflow diffusion flame of ethyl alcohol," *Combust. Sci. Tech.* **5**, 83-88.

Pandya , T. P., and Srivastava, N. K. (1975). "Structure of counterflow diffusion flame of ethanol," *Combust. Sci. Tech.* **11**, 165-180.

Partridge, W. P., Jr., Klassen, M. S., Thomsen, D. D., and Laurendeau, N. M., (1996). "Experimental assessment of O_2 interferences on LIF measurements of NO in high-pressure, lean premixed flames using narrow-band and broad-band detection," *Appl. Opt.* **34**, 4890-4904.

Partridge, Jr., W. P. (1996). *Experimental assessment and enhancement of planar laser-induced fluorescence measurements of nitric oxide in an inverse diffusion flame*, Ph.D. Thesis, School of Mechanical Engineering, Purdue University, West Lafayette, IN.

Patel, N. K., and Chu, C. (1970). "Studies of opposed jet diffusion flames," *Combust. Flame* **14**, 137-143.

Paul, P. H., Gray, J. A., Durant, Jr., J. L., and Thoman, J. W. (1993). "A model for temperature-dependent collisional quenching of NO $A^2\Sigma^+$," *Appl. Phys.* B **57**, 249-259.

Paul, P. H., Gray, J. A., Durant, Jr., J. L., and Thoman, J. W. (1994). "Collisional quenching corrections for laser-induced fluorescence measurements of NO $A^2\Sigma^+$," *AIAA J.* **32** , 1670-1675.

Paul, P. H., Carter, C. D., Gray, J. A., Durant, Jr., J. L., Thoman, J. W., and Furlanetto, M. R. (1995). *Correlations for the NO $A^2\Sigma^+$ Electronic Quenching Cross-section,* Sandia National Laboratories Report No. SAND94-8237.

Puri, I. K., and Seshadri, K. (1986). "Extinction of diffusion flames burning diluted methane and diluted propane in diluted air," *Combust. Flame* **65**, 137-150.

Ramakrishna, Ch., Zhan, N. J., Kelkar, A. S., and Gore, J. P. (1995). "A study of structure of partially-premixed laminar co-flow jet flames," *Proceedings of the Joint Technical Meeting of the Central States, Western States and Mexican National Sections of the International Combustion Institute and American Flame Research Committee*, San Antonio.

Ravikrishna, R. V., Cooper, C. S., and Laurendeau, N. M. (1999). "Comparison of laser-saturated and linear fluorescence measurements of nitric oxide in counterflow diffusion flames," *Combust. Flame* **116**, 810-820.

Ravikrishna, R. V., and Laurendeau, N. M. (1997). "Laser-induced fluorescence measurements and modeling of nitric oxide in counterflow diffusion flames," *Proceedings of the Western States Section of the Combustion Institute*, Livermore, CA.

Ravikrishna, R. V., and Laurendeau, N. M. (1998). "Laser-saturated fluorescence measurements of nitric oxide in a counterflow diffusion flame," *Combust. Flame* **113**, 473-475.

Ravikrishna, R. V. and Laurendeau, N. M. (1999a). "Laser-induced fluorescence measurements and modeling of nitric oxide in ethane-air and methane-air counterflow diffusion flames," *Combust. Flame*, in press.

Ravikrishna, R. V. and Laurendeau, N. M. (1999b). "Laser-induced fluorescence measurements and modeling of nitric oxide in counterflow partially-premixed flames," Submitted for publication.

Reisel, J. R. (1994). *Laser-induced fluorescence measurements and modeling of nitric oxide in laminar high-pressure flames*, Ph.D. Thesis, School of Mechanical Engineering, Purdue University, West Lafayette, IN.

Reisel, J. R., Carter, C. D., Laurendeau, N. M., and Drake, M. C. (1993). "Laser-saturated fluorescence measurements of nitric oxide in laminar, flat, $C_2H_6/O_2/N_2$ flames at atmospheric pressure," *Combust. Sci. Tech.* **91**, 271-295.

Reisel, J. R., and Laurendeau, N. M. (1994). "Laser-induced fluorescence measurements and modeling of nitric oxide formation in high-pressure flames," *Comb. Sci. Tech.* **98**, 137-160.

Reisel, J. R., and Laurendeau, N. M. (1995). "Quantitative LIF measurements and modeling of nitric oxide in high-pressure $C_2H_4/O_2/N_2$ flames," *Combust. Flame* **101**, 141-152.

Sick, V., Hildenbrand, F., and Lindstedt, P. (1998). "Quantitative laser-based measurements and detailed chemical kinetic modeling of nitric oxide concentrations in methane/air counterflow diffusion flames," *Twenty-Seventh Symposium (International) on Combustion*, The Combustion Institute, Pittsburgh, 1401-1409.

Simmons, R. F., and Wolfhard, H. G. (1957). "Some limiting oxygen concentrations for diffusion flames in air diluted with nitrogen," *Combust. Flame* **1**, 155-161.

Smooke, M. D., Seshadri, K., and Puri, I. K. (1988). "The structure and extinction of partially premixed flames burning methane in air," *Twenty-Second Symposium (International) on Combustion*, The Combustion Institute, Pittsburgh, 1555-1563.

Spalding, D. B. (1953). "The combustion of liquid fuels," *Fourth Symposium (International) on Combustion,* The Combustion Institute, Pittsburgh, 847-864.

Sun, C. J., Sung, C. J., Zhu, D. L., and Law, C. K. (1996a). "Response of counterflow premixed and diffusion flames to strain rate variations at reduced and elevated pressures," *Twenty-Sixth Symposium (International) on Combustion*, The Combustion Institute, Pittsburgh, 1111-1120.

Sun, C. J., Sung, C. J., Wang, H., and Law, C. K. (1996b). "On the structure of nonsooting counterflow ethylene and acetylene diffusion flames," *Combust. Flame* **107**, 321-335.

Sung, C. J., Li, B., Wang, H., and Law, C. K. (1998). "Structure and sooting limits in counterflow methane/air and propane/air diffusion flames from 1 to 5 atmospheres," *Twenty-Seventh Symposium (International) on Combustion*, The Combustion Institute, Pittsburgh, 1523-1529.

Tanoff, M. A., Smooke, M. D., Osborne, R. J., Brown, T. M., and Pitz, R. W. (1996). "The sensistive structure of partially-premixed methane-air vs. air counterflow flames," *Twenty-Sixth Symposium (International) on Combustion*, The Combustion Institute, Pittsburgh, 1121-1128.

Taylor, J. R. (1982). *An Introduction to Error Analysis, The Study of Uncertainties in Physical Measurements*, University Science Books, Mill Valley, CA.

Thomsen, D. D. (1996). *Measurements and modeling of nitric oxide formation in high-pressure, premixed $CH_4/O_2/N_2$ flames*, M.S. Thesis, School of Mechanical Engineering, Purdue University, West Lafayette, IN.

Thomsen, D. D. (1999). *Personal Communication.*

Thomsen, D. D., Kuligowski, F. F., and Laurendeau, N. M. (1997). "Background corrections for laser-induced fluorescence measurements of NO in lean, high-pressure, premixed methane flames," *Appl. Opt.* **36**, 3244-3252.

Thomsen, D. D., and Laurendeau, N. M. (1999). "LIF measurements of NO concentration in lean, counterflow premixed flames," *Proceedings of the Joint Technical Meeting of the United States Sections of the Combustion Institute*, Washington D.C.

Trees, D., Brown, T. M., Seshadri, K., Smooke, M. D., Balakrishnan, G., Pitz, R. W., Giovangigli, V., and Nandula, S. P. (1995). "The Structure of Nonpremixed Hydrogen-Air Flames," *Comb. Sci. Tech.* **104**, 427-439.

Tseng, L.-K., Gore, J. P., Puri, I. K., and Takeno, T. (1996). "Acetylene and ethylene mole fractions in methane/air partially premixed flames," *Twenty-Sixth Symposium (International) on Combustion*, The Combustion Institute, Pittsburgh, 993-999.

Tsuji, H., and Yamaoka, I. (1967). "The counterflow diffusion flame in the forward stagnation region of a porous cylinder," *Eleventh Symposium (International) on Combustion*, The Combustion Institute, Pittsburgh, 979-984.

Tsuji, H., and Yamaoka, I. (1969). "The structure of counterflow diffusion flames in the forward stagnation region of a porous cylinder," *Twelfth Symposium (International) on Combustion*, The Combustion Institute, Pittsburgh, 997-1005.

Tsuji, H., and Yamaoka, I. (1971). "Structure analysis of counterflow diffusion flames in the forward stagnation region of a porous cylinder," *Thirteenth Symposium (International) on Combustion*, The Combustion Institute, Pittsburgh, 723-731.

Tsuji, H. (1982). "Counterflow diffusion flames," *Prog. Ener. Combust. Sci.* **8**, 93-119.

Vandooren, J. (1992). "Comparison of the experimental structure of an ammonia seeded rich-hydrogen-oxygen-argon flame with calculated ones along several reaction mechanisms," *Combust. Sci. Tech.* **84**, 767-769.

Vilimpoc, V., and Goss, L. P. (1988). "SiC-based thin-filament pyrometry: Theory and thermal properties," *Twenty-Second Symposium (International) on Combustion*, The Combustion Institute, Pittsburgh, 1907-1914.

Vilimpoc, V., Goss, L.P., and Sarka, B. (1988). "Spatial temperature profile measurements by the thin-filament-pyrometry technique," *Opt. Letters* **13**, 93-95.

Williams, F. A. (1975). "Recent advances in theoretical descriptions of turbulent diffusion flames", Murthy, S. N. B. (Ed.), *Turbulent Mixing in Nonreactive and Reactive Flows*, Plenum Press, New York, 189-208.

Woiki, D., Votsmeier, M., Davidson, D., Hanson, R. K., and Bowman, C. T. (1998). "CH-radical concentration measurements in fuel-rich $CH_4/O_2/Ar$ and $CH_4/O_2/NO/Ar$ mixtures behind shock waves," *Combust. Flame* **113**, 624-626.

Yamaoka, I., and Tsuji, H. (1974). "The structure of rich fuel-air flames in the forward stagnation region of a porous cylinder," *Fifteenth Symposium (International) on Combustion*, The Combustion Institute, Pittsburgh, 637-644.

Yamaoka, I., and Tsuji, H. (1976). "Structure analysis of rich fuel-air flames in the forward stagnation region of a porous cylinder," *Sixteenth Symposium (International) on Combustion*, The Combustion Institute, Pittsburgh, 1145-1153.

Yamaoka, I., and Tsuji, H. (1978). "An experimental study of flammability limits using counterflow flames," *Seventeenth Symposium (International) on Combustion*, The Combustion Institute, Pittsburgh, 843-855.

Yang, M. H., and Puri, I. K. (1993). "Experimental investigation of stretched premixed flames burning mixtures of methane and methyl chloride in air and comparison with numerical simulations," *Combust. Flame* **94**, 25-34.

Zeldovich, J. (1946). "The oxidation of nitrogen in combustion and explosions," *ACTA Physicochem. URSS* **21**, 577-628.

Zhu, X. L., Takeno, T., and Gore, J. P. (1999). "A study of the effects of thermal radiation on methane/air counterflow partially-premixed flames by using detailed kinetics," *Proceedings of the Joint Technical Meeting of the United States Sections of the Combustion Institute*, Washington D.C.

APPENDICES

Appendix A: Thin Filament Pyrometry

This appendix presents additional details on the thin filament pyrometry technique which was used in obtaining temperature measurements in atmospheric pressure counterflow diffusion and partially-premixed flames. The filament used was a silicon carbide ceramic fiber (NICALON, Dow Corning). It is supplied as a 15-μm continuous fiber in the form of a multi-filament tow (500 filaments/tow) spooled on a bobbin. Since it is very important to isolate a single filament from the multi-filament tow, a magnifying lens is used to ensure that the specimen consists of only one filament. An approximately 15-cm long portion of the single isolated filament is then used for the experiment. Each end of the filament is glued to a weight, and the filament is extended with the weighted free ends across the flame. The radiant emission from the filament is then measured and related to the temperature.

The conversion of detector output voltage to temperature requires a non-linear calibration since the detector output is directly proportional to the emitted radiation and not to the temperature. The spectral emissive power from the surface of a heated fiber is adequately approximated by treating the fiber as a gray body (Vilimpoc et al., 1988) and can be written as

$$E_g(\lambda,T) = \frac{2\pi\varepsilon hc^2}{\lambda^5\left[e^{\frac{hc}{\lambda kT}}-1\right]} \quad , \tag{A.1}$$

where λ is the wavelength, T is the temperature, ε is the apparent emissivity of the fiber, h is the Planck constant, c is the speed of light, and k is the Boltzmann constant. The overall signal generated by the indium antimonide (InSb) detector is given by

$$S(T) = k_{\exp}\int_{\lambda_1}^{\lambda_2} E_g(\lambda,T)R(\lambda)T_r(\lambda)d\lambda \quad , \tag{A.2}$$

where $R(\lambda)$ is the detector response function, $T_r(\lambda)$ represents the transmission characteristics of the optics, λ_1 and λ_2 are the lower and upper limits of the detector response, respectively, and k_{exp} is an experimental constant which takes into account the efficiency of the collection optics and the gain of the detector electronics. The detector

has a response between 1.1 and 5.6 μm, and the response curve, $R(\lambda)$, is provided by the manufacturer (Graseby Infrared). The calcium fluoride lenses used for collimating and focusing the infrared radiation have a constant transmission over the range of detector response wavelengths. In other words, $T_f(\lambda)$ is constant between 1.1 and 5.6 μm. Writing Eq. (A.2) twice, once for the actual flame and again for the calibration flame, and dividing the two resulting equations, we obtain

$$\frac{S(T)}{S(T_c)} = \frac{\int_{\lambda_1}^{\lambda_2} E_g(\lambda,T)R(\lambda)d\lambda}{\int_{\lambda_1}^{\lambda_2} E_g(\lambda,T_c)R(\lambda)d\lambda} \quad , \tag{A.3}$$

where the subscript c refers to the calibration flame. The integral in the numerator of Eq. (A.3) can be numerically evaluated for each temperature. Figure A.1 shows the flame temperature as a function of the ratio of the integrals in Eq. (A.3) for a calibration flame temperature of 1383 K.

The experimental procedure for thin filament pyrometry is as follows. First, the filament is placed in the calibration flame and the detector signal is noted. The detector signal corresponding to the actual flame is then divided by this calibration signal, and the temperature corresponding to this ratio is obtained from Fig. A.1. This temperature represents the filament temperature in the actual flame. Since it is difficult to accurately read the temperature from Fig. A.1, a fifth-order polynomial fit is developed to match the curve in Fig. A.1. Once the detector signal ratio is known, this polynomial equation can be used to obtain the filament temperature. The flame temperature is then calculated via a radiative heat loss calculation following the procedure developed by Bradley and Matthews (1968). The filament emissivity for this calculation is taken as 0.88 (Vilimpoc and Goss, 1988).

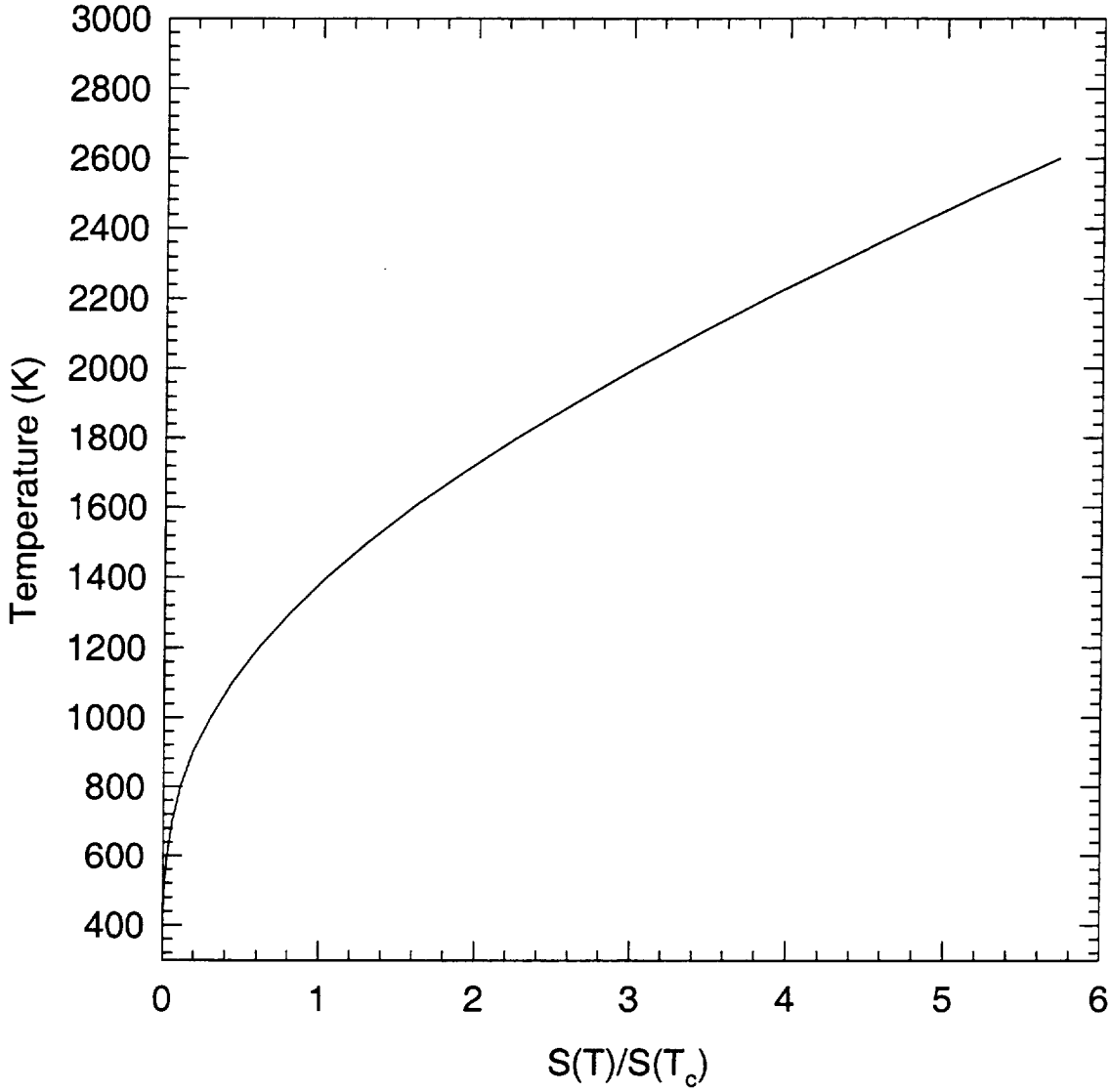

Figure A.1: Temperature as a function of the ratio of the detector signal in the actual flame to that in the calibration flame. The calibration flame temperature is 1383 K.

Appendix B: Error Analysis

To assess the quantitative nature of any measurement, it is important to estimate the uncertainty in the measurement process. All fluorescence measurements have an uncertainty associated with their repeatability. The process of converting measured fluorescence signal to NO concentration requires use of a calibration, which introduces an additional uncertainty. The net uncertainty has two components, the accuracy and the precision. Precision reflects the repeatability of the measurements, while the accuracy is an estimate of any systematic errors. The overall uncertainty of our measurements is a combination of three uncertainties, viz., precision of the fluorescence measurements, precision of the calibration factor, and accuracy of the calibration factor.

The precision associated with the fluorescence measurements is mainly affected by photomultiplier tube shot noise and noise associated with data acquisition. The accuracy of the calibration factor depends on the accuracy of the doped NO concentrations and possible destruction of NO in the calibration flame. The uncertainty analysis will be presented separately for the atmospheric pressure and the high-pressure NO measurements. All uncertainties are based on a 95% confidence level.

B.1 Propagation of Errors

Since all uncertainties are based on a 95% confidence level, the uncertainty of a measured quantity is defined as twice the standard deviation of the mean. For a given measured variable y with standard deviation σ that has been sampled N times, the uncertainty δy is then

$$\delta y = \frac{2\sigma}{\sqrt{N}} \quad . \tag{B.1}$$

To determine the effect of the uncertainty in one portion of a measurement scheme on the uncertainty of the quantity finally measured, we use the method of propagation of errors (Taylor, 1982). For a given function q(x,....,z) where x and z are independent, random,

measured quantities with respective uncertainties $\delta x, \ldots, \delta z$, the uncertainty in q is defined as

$$\delta q = \sqrt{\left(\frac{\partial q}{\partial x}\delta x\right)^2 + \ldots + \left(\frac{\partial q}{\partial z}\delta z\right)^2} \quad . \tag{B.2}$$

Thus, for a given function of the type

$$q = x + \ldots + z \quad , \tag{B.3}$$

the resulting uncertainty in q is

$$\delta q = \sqrt{(\delta x)^2 + \ldots + (\delta z)^2} \quad . \tag{B.4}$$

For a function of the type

$$q = x \times \ldots \times z \quad , \tag{B.5}$$

the uncertainty in q is

$$\delta q = \sqrt{(z \bullet \delta x)^2 + \ldots + (x \bullet \delta z)^2} \quad . \tag{B.6}$$

Equation (B.6) can be framed in the form of a relative uncertainty, $\varepsilon(q) = \delta q / q$, to yield

$$\varepsilon(q) = \sqrt{\varepsilon(x)^2 + \ldots + \varepsilon(z)^2} \quad . \tag{B.7}$$

In the case where x and z are not independent or are not random, the uncertainty δq for a function of the form of Eq. (B.3) is

$$\delta q = \delta x + \ldots + \delta z \quad , \tag{B.8}$$

whereas for a function of the form of Eq. (B.5), the relative uncertainty is

$$\varepsilon(q) = \varepsilon(x) + \ldots + \varepsilon(z) \quad . \tag{B.9}$$

B.2 Atmospheric pressure LIF Measurements

To determine the accuracy associated with the calibration factor, we must consider the following equation for the amount of NO doped in the calibration flame (Partridge, 1996),

$$D_P = \frac{n_R}{n_P} \dot{V}R \, C_B \, L \quad , \tag{B.10}$$

where D_P is the doped [NO] in ppm relative to calibration flame products, C_B is the concentration of the NO standard gas, L is the fraction of NO that is destroyed in the flame, $\dot{V}R$ is the ratio of the standard NO gas flow rate to the total volumetric flow rate, and (n_R/n_P) is the total molar ratio of reactants to products. Since the calibration factor is in ppm/V, the accuracy of the calibration factor is directly related to the systematic errors associated with the doped NO. Propagating the error associated with the individual terms in Eq. (B.10), we get the following expression for the accuracy of the calibration factor

$$\varepsilon CF_{ACC} = \left[\left(\varepsilon \dot{V}R \right)^2 + (\varepsilon C_B)^2 + (\varepsilon L)^2 \right]^{0.5} \quad . \tag{B.11}$$

The uncertainty in the volumetric flow rate was calculated by assuming that the maximum fluctuation in the flow rates of the individual gases was one scale reading from the rotameter setting. The average uncertainty in the volumetric flow rate was determined to be ~3%. The relative uncertainty in C_B was taken to be 4% based on manufacturer's specifications (Airco, 1993), and that due to L was taken to be 5% based on previous modeling (Reisel, 1994). The precision of the calibration factor was determined as twice the standard deviation of samples from multiple calibrations. Hence, the precision was determined to be approximately 19%. The cumulative uncertainty in the calibration factor can then be determined from

$$\varepsilon CF = \left[(\varepsilon CF_{PRE})^2 + (\varepsilon CF_{ACC})^2 \right]^{0.5} \quad , \tag{B.12}$$

where the subscripts PRE and ACC refer to the precision and accuracy components of the uncertainty in the calibration factor, respectively. Now the cumulative uncertainty in the [NO] measurement is given by

$$\varepsilon N_{NO} = \left[(\varepsilon CF)^2 + (\varepsilon S_{NO})^2 \right]^{0.5} \quad , \tag{B.13}$$

where εS_{NO} is the uncertainty in the digital NO fluorescence signal. For LSF measurements, this can be expressed as

$$\varepsilon S_{NO} = \left[(\varepsilon S)^2 + (\varepsilon S_b)^2 \right]^{0.5} \quad , \tag{B.14}$$

where εS is the uncertainty in the uncorrected LSF signal and εS_b is the uncertainty in the background signal. In the case of linear LIF measurements, the uncertainty in the NO fluorescence signal can be shown to be (Thomsen, 1996)

$$\varepsilon S_{NO} = \sqrt{\left(\frac{\sqrt{(\delta S)^2 + (\delta S_b)^2}}{S - S_b}\right)^2 + \left(\frac{\sqrt{(\delta L_P)^2 + (\delta L_{P,b})^2}}{L_P - L_{P,b}}\right)^2} \quad , \qquad \text{(B.15)}$$

where δS, δS_b, δL_p, *and* $\delta L_{p,b}$ are twice the standard deviation of the mean for the uncorrected LIF signal, the LIF signal background, the laser power, and the laser power background, respectively. Both δS_b and δL_p are negligible and can be neglected in Eq. (B.15). For the PLIF measurements, the overall uncertainty was estimated to be 28% previously (Partridge, 1996). Hence, the analysis for the PLIF measurements is not repeated here.

B.3 High-pressure LIF Measurements

Since all measurements at high pressure involved use of the linear LIF technique, the uncertainty in the digital NO fluorescence signal, εS_{NO}, can be calculated using Eq. (B.15). To assess the uncertainty associated with the calibration, a slightly different approach is followed from the atmospheric pressure measurements. The error arising from volumetric flow rate fluctuations is not considered separately. One reason is that high-accuracy mass flow controllers were used instead of rotameters for the high-pressure NO measurements. Secondly, the relative precision of the calibration, εCF_{PRE} is taken as twice the standard error of the calibration slope (Thomsen, 1996). This strategy ensures that any error arising from gas delivery system fluctuations is included as it would appear in the standard error of the calibration slope. Thus, the cumulative uncertainty of the calibration factor is

$$\varepsilon CF = \left[(\varepsilon CF_{PRE})^2 + (\varepsilon C_B)^2 + (\varepsilon L)^2\right]^{0.5} \quad . \qquad \text{(B.16)}$$

It is difficult to assess the uncertainty due to the background signal in diffusion flames. This is because the concentration of interfering species such as O_2 changes drastically across a diffusion flame, unlike in premixed flames. The effect of PAH interferences in the fuel-rich region has been shown to be less than 10%. Nevertheless, as the effect of PAH interferences varies spatially in a diffusion flame, it is difficult to assess the uncertainty arising from PAH interferences at each point. At 5 atm, which is the highest pressure at which calibrated measurements of [NO] were obtained in diffusion flames, the background signal in the counterflow premixed flame is ~11%. Thus, to account for such effects, we assign a 10% relative uncertainty due to the background signal and interferences in all diffusion flames (εS_I). Since this source of error is not random, it cannot be added in quadrature as for the other errors. Hence, it must be added directly to the net uncertainty via Eq. (B.9). Thus, the cumulative uncertainty in the [NO] measurement is given by

$$\varepsilon N_{NO} = \left[(\varepsilon CF)^2 + (\varepsilon S_{NO})^2\right]^{0.5} + \varepsilon S_I \quad . \tag{B.17}$$

The total uncertainty in the [NO] measurement is the product of the relative uncertainty given by Eq. (B.17) and the measured [NO].

B.4 Error Calculations

Table B.1 lists typical values used in the uncertainty analysis for both atmospheric and high-pressure flames. All values presented correspond to peak [NO] in methane-air counterflow diffusion flames.

Table B.1 Typical values used in the uncertainty analysis of [NO] measurements

Pressure = 1 atm, Strain rate = 35 s^{-1}		Pressure = 5 atm, Strain rate = 30 s^{-1}	
Parameter	Value	Parameter	Value
$\varepsilon \dot{V}R$	0.03	εC_B	0.04
εC_B	0.04	εL	0.05
εL	0.05	$\varepsilon C_{F,PRE}$	0.022
$\varepsilon C_{F,PRE}$	0.19	εC_F	0.068
εC_F	0.203	L_P-$L_{p,b}$	5.37
L_P-$L_{p,b}$	3.55	δL_P	0.03
δL_P	0.056	S-S_b	2.51
S-S_b	0.34	δS	0.117
δS	0.06	εS_{NO}	0.047
εS_{NO}	0.177	εS_I	0.10
εN_{NO}	0.269	εN_{NO}	0.182
N_{NO}	22.09	N_{NO}	38.45
δN_{NO}	5.94	δN_{NO}	7.01

Appendix C: [NO] Measurements Data

The [NO] data resulting from the various measurements are presented in this appendix. The [NO] data in the atmospheric pressure ethane-air and methane-air counterflow diffusion flames are presented in Tables C.1 and C.2, respectively. [NO] measurements in the methane-air counterflow partially-premixed flames are presented in Table C.3. The [NO] data for the methane-air counterflow diffusion flames at 2, 3, 4, and 5 atm are presented in Tables C.4-C.7, respectively. In all tables, *x* represents the distance measured from the end of the burner used to supply the fuel.

Table C.1 [NO] data in ethane-air counterflow diffusion flames at 1atm.

STRAIN RATE = 48 S^{-1}		STRAIN RATE = 35 S^{-1}		STRAIN RATE = 20 S^{-1}		STRAIN RATE = 5 S^{-1}	
x (cm)	[NO] (ppm)	x (cm)	[NO] (ppm)	x (cm)	[NO] (ppm)	x (cm)	[NO] (ppm)
0.80	0.09	0.80	0.02	0.80	0.36	0.80	0.26
0.85	1.65	0.85	0.59	0.85	2.37	0.90	1.38
0.90	6.64	0.90	3.21	0.90	7.83	1.00	5.79
0.95	13.18	0.95	9.31	0.95	15.81	1.05	9.59
1.00	23.53	1.00	16.11	1.00	21.81	1.10	14.94
1.05	28.46	1.05	22.43	1.05	27.33	1.15	17.73
1.10	20.48	1.10	31.74	1.10	36.04	1.20	20.88
1.15	6.70	1.15	23.17	1.15	31.13	1.25	24.34
1.20	0.90	1.20	11.53	1.20	22.37	1.30	26.62
		1.25	3.04	1.25	12.02	1.35	36.88
		1.30	0.45	1.30	3.92	1.40	40.47
				1.40	0.10	1.45	40.75
						1.50	36.46
						1.55	27.21
						1.60	20.53
						1.65	10.79
						1.70	2.02

Table C.2 [NO] data in methane-air counterflow diffusion flames at 1atm.

STRAIN RATE = 35 S^{-1}		STRAIN RATE = 20 S^{-1}		STRAIN RATE = 5 S^{-1}	
x (cm)	[NO] (ppm)	x (cm)	[NO] (ppm)	x (cm)	[NO] (ppm)
0.85	0.19	0.80	0.12	1.00	0.43
0.90	1.74	0.85	0.91	1.10	2.65
0.95	5.41	0.90	3.48	1.15	5.78
1.00	9.89	0.95	6.87	1.20	12.37
1.05	10.87	1.00	10.67	1.25	16.51
1.10	19.00	1.05	15.25	1.30	20.75
1.15	22.09	1.10	19.91	1.40	25.87
1.20	12.63	1.15	24.32	1.45	34.48
1.25	2.98	1.20	28.83	1.50	43.17
1.30	0.47	1.25	19.55	1.55	35.96
1.35	0.30	1.30	7.74	1.60	33.58
1.40	0.14	1.35	1.82	1.65	26.04
		1.40	0.19	1.70	13.96
				1.75	9.27
				1.80	4.10

Table C.3 [NO] data in methane-air counterflow partially-premixed flames at 1 atm.

ϕ_B = 1.45		ϕ_B = 1.6		ϕ_B = 1.8		ϕ_B = 2.0	
x (cm)	[NO] (ppm)	x (cm)	[NO] (ppm)	x (cm)	[NO] (ppm)	x (cm)	[NO] (ppm)
0.40	0.15	0.40	0.07	0.50	0.04	0.50	0.07
0.50	2.56	0.50	0.14	0.60	0.00	0.60	0.05
0.55	7.54	0.60	0.13	0.70	0.00	0.70	0.03
0.60	14.26	0.70	1.67	0.80	1.57	0.80	2.07
0.65	21.72	0.80	5.47	0.90	8.53	0.85	6.40
0.70	24.67	0.85	12.81	0.95	16.79	0.90	13.68
0.75	24.73	0.90	28.90	1.00	36.39	0.95	15.26
0.80	34.35	0.95	37.05	1.05	57.19	1.00	27.67
0.85	35.04	1.00	51.05	1.10	61.90	1.05	52.29
0.90	39.24	1.05	54.39	1.15	63.09	1.10	65.04
0.95	38.60	1.10	56.34	1.20	66.79	1.15	57.50
1.00	46.22	1.15	59.61	1.25	58.20	1.20	52.49
1.05	48.42	1.20	55.38	1.30	55.22	1.25	38.69
1.10	53.45	1.25	45.46	1.35	40.13	1.30	33.97
1.15	57.68	1.30	38.57	1.40	32.57	1.35	28.43
1.20	52.15	1.35	29.35	1.45	4.38	1.40	12.78
1.25	43.45	1.40	20.60	1.50	1.47	1.45	4.24
1.30	38.51	1.45	10.61	1.60	0.03	1.50	0.84
1.35	32.29	1.50	2.09				
1.40	23.18						
1.45	10.31						
1.50	2.35						
1.60	0.09						
1.70	0.04						
1.80	0.06						

Table C.4 [NO] data in methane-air counterflow diffusion flames at 2 atm.

STRAIN RATE = 20 S^{-1}		STRAIN RATE = 30 S^{-1}		STRAIN RATE = 40 S^{-1}	
x (cm)	[NO] (ppm)	x (cm)	[NO] (ppm)	x (cm)	[NO] (ppm)
0.225	0.05	0.275	0.03	0.300	0.01
0.250	0.18	0.300	0.26	0.325	0.15
0.275	0.68	0.325	1.28	0.350	0.95
0.300	2.26	0.350	5.29	0.375	4.37
0.325	6.33	0.375	13.04	0.400	12.71
0.350	13.24	0.400	24.29	0.425	22.29
0.375	21.44	0.425	34.12	0.450	32.79
0.400	32.63	0.450	44.43	0.475	41.02
0.425	39.94	0.475	54.23	0.500	48.32
0.450	50.48	0.500	61.84	0.525	56.45
0.475	54.03	0.525	74.18	0.550	46.86
0.500	64.79	0.550	61.17	0.575	31.02
0.525	74.20	0.575	45.89	0.600	15.89
0.550	66.61	0.600	29.19	0.625	4.84
0.575	53.41	0.625	11.21	0.650	0.94
0.600	39.46	0.650	2.95	0.675	0.13
0.625	25.39	0.675	0.48		
0.650	12.17				
0.675	3.55				
0.700	0.95				
0.725	0.20				

Table C.5 [NO] data in methane-air counterflow diffusion flames at 3 atm.

STRAIN RATE = 15 S^{-1}		STRAIN RATE = 20 S^{-1}		STRAIN RATE = 30 S^{-1}		STRAIN RATE = 40 S^{-1}	
x (cm)	[NO] (ppm)	x (cm)	[NO] (ppm)	x (cm)	[NO] (ppm)	x (cm)	[NO] (ppm)
0.275	0.03	0.275	0.01	0.325	0.01	0.350	0.01
0.300	0.15	0.300	0.09	0.350	0.18	0.375	0.13
0.325	0.62	0.325	0.53	0.375	1.58	0.400	1.21
0.350	2.33	0.350	2.69	0.400	5.72	0.425	6.90
0.375	6.10	0.375	7.41	0.425	14.84	0.450	18.24
0.400	13.03	0.400	16.65	0.450	27.44	0.475	32.56
0.425	23.20	0.425	28.21	0.475	39.72	0.500	46.06
0.450	33.27	0.450	40.82	0.500	49.27	0.525	59.90
0.475	42.83	0.475	52.72	0.525	62.75	0.550	68.90
0.500	55.51	0.500	61.55	0.550	72.14	0.575	46.03
0.525	61.17	0.525	77.11	0.575	52.03	0.600	20.81
0.550	75.07	0.550	85.22	0.600	26.61	0.625	4.04
0.575	85.36	0.575	70.58	0.625	6.56	0.650	0.57
0.600	72.04	0.600	48.19	0.650	1.32	0.675	0.11
0.625	52.38	0.625	22.41	0.675	0.18		
0.650	32.26	0.650	7.64				
0.675	13.88	0.675	1.56				
0.700	3.83	0.700	0.32				
0.725	0.95						
0.750	0.24						

Table C.6 [NO] data in methane-air counterflow diffusion flames at 4 atm.

STRAIN RATE = 15 S^{-1}		STRAIN RATE = 20 S^{-1}		STRAIN RATE = 30 S^{-1}		STRAIN RATE = 40 S^{-1}	
x (cm)	[NO] (ppm)	x (cm)	[NO] (ppm)	x (cm)	[NO] (ppm)	x (cm)	[NO] (ppm)
0.325	0.02	0.350	0.05	0.325	0.01	0.350	0.01
0.350	0.10	0.375	0.48	0.350	0.14	0.375	0.15
0.375	0.59	0.400	2.32	0.375	0.87	0.400	1.16
0.400	2.29	0.425	6.71	0.400	3.14	0.425	4.39
0.425	6.45	0.450	14.34	0.425	11.28	0.450	15.77
0.450	13.12	0.475	23.68	0.450	25.36	0.475	33.64
0.475	22.18	0.500	32.59	0.475	38.53	0.500	44.45
0.500	30.71	0.525	40.10	0.500	44.95	0.525	33.24
0.525	38.83	0.550	50.01	0.525	35.15	0.550	23.36
0.550	45.61	0.575	56.86	0.550	27.05	0.575	16.75
0.575	58.53	0.600	46.40	0.575	20.03	0.600	7.91
0.600	64.94	0.625	25.81	0.600	11.73	0.625	2.11
0.625	51.82	0.650	9.09	0.625	3.83	0.650	0.42
0.650	30.66	0.675	1.92	0.650	0.90	0.675	0.08
0.675	12.83	0.700	0.35	0.675	0.17	0.700	0.03
0.700	3.31	0.725	0.09	0.700	0.03		
0.725	0.84						
0.750	0.17						

Table C.7 [NO] data in methane-air counterflow diffusion flames at 5 atm.

STRAIN RATE = 20 S^{-1}		STRAIN RATE = 30 S^{-1}		STRAIN RATE = 40 S^{-1}	
x (cm)	[NO] (ppm)	x (cm)	[NO] (ppm)	x (cm)	[NO] (ppm)
0.350	0.09	0.350	0.02	0.400	0.08
0.375	0.60	0.375	0.18	0.425	0.70
0.400	1.97	0.400	1.24	0.450	3.01
0.425	6.75	0.425	4.02	0.475	13.19
0.450	15.55	0.450	13.76	0.500	27.20
0.475	28.29	0.475	29.71	0.525	33.63
0.500	37.29	0.500	38.45	0.550	24.58
0.525	41.25	0.525	29.42	0.575	15.29
0.550	30.99	0.550	19.97	0.600	8.59
0.575	23.80	0.575	14.45	0.625	1.91
0.600	18.64	0.600	9.13	0.650	0.27
0.625	11.41	0.625	4.16	0.675	0.06
0.650	4.49	0.650	0.80		
0.675	1.25	0.675	0.17		
0.700	0.30	0.700	0.07		
0.725	0.09				

Appendix D: [NO] Measurements in Counterflow Diffusion Flames at 6-12 atm

The [NO] measurements in the counterflow diffusion flames from 2 to 5 atm were calibrated using a counterflow premixed flame at each pressure. Unfortunately, a counterflow premixed flame could not be stabilized above 5 atm owing to buoyancy effects. However, counterflow diffusion flames could be stabilized up to 12 atm and perhaps higher. Hence, relative [NO] measurements were obtained in a 30 s^{-1} strain rate flame at pressures of 6, 8, 10 and 12 atm. In this appendix, we present a preliminary method to quantify these measurements. The fuel stream in these flames consists of 25% CH_4 and 75% N_2 by volume.

Since we could calibrate in counterflow premixed flames up to 5 atm, a strategy was needed to extrapolate the calibration up to 12 atm. Motivated by this goal, [NO] measurements were obtained in the premixed calibration flames at various pressures up to 5 atm on the same day. This was done so that the measurements would not be affected by day to day fluctuations and could all be compared relative to one another. Figure D.1 shows a comparison of the ratio of NO fluorescence signal to the actual ppm level in counterflow premixed flames at various pressures. The equivalence ratio of the flame was maintained at 0.7 for pressures of 1-4 atm, and 0.65 at 5 atm. From Fig. B.1, we observe that the ratio of NO signal to the actual ppm level of NO varies by approximately ±20% about a mean value. In other words, the calibration factor at 1-5 atm can be assumed to be nearly constant within ±20%.

Let us consider now the various effects at high pressure. Substituting Eq. (2.21) in Eq. (2.14) and rearranging, we obtain

$$\frac{S_F}{N_{ppm}} = \beta\left(\frac{\nu_f}{\nu_L}\right) G V_c \sigma \left(\frac{\Omega_c}{4\pi}\right)\left(\frac{A_{ul}}{Q_{ul}}\right) \Gamma\, I_L^{\circ} f_B(T) \left(\frac{P N_A}{R_u T}\right)\left(\frac{1}{10^6}\right) \quad . \tag{D.1}$$

From the above equation, we observe that the ratio of the NO signal to the actual ppm is directly proportional to the absolute pressure and the spectral overlap fraction, and inversely proportional to the electronic quenching rate coefficient. The electronic quenching rate coefficient increases linearly with pressure, mainly owing to an increase in the collision rate with pressure. The electronic quenching rate coefficient is also a

function of temperature; however, the temperature doesn't vary much with pressure in these flames. Thus, the effects of the absolute pressure and the electronic quenching rate coefficient nullify one another. However, the spectral overlap fraction, which is measure of the spectral overlap between the laser linewidth and the NO absorption linewidth, decreases with pressure owing to line broadening at higher pressure. Thus, the ratio of NO signal to actual ppm should follow the trend of the spectral overlap fraction with pressure.

Figure D.2 indicates the variation of the absorption coefficient with pressure at a constant temperature of 1800 K obtained through modeling (Thomsen, 1999). Although Fig. D.2 includes variations in the Boltzmann fraction, the trend shown is basically that of the spectral overlap fraction with pressure since the temperature is constant. There is expectedly a sharp decrease in the overlap fraction at lower pressures, as the laser linewidth is much less than the NO absorption linewidth; consequently, the effect of broadening is more pronounced at lower pressures ($P < 3$ atm) and becomes less so at higher pressures. The measured ratio of NO signal to actual ppm, on the other hand, does not show the same behavior as the model at low pressures. At this time, we cannot explain this result. It may either be an effect in the experiment that we have not yet considered, or a shortcoming in the model. However, the encouraging result from the modeling in Fig. D.2 is that the ratio of signal to ppm varies very little at higher pressures. This leads us to extrapolate our calibration and assume for now that the ratio of NO signal to ppm is relatively constant up to 12 atm. Thus, [NO] measurements at 6, 8, 10, and 12 atm were calibrated based on our measurement in the ϕ=0.7 counterflow premixed flame at 4 atm, with corrections for quenching variations via Eq. (8.2).

The resulting [NO] measurements at 6, 8, 10, and 12 atm are compared with model predictions in Figs. D.3-D.6, respectively. The [NO] data are tabulated in Table D.1. The dashed line indicates modeling with the OPPDIF code when accounting for radiation and utilizing the GRI (version 2.11) mechanism for the NO kinetics. The dotted line indicates modeling using a previously modified rate coefficient for the prompt-NO initiation reaction (Ravikrishna and Laurendeau, 1999a). The comparison indicates that

there is still some underprediction of NO at 6-12 atm, although the underprediction decreases from 6 to 12 atm, continuing the trend observed from 3 to 5 atm. It is interesting to note that the predictions with the modified rate coefficient agree very well with measurements at 10 and 12 atm. This result might indicate that CH concentrations are predicted accurately by the GRI mechanism at these pressures.

Table D.1 [NO] Data in methane-air counterflow diffusion flames at 6-12 atm.

Pressure = 6 atm		Pressure = 8 atm		Pressure = 10 atm		Pressure = 12 atm	
x (cm)	[NO] (ppm)	x (cm)	[NO] (ppm)	x (cm)	[NO] (ppm)	x (cm)	[NO] (ppm)
0.400	0.02	0.450	0.03	0.550	0.03	0.575	0.14
0.425	0.33	0.475	0.49	0.575	0.58	0.600	1.08
0.450	1.53	0.500	2.23	0.600	3.39	0.625	5.12
0.475	6.50	0.525	7.45	0.625	8.97	0.650	12.52
0.500	14.31	0.550	18.07	0.650	14.62	0.675	18.15
0.525	24.81	0.575	25.01	0.675	19.20	0.700	9.81
0.550	28.29	0.600	17.64	0.700	11.14	0.725	5.08
0.575	21.24	0.625	11.02	0.725	5.33	0.750	2.91
0.600	14.59	0.650	6.27	0.750	2.67	0.775	2.06
0.625	6.07	0.675	2.49	0.775	1.36	0.800	1.54
0.650	1.39	0.700	1.03	0.800	0.64	0.825	0.91
0.675	0.22	0.725	0.33	0.825	0.32	0.850	0.53
0.700	0.04	0.750	0.08	0.850	0.15	0.875	0.24
				0.875	0.07	0.900	0.12
						0.925	0.06

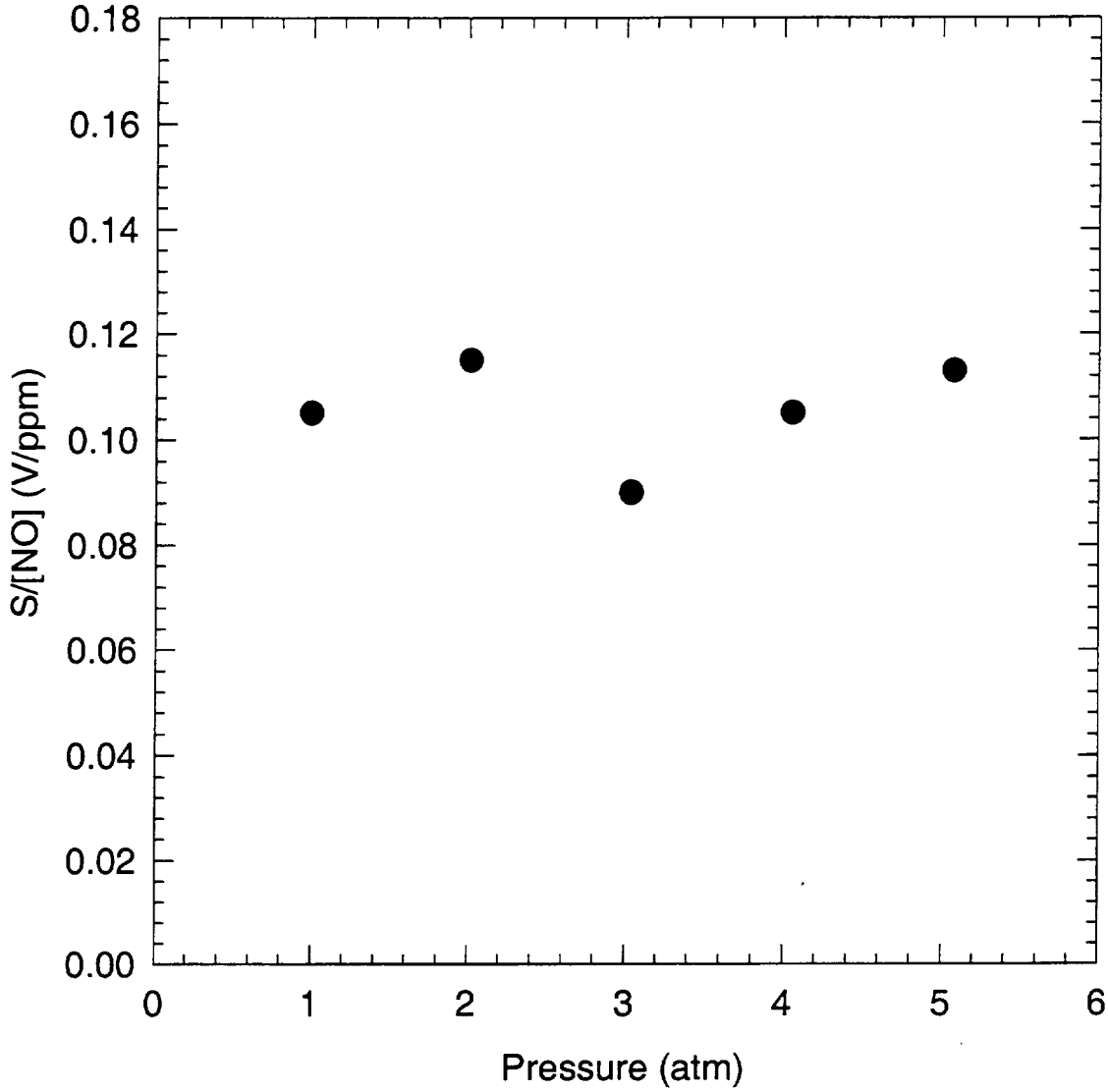

Figure D.1: Ratio of NO fluorescence signal to actual NO concentration in ppm for counterflow premixed flames as a function of pressure.

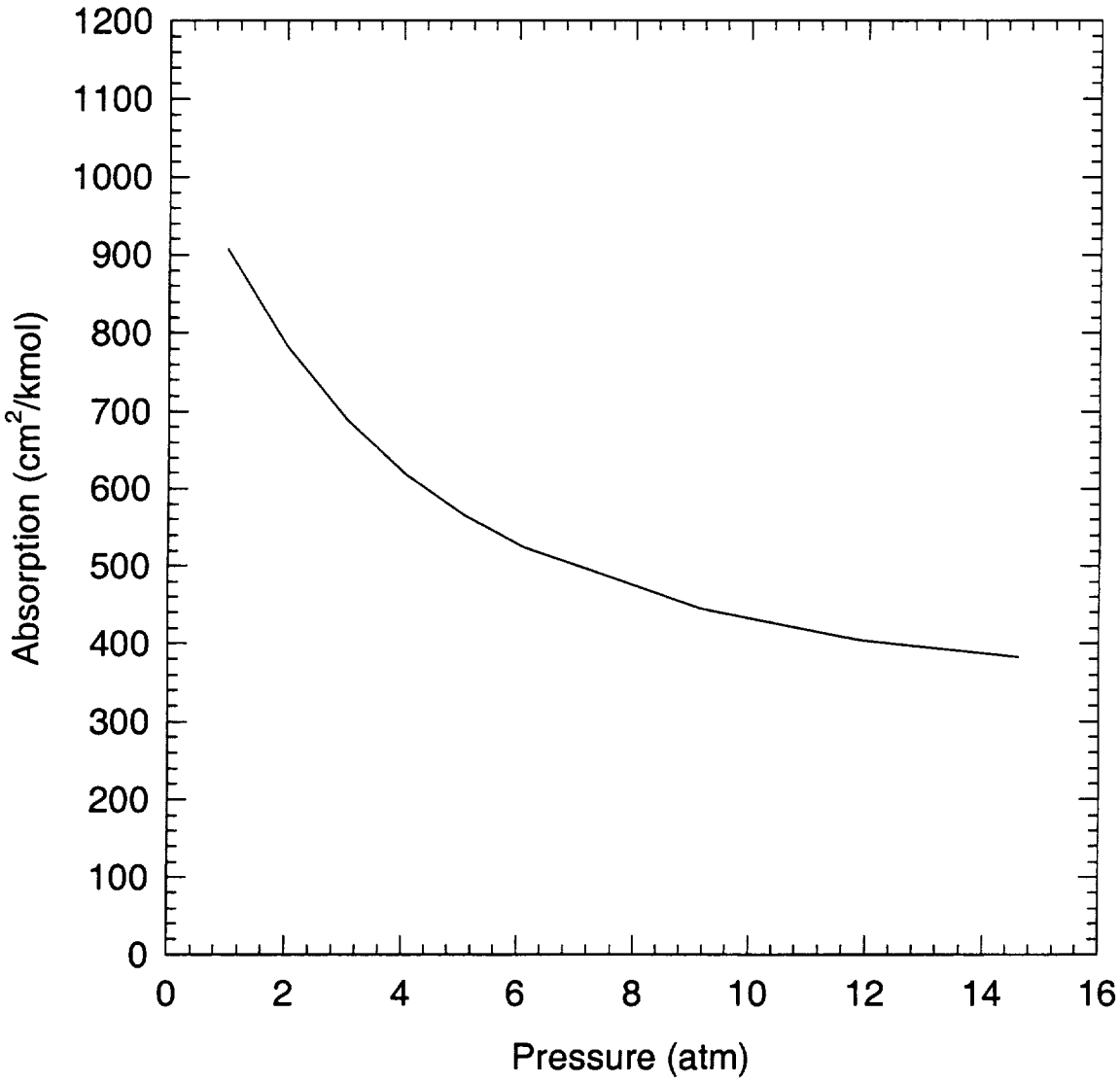

Figure D.2: The variation of NO absorption coefficient with pressure. The absorption is calculated at a temperature of 1800 K at each pressure.

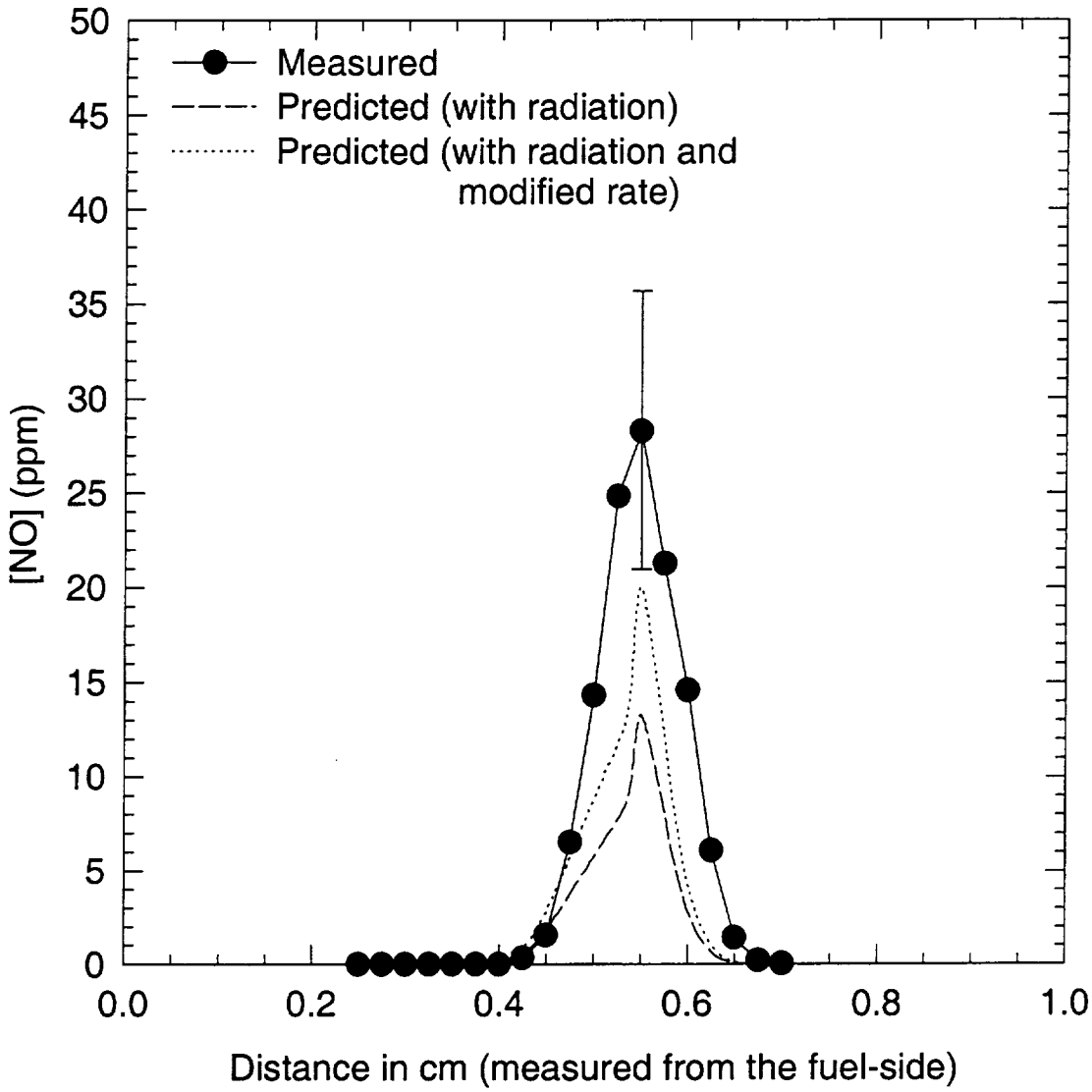

Figure D.3: Comparison of LIF Measurements of [NO] and model predictions in a 30 s^{-1} strain rate flame at 6 atm. The dashed line indicates predictions accounting for radiation, whereas the dotted line indicates predictions with radiation and a previously modified rate coefficient for the prompt-NO initiation reaction.

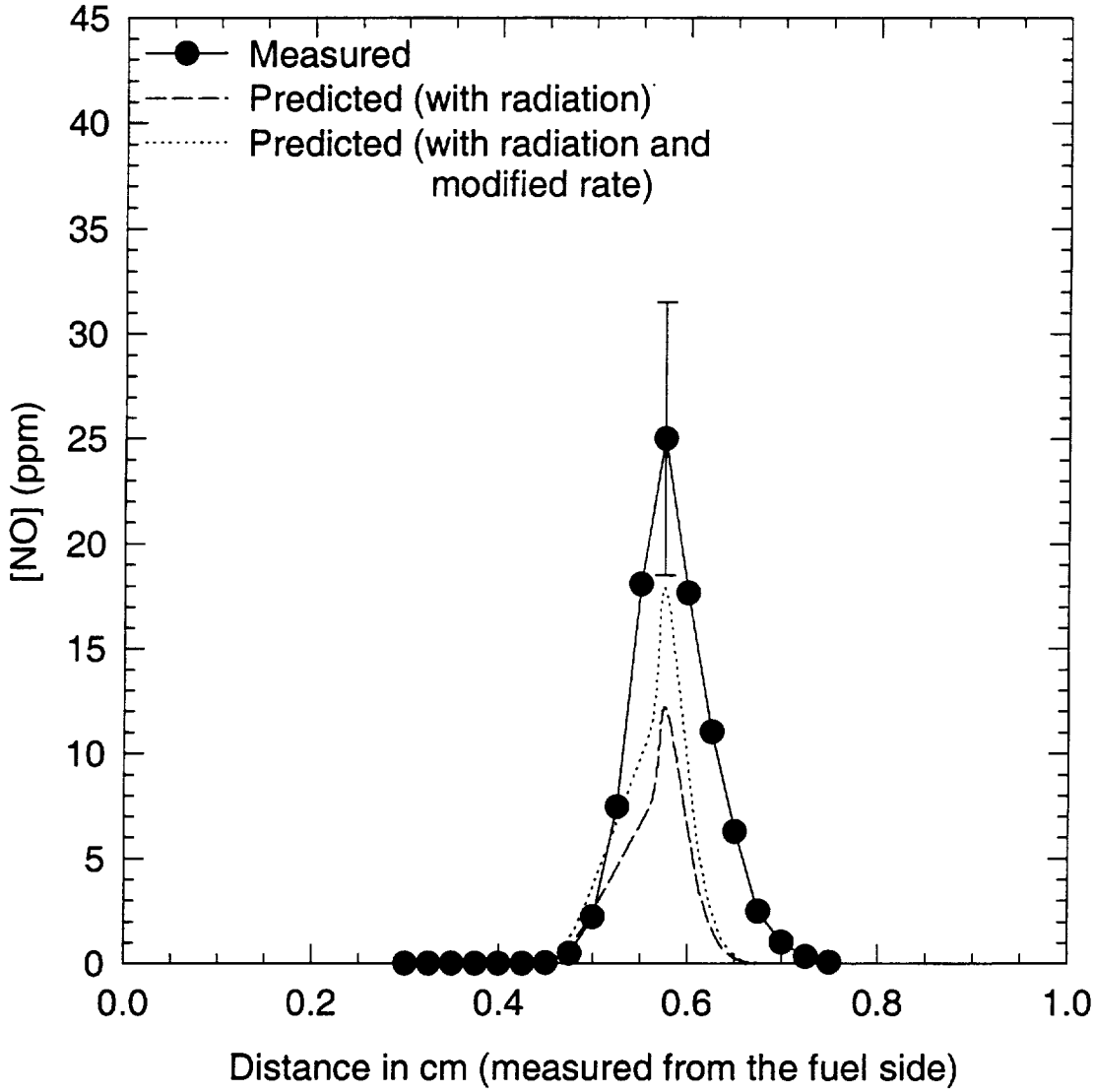

Figure D.4: Comparison of LIF Measurements of [NO] and model predictions in a 30 s^{-1} strain rate flame at 8 atm. The dashed line indicates predictions accounting for radiation, whereas the dotted line indicates predictions with radiation and a previously modified rate coefficient for the prompt-NO initiation reaction.

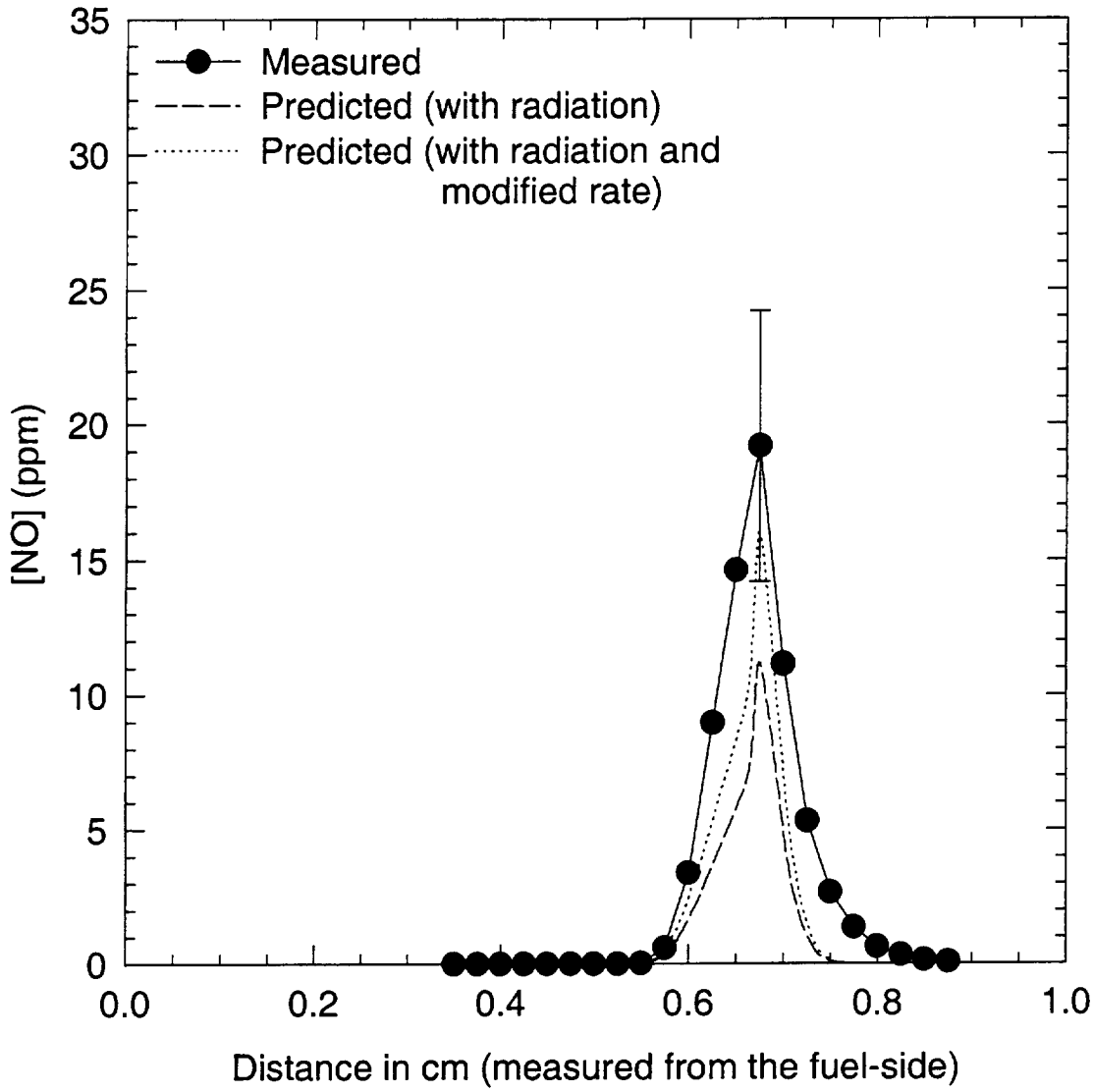

Figure D.5: Comparison of LIF Measurements of [NO] and model predictions in a 30 s^{-1} strain rate flame at 10 atm. The dashed line indicates predictions accounting for radiation, whereas the dotted line indicates predictions with radiation and a previously modified rate coefficient for the prompt-NO initiation reaction.

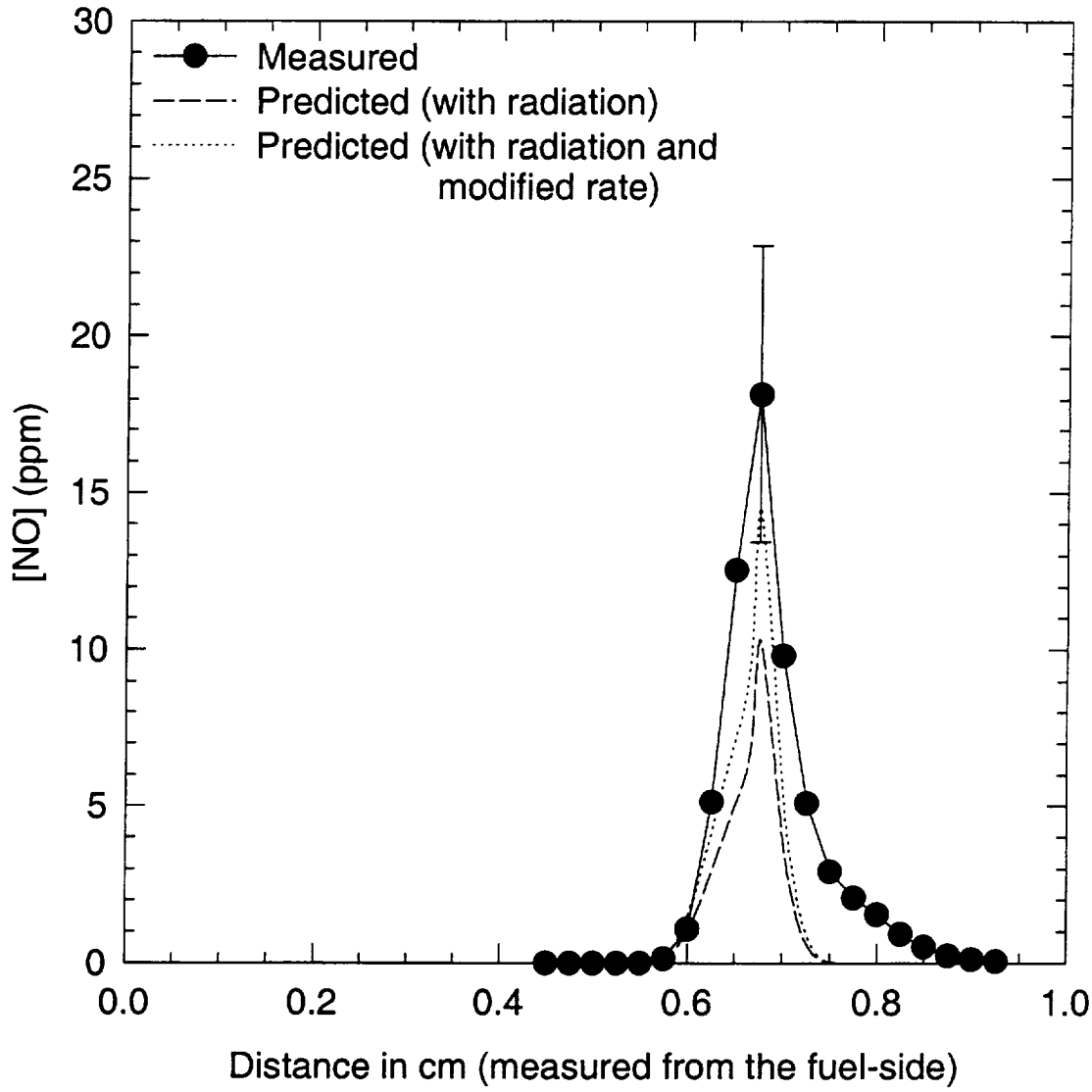

Figure D.6: Comparison of LIF Measurements of [NO] and model predictions in a 30 s^{-1} strain rate flame at 12 atm. The dashed line indicates predictions accounting for radiation, whereas the dotted line indicates predictions with radiation and a previously modified rate coefficient for the prompt-NO initiation reaction.

REPORT DOCUMENTATION PAGE

Form Approved
OMB No. 0704-0188

Public reporting burden for this collection of information is estimated to average 1 hour per response, including the time for reviewing instructions, searching existing data sources, gathering and maintaining the data needed, and completing and reviewing the collection of information. Send comments regarding this burden estimate or any other aspect of this collection of information, including suggestions for reducing this burden, to Washington Headquarters Services, Directorate for Information Operations and Reports, 1215 Jefferson Davis Highway, Suite 1204, Arlington, VA 22202-4302, and to the Office of Management and Budget, Paperwork Reduction Project (0704-0188), Washington, DC 20503.

1. AGENCY USE ONLY (*Leave blank*)	2. REPORT DATE	3. REPORT TYPE AND DATES COVERED
	February 2000	Final Contractor Report

4. TITLE AND SUBTITLE

Laser-Induced Fluorescence Measurements and Modeling of Nitric Oxide in Couterflow Diffusion Flames

5. FUNDING NUMBERS

WU–538–17–10–00
NAG3–1782 and
NAG3–2251

6. AUTHOR(S)

Rayavarapu V. Ravikrishna and Normand M. Laurendeau

7. PERFORMING ORGANIZATION NAME(S) AND ADDRESS(ES)

Purdue University
West Lafayette, Indiana 47907

8. PERFORMING ORGANIZATION REPORT NUMBER

E–12111

9. SPONSORING/MONITORING AGENCY NAME(S) AND ADDRESS(ES)

National Aeronautics and Space Administration
John H. Glenn Research Center at Lewis Field
Cleveland, Ohio 44135–3191

10. SPONSORING/MONITORING AGENCY REPORT NUMBER

NASA CR—2000-209805

11. SUPPLEMENTARY NOTES

Project Manager, Yolanda R. Hicks, Turbomachinery and Propulsion Systems Division, NASA Glenn Research Center, organization code 5830, (216) 433–3410.

12a. DISTRIBUTION/AVAILABILITY STATEMENT

Unclassified - Unlimited
Subject Categories: 09, 23, 34, and 35 Distribution: Nonstandard

This publication is available from the NASA Center for AeroSpace Information, (301) 621–0390.

12b. DISTRIBUTION CODE

13. ABSTRACT ***(Maximum 200 words)***

The feasibility of making quantitative nonintrusive NO concentration ([NO]) measurements in nonpremixed flames has been assessed by obtaining laser-induced fluorescence (LIF) measurements of [NO] in counterflow diffusion flames at atmospheric and higher pressures. Comparisons at atmospheric pressure between laser-saturated fluorescence (LSF) and linear LIF measurements in four diluted ethane-air counterflow diffusion flames with strain rates from 5 to 48 s^{-1} yielded excellent agreement from fuel-lean to moderately fuel-rich conditions, thus indicating the utility of a model-based quenching correction technique, which was then extended to higher pressures. Quantitative LIF measurements of [NO] in three diluted methane-air counterflow diffusion flames with strain rates from 5 to 35 s^{-1} were compared with OPPDIF model predictions using the GRI (version 2.11) chemical kinetic mechanism. The comparisons revealed that the GRI mechanism underpredicts prompt-NO by 30-50% at atmospheric pressure. Based on these measurements, a modified reaction rate coefficient for the prompt-NO initiation reaction was proposed which causes the predictions to match experimental data. Temperature measurements using thin filament pyrometry (TFP) in conjunction with a new calibration method utilizing a near-adiabatic H_2-air Hencken burner gave very good comparisons with model predictions in these counterflow diffusion flames. Quantitative LIF measurements of [NO] were also obtained in four methane-air counterflow partially-premixed flames with fuel-side equivalence ratios (ϕ_B) of 1.45, 1.6, 1.8 and 2.0. The measurements were in excellent agreement with model predictions when accounting for radiative heat loss. Spatial separation between regions dominated by the prompt and thermal NO mechanisms was observed in the $\phi_B = 1.45$ flame. The modified rate coefficient proposed earlier for the prompt-NO initiation reaction improved agreement between code predictions and measurements in the region where prompt-NO dominates. Finally, LIF measurements of NO were obtained in counterflow diffusion flames at 2 to 5 atm. Comparisons between [NO] measurements and predictions show that the GRI mechanism underpredicts prompt-NO by a factor of two to three at all pressures. In general, the results indicate a need for refinement of the CH chemistry, especially the pressure-dependent CH formation and destruction reactions.

14. SUBJECT TERMS

Combustion; Counterflow diffusion flames optical measurements; Laser-induced fluorescence

15. NUMBER OF PAGES

197

16. PRICE CODE

A09

17. SECURITY CLASSIFICATION OF REPORT	18. SECURITY CLASSIFICATION OF THIS PAGE	19. SECURITY CLASSIFICATION OF ABSTRACT	20. LIMITATION OF ABSTRACT
Unclassified	Unclassified	Unclassified	